
**THREE-DIMENSIONAL
MAGNETOHYDRODYNAMIC SIMULATIONS OF
IO'S NON-LINEAR INTERACTION WITH THE
JOVIAN MAGNETOSPHERE**

INAUGURAL-DISSERTATION

ZUR

ERLANGUNG DES DOKTORGRADES

DER MATHEMATISCH-NATURWISSENSCHAFTLICHEN FAKULTÄT

DER UNIVERSITÄT ZU KÖLN

VORGELEGT VON
SVEN JACOBSEN
AUS HAMM (WESTF.)

Berichterstatter: Prof. Dr. J. Saur
Prof. Dr. F. M. Neubauer

Tag der mündlichen Prüfung: 19.05.2011

In an extreme instance, in which there is a Propervirt of less than 0.9%, the TEXT OF THE PRESENT PROSPECTUS may likewise undergo an ABRUPT change. If, while you are reading these sentences, the words begin to jump about, and the letters quiver and blur, please interrupt your reading for ten or twenty seconds to wipe your glasses, adjust your clothing, or the like, and then start reading AGAIN from the beginning, and NOT JUST from the place where your reading was interrupted, since such a TRANSFORMATION indicates that a correction of DEFICIENCIES is now taking place.

Stanisław Lem (Imaginary Magnitude, 1984)

Abstract

For the present dissertation an advanced three-dimensional MHD model has been developed to investigate the interaction of Io with the Jovian magnetosphere. The interrelation we study in the present work originates from the relative movement of a satellite with respect to the surrounding magnetic field and magnetospheric plasma. Several phenomena like auroral, radio emissions and energetic electron beams are associated with such interaction. The type of interaction is common in the Jovian system. Besides Io, other Galilean moons like Europa and Ganymede likewise interact with the surrounding magnetoplasma. Moreover Saturn's moon Enceladus exhibits similar interplay. Hence, the plasmaphysical satellite-planet interaction, best known for Io, is most likely common in the universe and thus worthwhile to be closely investigated.

Io's relative motion in the plasma torus perturbs the magnetospheric plasma. The generated plasma waves are partly reflected at plasma density gradients, but also at the auroral acceleration region. The result is a complex and fluctuating wave pattern located downstream of Io. This is documented by the highly structured auroral imprint of this pattern which was found to exhibit considerable temporal variations. Another consequence of the electromagnetic interaction of Io with the magnetoplasma is the generation of trans-hemispheric energetic electron beams in the auroral acceleration region. These beams have been detected in-situ in the equatorial plane by the *Galileo* probe. Auroral spots in the conjugate hemisphere associated with these beams were also identified remotely in HST observations. They have the outstanding property, that they are, other than the reflection associated footprint pattern, sometimes located upstream of the main Io footprint. However, also this position was found to vary notably. Partly the variations of Io's imprint in the aurora can be described, by Io's oscillation in the plasma torus. Yet, this concept cannot explain all observations.

In order to study the interaction system in detail, we enhance an ideal MHD model by incorporating an effective collision frequency to account for Io's interaction with the incoming plasma. Moreover, we implement resistivity in order to allow for the potential drop in the auroral acceleration region. Different plasma density domains represent the various plasma regimes along the travel path of the waves. We investigate how and to what extent different factors influence the Io footprint morphology and conclude that particularly the interaction strength has an impact on the reflection geometry and thus on the footprint pattern. Our results agree qualitatively with observational findings. Our model allows furthermore to deduce locations of equatorial electron beams. The results match the locations of actual beam detections by *Galileo*. We also present a separate model to estimate inter-spot distances and compare our predictions to both, the observations and the Simulation results. Besides to Io, we apply our model to the interaction of Enceladus with Saturn. We weight the possibility of Alfvén wave reflection in this particular case, and find possible evidence for a reflected Alfvén wave signature in the Cassini magnetic field observations. We support this hypotheses by results obtained with our numerical model.

Zusammenfassung

Die vorliegende Dissertation beschäftigt sich mit der plasmaphysikalischen Kopplung zwischen Jupiter und seinem Mond Io. Der Innerste der vier großen Galileischen Monde ruft Polarlichterscheinung in Jupiters Ionosphäre, Radioemissionen und energetische Teilchenströme entlang des lokalen Magnetfelds hervor. Wie genau die Kopplung der Prozesse bei Io an die weit entfernten Phänomene in Jupiters Polarregionen erfolgt und was diese Kopplung beeinflusst ist Gegenstand dieser Arbeit.

Ios Umlaufbahn um Jupiter befindet sich in einer Region besonders dichten magnetosphärischen Plasmas. Es bildet einen Gürtel oder Ring um Jupiter, den sogenannten Plasmatorus. Dieser Torus, wie auch das gesamte Plasma in der inneren Jupitermagnetosphäre, steht nicht still, sondern rotiert fast synchron mit Jupiter. Die geladenen Teilchen sind aufgrund elektromagnetischer Kräfte an Jupiters Magnetfeld gebunden und werden so zur Korotation gezwungen. Io besitzt eine niedrigere Geschwindigkeit als das ihn umgebende Plasma und ist dadurch einem kontinuierlichen Strom geladener Teilchen ausgesetzt. Darüberhinaus besitzt Io selbst eine elektrisch leitfähige Ionosphäre. Zusammenfassend stellt er so ein leitfähiges Hindernis in einem Strom geladener Teilchen dar, die über das Magnetfeld mit Jupiters Polarregionen verbunden sind: Dies sind die Zutaten für die Wechselwirkung zwischen Io und Jupiter.

Io lenkt das anströmende Plasma um und stört so das Strömungsbild. Die Störung breitet sich nun in Form von Plasmawellen in der Magnetosphäre aus. Eine Wellenmode, die dabei angeregt wird, besitzt die besondere Eigenschaft elektrischen Strom nahezu verlustfrei entlang des Magnetfelds zu transportieren, die sogenannte Alfvénmode. Sie ist in erster Linie für die elektromagnetische Kopplung zwischen Io und Jupiter verantwortlich. Das Plasma, durch das sich diese Welle fortpflanzt, ist jedoch heterogen und an Grenzflächen zwischen verschiedenen Plasmabereichen wie z.B. am Rand des Plasmatorus wird die Welle teilweise reflektiert. Es gibt noch weitere Reflektoren wie zum Beispiel Jupiters Ionosphäre. Oberhalb der Jupiterionosphäre befindet sich die sogenannte Beschleunigungsregion und auch hier treten partielle Reflexionen auf. In diesem Bereich beschleunigt die Welle Elektronen parallel und antiparallel zum Magnetfeld. Die schnellen, hoch energetischen Elektronen stürzen so zum einen weiter in Jupiters Ionosphäre, wo sie Aurora hervorrufen, zum anderen bewegen sie sich entlang der Feldlinie von Jupiter weg und durchstoßen die Äquatorebene. Hier wurde dieser Strahl von Elektronen von der *Galileo* Sonde detektiert [Williams *et al.*, 1999; Williams and Thorne, 2003]. Der Strahl setzt sich jedoch fort und folgt dem Magnetfeld bis in die Polarregion auf der gegenüberliegenden Hemisphäre. Dort macht sich dieser Teil der beschleunigten Elektronen ebenfalls durch Polarlichterscheinungen bemerkbar Bonfond *et al.* [2008]. Alles in allem entsteht auf diese Weise ein kompliziertes Wellenmuster im Plasma "stromabwärts" hinter Io. Eingebettet in das Wellenfeld finden sich zudem Elektronenstrahlen.

Dieses Wellenmuster und die Elektronenstrahlen hinterlassen sozusagen einen Fußabdruck im Polarlicht von Jupiter. Er ist dort erstmals von Connerney *et al.* [1993] beobachtet worden. Nachfolgende Untersuchungen zeigten die Feinstruktur des

sogenannten Io-Fußpunkts [z.B. *Gérard et al.*, 2006]. Die Emission besteht aus einem Hauptmaximum und einer ausgedehnten Schweifstruktur mit mehreren eingebetteten lokalen Helligkeitsmaxima. Letztere sind den unterschiedlichen Reflexionen und energetischen Teilchenströmen zuzuordnen. Langzeitbeobachtungen haben gezeigt, dass die Morphologie der Fußpunktmission stark mit Ios orbitaler Position variiert. Zum Teil ist dies geometrischen Effekten zuzuschreiben. Die Mittelebene des Plasmatorus ist nämlich gegenüber Ios Umlaufebene geneigt, so dass sich Io im Torus auf und ab bewegt. Dadurch verändern sich stetig die Abstände zu den reflektierenden Grenzflächen und letztendlich auch das Fußpunktmuster in der Aurora. Allein mit diesem Ansatz lassen sich allerdings die Beobachtungen nicht erklären.

In dieser Arbeit entwickeln wir ein numerisches Modell zur Untersuchung des von Io angeregten Wellenmusters. Unser Modell ist das erste dreidimensionale Modell, das Entsprechungen für alle an Reflexionen beteiligten Plasmabereiche enthält. Zudem beinhaltet es eine elektrisch resistive Schicht, die die Beschleunigungsregion repräsentiert.

In grundlegenden Studien gelingt es uns nachzuweisen, dass die Wellenamplitude einen bedeutenden Einfluss auf den Reflexionsprozess hat. Nichtlineare Effekte sorgen im Fall großer Wellenamplituden dafür, dass ein reguläres Reflexionsgesetz mit identischem Ein- und Ausfallswinkel hier nicht gilt. Vielmehr kann die Welle im Extremfall sogar in sich zurücklaufen. Dies hat natürlich auch Auswirkungen auf die Morphologie des Io Fußpunkts. Konkret verringern sich die Abstände der einzelnen Helligkeitsmaxima und sie verschmelzen gegebenenfalls zu einem einzigen verlängerten Fußpunkt. Dieser Zusammenhang war bisher nicht bekannt und unsere Simulationsergebnisse bestätigen damit erstmals Beobachtungen, die zeigen, dass keine lokalen Emissionsmaxima im Fußpunktschweif festzustellen sind, wenn Io sich im Zentrum des Plasmatorus befindet [*Gérard et al.*, 2006], wo die Wellenamplitude am größten ist.

Desweiteren untersuchen wir den Einfluss unterschiedlicher Reflektoren auf das Wellenmuster. Wir vergleichen Reflexionen an der Beschleunigungsregion mit denen an der Jupiterionosphäre und stellen im Detail große Unterschiede fest. Auf die großskalige Struktur des Fußpunktmusters wirkt sich die Art des Reflektors jedoch weniger aus.

Zusätzlich zur Untersuchung von Ios Wellenfeld verwenden wir unser Modell, um die Lage der energetischen Teilchenströme zu ermitteln. Da weder die mikrophysikalischen Prozesse, die zur Erzeugung dieses Elektronenstrahls führen, noch die Ausbreitung der Teilchen selbst in unserem Modell enthalten sind, verwenden wir ein indirektes Verfahren das auf unseren Simulationsergebnissen beruht. Die Ergebnisse bestätigen erstmals numerisch die in-situ Beobachtungen energetischer Elektronen der *Galileo* Sonde von *Williams et al.* [1999] und *Williams and Thorne* [2003]. Verfolgt man den Elektronenstrahl weiter, so stimmt die Position des zu erwartenden Fußpunktmerkmals mit den Beobachtungen von *Bonfond et al.* [2008] und *Bonfond et al.* [2009] weitestgehend überein. Dieses Ergebnis legt nahe, dass die beiden unabhängigen Beobachtungen auf den gleichen Strahl energetischer Elektronen zurückzuführen sind.

In unserer Arbeit kombinieren wir unter anderem ein Magnetfeldmodell [*Connerney et al.*, 1998] mit einem Plasmadichtemodell [*Bagenal*, 1994]. Dieser Bestandteil

unseres Modells dient der Implementierung eines möglichst realistischen Profils der Ausbreitungsgeschwindigkeit der Alfvénwelle. Unabhängig von dieser Anwendung jedoch benutzen wir diesen Teil unserer Arbeit auch dazu, erstmalig modellbasierte Abschätzungen für die zu erwartenden Abstände der einzelnen Fußpunkte zu bekommen. Wir vergleichen diese Erwartungswerte mit den Beobachtungen und bemerken teils sehr gute Übereinstimmung aber auch systematische Abweichungen, die nach unseren Erkenntnissen auf die nichtlineare Natur der Reflexionen zurückzuführen sind.

Laut neuesten Veröffentlichungen weist auch der Saturnmond Enceladus eine ähnliche Wechselbeziehung zu seinem Mutterplaneten auf wie Io. Wir wenden daher unser Modell auch auf dieses System an. Unsere Simulationen zeigen einen Elektronenstrahl, dessen Lage qualitativ mit den Beobachtungen übereinstimmt [Pryor *et al.*, 2011]. Ausserdem interpretieren eine gemessene Magnetfeldstörung [Jia *et al.*, 2010a] erstmals als Signatur einer reflektierten Alfvénwelle und finden Bestätigung dafür in unseren Simulationsdaten.

Alles in allem wenden wir unser Modell mit Erfolg auf verschiedene Aspekte der elektromagnetischen Wechselwirkung zwischen Monden und Planeten an. Auf diese Weise können wir sowohl einige bisherige Beobachtungen numerisch bestätigen, als auch neue Zusammenhänge feststellen.

Contents

| | | |
|----------|--|-----------|
| I | Background | 1 |
| 1 | Introduction | 3 |
| 2 | Io: Observations and Previous Models | 7 |
| 2.1 | Io in the Spotlight | 7 |
| 2.2 | Jupiter’s Magnetosphere | 9 |
| 2.3 | Volcanism and Atmosphere | 11 |
| 2.4 | Properties of the Ambient Plasma Flow | 12 |
| 2.5 | Io’s Local Interaction: The Generator | 14 |
| 2.5.1 | The Unipolar Inductor Model | 15 |
| 2.5.2 | The Alfvén Wing Model | 17 |
| 2.5.3 | Other Models | 18 |
| 2.6 | The Far Field Interaction: The Coupling | 19 |
| 2.6.1 | Alfvén Wave Propagation and Reflections | 19 |
| 2.6.2 | Acceleration Region | 21 |
| 2.6.3 | Equatorial Electron Beams | 21 |
| 2.7 | Emissions from Jupiter’s Polar Regions: The Load | 24 |
| 2.7.1 | Radio Emissions | 24 |
| 2.7.2 | Auroral Footprints | 25 |
| 3 | Enceladus: Observations and Previous Models | 32 |
| 3.1 | General Overview | 32 |
| 3.2 | Saturn’s Magnetic Field and Ring System | 34 |
| 3.3 | Cryovolcanism, Atmosphere and Plume Material | 34 |
| 3.4 | The Ambient Plasma | 36 |
| 3.5 | Analytical and Numerical Models of the Local Interaction | 37 |
| 3.6 | The Enceladus Footprint | 38 |

| | | |
|------------|--|-----------|
| II | Model | 41 |
| 4 | Theoretical Framework | 43 |
| 4.1 | The Ideal MHD Equations | 43 |
| 4.2 | The General Alfvén Wing Model | 45 |
| 4.3 | Parallel Electric Fields and the Knight Formula | 47 |
| 4.4 | Non-Ideal MHD: Additional Terms | 49 |
| 4.4.1 | Effective Collision Frequency | 49 |
| 4.4.2 | Resistivity | 50 |
| 4.5 | Alfvén Wave Reflection | 52 |
| 4.5.1 | Reflections at Density Gradients | 52 |
| 4.5.2 | Reflections at the Auroral Acceleration Region | 54 |
| 4.6 | Electron Beams | 55 |
| 4.6.1 | Poynting Flux as Surrogate for Electron Beam Intensity | 58 |
| 4.6.2 | Equatorial Electron Beam Position | 59 |
| 5 | Numerical Implementation | 62 |
| 5.1 | The Solver: ZEUS-MP | 62 |
| 5.2 | Simulation Geometry and Setups | 63 |
| 5.2.1 | Basic Setup | 64 |
| 5.2.2 | Electron Beam Setup | 65 |
| 5.2.3 | The Density Model | 68 |
| 5.2.4 | The Magnetic Field Model | 69 |
| 5.2.5 | The Alfvén Velocity and Travel Times Model | 71 |
| III | Results | 77 |
| 6 | Io | 79 |
| 6.1 | Alfvén Wave Generation | 79 |
| 6.2 | Alfvén Wave Reflection | 85 |
| 6.3 | Footprint Morphology | 87 |
| 6.4 | Equatorial Electron Beams | 93 |
| 6.5 | Trans Hemispheric Electron Beams | 108 |
| 6.6 | Inter-Spot Distances | 111 |
| 6.6.1 | Estimates Derived From the Travel Time Model | 111 |
| 6.6.2 | Comparison with Observations | 114 |
| 6.6.3 | Comparison with Simulation Results | 117 |

| | | |
|-----------|---|------------|
| 7 | Enceladus | 122 |
| 7.1 | Hints for Alfvén Wave Reflections | 122 |
| 7.2 | Magnetic Field Data | 128 |
| 7.3 | Equatorial Electron Beams | 130 |
| 8 | Conclusions | 131 |
| | | |
| IV | Appendix | 135 |
| 8.1 | Coordinate Systems Jupiter | 137 |
| 8.1.1 | System III | 137 |
| 8.1.2 | Latitudinal Reference Systems | 138 |
| 8.2 | Code Modifications | 139 |
| 8.2.1 | Time Step Size | 141 |
| | References | 143 |

Part I

Background

Chapter 1

Introduction

When Galileo Galilei pointed one of the world's first telescopes at Jupiter in 1610, he discovered four satellites: Io, Europa, Ganymede and Callisto (Figure 2.1). They are called *Galilean Moons* after their discoverer. Io, the innermost moon was named after one of the liaisons of Zeus, the father of the gods (Jupiter in Roman mythology). Unwittingly, the name for the satellite was felicitously chosen, for we know today that from the plasmaphysical point of view there is indeed a close connection between Jupiter and Io. The details of this interaction are the subject of this work.

Io orbits Jupiter at a distance of only 5.9 Jovian radii. It is embedded in a torus of dense plasma. The charged plasma particles are sensitive to electromagnetic forces and are thus linked to Jupiter's magnetic field. The magnetic field, however, rotates with the planet and hence this belt of dense ionized material is almost rigidly revolving with Jupiter. Io's orbital velocity is considerably smaller than the spinning plasma. Thus there is a continuous flow of plasma around the satellite. Io possesses moreover an ionosphere and therefore represents a conductive obstacle in a stream of charged particles that are connected to Jupiter by the magnetic field. These are the ingredients for the electromagnetic Io-Jupiter interaction.

Io deflects and distorts the incoming plasma flow and this perturbation propagates away from the obstacle in the form of plasma waves. Although different wave modes are generated, the most important for the interaction is the Alfvén wave named after *Hannes Alfvén*, the Nobel Prize winner in physics of 1970. The outstanding property of these plasma waves is that they are able to communicate electric currents almost lossless over large distances, predominantly along the ambient magnetic field. In the Io-Jupiter case, these waves generated at Io follow the Jovian magnetic field and eventually reach Jupiter's polar regions. Here, the current system closes and the interaction causes numerous effects. Among these are intense radio emissions that emerge from magnetic field lines connected to Io. Most important for the present thesis are, however, auroral emissions generated in Jupiter's ionosphere at the footprints of the perturbed magnetic field lines. This feature in the aurora is called the "Io footprint" and is visible at infrared (IR), ultraviolet (UV) and visible wavelengths.

In analogy to electric circuits we could regard Io as the generator and Jupiter as the load. Both are connected via the magnetospheric plasma that is linked to the wire-

like magnetic field lines. This picture is convenient and comprehensibly represents the interconnectedness of different magnetospheric regions. Nonetheless, there are pitfalls to this approach as there are no discrete wires in space but currents flow in distributed plasmas.

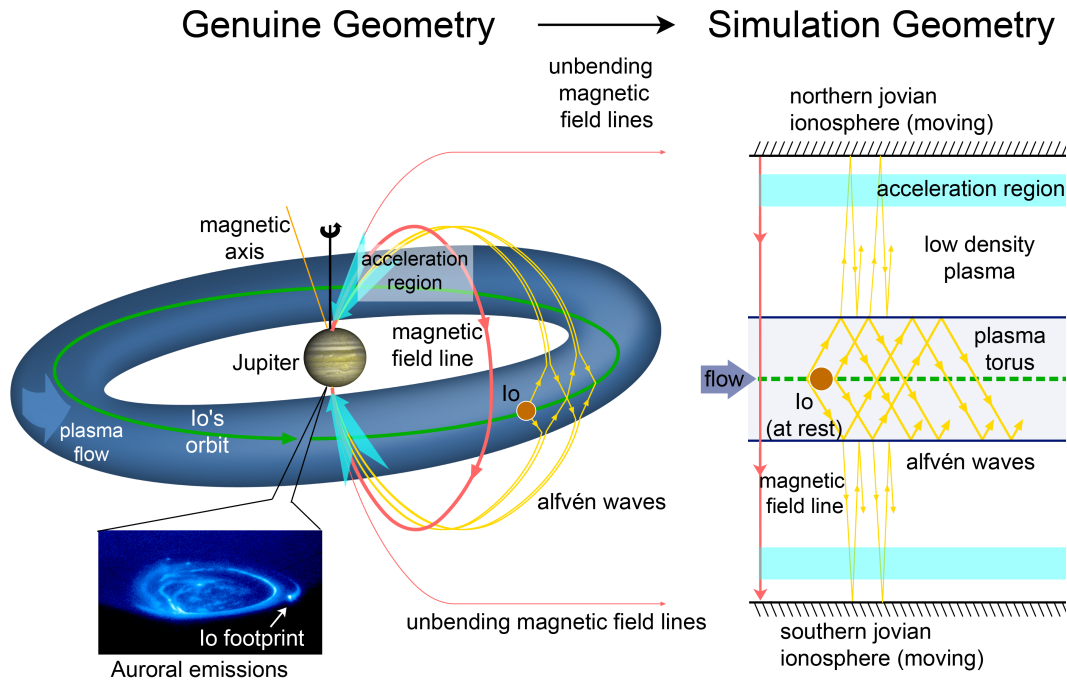


Figure 1.1: Schematic view of the Io-Jupiter interaction in actual geometry (left) and in the rectified geometry applied in our numeric implementation (right).

In the Io-Jupiter scenario, the currents are transmitted via Alfvén waves that on their way to Jupiter's polar regions eventually leave the dense medium of the plasma torus. Like other waves, they are partly reflected at interfaces between different propagation mediums. Hence the perturbation partly returns into the torus and further disturbs the plasma in Io's corotational wake. Downstream of Io a complicated pattern of reflected waves forms, which are able to partly escape the torus and leave eventually an imprint in the Jovian aurora. This is manifested by an extended tail emission structure that trails the main auroral spot and comprises multiple luminosity maxima which are the counterparts of the reflections. In this sense the auroral pattern represents the "screen" for the magnetospheric wave sequence.

The comparison of the Jovian ionospheric response with a screen is apt also in another sense. In fact, the auroral emissions on Jupiter are generally not excited directly by the Alfvén waves themselves but the waves accelerate electrons that eventually precipitate into the ionosphere. This takes place in the auroral acceleration region (AAR) close to Jupiter. The beam of accelerated highly energetic electrons that causes luminous effects on the ionospheric "screen" is to some extent reminiscent of the layout of a Braun tube or cathode ray tube (CRT) as used in many old monitors and TVs. Apart from electrons that are beamed directly down into the Jovian Ionosphere, some electrons are also accelerated upward. These beams pen-

trate the equatorial plane close to Io and continue to the conjugate hemisphere, where they cause likewise auroral emissions separated by a few degrees from the main auroral spot.

Observation campaigns of Jupiter's UV aurora by the *Hubble Space Telescope* (HST) revealed notable variation of the footprint morphology such as the spacing between the different footprints, but also the number of observed emission maxima downstream in the tail. Partly these changes can be attributed to a tilt of the torus central plane with respect to Io's orbital plane (see Figure 1.1). This inclination causes Io to move up and down in the plasma torus and thus the reflection geometry changes as the distances to the reflecting interfaces varies. Yet, this concept cannot account for all variations observed in the spot pattern. It is known that the interaction strength varies when Io moves from the torus center to the edges, as the impinging plasma density changes from dense to dilute. This has also implications for reflection pattern and the footprint morphology. Finally, apart from reflections that occur at the torus boundaries, the ionosphere and the acceleration region represent additional reflectors. The result of all these superimposed wave reflections that interact and interfere is a complicated pattern which furthermore fluctuates with Io's position in the plasma torus. Our aim is to increase the understanding of the processes that influence this pattern.

Analytical theory has been successfully applied to describe certain aspects of the wave pattern and the interaction. The global description including all plasma regimes, all reflectors and moreover the interrelation between different reflections is not accessible with analytical methods. Therefore we chose a numerical approach to investigate the electromagnetic coupling between Io and Jupiter.

We use a three-dimensional single fluid magnetohydrodynamical (MHD) model to describe the wave generation, propagation, reflections and wave-wave interactions. Figure 1.1 illustrates how the genuine interaction geometry is converted to our numerical realization. Our simulation geometry is idealized in the sense that we use straight, unbended magnetic field lines (see right part of Figure 1.1). In this configuration, the northern and southern Jovian ionosphere is located at the top and bottom of the simulation box, respectively. The other plasma regimes like the dense torus plasma and the low density plasma population between torus and ionosphere are arranged in layers in our numerical implementation. The AAR is represented likewise by a layer located between torus and ionosphere. As we investigate the interaction in Io's rest frame, the whole density profile is moving from left to right, while Io stays at rest. The resulting wave pattern evolves downstream, i.e. right of Io.

The application of our model is manifold. First we study the influence of the interaction strength on the footprint morphology. Moreover we infer the location of trans-hemispheric electron beams in the equatorial plane near Io. We trace these beams also further to the conjugate hemisphere and determine the location of the resulting auroral spot. Recently, an interrelation similar to the one we observe between Io and Jupiter was reported to occur between Enceladus and Saturn. Hence we also apply our model to this interaction scenario and discuss the differences.

This brief outline of the Io-Jupiter interaction (or Enceladus-Saturn interaction) and our numerical implementation is intended to provide a rough background. We will revisit the different aspects in detail in the remainder of this dissertation.

- In *Part I* we introduce Io and its plasma and magnetic surroundings. We divide the interaction into sub areas and discuss each against the background of observations and previous models. We process Enceladus similarly but more briefly in chapter two.
- *Part II* includes the model description after introducing the theoretical framework it is founded on.
- *Part III* contains our results and a detailed discussion. Furthermore, we qualitatively compare to observational data by the *Galileo* and *Cassini* spacecrafts as well as to HST findings.

Chapter 2

Io: Observations and Previous Models

2.1 Io in the Spotlight

The first historical document that mentions Io (not explicitly under that name) is a letter by Galileo Galilei dated January 7, 1610. He reports his observation of three "stars" near Jupiter. (He discovered the fourth Galilean moon some months later). Figure 2.1 shows a comparison of the four Galilean moons. Subsequent studies determined the orbital periods of the satellites and Pierre-Simon Laplace revealed the orbital resonance (1:2:4) between Io, Europa and Ganymede in 1788.

In this century, the detection of Jupiter's radio emissions by *Burke and Franklin* [1955] was a scientific sensation. Subsequent investigation of the signal's polarization properties proved that the Earth was not the only planet with an intrinsic magnetic field. An Australian meteorologist further discovered the strong correlation between the periodicity of some of the radio burst and Io's orbital position [*Bigg, 1964*] suggesting an electromagnetic coupling between the satellite and the planet, a phenomenon which had not been observed before. These findings boosted Jupiter's attractiveness for space missions and thus with *Pioneer10* and *Pioneer11* the first space probes visited the gas giant in 1973 and 1974, respectively. They provided further insight into Io's interaction with Jupiter and gave first hints of Io's atmosphere [*Kliore et al., 1975*]. Moreover the *Pioneer* findings revealed the high degree of diversity among the Galilean moons. The pictorial idea arose that Jupiter and its satellites represent a "miniature solar system". Hitherto, eight space probes visited Jupiter and scientists have learnt a lot about the electromagnetic coupling between the satellites and Jupiter.

On the other hand, major progress in this field can be attributed to the systematic observation of Jupiter's aurorae e.g. by the HST. Ultraviolet and infrared Emissions emerging from the footprints of the Galilean moons were detected of which the Io footprint is the most intense. Caused by high energy particles precipitating into the atmosphere, aurorae are thought to represent the signature of magnetospheric processes. In this sense, Io's auroral footprint comprises valuable information about

the interaction itself. Recent studies suggest that Enceladus is electrodynamically connected to Saturn in a similar way [Pryor *et al.*, 2011]. Even outside our solar system there are strong hints that Alfvénic coupling possibly takes place between extrasolar planets and their parent stars [Shkolnik *et al.*, 2003; 2005, e.g]. Hence, electrodynamic interplay between two celestial bodies may be common in the universe.

However, Io's interaction in particular remains an outstanding prime example for ongoing science and also for the present thesis for several reasons. First of all,

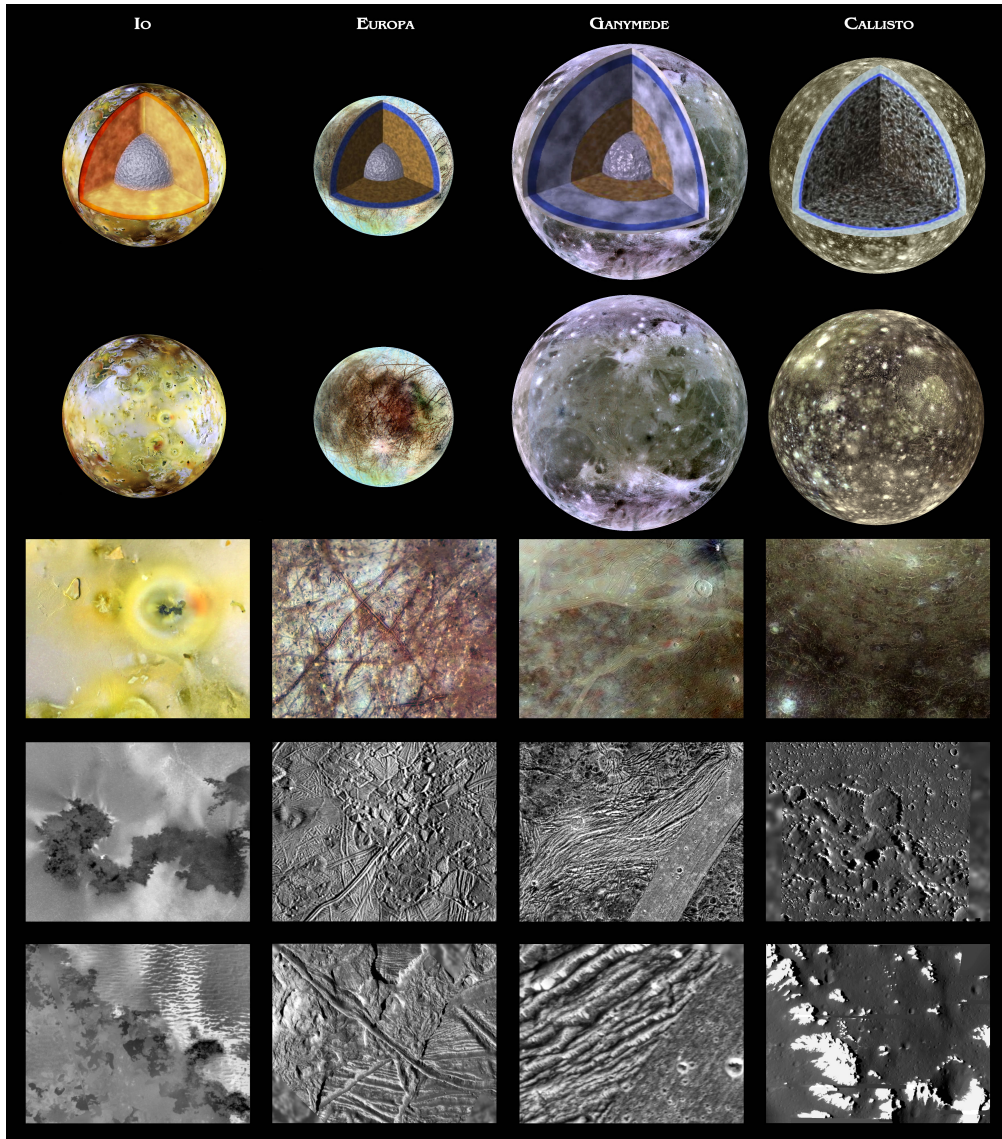


Figure 2.1: The four Galilean moons. The top two rows display global views, one with cut-away views showing current concepts of the interiors. The bottom views show how the surface changes as we zoom in on selected features at progressively higher resolution. Each row down represents an increase in resolution of roughly a factor of ten: the first two rows are at 10 kilometers resolution, increasing to 1 kilometer, 100 meters, and finally 10 meters (bottom). What stands out is the diversity of features at different scales and on the different satellites. [after Schenk, 2010]

the target is relatively close, and the electromagnetic interaction is the most intense in our solar system. The effects are therefore well observable from Earth. Sending probes and collecting in-situ data is possible and has already been done. Moreover, the unique interaction geometry results in a varying strength of the interaction which allows the investigation of a broad range of possible interaction scenarios. Furthermore as we will see in section 2.6.1, the transition of the Alfvén waves between different plasma regimes causes reflections - a very interesting subject and the main topics of the present work. These reflections leave an imprint in the Jovian aurora as well and thus can be remotely sensed by earthbound observations. For these reasons it is not surprising that an extensive data set of Io footprint surveys and Jovian aurora observations was produced during several HST campaigns. The comprehensive database of remote and in-situ observations allows the comparison of numerical simulation results with measurements and thus provides valuable constraints.

2.2 Jupiter's Magnetosphere

The observations of radio emissions by *Burke and Franklin* [1955] cannot only be regarded as a basis for the evidence that Jupiter possesses an intrinsic magnetic field and a magnetosphere, but also provided a means to determine Jupiter's rotation rate. As the gaseous visible surface rotates differentially, it was cumbersome to find an exact rotation period via cloud tracking. However, in absence of alternatives, the first Jovigraphic reference systems called System I and System II were founded on this method. After the detection of Jupiter's radio pulses, the periodicity in the radio signal was considered to reflect the rotation of the Jovian magnetic field and thus its interior [*Shain*, 1955]. The resulting coordinate system is called System III. In the present thesis we will use this system when referring to Jovigraphic coordinates and we denote the longitude by λ_{III} . The definition is given in appendix 8.1.

The next major progress in the exploration of Jupiter's magnetosphere was made particularly by space probe in-situ measurements. The *Pioneer* and *Voyager* observations exposed two significant differences to the Earth's magnetosphere. First of all they discovered the enormous strength of Jupiter's internal dipole. With a magnetic moment of $\sim 1.5 \times 10^{20} \text{ Tm}^3$ it is about 18,000 times larger than the terrestrial value. The strong magnetic field forces the plasma in the inner magnetosphere to fully corotate with the planet. Hence, large parts of the magnetosphere are strongly dominated by the Jovian rotation. Moreover, unlike at Earth, Jupiter's magnetosphere is not populated with primarily heliogenic plasma. The Galilean moons, especially Io, represent the main source of plasma in the magnetosphere. Overall, in Jupiter's magnetosphere internal sources of energy and plasma are much more important than at Earth, where the solar wind is the dominating factor.

After the visits of the *Pioneer* and *Voyager* probes, the *Ulysses* spacecraft carried out a swing-by maneuver at the gas giant. While the first two probes mainly provided in-situ measurements near the equatorial plane, the latter traveled through the Jovian magnetosphere from north to south and yielded rare data from high latitudes. Still, all of these campaigns performed only short-term observations during their flybys. The *Galileo* mission reached the Jovian system in 1995

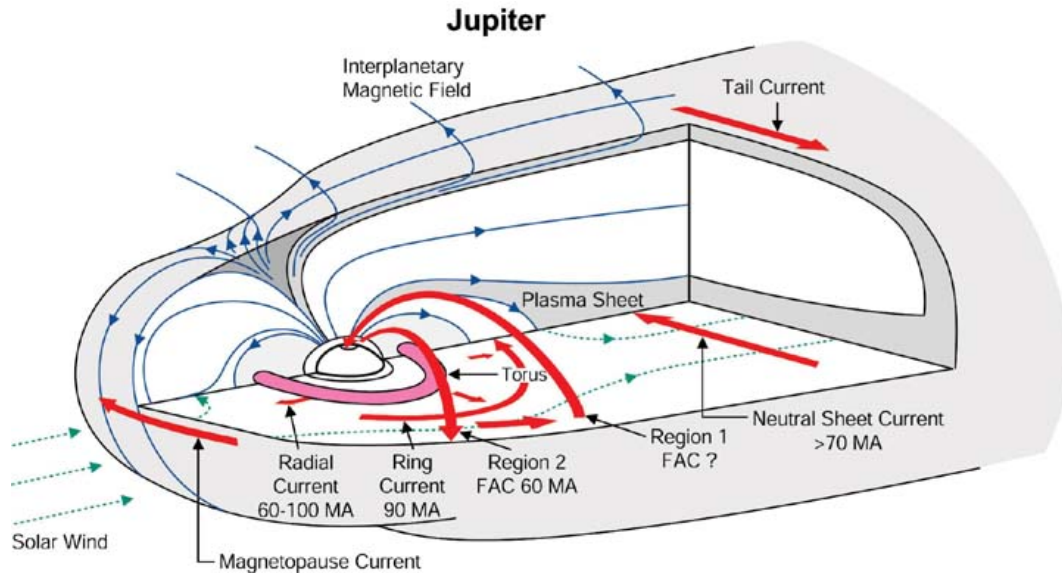


Figure 2.2: A Schematic view of the Jovian magnetosphere [Khurana et al., 2004]. (Dimensions are not to scale)

and provided eight years of long-term observations and also included some high-inclination orbits. However, measurements of a single spacecraft cannot distinguish between spacial and temporal changes in the magnetic field. Thus, the available magnetic field models are still imperfect. The current understanding is as follows: Jupiter's magnetic field can be approximated by a dipole that is tilted by 9.6° against the rotational axis towards $\lambda_{III} = 202^\circ$. Additionally, there is a slight offset of the dipole by $\sim 0.13 R_J$ towards $\lambda_{III} = 148^\circ$ and $\Theta_R = -6^\circ$ (see Figure 8.2 in appendix 8.1 for an illustration and coordinate definitions). However this is just an approximation, as besides the dipole moment there is a substantial contribution of higher order magnetic field terms. Connerney et al. [1982] developed a magnetic field model called *O6*, with Gauss coefficients up to sixth order on the basis of *Voyager1* data. However, due to large errors, only coefficients up to third order are reliable. Higher order constituents decay faster with distance and as space probes keep a safety distance to Jupiter to avoid high radiation environment, the measurement of short wavelength spherical harmonics is only possible with large errors. A means to remotely sense the surface magnetic field topology is to analyze the track of the auroral footprints of the Galilean moons. This technique has been applied by Connerney et al. [1998] who constructed the *VIP4* model in a way such that the observed Io footprints map to the radial distance of the satellite. This model is best suitable for our work, as it further reduces errors especially at Io's orbital distance and it is most commonly used. However, it has not been optimized by footprint mapping in the azimuthal direction and thus still might contain errors in the longitudinal sense. Recent efforts to improve the surface and small wavelength magnetic field model by introducing a local interior anomaly have been made by Grodent et al. [2008]. The authors improve the predicted latitudinal mapping of all visible Galilean moon footprints in the aurora. However, the benefit for Io is least among the Galilean moons and Io's predicted footprint track does only slightly differ from *VIP4* based predictions (cf. Figure 2.13). Moreover, unlike other magnetic models, their method introduces an additional shallow and weaker dipole instead

of spherical harmonic decomposition up to high orders. Most importantly, it would hamper comparability of our results with those based on the wide-spread *VIP4*. We thus use to the *VIP4* magnetic field model in the present thesis.

In the middle magnetosphere there is a non-negligible contribution to the magnetic field of the current sheet. Nevertheless, a model by *Khurana* [1997] that includes this magnetic constituent and also recent calculations of the field fluctuations at Io by *Seufert et al.* [2011] predict minor influence for regions as close to Jupiter as Io's orbit. In this area, the internal Jovian field dominates. Hence, we do not discuss the outer and middle parts of the Jovian magnetosphere here and refer the interested reader to the review paper by *Khurana et al.* [2004].

2.3 Volcanism and Atmosphere

Even before the detection of Io's volcanic activity, earthbound observations of a neutral sodium (Na) line near Io by *Brown and Chaffee* [1974] and the detection of a sodium ionosphere by *Pioneer10* radio occultations [*Kliore et al.*, 1975] led to speculations about the existence of an atmosphere on Io. Evidence for an ionized sulfur component in the Jovian magnetosphere by *Kupo et al.* [1976] were also interpreted as hints for an Ionian atmosphere as it was soon confirmed that the observed material had escaped from Io. *Voyager* later observed an SO₂ absorption profile in the IR band [*Pearl et al.*, 1979] caused by a volcanic plume, indicating a possible source for the atmosphere. Subsequent observations confirmed SO₂ as main atmospheric species with minor other constituents like sulfur monoxide (SO), sodium chloride (NaCl), and atomic sulfur and oxygen [e.g. *Lellouch et al.*, 2007, and references therein].

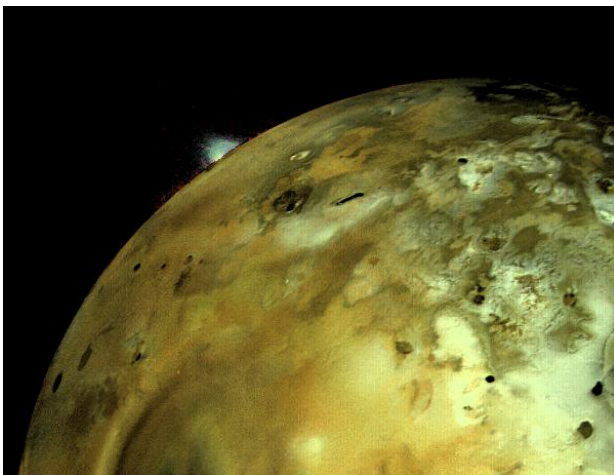


Figure 2.3: Picture of an active volcano on Io taken by the *Galileo* spacecraft. [source: NASA/JPL]

Shortly before the *Voyager* probes flew through the Jupiter system in 1979, *Peale et al.* [1979] predicted volcanic activity on Io. *Voyager1* confirmed this presumption by a series of spectacular photos of Io's active volcanoes [*Smith et al.*, 1979b; *Morabito et al.*, 1979; *Smith et al.*, 1979a]. During the eight years of the *Galileo* cruise phase at Jupiter, Io and its volcanic activity have been extensively studied (Figure 2.3). More than 100 active volcanoes have been identified - partly effusive, partly eruptive. For a detailed summary of the numerous observations and conclusions we refer the reader to reviews by *Williams and Howell* [2007] and *Geissler and Goldstein* [2007]. The fact that the *Galileo* epoch was not exceptional but Io's volcanic activity persists was proved by recent images taken by the *Long-Range Reconnaissance Imager* (LORRI) on-board

summary of the numerous observations and conclusions we refer the reader to reviews by *Williams and Howell* [2007] and *Geissler and Goldstein* [2007]. The fact that the *Galileo* epoch was not exceptional but Io's volcanic activity persists was proved by recent images taken by the *Long-Range Reconnaissance Imager* (LORRI) on-board

the *New Horizons* spacecraft. They revealed a major eruption of the Tvashtar volcano in the north polar region of Io [Spencer *et al.*, 2007] with an enormous plume.

After several earthbound observation campaigns and the insights given by *Galileo* (see review by McGrath *et al.* [2004]), the current understanding is that Io's atmosphere consists of a patchy component localized at active volcanoes and a second, more homogeneous distribution generated by surface sublimation of volcanic deposits and frosts. To what extent both constituents contribute to the atmospheric density is still under debate. Saur and Strobel [2005] use observations of Io's atmosphere in eclipse, i.e. in absence of sublimation, and derive a minor role of the direct volcanic component (<10%) for the global atmosphere. Conversely Zhang *et al.* [2003; 2004] successfully reproduce the local atmospheric density structure over volcanic plumes solely with a plume density model which favors partly the volcanic atmosphere concept. A current comparison of numerical results with new observations of Io's aurora in eclipse by Roth *et al.* [2011] yields also a minor contribution of volcanoes and supports the hypothesis by Saur and Strobel [2005]. For more detailed background information and discussion the reader is referred to reviews by Lellouch *et al.* [2007] and McGrath *et al.* [2004] and references therein.

2.4 Properties of the Ambient Plasma Flow

Before spacecraft missions targeted the giant gas planet, knowledge about the contents of Jupiter magnetosphere was limited. Based on findings obtained at Earth, it was believed to be filled with tenuous Heliogenic plasma [e.g. Warwick and Dulk, 1964]. However, earthbound observations provided first evidence for a substantial heavy sulfur plasma component in the inner Jovian magnetosphere [Kupo *et al.*, 1976], which Broadfoot *et al.* [1979] later identified as a dense plasma torus around Io's orbit using the *Voyager1* ultraviolet spectrometer (UVS) data.

Along with these remote sensing techniques, in-situ measurements by the Plasma Science (PLS) instrument on-board *Voyager* provided better spatial resolution and further insight [Bridge *et al.*, 1979]. Based on the data collected by *Voyager*, Bagenal [1994] developed an empirical density model by solving multi species diffusive equilibrium equations. Reanalysis of UVS and PLS instrument data provide the basis of this approach as the knowledge of the plasma properties is crucial for this method. More recent *Galileo* measurements have basically confirmed this model [Frank and Paterson, 2004]. However, *Ulysses* observations [Hoang *et al.*, 1993] indicate a substantially different latitudinal electron temperature profile which leads to a plasma density model with a steeper gradient at the torus edges [Moncuquet *et al.*, 2002]. In all density models, the torus' central plane is inclined against Io's orbital plane. The explanation of this phenomenon lies in the magnetic axis tilt of $\sim 9.6^\circ$ with respect to the rotational axis (Figure 2.4). The plasma is believed to be generally confined to a magnetic field line. Consequently centrifugal forces drive the plasma towards the point on the specific field line that is farthest away from the rotation axis. All of these points together define a plane called the centrifugal equator (Figure 8.2). It represents the symmetry plane for the latitudinal torus structure and is tilted by $\sim 6.4^\circ$ against the rotational equator. Due to this tilt, Io moves up and down in the plasma torus on its orbit, periodically approaching the northern and the southern edge of this dense plasma ring (Figure 2.4).

| Physical property | Symbol [unit] | av. value (min-max) |
|-------------------------------|--------------------------------|---------------------|
| Jovian magnetic field (max) | B_0 [nT] | 1720 (2080) |
| Electron density | n_e [cm ⁻³] | 2500 (1200-3800) |
| Mean ion charge number | Z_i [e] | 1.3 |
| Mean Ion mass number | A_i [amu] | 22 |
| Ion Mass density | ρ [amu cm ⁻³] | 42300 (18000-64300) |
| Ion temperature | $k_B T_i$ [eV] | 70 (20-90) |
| Electron temperature | $k_B T_e$ [eV] | 6 |
| Thermal plasma pressure | $p_{i,th}$ [nPa] | 22 (3-42) |
| Energetic plasma pressure | $p_{i,en}$ [nPa] | 10 |
| Total pressure | p [nPa] | 34 |
| Magnetic pressure | $B_0^2/2\mu_0$ [nPa] | 1200 |
| Ram pressure | ρV_0^2 [nPa] | 230 |
| Local corotation velocity | V_{corot} [km/s] | 74 |
| Satellite orbit velocity | V_{Io} [km/s] | 17 |
| Relative plasma velocity | V_0 [km/s] | 57 |
| Alfvén speed | V_A [km/s] | 180 (150-340) |
| Sound speed | c_s [km/s] | 29 |
| Alfvén Mach number | M_A | 0.31 (0.16-0.39) |
| Sonic Mach number | M_S | 2.0 (1.0-2.1) |
| Fast magnetosonic Mach number | M_F | 0.31 (0.16-0.38) |
| Alfvén angle | θ_A [°] | 17 (9-21) |
| Plasma beta | β | ~0.32 |
| Alfvén conductance | Σ_A [S] | 4.4 (2.4-5.4) |
| Pedersen conductance | Σ_P [S] | ~200 |
| Hall conductance | Σ_H [S] | 100-200 |
| Electron plasma frequency | f_{pe} [kHz] | 450 (310-550) |
| Ion plasma frequency | f_{pi} [Hz] | 2500 (1900-5700) |
| Electron cyclotron frequency | f_{ce} [kHz] | ~48 |
| Ion cyclotron frequency | f_{ci} [Hz] | ~1.5 |

Table 2.1: *Physical parameters of the magnetoplasma in the Io torus [Kivelson et al., 2004, and references therein].*

The plasma torus rotates with the planets rotation period of 9h 55m 29s which corresponds to ~ 74 km/s on Io's orbit. Io revolves prograde around Jupiter in 42h 27m 33s, giving an orbital velocity of ~ 17 km/s. This yields a relative velocity of ~ 57 km/s for the incoming plasma and a period of 12h 57m 10s for one oscillation of Io in the torus. Consequently, Io is exposed to constantly changing plasma conditions depending on its centrifugal latitude.

After the discovery of the torus it has been systematically observed by many scientists who discovered substantial temporal and azimuthal variabilities [e.g. *Thomas*, 1993, and references therein]. A recent publication by *Steffl et al.* [2006] using Cassini spacecrafts Ultraviolet Imaging Spectrograph (UVIS) data infers variations of $\pm 5\%$ in the torus density. They are correlated with System III longitude with the maximum at 170° . These results are obtained by long-term stacking of the measure-

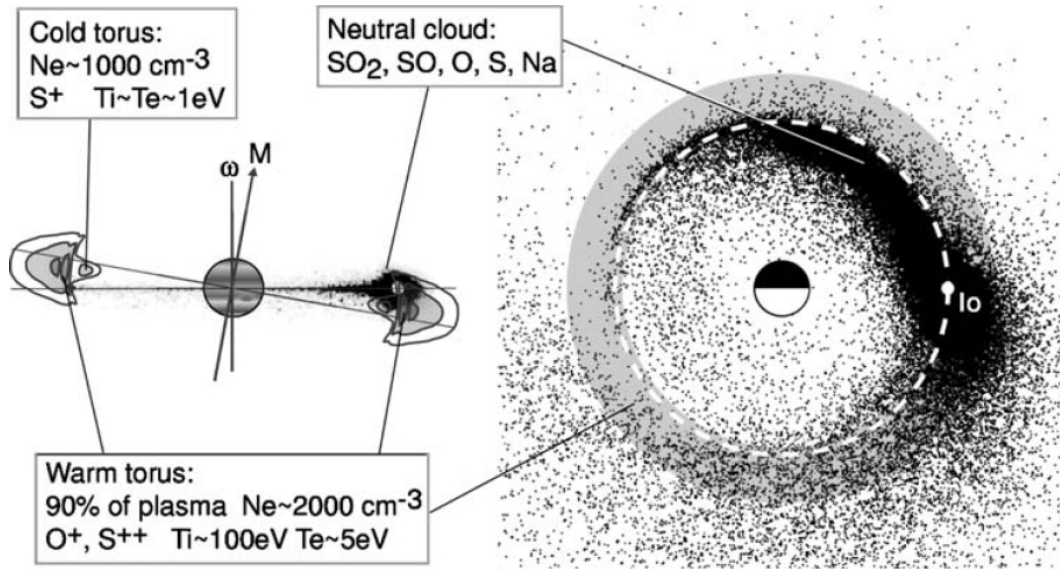


Figure 2.4: Sketch of the Io plasma torus and neutral clouds. Left: view from $\lambda_{III}=292^\circ$. ω marks the rotation axis. The vertical line represents the rotational equator. M denotes the magnetic axis tilted by $\sim 9.6^\circ$ against the rotational axis. The magnetic equator is perpendicular to M . The torus symmetry plane (centrifugal equator, not displayed) inclined by 6.4° with respect to rotational equator. Right: Look down on Jovian north pole. Black dots represent neutrals of different species. Grey circle represents the plasma torus. [after Thomas *et al.*, 2004]

ments as they contain considerable scattering of the data due to much larger temporal variations. Moreover, there is strong observational evidence that the torus structure also varies with local-time (see review by Thomas *et al.* [2004] for details). Overall, the Io plasma torus properties remain highly transient and, though extensively studied, not fully understood. Yet, a publication currently in press by Smyth *et al.* [2011] presents a four dimensional (three spatial dimensions and local time) empirical torus model that reproduces torus observations for various epochs and thus might be the basis for a better future comprehension.

2.5 Io's Local Interaction: The Generator

Io's interrelation with the Jovian magnetosphere has been of substantial interest ever since Bigg [1964] discovered the correlation of Jupiter's decametric radio emission (DAM) and Io's orbital position. An accurate description of the interaction requires both, detailed knowledge of the obstacle properties and the characteristics of the incoming magnetoplasma. As we outlined these two factors in the previous sections, we now turn to the interaction itself.

In a simplified electrostatic image, the interaction can be divided into three parts: the generator, the load and the coupling region. We describe the generator region in this paragraph and will subsequently elucidate the observations and models available for the load in the system where the energy is dissipated: Io's footprints in the Jovian aurora and the radio emissions.

Most of the theoretical concepts of Io's local interaction that have been developed to explain this electrodynamic interaction employ the framework of magnetohydrodynamics (MHD), which is a convenient albeit not complete description. Within the ideal MHD theory, three wave modes exist. Two of them are compressional modes called slow and fast magnetosonic waves. The third mode is a transverse mode with the outstanding ability to carry electric currents almost lossless parallel to the ambient magnetic field. This mode is essential for the coupling of Io to the Jovian ionosphere and to interconnect magnetospheric processes and ionospheric response.

The description of the plasma as a fluid is legitimate when the characteristic macroscopic length and time scales (i.e. Io's radius and plasma convection time) are much larger than their microscopic counterparts (i.e. the ion gyro radii and periods). The characteristic plasma parameters at Io are presented in Table 2.1. One can see that the conditions for the fluid approximation are well fulfilled.

We note that some important aspects of the interaction take place on smaller scales. However, the focus of this work is put on the far field MHD wave pattern and related phenomena and not on the precise description of the Alfvén wave generator region on all scales. For the aim of our study the fluid approach provides the required precision whilst reducing complexity.

It is notable that within the continuum description, two rival paradigms exist. Some models favor the formulation with the electric field \mathbf{E} and the current density \mathbf{j} as fundamental variables, others use the magnetic field \mathbf{B} and bulk velocities \mathbf{v} as principle quantities. The pros and cons of both paradigms are discussed and weighted for instance by *Vasyliūnas* [2001; 2005]. Yet, there is an ongoing discussion about which is the best formulation. However, since both theories have been successfully applied to describe different aspects of the Io-Jupiter interaction we will make use of both concepts to explain the physics of the interaction whichever is more intuitive. In the following paragraphs we will discuss the different models that have been developed to characterize the interaction.

2.5.1 The Unipolar Inductor Model

While Io orbits Jupiter, it is continually overtaken by the corotating magnetospheric plasma linked to the Jovian magnetic field. In the satellites rest frame the relative motion \mathbf{V}_0 with respect to the rotating magnetic field \mathbf{B}_0 creates a motional electric field

$$\mathbf{E}_0 = -\mathbf{V}_0 \times \mathbf{B}_0 . \quad (2.1)$$

It is roughly directed radially away from Jupiter (Figure 2.5). While in most space plasmas conductivity is generally high along the magnetic field direction, it is small in the perpendicular plane. A way to short-circuit the electric field is a potent conductor. Early concepts of the interaction by *Piddington and Drake* [1968] and *Goldreich and Lynden-Bell* [1969] hence assume Io's surface to be highly or even infinitely conductive, so that the motional electric field can drive currents in the surface layer. As *Goldreich and Lynden-Bell* [1969] also assume infinite conductivity along the magnetic field direction, these currents can continue along the magnetic field and close in the Jovian ionosphere. The result is a current circuit as depicted in Figure 2.5. The assumption of a perfectly conductor Io implies that the magnetospheric cur-

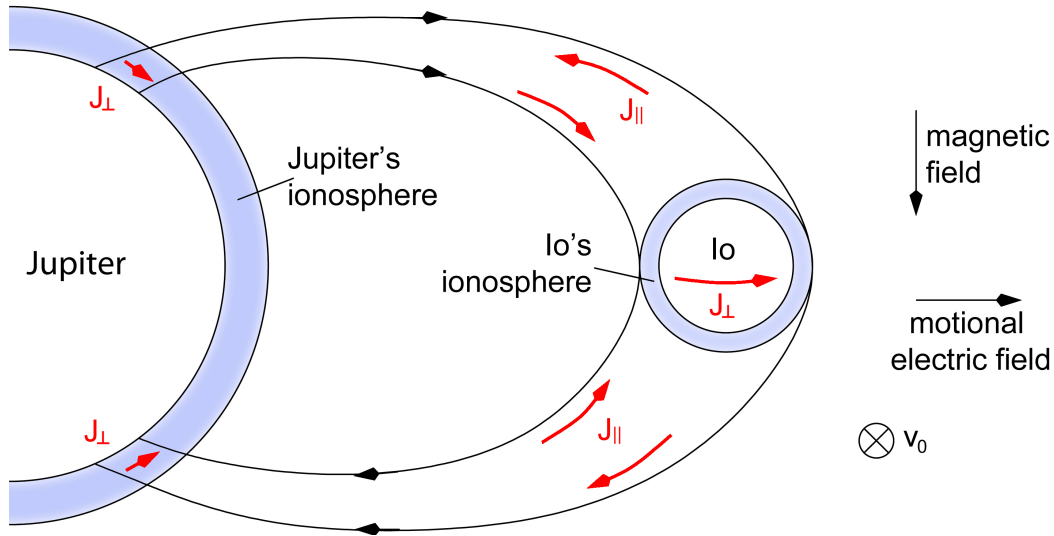


Figure 2.5: The current loop model: Io as unipolar inductor. Magnetic field lines are plotted in black. Red arrows represent electric currents.

rents are confined to the surface of the magnetic flux tube connected to Io. The interior of the flux tube is force-free in Io's rest frame, hence it is rigidly attached to Io. It is therefore termed Io flux tube (IFT). The current system thus forms a steady loop in which Io acts as a unipolar inductor. Consequently this model is called *current loop model*

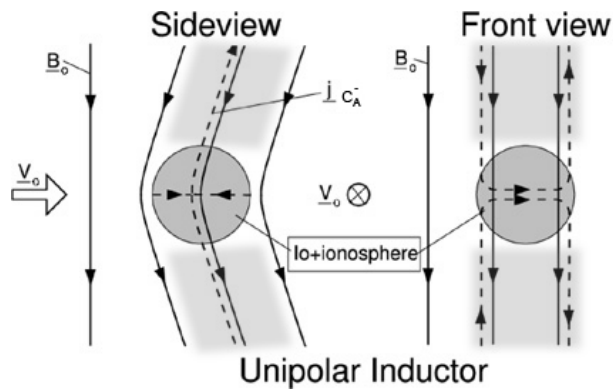


Figure 2.6: Current loop or unipolar inductor setup. Left: side view; Right: front view. Currents are strictly field aligned. [after Saur et al., 2004]

In this setup, the currents flowing between Io and Jupiter are carried by Alfvén waves. The authors note that their model is only valid, if the Alfvén waves reflected at the Jovian Ionosphere are able to reach Io before it has moved away. In other words, they require the round-trip travel time τ_A of the Alfvén mode to be small compared to the convection time t_c of the plasma past Io:

$$\frac{\tau_A}{t_c} \ll 1. \quad (2.2)$$

Goldreich and Lynden-Bell [1969] assumed a low density plasma in the Jovian magnetosphere. This implies a high Alfvén wave velocity V_A which is given by

$$V_A = \frac{B}{\sqrt{\mu_0 \rho}}, \quad (2.3)$$

where ρ represents the plasma mass density and μ_0 the vacuum permeability. Consequently, the authors hypothesize that the required travel time ratio (2.2) would be easily fulfilled. This assumption was reasonable at the time. However, it became arguable with the detection of the dense plasma torus.

The current loop model also assumes that the currents which couple Io to Jupiter are strictly field aligned [e.g. *Piddington and Drake, 1968*]. This approach neglects plasma inertia. As Io's conductance short circuits the motional electric field, the currents that are partly compensating the charge separation between the Jupiter facing and the anti-Jupiter hemisphere perturb the original electric field. This implies acceleration or deceleration of the surrounding plasma. These acceleration terms must be compensated by $\mathbf{J} \times \mathbf{B}$ forces [*Neubauer, 1980*]. This component of the current system perpendicular to \mathbf{B} gains relative importance with increasing plasma momentum and thus with the mass density of the incoming plasma. Since the quantity of ρ also affects the Alfvén velocity (2.3), one can assess the significance of plasma inertia by the Alfvén Mach number

$$M_A = \frac{V_0}{V_A}. \quad (2.4)$$

The detection of the dense plasma torus put new constraints on the local Alfvén Mach number on Io's orbit and the restriction to strictly field aligned currents is hardly maintainable. Moreover, with the observation of Io's ionosphere, Io's surface conductivity needed to be replaced by typical ionospheric Hall and Pedersen conductivities. This questions the assumption of a force-free Io flux tube and thus a rigid connection of the IFT plasma to Io. Hence two major aspects challenge the current loop model. First, the convection time of the plasma past Io is smaller than initially believed since the IFT is not force-free and a non-zero plasma velocity remains. Secondly, the Alfvénic travel time is larger than believed, due to the dense torus plasma that slows down propagation of Alfvén waves. Hence condition (2.2) is not always fulfilled and the validity of the model is questionable.

The new observations triggered the development of new models, such as the Alfvén wing model which we present in the next paragraph.

2.5.2 The Alfvén Wing Model

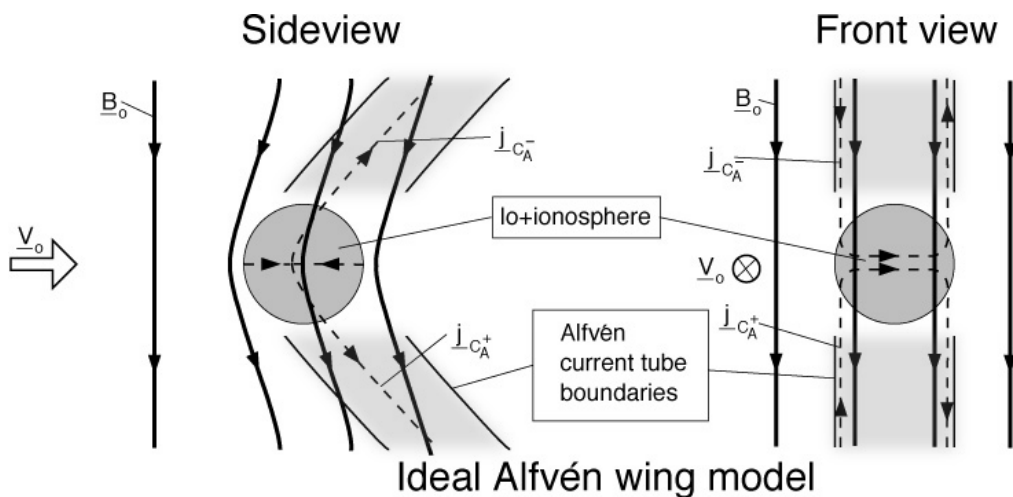


Figure 2.7: Side and front view of the Alfvén wing model [*Neubauer, 1980*]. Currents flow along the Alfvén characteristics and are closed at far distances (not shown).

Goertz and Deift [1973] discuss certain aspects of the effects of a weaker Io-Jupiter

interaction as it is the case for a low conducting Io. A model by *Drell et al.* [1965] studies Alfvénic perturbations that were observed to decelerate the satellite *ECHO* at Earth. However, they consider small perturbations only and thus justify a linearization of the equations and disregard second order terms.

Neubauer [1980] developed the first consistent theoretical framework of the standing Alfvénic current system. It is valid for weak and strong interaction settings. It is a fully nonlinear treatment of the problem and valid for an isotropic plasma. However, it is intended to be applied for the current system at some distance of Io, not for the direct interaction region, as e.g. compressional modes cause plasma anisotropy. To some extent contrary to the current-loop approach, the author finds that the currents flow along the Alfvén characteristics. They are defined as:

$$\mathbf{C}_A^\pm : \mathbf{V}_A^\pm = \mathbf{V} \pm \mathbf{V}_A = \mathbf{V} \pm \frac{\mathbf{B}}{\sqrt{\mu_0 \rho}} \quad (2.5)$$

and prescribe the propagation direction of Alfvén waves with respect to Io (\mathbf{V} represents the plasma bulk velocity field in Io's rest frame). The waves generated at Io propagate away in the \mathbf{C}_A^\pm -directions and form a wing-like structure (see Figure 2.7). Thus the currents are not strictly field-aligned.

However, when the plasma is at rest inside the magnetic flux tube connected to Io, i.e. for a saturated interaction as considered in the current loop model, the propagation is strictly field aligned (Figure 2.6). In this case the magnetic field direction and the Alfvén characteristics coincide.

The Alfvén wing model represents the basis for the work at hand and because of its importance we revisit this model in section 4.2 of this work.

2.5.3 Other Models

As the enigma of Io's interaction attracted considerable attention, many theories and models have been published. Because of the complexity but also due to numerical difficulties and limited computational resources, different groups have focused on particular aspects of the problem. We will try to extract the most influential ones and give a very brief summary of the major aspects.

Deift and Goertz [1973] consider an inhomogeneous plasma density, but solve the wave equations linearly. However, they predict reflections and discuss wave-wave interaction (see subsequent section). Other models include pickup processes for current closure in Io's vicinity [*Goertz, 1980*] or in its corotational wake [*Southwood and Dunlop, 1984*].

Saur et al. [1999] focused on the local interaction properties and addressed the problem in a stationary, 3D, two fluid model including aeronomic processes and a detailed description of the ionosphere (involving ion production rates and collision frequencies). They find that the resulting anisotropic electric conductivity distribution has important effects on the local interaction. Most importantly, the authors realize for the first time the importance of the Hall effect in Io's close vicinity. It significantly rotates the motional electric field in the satellites ionosphere. *Dols et al.* [2008] include a more detailed description of Io's atmospheric chemistry and focus on a multi-species description of the local interaction. They stress the possibility of

an enhanced ionospheric conductivity caused by precipitating energetic electrons associated with observed equatorial electron beams.

With increasing computer power, numerical approaches to describe the Io interaction became possible. *Wolf-Gladrow et al.* [1987] published one of the first 3D models. It calculates self-consistently electric field, electric current and magnetic field data. Meanwhile *Linker et al.* [1988; 1989; 1991] also developed a 3D model using a single fluid resistive MHD approach and thus also included compressional MHD wave modes. However, they focus on the local interaction only. *Kopp* [1996] use their 3D resistive MHD code with implemented mass loading to qualitatively deduce plasma production rates. They also find in their data a current system in Io's wake, thus confirming the results of *Southwood and Dunlop* [1984]. *Combi et al.* [1998] also apply an ideal single fluid MHD code, but with a very good spatial resolution owing to adaptive mesh refinement. They successfully reproduce single features of data collected on the *Galileo* IO flyby.

2.6 The Far Field Interaction: The Coupling

The coupling region between Io, the generator, and the load in Jupiter's polar regions is a large and heterogeneous area. Along the travel path of the generated waves, the propagation medium and the ambient magnetic field vary significantly. On the one hand this implies wave reflections and interference, on the other hand kinetic effects gain importance in low-density areas located at high magnetic latitudes. We classify these phenomena as far-field interaction and outline the associated physical effects in this section.

2.6.1 Alfvén Wave Propagation and Reflections

When Alfvén waves generated in Io's vicinity eventually reach the edge of the plasma torus (Figure 2.8), the wave velocity changes due to the plasma density gradient (2.3) and the wave is partially reflected as illustrated in Figures 2.8 and 2.9. The strongest observational evidence for this phenomenon is given by multiple emission maxima detected in the auroral tail emission by HST [*Connerney and Satoh*, 2000] and sets of DAM arcs in the time-frequency spectra of Jupiter's radio emissions. The subject of reflections was addressed analytically and numerically before and very different results have been found by different authors. *Goertz* [1980] calculates the reflection coefficient for a constant magnetic field and concludes, in contrast to *Neubauer* [1980], that torus-internal reflections are negligible. Subsequent 1D numerical studies by *Wright* [1987] and *Wright and Schwartz* [1989] investigate the reflection of Alfvén waves with updated torus density profiles and an additional magnetic field gradient and derive a reflection coefficient of 50%. A one-dimensional MHD model by *Dols* [2001] indicates that only 40% of the Alfvén wave energy is able to leave the torus. In a 2D MHD model *Delamere et al.* [2003] observe that only 20% energy can escape the torus. *Su et al.* [2006] use a gyro-fluid model and infer likewise a reflection intensity of $\sim 80\%$. These models give essentially different results which can be mainly attributed to the model and the use of different density profiles. Uncertainties in the magnetic field model and the absence of measured plasma density profiles along the magnetic field lines (not to

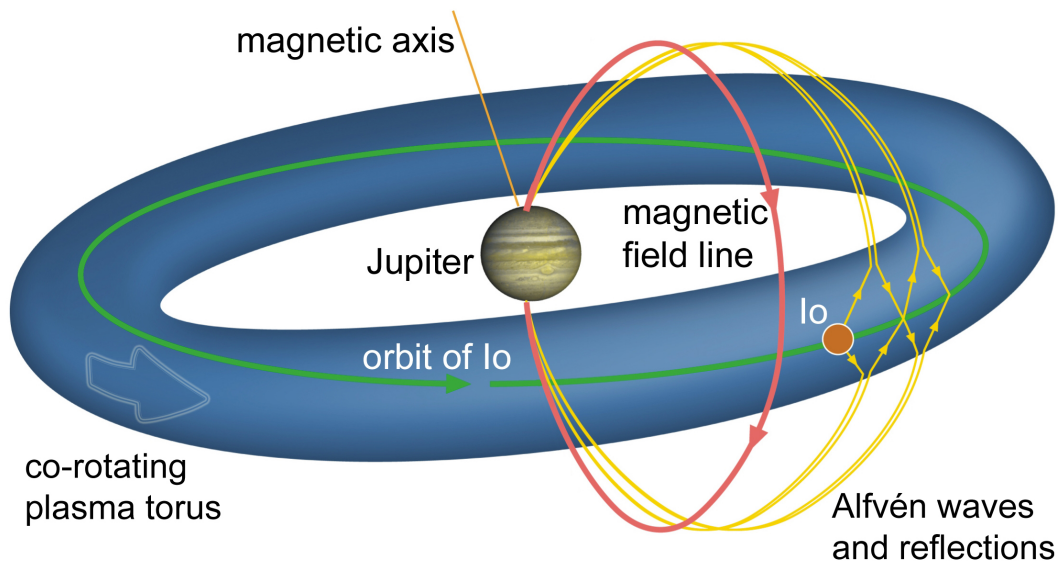


Figure 2.8: *Io is embedded in the dense corotating torus. The motion of the plasma relative to the satellite generates Alfvén waves that are partly reflected at the torus edges and Jupiter’s ionosphere.*

mention the spatial and temporal variability of the density) hampers the quantitative assessment of the reflection coefficient.

Besides the amplitude of wave reflections, the resulting wave pattern in the wake region downstream of the obstacle and the initial Alfvén wing is of particular interest. In the pure Alfvén wing approach, the angle of incidence equals the angle of reflection [e.g *Saur et al.*, 2004], the resulting wave field looks as depicted in the top panel of Figure 2.9. This holds only for a weak interaction, when the magnetic field and velocity perturbations are small. Strong interactions greatly modify the Alfvén characteristics which determine the travel path of incoming wave and wave reflection. The consequence is a breakdown of the regular reflection law [*Jacobsen*, 2006; *Jacobsen et al.*, 2007] as illustrated in the lower panel of Figure 2.9. In extreme cases the reflection follows the travel path of the incoming wave back to the Alfvén wave generator. This scenario can be described with the unipolar inductor model. Hence, this framework represents a special case of the general Alfvén wing model [*Neubauer*, 1980].

All models mentioned so far neglect nonlinear effects between the incident and the reflected wave. Yet, they are indispensable for the description of the Io-Jupiter interaction. At the torus boundary, the incoming wave interacts with the reflection and both perturbations superimpose and interfere. Moreover, other wave modes are excited upon reflection, modulating the reflection energy budget and again mutually interacting with other waves and wave modes. The question arises to what extent these effects influence the MHD wave pattern. *Jacobsen* [2006] and *Jacobsen et al.* [2007] address this problem with a 3D MHD model and perform detailed studies with emphasis on the resulting MHD wave pattern depending on the strength of the interaction. They compare the results qualitatively to auroral footprint observations which provide a valuable means to evaluate the findings as they represent

a two-dimensional cross section through the Alfvén wave pattern. Additionally, the breakdown of the reflection law can be observed in these simulations. As these results represent the basis for the present study and they are essential for the interpretation of the findings presented here, we reformulate the results in part III of this work.

2.6.2 Acceleration Region

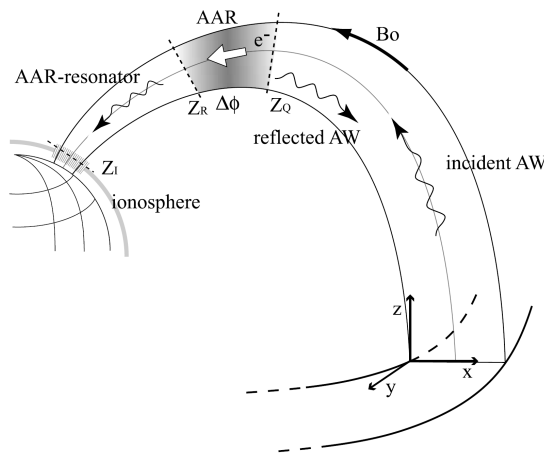


Figure 2.10: Concept of the auroral acceleration region. [after Pilipenko et al., 2004]

Outside the dense plasma torus the number of charge carriers decreases rapidly, whereas the magnetic field strength increases and the cross-section of the current channeling flux-tubes becomes smaller. Superficially, current maintenance thus demands electron acceleration. This happens where the ion density decreases below a certain threshold value in the region where the maximum Alfvén velocity is reached [Knight, 1973], the so-called auroral acceleration region (AAR). Figure 2.10 shows a sketch of the acceleration region.

Observational evidence for such phenomena at Jupiter comes from detected short-burst radio emissions near 20 MHz presumably triggered by the acceleration [Zarka, 1998]. The acceleration region is located between an altitude of approximately $0.9 R_J$ and $2.9 R_J$ above the ionosphere [Hess et al., 2007; Ray et al., 2009]. The acceleration mechanism has been widely discussed and is still under debate. Concepts like electrostatic double layers [Smith and Goertz, 1978], kinetic or inertial Alfvén waves [Swift, 2007; Jones and Su, 2008] and repeated Fermi accelerations [Crary and Bagenal, 1997] have been brought up and modeled. These studies were mostly motivated by the interpretation of the planetward electron beams as a source for the aurora. For Earth, Mauk et al. [2002] distinguish between three types of aurora: (1.) Alfvén aurorae, and aurorae associated with (2.) upward and (3.) downward current regions. For Jupiter, Su et al. [2003] follow this argumentation and identify the main spot emission as Alfvén aurora. However, some electrons are also accelerated upward, i.e. in the anti-planetward direction. They have been observed in the equatorial plane near Io and are treated in the next paragraph.

2.6.3 Equatorial Electron Beams

Associated with Io's interaction with the ambient magnetoplasma, energetic field-aligned electron populations have also been observed in-situ by the *Galileo* spacecraft near Io. Williams et al. [1996; 1999] and Frank and Paterson [1999] report intense bi-directional electron beams in Io's wake. Williams and Thorne [2003] and Frank

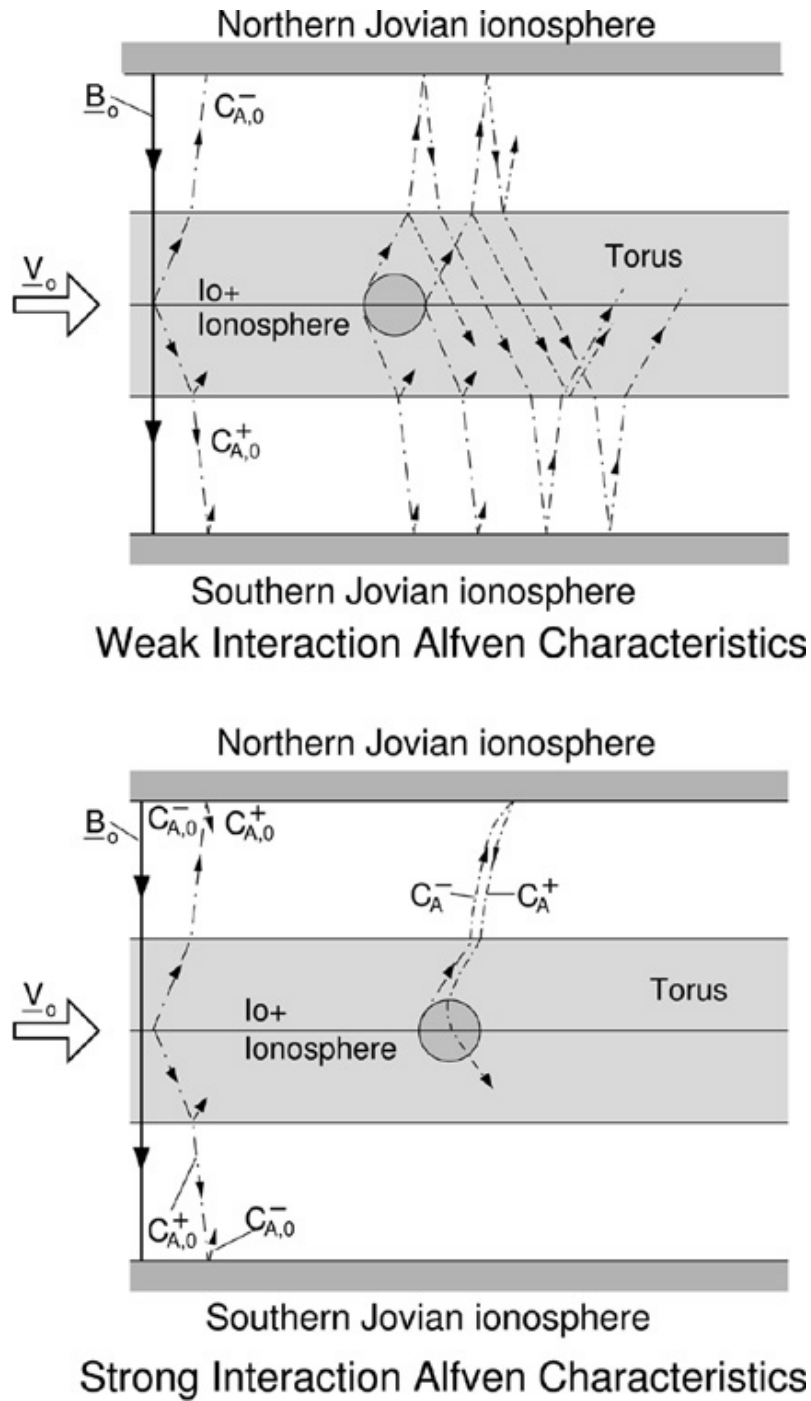


Figure 2.9: Schematic view of the Alfvén characteristics for different interaction scenarios. Top panel represents a weak interaction. In this case the angle of incidence equals the angle of reflection. The result is a rhombic wave pattern in the downstream direction. Bottom panel depicts the strong interaction scenario. Conversely, a regular law of reflection does not apply here [after Saur et al., 2004].

and Paterson [2002b] detect high-energy electrons streaming onto Io's poles during

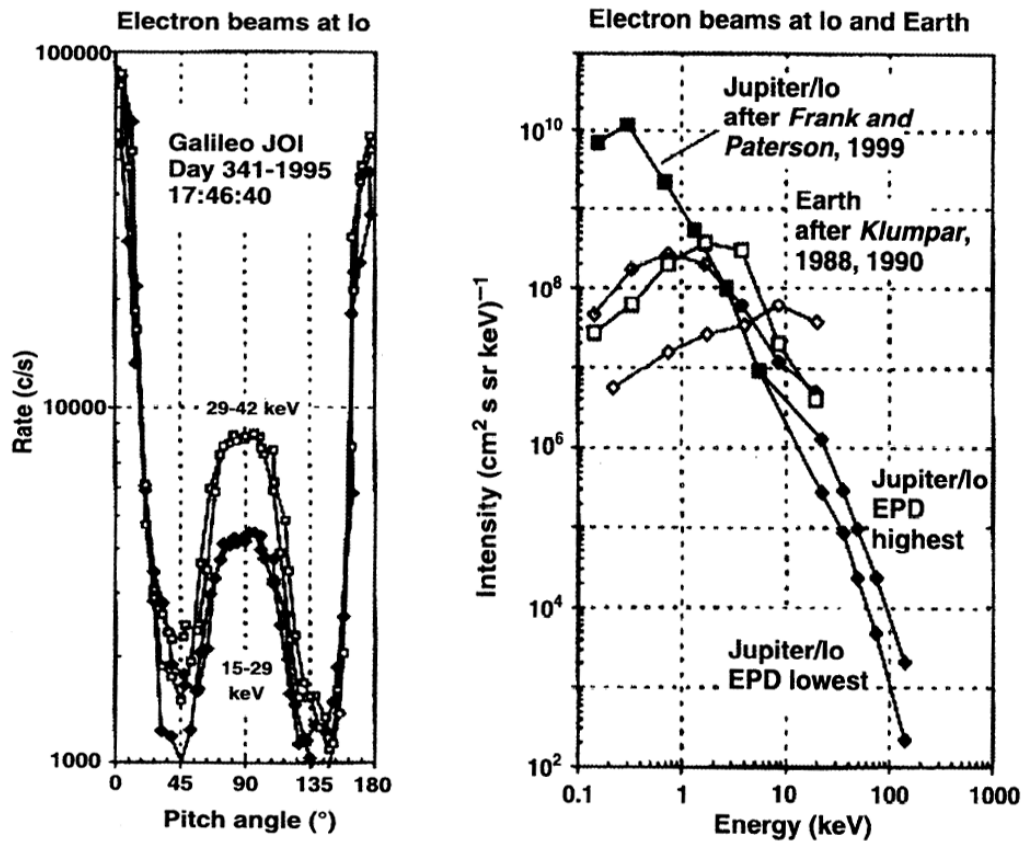


Figure 2.11: Properties of observed electron beams at Io and at Earth. Left: Pitch angle distribution of electron counts in the different energy channels of the detector for the Galileo IO flyby. Right: Phase space density spectra of field aligned electron beams. Hollow symbols represent observations at Earth. Filled symbols depict a combination of electron measurements by Galileo [after Mauk et al., 2001].

two polar flybys (I31 and I32). The measured pitch-angle¹ distributions suggest that these electron beams originate at high latitudes close to Jupiter where electrons are accelerated upward (anti-planetward), towards Io. Even though the exact link between the planetward and anti-planetward electron beams at Io is not fully understood, the process of anti-planetward electron beams in association with auroral features appears to be a universal property of aurorae [Saur et al., 2006]. These beams are known to occur close to Io, in the magnetosphere of Earth [Klumpar, 1990; Carlson et al., 1998], Jupiter [Tomás et al., 2004; Frank and Paterson, 2002a; Mauk and Saur, 2007] and Saturn [Saur et al., 2006; Mitchell et al., 2009]. The main advantage of studying Io's auroral footprints and energetic particle populations compared to other solar system auroral features is that the location of the initial source region, i.e. Io's interaction region, is known and the perturbation is continuous.

The electron beams at Jupiter have first been observed near the equator with the *Energetic Particle Detector* (EPD) on the *Galileo* spacecraft. In December 1995, during the first Io flyby an energetic field-aligned electron population was measured in Io's wake [Williams et al., 1996]. The pitch angle distribution was bidirectional. In

¹The pitch angle is defined as angle between the particle velocity vector and the magnetic field vector.

2001 two polar flybys took place. According to *Williams and Thorne* [2003], the *I31* (northern pass) and *I32* (southern pass) both showed energetic electrons streaming onto Io's polar caps and bidirectional beams in the wake region. The authors present the flux and pitch angle distribution of electrons with energies of 15 to 93 keV. The number of electrons with a pitch angle near 0° and 180° exceeds the counts of electrons around 90° by a factor of ten. The spectral distribution of electrons with energies of 15 to 188 keV reveals a decrease following a power law in the flux with increasing energy [*Williams et al.*, 1999].

Saur et al. [2002] and *Dols et al.* [2008] have shown that precipitating electrons with energies between 0.1 and several keV contribute significantly to the formation of Io's ionosphere. Thus, investigation of these electron beams is also important because models of the local interaction require the spatial distribution of the ionization rate which is partly related to the precipitating energetic electrons. This parameter is not well determined and future models will benefit from improved constraints. Moreover, this aspect of the Io-Jupiter coupling, although classified as far field interaction, represents a feedback mechanism for the generator region in the following sense: Io's ionospheric conductivity increases in presence of an energetic electron beam which overall enhances the generator efficiency. The resulting increase in interaction intensity could again boost the beam intensity and so forth. Whether this concept is actually applying to the Io interaction is still an open question.

2.7 Emissions from Jupiter's Polar Regions: The Load

The signals originating from Jupiter's polar regions that dissipate energy from the Io interaction are multifaceted and cover a broad range of the electromagnetic spectrum. UV, visible and infrared auroral features have been identified as well as intense radio emissions. We will discuss the most important aspects of the emissions in the following subsections.

2.7.1 Radio Emissions

Bigg [1964] showed that Io triggers Radio emissions in Jupiter's polar regions, which is the first proof of the electrodynamic coupling between Io and Jupiter. The emissions with decameter wavelengths (DAM), i.e. at frequencies between 2 MHz and 40 MHz, originate from above Jupiter's ionosphere. Since then they have been intensively studied and several regions of radio emissions have been identified. Not all of them are related to Io, so the common nomenclature divides the emissions into Io-DAM and non-Io-DAM. The emissions appear as arcs in time-frequency plots and are arranged in multiples. These multiples could be the radio counterpart of the multiple wave reflections discussed before, although there are other possible interpretations like slow mode waves excited by Io. However, the observation geometry of radio signals is considerably more complicated as the emission is beamed along the mantle surface of a hollow cone. The cone opening angle depends on constraints given by magnetic field and upper ionosphere characteristics. The cone geometry is crucial for the time of the signal reception which is later used to determine the location of the source region. Due to the uncertainties in e.g. the

magnetic field models and the deduced opening cones, the reliability of the derived longitude of the emission source is limited.

2.7.2 Auroral Footprints

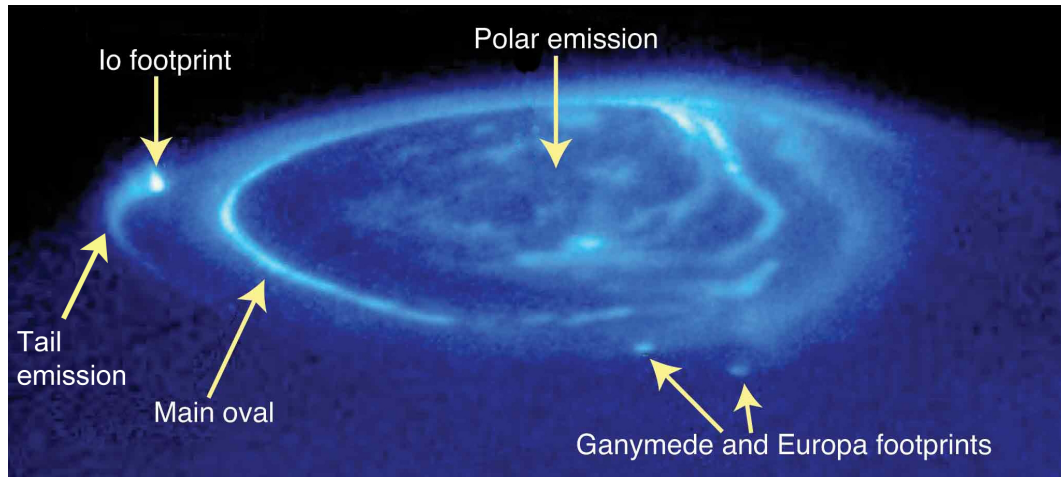


Figure 2.12: Northern Jovian aurora at UV wavelengths. Polar emissions, main oval and satellite footprints are labeled. [after Gérard *et al.*, 2002]

Io's auroral footprint was first observed by Connerney *et al.* [1993] in the infrared (IR) spectrum. Later, also far ultraviolet (FUV) emissions were detected with the HST [Clarke *et al.*, 1996; Prangé *et al.*, 1996]. In the present work we concentrate on the UV observations owing to a more extensive data set. The emission region is located $\sim 8^\circ$ equatorward of the main auroral oval (see Figure 2.12). Besides the main spot, faint trailing emissions were found to extend up to 100° downstream in System III longitude [Clarke *et al.*, 2002]. It is generally referred to as "tail emission" (see Figure 2.12). The UV footprints are assumed to be generated by collisions of atmospheric H and H₂ particles with energetic electrons in the energy range of 40-70 keV [Gérard *et al.*, 2002] which precipitate into Jupiter's upper atmosphere [Dols *et al.*, 2000; Gérard *et al.*, 2006]. The particle energy is highest in the main spot and gradually decreases towards the tail. The peak emission originates from the ionosphere at altitudes of approximately 900 km above the 1 bar limit [Bonfond *et al.*, 2009].

As the waves generated at Io do not instantly arrive in Jupiter's auroral region, there is an azimuthal offset between Io's magnetic longitude and the longitudinal position of the main auroral spot. This parameter is called *lead angle* and was expected to provide valuable constraints for the magnetic field topology and Alfvén wave travel time. Unfortunately, large uncertainties in the magnetic field models lead to errors in the determination of Io's magnetic longitude. Hence, inconsistencies between different lead angles derived from UV, IR and radio observations might be assigned to underlying magnetic model discrepancies. Moreover, the lead angle is expected to vary with the Alfvén wave travel time, which itself *inter alia* depends on the plasma density along the propagation path of the wave. Since Io on its orbit wobbles around inside the heterogeneous plasma torus, the travel time is a function of the longitude. Furthermore it differs for both hemispheres. Estimates of

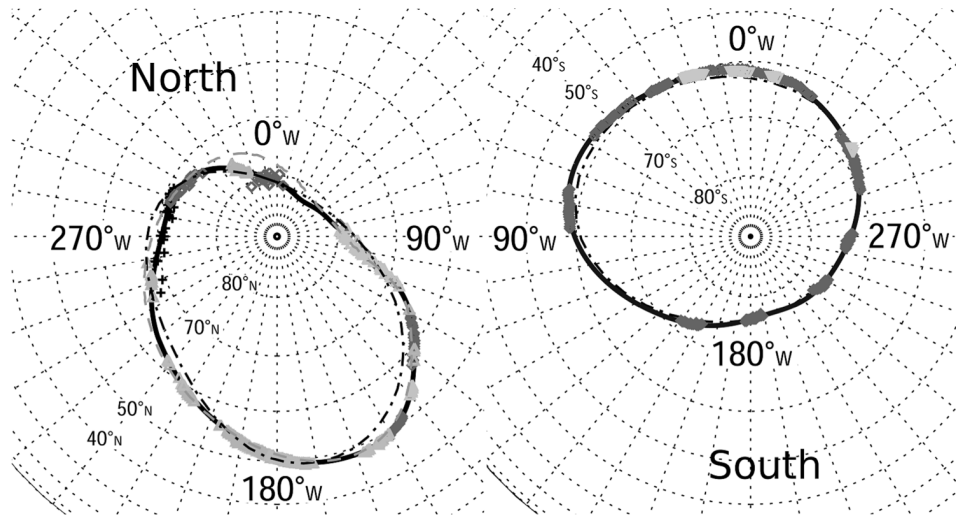


Figure 2.13: Footprint path in the northern (left) and southern (right) polar regions. Diamond, triangle and cross symbols represent various HST IFP observations. The black dash-dotted line is the projection of Io's orbit with the VIP4 model, the dashed grey line is the IFP contour inferred from magnetic field model by Grodent et al. [2008]. The thick solid black line is the best fit to the observation points. [after Bonfond et al., 2009].

the travel time are therefore sensitive to the associated torus plasma density model. Moreover, the torus plasma content has been shown to vary substantially with time [Thomas et al., 2004, and references therein], thus representing an additional transient and weakly determined factor controlling the lead angle. Altogether, these uncertainties possibly lead to substantial errors. In fact, negative lead angles have been derived [e.g. Clarke et al., 1998], which can not be explained by any theory so far and would violate causality if related to Io's Alfvén wings. Hence, the results concerning the lead angle have never met the expectations, yet.

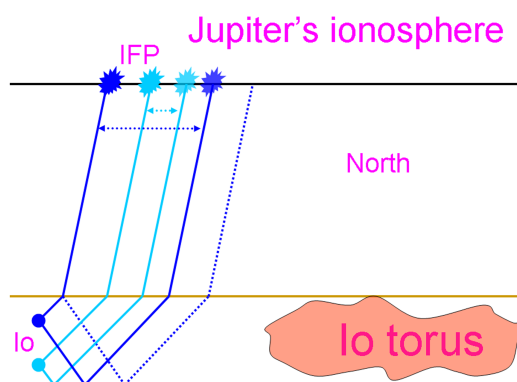


Figure 2.15: Sketch of inter-spot distance variation due to changing reflection geometry [after Gérard et al., 2006].

However, Io's auroral footprint comprises also other information about the remote interaction in the magnetosphere. The emission intensity, i.e. the footprint brightness, has been consulted to estimate the energy conversion in the interaction region. Although it is only one constituent in the energy budget it has been found, that the UV emission of the Alfvén wing spot varies with longitude and that it is brightest when Io resides in the torus center [Gérard et al., 2006]. Here, where the ambient plasma is most dense, the interaction seems to be strongest. Superficially, in this configuration the maximum momentum

of the incoming plasma is converted to electromagnetic energy and radiated to Jupiter's poles.

An observed double peak structure of the main spot [Clarke *et al.*, 2002] and multiple local maxima in the footprint tail emission [Connerney and Satoh, 2000] have been interpreted as secondary footprints and auroral manifestation of multiple Alfvén wave reflections as described in section 2.6.1. Gérard *et al.* [2006] discovered a systematic correlation between the number of multiples and Io's position in the torus, i.e. the centrifugal latitude. Figure 2.14 shows an excerpt of their data set. Notably, no secondary spots are visible when Io is located near the torus center, whereas the authors identified up to four trailing spots when Io was close to the torus edges (see Figure 7 in Gérard *et al.* [2006]).

The authors also discuss a link between Io's position in the torus and the distance between the primary and secondary spot. Figure 2.15 illustrates their findings, that the offset in the northern aurora is maximum when Io is located northernmost in the torus and vice versa for the southern feature. This agrees qualitatively with the observations as plotted in Figure 2.14. However, a more quantitative assessment of the inter-spot distances as illustrated in Figure 2.16 shows that the linear fits applied to the observations tend towards zero angular separation for Io located in the torus center. This is not expected according to the scheme depicted in Figure 2.15. One would assume a medium separation of the auroral spots when Io is near the centrifugal equator. Consequently, there seems to be an additional effect that

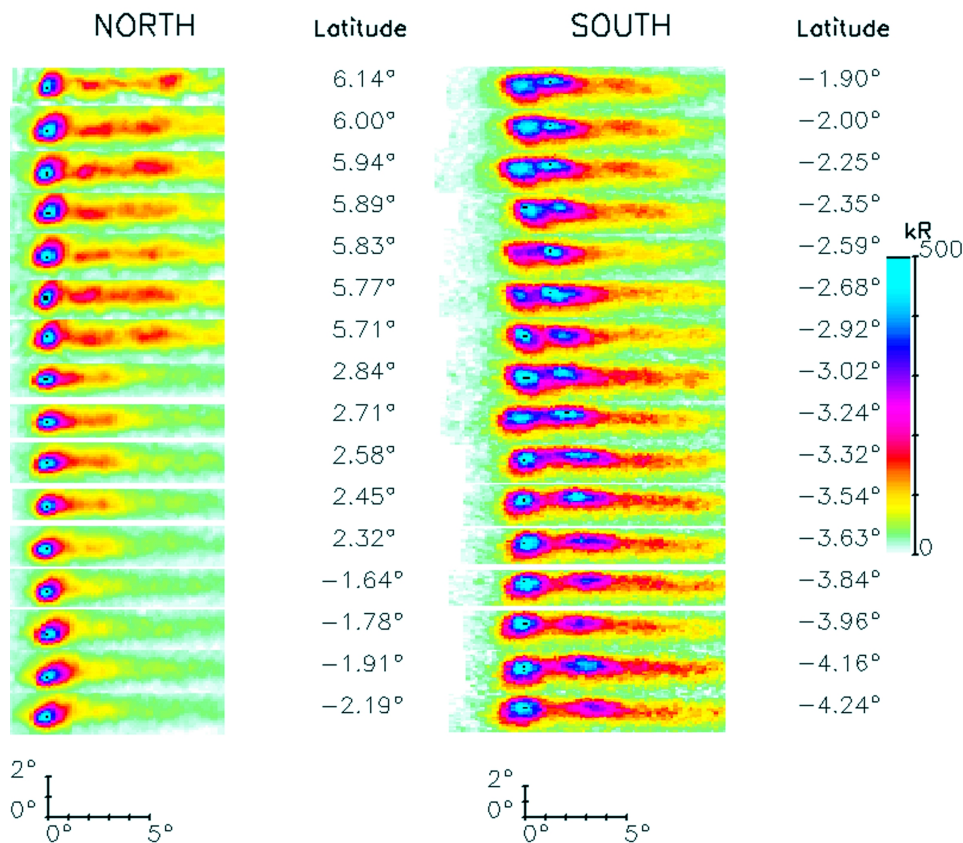


Figure 2.14: Details of Io's auroral feature in the northern and southern hemisphere for different positions of Io in the torus, i.e. centrifugal latitudes. Multiple spots can be identified and the inter-spot distance varies with Io's centrifugal latitude. [adapted from Gérard *et al.* [2006]]

controls the inter-spot distance and footprint merging, not only the topology of Io and the reflection boundaries.

Recently, a leading spot that precedes the main auroral spot in the Jovian aurora has been reported by *Bonfond et al.* [2008] on the basis of HST observations. In their publication, they propose a trans-hemispheric electron beam to trigger an auroral emission in the conjugate hemisphere. This might be either a leading spot or a secondary spot feature depending on Io's position in the torus as illustrated in Figure 2.17. On the basis of this scheme one can deduce that the spot resulting from a trans-hemispheric beam and the main Alfvén wing spot coincide when Io is centermost in the torus. Conversely, this feature is well separated from the main spot only when Io is located at high centrifugal latitudes (cf. Figure 2 in *Bonfond et al.* [2008]). Because of the different origin, *Bonfond et al.* [2008] propose a more precise terminology for the spot notation. They distinguish between the *main Alfvén wing spot* (MAW), the *reflected Alfvén wing spot* (RAW) and the *trans-hemispheric electron beam spot* (TEB) as displayed in Figure 2.17. We will follow this nomenclature for the remainder of this work.

Bonfond et al. [2009] extend the data set of footprint observations and distinguish systematically between angular separation of the TEB and MAW spots on the one hand and the MAW and RAW spots on the other hand. Their findings for the different inter-spot distances are shown in Figure 2.18. A sinusoidal interrelation between the MAW-TEB offset can be deduced from the conception in Figure 2.17. This is reflected in the curves in Figure 2.18. However, the offset should vary harmonically rather in longitudinal separation than in distance in kilometers, because the latitude of the footprint track varies substantially (see Figure 2.13) and so does

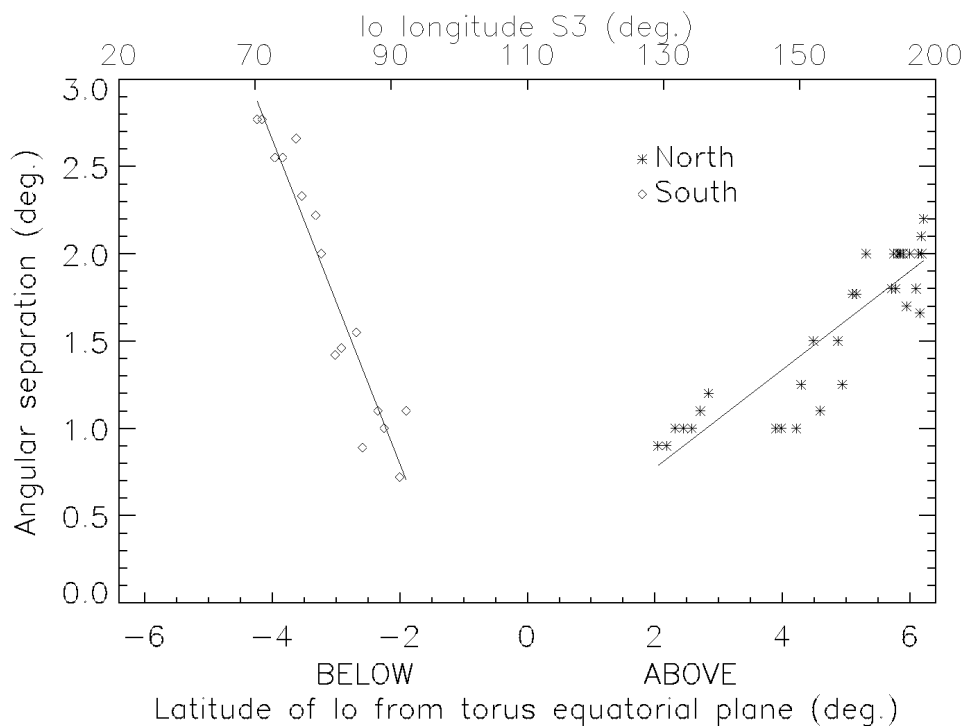


Figure 2.16: Inter-spot distances as observed in the northern and southern hemisphere. A linear fit has been applied.[after Gérard et al., 2006]

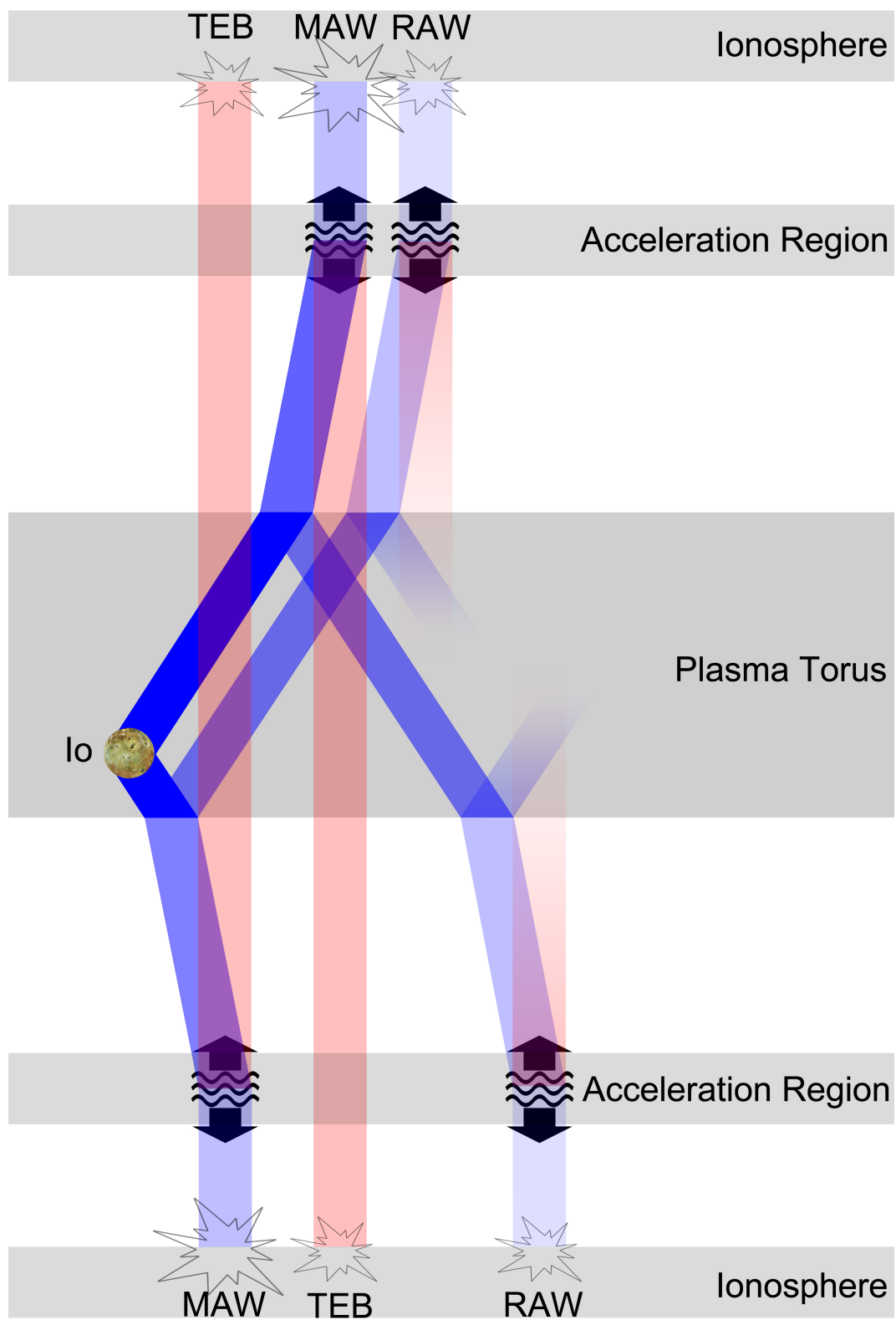


Figure 2.17: Sketch of reflection pattern including trans-hemispheric electron beams. Footprint nomenclature following Bonfond et al. [2009]

the conversion between angular distance and kilometers.

Besides distinct spots, the extended tail in the wake of the Io footprint is a feature worthwhile discussing. However, only few models deal with this topic. *Hill and Vasyliūnas* [2002] follow *Southwood and Dunlop* [1984] and interpret the auroral tail as imprint of a steady state Birkeland current system that closes in Io's wake and accelerates the plasma to full corotation via $\mathbf{j} \times \mathbf{B}$ forces. Hence, it transfers momentum to the sub-corotating plasma leeward of Io. A similar idea for the momentum transfer was independently presented by *Delamere et al.* [2003] including a numerical model.

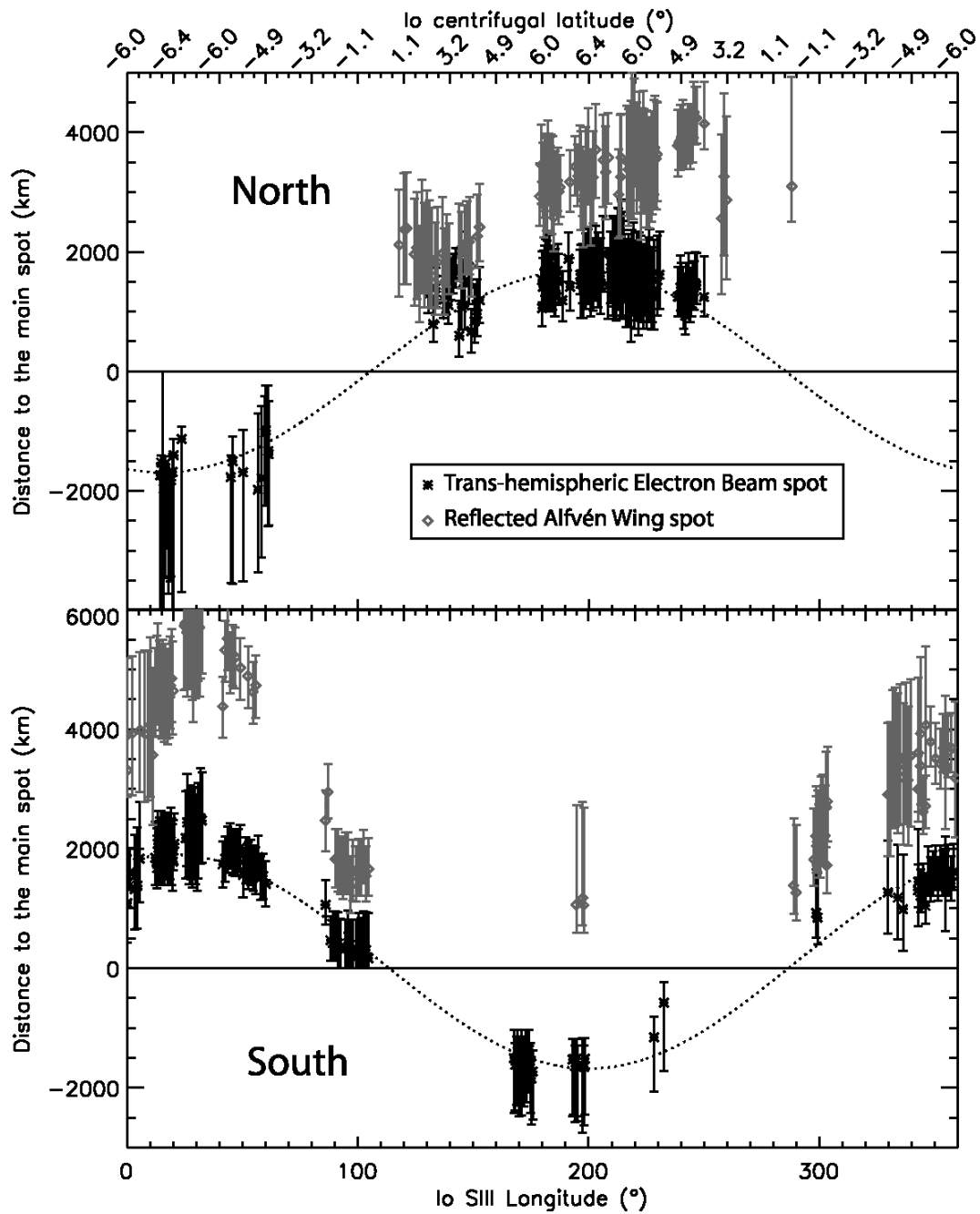


Figure 2.18: Inter-spot distances for both hemispheres against System III longitude after Bonfond et al. [2009]. The two curves represent the best fit of the points with a sinusoidal function.

Chapter 3

Enceladus: Observations and Previous Models

3.1 General Overview

The German-British astronomer William Herschel discovered Enceladus (Figure 3.1) on August the 28th, 1789. Ordered by distance it is the fourteenth moon of Saturn. Ordered by size it is the sixth biggest. Named after one of the titans in Greek mythology it orbits deep inside the Kronian magnetosphere at a distance of 3.95 Saturn radii (R_S). It is located inside Saturn's ring system and marks the area with the highest density within the E-ring, the outermost and most extended of the rings. With a radius of $R_E = 252.1$ km it is small compared to the biggest of the Kronian satellites Titan which has a mean radius of 2575 km. Despite its small size, the early discovery was possible due to the high albedo of 0.89, which is the highest value in the whole solar system. With a surface temperature of 76 K, Enceladus is covered entirely with white water ice, which causes the high amount of light reflection and make it appear very bright. The mean density of 1.6 g/cm^3 suggests a silicate core beneath the ice layer. The escape velocity is very small (239 m/s) and thus Enceladus does not possess a significant atmosphere.

In the past few years a pronounced gas and dust plume has been discovered over the south polar area of Enceladus. It extends to several R_E distance (see Figure 3.2). This plume is partly ionized and, like the ionosphere in the Io-scenario, interacts with the Kronian magnetoplasma that corotates with the planet. The perturbation then travels through the magnetosphere and thus couples Enceladus to the Saturnian ionosphere causing auroral emissions [Pryor *et al.*, 2011].

Being another case of magnetosphere-ionosphere coupling generated by an inner moon this scenario is worthwhile discussing in the present thesis. The nature of Enceladus' interaction is similar to some extent, yet profoundly different concerning other aspects. The main difference is the nature of the obstacle. Io and its atmosphere and ionosphere perturb the magnetoplasma as one unit, whereas Enceladus and its southern plume need to be treated separately. The partly ionized plume material represents an obstacle to the incoming plasma, whereas the satellite itself

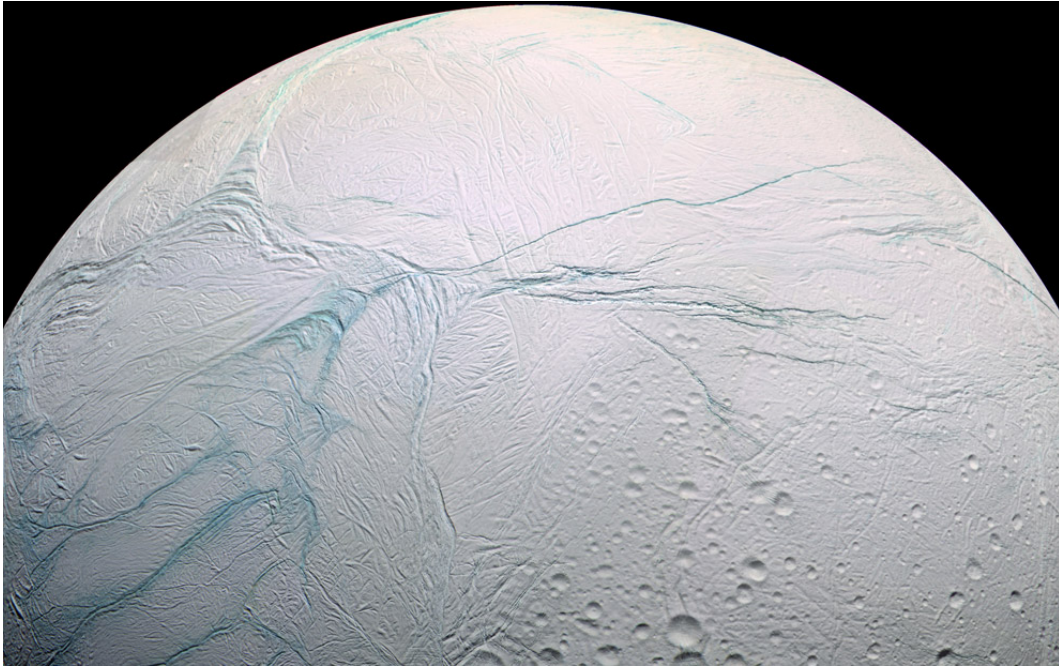


Figure 3.1: Cassini mosaic of Enceladus' south polar region. "Tiger stripes" light blue in lower right corner.

hardly interacts directly with the plasma, since it does not have a significant conductive ionosphere. However, the solid satellite body represents a notable asymmetry for the current system that couples to Saturn's polar regions and thus for the MHD wave pattern generated.

In the following sections we introduce observations and models that concern Enceladus. We elaborate similarities and differences between the two satellites and the nature of their interaction.

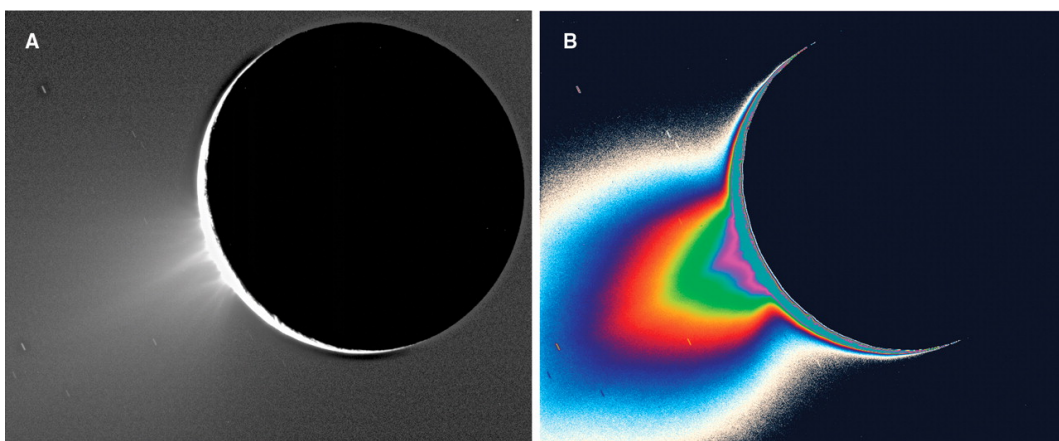


Figure 3.2: Cassini images of Enceladus' south polar region and the plume. A: Clear-filter image. Single jets can be identified. B: Processed version with faint light levels in color-code, more suitable to estimate the extent of the plume. [Porco et al., 2006]

3.2 Saturn's Magnetic Field and Ring System

Unlike Jupiter's magnetic field, Saturn's magnetic dipole is almost perfectly aligned with the rotational axis with just a small northward offset [Burton *et al.*, 2009]. Higher order Gauss coefficients are negligibly small. The magnetic moment is 30 times smaller than Jupiter's with a value of $\sim 4.6 \times 10^{18} \text{ Tm}^3$, still this value is 580 times larger than that of the Earth. However, owing to a fast decay with distance and the size of Saturn, the equatorial surface magnetic field is twenty times smaller than Jupiter's and with 20,000 nT Gauss even smaller than the terrestrial one of 30,000 nT. On Enceladus' orbit the background magnetic field amounts to 350 nT. Similar to Jupiter, Saturn emits radio signals, but unlike its "big brother" where the emission reminds of a lighthouse as the cone rotates with the planet, Saturn sends distinct bursts in a sense comparable to a stroboscope. Cassini observations proved a significant drift in the signal's periodicity, which is impossible to mirror a change in the rotation rate of the deep interior due to the massive moment of inertia of the planet. Just recently Gurnett *et al.* [2009] report a difference in Saturn's kilometric radio (SKR) emission periods between the northern and southern hemisphere which is again not consistent with any direct connection between radio signals and internal rotation. Consequently, the Saturn's radio flash signals seem only limitedly suitable for the exact determination of the rotation rate of the deep interior and thus for the definition of a longitudinal reference system. However, the SKR period is believed to provide at least an estimate of the rotation period. The observed drift is on the order of 1%. In combination with an approximately perfect magnetic dipole field, the effect on the ambient magnetic field and the velocity of the corotating plasma at Enceladus is little. We will use a value of 10.7h for Saturn's rotation period.

Although Enceladus is located deep within the ring system and marks the most dense part of the outermost E-ring, the ambient ring material consists of particles that are small compared to the one found in the inner rings (A-F). The source of the inner Ring material is still one of the enigmas fascinating scientists. Spectroscopic observations derive a very young age of the particles. Yet, there is no hint for a continuous source or a specific event that created the rings in younger history. Conversely the source of the E ring material seems to be found: Enceladus.

3.3 Cryovolcanism, Atmosphere and Plume Material

Before the flybys of the *Voyager* probes, very little was known about Enceladus. In 1980 and 1981 *Voyager1* and *Voyager2* flew by the ringed gas planet. Unfortunately the trajectory was located at some distance to Enceladus, so that no in-situ measurements of the local environment were possible. However, the pass was close enough to shoot a picture of the satellite with a resolution that allowed identification of surface features. The photo instantly attracted attention in the scientific community. The detailed structure of the surface is characterized by a distinct dichotomy. While the northern hemisphere is rich in craters, the southern half is relatively smooth with very few craters but numerous rifts. This suggest recent resurfacing on geological timescales. Squyres *et al.* [1983] proposes volcanism of water enriched with ammonia acting as anti-freezing compound as resurfacing mecha-

| Parameter | Value |
|---------------------------------------|----------------------------------|
| Mass ¹ | 1.08 10 ²⁰ kg |
| Mean radius ¹ | 252.1 km |
| Mean orbital distance ² | 238200 km (3.95 R _S) |
| Mean surface temperature ³ | 76 K |
| Mean density ¹ | 1.608 g cm ⁻³ |
| Escape velocity ¹ | 235 m s ⁻¹ |
| Orbital period ¹ | 32.88 h |
| Orbital velocity ² | 12.6 km s ⁻¹ |

Table 3.1: Physical and dynamic parameters of Enceladus. Sources: [1] Porco et al. [2006], [2] Tokar et al. [2006], [3] Spencer et al. [2006].

nism. Haff et al. [1983] speculate about possible cryovolcanism or geysers in a similar way. Their conclusion is motivated by *Voyager* results that indicate a lifetime for the E-ring particles of only a few thousand years. This implies a continuous source that feeds the ring.

Clear evidence for active cryovolcanism was provided by the *Cassini* mission. Dougherty et al. [2006] report the identification of an atmospheric plume owing to perturbations in the local magnetic field. Other *Cassini* instruments later confirmed their conclusions [e.g. Tokar et al., 2006; Spahn et al., 2006]. Figure 3.2 shows pictures taken by the *Imaging Science Subsystem* (ISS) on *Cassini* [Porco et al., 2006]. The plume is clearly visible and even single jets can be identified.

Infrared imaging of the south polar region also shows different ridges that are substantially warmer than the surrounding terrain. These observations confirmed the assumption that the so-called "tiger stripes" are the source area of the plume material, which itself is the source for the E-ring particles [Spahn et al., 2006]. However, the plume activity exposes considerable variability [Saur et al., 2008] which eventually affects the electromagnetic interaction.

The *Cassini Ion and Neutral Mass Spectrometer* (INMS) analyzed the composition of the plume material [Waite et al., 2006]. It consists mainly of water (91%) and carbon dioxide (3.2%). Due to the similar molecular mass the instrument can hardly differentiate between CO and molecular nitrogen, which account for 4% of the material. Minor traces of methane and complex organic molecules were measured (~2% altogether).

Like the Galilean satellites, Enceladus and Dione are in orbital resonance (2:1). Haff et al. [1983] speculated that tidal heating might cause cryovolcanism that feeds the E ring. Porco et al. [2006] calculate an upper limit of 0.12 GW for tidal heating and 0.32 GW for the energy from radioactive decay. Both values are far below the value needed to explain infrared images that show the "tiger stripes" at the south pole. The IR radiation on these images adds up to 6 GW [Spencer et al., 2006] not including lower wavelengths. Altogether, Enceladus' heat source remains a puzzle.

Regardless of the energy source for the heating of Enceladus is, it is accepted that the ejected material is the main plasma source for the E ring which we will discuss

| Physical property | Symbol [unit] | av. value (min-max) |
|------------------------------|----------------------------|---------------------|
| Saturnian magnetic field | B_0 [nT] | 325 |
| Electron density | n_e [cm^{-3}] | 70.5 (45-90) |
| Mean ion charge number | Z_i [e] | 1.0 |
| Mean Ion mass number | A_i [amu] | 17.6 |
| Mass density | ρ [amu] | 1241 (792-1584) |
| Ion temperature | kT_i [eV] | 35 |
| Electron temperature | kT_e [eV] | 1.35 |
| Local corotation velocity | V_{corot} [km/s] | 39 |
| Satellite orbit velocity | V_E [km/s] | 12.6 |
| Relative plasma velocity | V_0 [km/s] | 26.4 |
| Alfvén speed | V_A [km/s] | 202.98 (180-254) |
| Sonic speed | c_s [km/s] | 20 |
| Magnetosonic speed | c_{ms} [km/s] | 202.96 |
| Alfvénic Mach number | M_A | 0.13 |
| Plasma beta | β | 0.01 |
| Electron cyclotron frequency | f_{ce} [kHz] | ~ 10 |
| Ion cyclotron frequency | f_{ci} [Hz] | ~ 0.3 |

Table 3.2: *Physical parameters of the magnetoplasma on Enceladus' orbit. Values adopted from Tokar et al. [2006] and Dougherty et al. [2006]*

in the next section.

Interestingly, long before the cryovolcanic activity that is the key to Enceladus' interaction was known, the name given to the satellite by John Herschel, the son of its discoverer, already alluded to a tectonic and volcanic activity. The ancient Greeks attributed earthquakes and volcanism to actions of the giant. According to the myth he was defeated by Athena, who smashed the island of Sicily onto him. Our ancestors believed that he is unable to escape, yet struggling to disengage, resulting in earthquakes and eruptions of Mount Aethna, the famous Sicilian volcano.

3.4 The Ambient Plasma

The E ring plasma, like the Io torus plasma, corotates with Saturn at a velocity of ~ 39 km/s at $3.95 R_S$. However there are hints that the plasma localized around Enceladus' orbit is sub-corotating by up to $\sim 25\%$, leading to a velocity of ~ 29 km/s [Wilson et al., 2009]. With Enceladus orbital velocity of 12.8 km/s, the relative plasma velocity lies hence between 16.5 km/s and 26.5 km/s. Interpretation of *Radio and Plasma Wave Science* (RPWS) experiment data from *Cassini* yields the electron density via the upper hybrid frequency. The results show a variation of a factor of two in the density ($n_e = (45 - 90) \text{ cm}^{-3}$) [Jia et al., 2010b]. With a mean ion mass of 17.6 amu, the local Alfvén velocity is ~ 203 km/s. These and other important plasma properties are compiled in Table 3.2.

Although the ambient plasma characteristics differ between Enceladus and Io, the dimensionless parameters that characterize the nature of the interaction are similar.

The incoming plasma flow is as well sub Alfvénic, supersonic and sub-magnetosonic. Also the low plasma-beta of ~ 0.01 , compared to ~ 0.3 for the the Io-Jupiter scenario, characterizes the interaction to be also dominated by the magnetic field pressure rather than by plasma thermal effects.

Perhaps due to the variable plume activity, considerable changes in the ambient plasma density have been observed [Jia *et al.*, 2010a]. This is also indicated by the electron density range in Table 3.2. Hence in analogy to Io, the strength of the interaction might undergo some variation not only according to direct plume (i.e. obstacle) modification but also through mutability of the impinging E ring plasma.

3.5 Analytical and Numerical Models of the Local Interaction

The profound difference between the Io-Jupiter interaction and the one of Enceladus in the Kronian magnetosphere is the nature of the obstacle. Thus analytical and numerical models were developed to describe this hitherto unseen configuration.

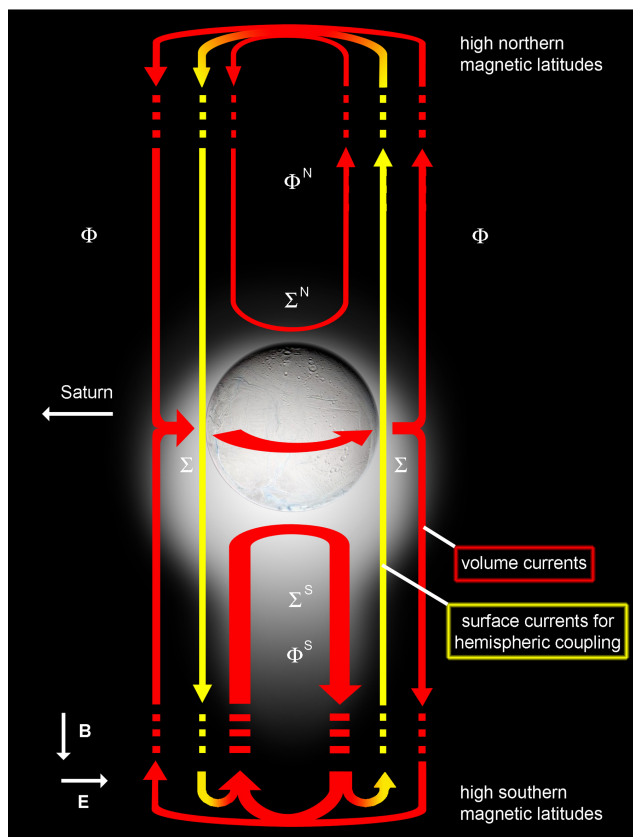


Figure 3.3: Sketch of the Enceladus current system. [after Saur *et al.*, 2007]

The absence of a significant atmosphere and a low conductivity make Enceladus an almost inert obstacle for the incident plasma that is basically lost when hitting the surface unhindered by atmospheric particles. The resulting plasma cavity in the geometrical wake is filled with plasma in the downstream region, due to pressure gradients. Conversely, the magnetic field diffuses through the moon almost unhindered. This type of obstacle is termed "inert". Inert satellites in the Kronian system are for instance Tethys and Rhea. Their interaction with the magnetosphere was investigated in detail by Khurana *et al.* [2008] and also Simon *et al.* [2009].

Enceladus' interaction as a whole, however, is profoundly different owing to the southern plume interaction with the impinging plasma. A current system similar to the one we study at Io develops, but in the particular case of Ence-

ladedus' interaction with the impinging plasma. A current system similar to the one we study at Io develops, but in the particular case of Ence-

Enceladus it is partially blocked in the north by the moon. *Saur et al.* [2007] gave an analytical solution of the resulting asymmetric current system and predicted additional currents to flow on the surface of the flux tube tangent to Enceladus' surface that couple the northern and southern hemisphere of Saturn. A sketch of the resulting current system is presented in Figure 3.3. The observations during several subsequent *Cassini* flybys show strong hints that this current system exists [*Simon et al.*, 2011]. In analogy to Io, *Saur et al.* [2007] expect the magnetic field inside the northern Alfvén wing to be rotated towards Saturn. This prediction, however, was proved to be wrong, as the magnetic field data shows on the contrary a turn of the vectors away from Saturn. This puzzling feature was successfully modelled by a possible substantial (30°) deviation of the incoming plasma flow direction by *Jia et al.* [2010c]. *Simon et al.* [2011] explain the inverse turn of the magnetic field without major constraints for the approaching plasma. They combine and expand the analytical models for Io and Enceladus by *Neubauer* [1980; 1998]; *Saur et al.* [1999] and *Saur et al.* [2007] and based on observational findings of a pronounced electron depletion, they introduce an additional plasma constituent, namely negatively charged heavy ions. The introduction of this new component leads to a reversal of the Hall effect held responsible for the turn towards Jupiter in the Io flux tube. They conclude that this "anti-Hall" effect twists the magnetic field in the direction observed by the *Cassini* magnetometer.

Various numerical models have been applied to study Enceladus' interplay with the Kronian magnetosphere. [*Jia et al.*, 2010d;c;b] use a single fluid MHD approach to systematically investigate certain aspects of the interaction. They compare the unique twofold composition of the obstacle to other cases such as comet-like or inert obstacles. From magnetic field data, they infer plume properties on the basis of their simulations. However, single-fluid MHD codes can not in principle investigate the effects of heavy negative ions as proposed by *Simon et al.* [2011]. This is possible with multi-fluid hybrid codes including kinetic effects. Such a code has been successfully applied to Enceladus by *Kriegel et al.* [2009].

The efforts mentioned so far concentrated mostly on the local interaction environment of Enceladus. On the contrary, some effort was spent on the ionospheric response to the coupling, i.e. the search for an auroral footprint. The detection was proclaimed just recently and we will give an outline of the results in the following section.

3.6 The Enceladus Footprint

A paper currently in press by *Pryor et al.* [2011] reports the observation of an Enceladus footprint in the Kronian ionosphere by the *Cassini* probe. In the same publication the authors proclaim the detection of intense electron beams by *Cassini* particle detectors. In detail, *Pryor et al.* [2011] declare the identification of electron and ion beams originating from Saturn's northern hemisphere by the *CASSINI Plasma Spectrometer* (CAPS) and the *Ion and Neutral CAMERA* (INCA). The observed protons have energies of 55-90 keV. The total electron energy distribution is split between a maximum at 10 eV and another at 1 keV. However, there are temporal or local variations as the beam extent is reported to range from 3.6 to 23.3 R_E downstream. We note that unlike at Io, the beams are clearly detached from

the obstacle and do not couple to the generator region. The authors use an empirical model to infer that the observed beams would produce a UV emission in the southern hemisphere between 3 and 12 kR, which is above the detection limit of the *Cassini UltraViolet Imaging Spectrograph* (UVIS). However, during none of the 28 exposures of UVIS to the southern aurora showed signs of a southern Enceladus footprint. By contrast, in observations of the northern aurora, the authors report the successful identification of a footprint in 3 successive out of 282 exposures. The rough location agrees with the expectations derived from Saturn's magnetic field model. The downstream offset in longitude of the footprint is provided with $1.7^\circ \pm 0.5^\circ$ and $0.8^\circ \pm 0.4^\circ$ for two of the detections. Pryor *et al.* [2011] conclude that the auroral spot is a transient feature within the UVIS detection limits. Likely the intensity is strongly fluctuating, perhaps due to variable plume activity and changing ambient plasma conditions.

Part II

Model

Chapter 4

Theoretical Framework

4.1 The Ideal MHD Equations

Natural plasmas consist of a large number of electrons and ions of different species. A full formulation of the interaction of Io with the ambient magnetoplasma would include equations for the different ion species, a detailed description of Io's ionosphere but also microphysical processes that lead e.g. to the generation of electron beams. Our aim, however, is the global description of the electrodynamic interaction between satellites and their parent planet with emphasis on the morphology of the wave reflection pattern and thus we employ a more general and idealized approach.

We choose a fluid description for the plasma-physical processes of the interaction our numerical model. In this section we will briefly summarize the steps that transfer the theory of the motion of particles to the continuum concept. A detailed derivation of the equations can be found in e.g. *Baumjohann and Treumann [1996]*.

If the macroscopic scales and frequencies that characterize the system under consideration are much larger than the scales and frequencies of single particle motion, we can easily neglect gyration effects of single particles. Before we continue, we thus need to verify that this assumption is true for our intended application.

The typical microscopic time and length scales have to be much smaller than those that characterize the macroscopic approach. A typical time scale of the interaction is the time t_c that the plasma needs to convect past the obstacle. This value has to be compared to the typical microscopic timescale given by the ion gyro or cyclotron frequency f_{ci} :

$$t_c \gg T_{ci} = \frac{1}{f_{ci}} = \frac{2\pi m_i}{(Z_i e)B}, \quad (4.1)$$

where m_i is the ion mass, Z_i the ion charge number and e the elementary charge. At Io, a given plasma velocity of 57 km/s and Io's diameter of 3642 km roughly gives a typical time t_c of one minute. Compared to a gyration time of less than a second for typical ion species at Io [*Kivelson et al., 2004*].

For Enceladus, a fully corotating plasma convects at 26.4 km/s past the 504 km

sized obstacle in approximately 20 seconds. This value is rather a lower boundary, as *Saur et al.* [2007] have shown that the convection time can be much larger and *Wilson et al.* [2009] report that at Enceladus' orbit the plasma is likely sub-corotation by 25%. The gyration time on the other hand is ~ 3 s [*Khurana et al.*, 2008]. Thus, even if the Enceladus plume is considerably smaller than Enceladus itself, condition (4.1) is fulfilled and condition (4.1) holds for both, the Enceladus and the Io scenario.

The macroscopic length L , i.e. the diameter of the satellite is required to be much larger than the gyroradius r_{ci} of the ions.

$$L \gg \frac{V_{th}}{2\pi f_{ci}} = \sqrt{\frac{2k_B T}{m_i}} \frac{m_i}{(Z_i e) B} = \sqrt{\frac{2k_B T m_i}{(Z_i e)^2 B^2}} = r_{ci}. \quad (4.2)$$

We denote the thermal velocity by V_{th} , the temperature by T and the Boltzmann constant by k_B . Using values found in common literature [*Kivelson et al.*, 2004; *Kriegel et al.*, 2009, and references therein], we obtain value of $r_{ci}=1.5$ km to $r_{ci}=3$ km for Io and ~ 15 km for Enceladus. Both values lie comfortably below the characteristic macroscopic length and fulfill condition (4.2). With this justification in mind we can advance in the derivation of the MHD fluid formulation.

The evolution of the distribution function f_s for electrons and different ion species (indicated by subscript s) is given by the *Boltzmann equation*

$$\frac{\partial f_s}{\partial t} + \mathbf{v} \cdot \nabla_{\mathbf{x}} f_s + \frac{q}{m} (\mathbf{E} + \mathbf{v} \times \mathbf{B}) \cdot \nabla_{\mathbf{v}} f_s = C_s = \left(\frac{\partial f_s}{\partial t} \right)_{coll}. \quad (4.3)$$

The LHS of (4.3) describes the influence of macroscopic fields like \mathbf{E} and \mathbf{B} on the particle motion. It contains external fields and internal fields resulting from long-range particle motion. Contrary, the RHS term of (4.3) represents the small scale interaction between particles, called collisions hereafter for convenience, albeit this expression suggests a simplistic concept of merely binary collisions.

Neglecting collisions, as demanded by the fluid approach, leads to the *Vlasov equation*

$$\frac{\partial f_s}{\partial t} + \mathbf{v} \cdot \nabla_{\mathbf{x}} f_s + \frac{q}{m} (\mathbf{E} + \mathbf{v} \times \mathbf{B}) \cdot \nabla_{\mathbf{v}} f_s = 0. \quad (4.4)$$

Multiplying (4.4) with powers of the velocity and subsequent integration in the velocity space gives the set of fluid equations. The number of equations that we obtain by repeating this procedure is unlimited as the moment of order N implies the next higher order. The set of equations can be closed by assuming an ideal gas, with adiabatic conditions, where $p \sim \rho^\gamma$. Motivated by our generalized approach, we do not distinguish between different ion species and introduce a single average ion species denoted by subscript i .

Moreover we use $m_e \ll m_i$ and assume quasi neutrality ($n_i * Z_i = n_e$) to derive the

set of single fluid ideal MHD equations:

$$\frac{\partial \rho}{\partial t} + \nabla \cdot (\rho \mathbf{v}) = 0 \quad (\text{continuity equation}) \quad (4.5)$$

$$\rho \left(\frac{\partial \mathbf{v}}{\partial t} + \mathbf{v} \cdot \nabla \mathbf{v} \right) = -\nabla p + \frac{1}{\mu_0} (\nabla \times \mathbf{B}) \times \mathbf{B} \quad (\text{momentum equation}) \quad (4.6)$$

$$\frac{\partial \mathbf{B}}{\partial t} = \nabla \times (\mathbf{v} \times \mathbf{B}) \quad (\text{induction equation}) \quad (4.7)$$

$$\frac{\partial \epsilon}{\partial t} + \nabla \cdot (\epsilon \mathbf{v}) = -p \nabla \cdot \mathbf{v} \quad (\text{energy equation}). \quad (4.8)$$

4.2 The General Alfvén Wing Model

Basically two competing models have been discussed to explain the Io-Jupiter interaction. The current loop model (section 2.5.1) and the Alfvén wave model (section 2.5.2). In this section we elaborate why both represent two extreme cases of one general formulation published by *Neubauer* [1980]. The author extends in his work the previous linear Alfvén wing model by *Drell et al.* [1965] that was only valid for weak perturbations to the fully nonlinear case. The solution is applicable for a homogeneous background plasma in terms of density ($\rho = \rho_0$), pressure ($p = p_0$) and a conserved magnetic field magnitude ($|\mathbf{B}| = B_0$).

The gist of the analytical framework is the introduction of new coordinates called the Alfvén characteristics. They are given by the expression

$$\mathbf{C}_A^\pm : \mathbf{V}_A^\pm = \mathbf{V}_p \pm \frac{\mathbf{B}}{(\mu_0 \rho)^{1/2}}. \quad (4.9)$$

They are Riemann invariants, sometimes also called Elsasser variables. They describe the causal connection of the wave generator, in this case Io, to any point in the far-field. The technique applied by *Neubauer* [1980] is known as method of characteristics and transfers the initial system of hyperbolic partial differential equations (PDEs) to ordinary PDEs, which can then be solved. The solution presented is independent of this coordinate and therefore the initially three-dimensional problem becomes two-dimensional. As these coordinates need to be valid also at some distance upstream of Io, the characteristic directions are easily obtained via

$$\mathbf{V}_A^\pm = \mathbf{V}_{A,0}^\pm = \mathbf{V}_0 \pm \frac{\mathbf{B}_0}{(\mu_0 \rho)^{1/2}}, \quad (4.10)$$

using the background values of the ambient plasma. The angle between the Alfvén characteristics and the magnetic field is given by

$$\theta_A = \arctan(M_{A,0}) = \arctan \left(\frac{V_0}{V_A} \right). \quad (4.11)$$

The definition of the coordinates is illustrated in Figure 4.1. Other than *Neubauer* [1980] who includes a more general geometry, we restrict the possible configurations to a single case where the magnetic field is perpendicular to the incoming plasma flow and perpendicular to the y-direction. This is the setup we use in our simulations, so we limit the interaction geometry to this case.

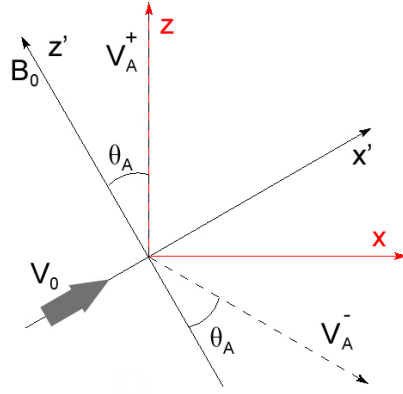


Figure 4.1: *Coordinates after Neubauer [1980].*

It is notable, that major aspects relevant for our work stem from *Neubauer [1980]*. While Alfvén waves in the plasma rest frame propagate along the magnetic field with the Alfvén velocity. *Neubauer [1980]* and the present thesis use Io's rest frame for the calculations. Thus an additional velocity component for the moving plasma needs to be considered for the Alfvén wave propagation. In Io's rest frame Alfvén waves that travel northward follow the C_A^- characteristic, whereas southward propagation takes place along the C_A^+ characteristic. We use the term primary Alfvén characteristics for the given propagation direction for the following reason: Let us regard the northern hemisphere where the waves generated at Io travel northward and thus follow the primary characteristic C_A^- . Regardless of the Alfvénic perturbations of the local magnetoplasma, the primary characteristic is essentially isotropic in the given hemisphere. Contrary, the complementary C_A^+ characteristic holds the effects of the Alfvénic perturbation and might be locally altered substantially depending of the amplitude of the disturbance. Thus we will term the homogeneous Alfvén characteristic that moreover depicts the propagation direction *primary Alfvén characteristic (PAC)*.

As the waves follow the PACs, the associated currents are likewise aligned with this direction. Besides the current component aligned with the PAC direction, there is another independent current system that forms closed loops in planes perpendicular to the Alfvén characteristic. Since they are independent, both systems have a divergence of zero, separately. Both complements together sum up to the current along the characteristics (see Figure 2.7). *Neubauer [1980]* deduced that the wings themselves act like an external conductance given by the expression

$$\Sigma_A = \frac{1}{\mu_0 V_A (1 + M_A^2)^{1/2}}. \quad (4.12)$$

Hence, the currents generated at Io can be closed by the Alfvén conductance Σ_A and the unipolar inductor works without current closure in the Jovian ionosphere.

At a closer look, both models discussed in section 2.6, the linear Alfvén wing model [*Drell et al., 1965*] and the current loop model [*Goldreich and Lynden-Bell, 1969*] are included in the formulation by *Neubauer [1980]*. This becomes most clear if we inspect the scenario for different generator efficiencies. When we use the term efficient generator, we mean an efficient deceleration of the incoming plasma, so that the velocity perturbation is of the order of the background velocity value $|\Delta V| \sim |V_0|$. We refer to this scenario also as strong interaction or non-linear interaction. On the other hand, we discuss a configuration with a small velocity perturbation $|\Delta V| \ll |V_0|$. This setup, we call weak or linear interaction.

For a strong interaction, the plasma inside the Alfvén wing is almost at halt. Since the magnetic field is "frozen-in" the plasma, this leads to field line draping around

the obstacle and an almost perfect alignment of the magnetic field direction with the wing axis given by the Alfvén characteristic. This becomes evident, when inspecting the definition of the Alfvén characteristics (4.9). Note that the PACs need to be identical to those derived from the local background values (4.10). Hence, the magnetic field needs to be parallel to the characteristic for zero plasma velocity. Consequently, currents that flow along the Alfvén characteristics are field aligned as presumed in the current loop model. With resting or almost resting plasma inside the wing, the convection time near Io approaches infinity ($t_c \rightarrow \infty$). Thus the Alfvén waves reflected from the Jovian ionosphere or a closer reflector can easily couple to Io. A steady current loop forms. It is noteworthy that *Neubauer* [1980] points out that the current loop model is valid for very low Mach numbers, only. If one considers M_A to be a local quantity, rather, than a background plasma parameter, the Mach number inside the Alfvén wing is very low. Thus, the assessment of the validity of the current loop model via the Mach number holds.

A weak interaction barely decelerates the plasma and the magnetic field perturbation is negligibly small. This scenario can be linearized regarding first order terms only. It then yields the solution elaborated by *Drell et al.* [1965].

Note that the direction of the total current flow is always along the PACs C_A^\pm . It is merely the direction of the perturbed magnetic field or in other words the magnetic field alignment with the wing that differs for both extreme scenarios as well as the residual plasma bulk velocity in the Alfvén wing.

4.3 Parallel Electric Fields and the Knight Formula

Since the cross section of the Io flux tube¹ decreases along the travel path of the Alfvén wave towards Jupiter, one expects the charge density to rise. High current densities trigger effective resistivities that force the flow of electric currents. These resistivities generate parallel electric fields, that accelerate the particles. They have been observed in-situ and are manifested in the mono energetic particle energy distribution derived from measurements of the discrete aurora. The exact source of these electric fields is still controversial and far from being fully understood. However, *Knight* [1973] investigated the interrelation between current magnitude and the potential drop and developed a model known as the *Knight relationship*. Starting with an anisotropic Maxwellian particle distribution in the magnetosphere the framework of collisionless plasma kinetic theory yields the following field-aligned component of the current density in the acceleration region:

$$j_{\parallel} = e n_e \left(\frac{k_B T_e}{2\pi m_e} \right)^{1/2} \frac{B_M}{B_I} \left(1 - \left(1 - \frac{B_M}{B_I} \right) \exp \left[\frac{-e \Delta \Phi_{\parallel}}{k_B T_e ((B_I/B_M) - 1)} \right] \right) \quad (4.13)$$

with the usual symbols for the electron mass and number density (m_e , n_e), the thermal energy (kT_e) and the magnetic field (B). Indices denote the location on the field line in the magnetosphere (M) and the ionosphere (I) and $\Delta \Phi_{\parallel}$ represents the potential drop between the two locations. While this expression appears intricate, it reduces to a linear law

$$j_{\parallel} = K \Delta \Phi_{\parallel} \quad (4.14)$$

¹Here we could more precisely use the term "flux funnel" to take account for the bunching of field lines when approaching Jupiter.

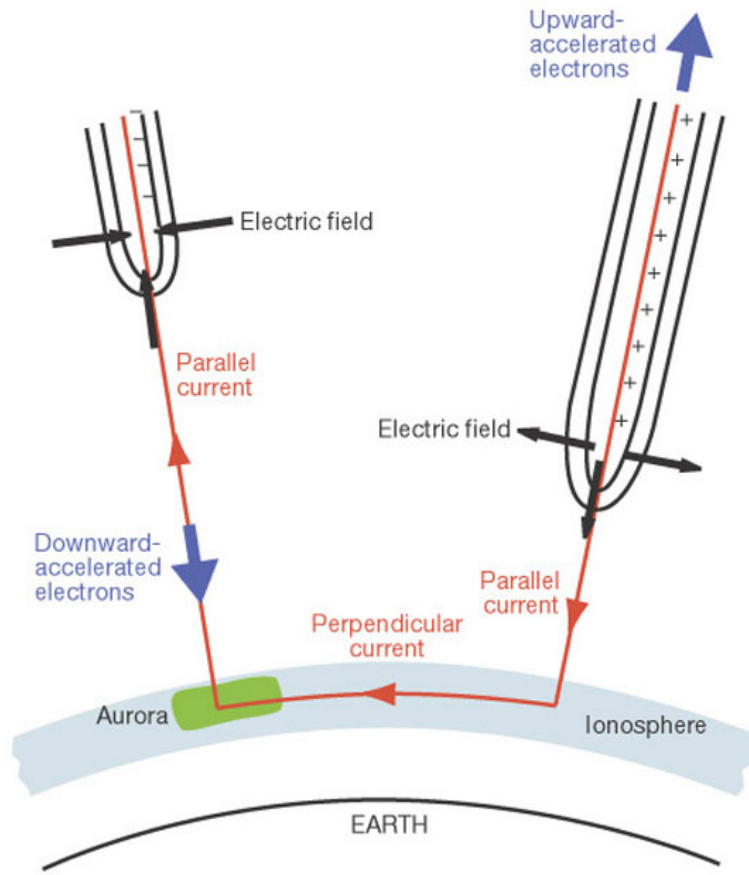


Figure 4.2: Sketch of the electric field topology at Earth. Equipotential contours of the electric field in black, currents in red. Electrons precipitate downwards in upward current regions. Upward acceleration occurs in downward current regions [after Marklund et al., 2001]

for

$$\frac{B_I}{B_M} \gg \frac{e \Delta \Phi_{\parallel}}{k_B T_e} \gg 1 . \quad (4.15)$$

The effective field-aligned conductance K is then given by

$$K = \frac{e^2 n_e}{(2\pi m_e k_B T_e)^{1/2}} . \quad (4.16)$$

Hence, the inverse $1/K$ has the dimension of a resistance². However, this resistance gives rise to electric fields parallel to the ambient magnetic field. Plasma particles subject to this field are being accelerated along the field line and are believed to cause more intense aurorae, the so-called discrete aurorae. The region where these

²More precisely the term impedance should be used for this phenomenon. While a "resistance" implies a linear current-voltage relationship, the word "impedance" is more general as it describes also alternating currents and includes nonlinear correlation. However, resistance is used more often and thus we will also apply this terminology.

parallel electric fields are found is thus called acceleration region. During the last years, the terrestrial auroral acceleration region or shortly AAR has been extensively studied by in-situ campaigns. Among others, measurement by the *FAST* probe attracted remarkable interest [e.g. *Carlson et al.*, 1998].

Condition (4.15) is easily fulfilled at Earth, using typical values for the magnetospheric generator region and the ionosphere [e.g. *Lysak and Song*, 2001]. For the Io-Jupiter system, however, this is to some extent disputable. For the magnetic field ratio, using a typical values of 2000 nT on Io's orbit and 1 mT at the top of the ionosphere, we obtain a ratio of 500. Thus for the cold torus electron population with energies of 6 eV, the condition is only valid for accelerated electrons of as much as ~ 1 keV. This means that the current-voltage relationship is likely nonlinear for the Io footprint electrons. Even using properties of the hot electron population with higher energies by roughly a factor of ten, the condition is not easily fulfilled for electrons with energies of ~ 40 -70 keV inferred from aurora observations [*Bonfond et al.*, 2009]. Other assumptions incorporated in the *Knight model* that are clearly valid for Earth, are questionable for Jupiter. Most importantly, *Knight* [1973] constitutes a monotonic potential structure between the magnetospheric generator and the ionosphere. For Jupiter, being a fast rotator, *Ray et al.* [2009] find that equatorially confined plasmas give rise to ambipolar electric fields resulting in a non-monotonical potential configuration between the ionosphere and Io's orbit. This contradicts the assumptions of *Knight* [1973]. Consequently *Ray et al.* [2009] present a modified current-voltage relationship taking these effects into account. However, they deduce a maximum current density 100 times lower than derived with the *Knight* relation for a given potential. On the other hand, for a given current density below saturation, the extended solution yields appreciably higher acceleration potentials.

It is noteworthy that *Knight* [1973] and subsequent works that focus on the current-voltage interrelation [e.g. *Lyons*, 1980] do not explain the exact mechanism that produces the electric field they investigate. These groups concentrate on quantitative constraints on the magnitude of the field in their studies. However, microscopic processes that induce parallel potentials are still subject of current research. For our approach this topic is of minor importance and we refer the keen reader to e.g. *Louarn* [2002].

4.4 Non-Ideal MHD: Additional Terms

4.4.1 Effective Collision Frequency

As the interaction involves an obstacle to the incoming plasma flow e.g. in the form of Io, we incorporate the effect of plasma collisions with neutrals into the original ideal MHD equations. *Neubauer* [1998] demonstrates that small scale plasma-neutral processes that characterize the interaction can be expressed through generalized collision frequencies. This includes elastic collisions, ion pickup and charge exchange. In the single fluid description chosen for our work, we introduce the effective collision frequency ν which represents the ion-neutral interaction. On the one hand collisions slow down the incoming plasma and reduce the directed component of the plasma velocity, i.e. the bulk velocity. On the other hand colli-

sions contribute an additional statistical velocity component, i.e. frictional heating. Hence, the introduction of an effective collision frequency decelerates and changes the plasma temperature. Consequently, we include a collision term into the momentum equation (4.6) and frictional heating and temperature coupling terms into the energy equation (4.8).

After some algebra the ideal equations (4.6) and (4.8) modify to:

$$\rho \left(\frac{\partial \mathbf{v}}{\partial t} + \mathbf{v} \cdot \nabla \mathbf{v} \right) = -\nabla p + \frac{1}{\mu_0} (\nabla \times \mathbf{B}) \times \mathbf{B} - \rho \nu \mathbf{v} \quad (4.17)$$

$$\frac{\partial \epsilon}{\partial t} + \nabla \cdot (\epsilon \mathbf{v}) = -p \nabla \cdot \mathbf{v} + \frac{\nu}{2} (\rho \mathbf{v}^2 + \epsilon_n - \epsilon), \quad (4.18)$$

where ϵ_n represents the internal energy of the neutrals. We point out that, even if our model does not include mass loading explicitly, it is represented in the energy equation (4.18) and the equation of momentum conservation (4.17) by the effective collision frequency ν (see *Neubauer [1998]* and *Hill and Pontius [1998]* for details). Only equation (4.5) would be qualitatively modified.

Inspection of equation (4.17) reveals, that the new force (i.e. the drag exerted on the plasma by the collisions) $\nu \rho \mathbf{v}$ not only depends on the effective collision frequency, but also on the ambient plasma density. This implies that for a given collision frequency, variation of the ambient plasma density scales the initial perturbation and thus the interaction strength. In the case of Io, this happens when Io oscillates between the densest inner plasma torus and the dilute outer parts. On the other hand modulation of ν can vary the interaction strength even for constant plasma density. While modification of ρ modifies also the Alfvén characteristics and thus the wave propagation and reflection geometry, adjustment of ν does not. We will make use of this profound difference to isolate the influence of the interaction strength on the footprint morphology.

4.4.2 Resistivity

Models of the auroral current system can generally be divided in to two groups. Kinetic models, that focus on particle motions of different species and fluid models, that emphasize the continuum character of the medium as whole. In the latter group, the MHD approach also applied in this work is most popular. The main disadvantage of ideal MHD is that in such framework is that the medium is considered collisionless (see 4.1) and thus does not allow parallel electric fields. As we apply our extension with effective collisions only locally to represent Io, we still have collisionless plasma outside the direct interaction region. In fact in ideal MHD, there is infinite conductivity along the magnetic field direction. However, there is a remedy widely found to patch this deficiency: The assumption of an effective resistivity in regions of high field aligned current densities. While our model does not allow the investigation of microscopic particle acceleration, other important macroscopic effects of the acceleration region are covered by the inclusion of an effective resistivity. Just as the AAR represents a load in the magnetosphere-ionosphere current system, a resistive layer serves in a similar way. It damps the wave and on the other hand, being a load, it parlay reflects the incoming Alfvén waves. The first aspect will certainly have impact on the energy budget of the coupling between Io and Jupiter; the latter effect is important for the MHD wave field morphology we are

investigating in the work at hand. We will discuss the reflections that take place at the AAR in section 4.5.2.

In order to include resistive effects, the ideal MHD equations require to be modified. The generalized form of Ohm's law is given by:

$$\mathbf{j} = \underline{\underline{\sigma}} (\mathbf{E} + \mathbf{v} \times \mathbf{B}) , \quad (4.19)$$

where $\underline{\underline{\sigma}}$ is the conductivity tensor

$$\underline{\underline{\sigma}} = \begin{pmatrix} \sigma_P & -\sigma_H & 0 \\ \sigma_H & \sigma_P & 0 \\ 0 & 0 & \sigma_{\parallel} \end{pmatrix} , \quad (4.20)$$

$$\mathbf{j} = \sigma_{\parallel} \mathbf{E}_{\parallel} + \sigma_P \mathbf{E}_{\perp} + \sigma_H \frac{\mathbf{B} \times \mathbf{E}}{B} . \quad (4.21)$$

If we neglect the Hall conductivity and in a first order approach demand an isotropic $\underline{\underline{\sigma}}$, then Ohm's law can be simplified to

$$\mathbf{E} = \frac{\mathbf{j}}{\sigma} - (\mathbf{v} \times \mathbf{B}) . \quad (4.22)$$

Using equation (4.22) combined with Ampère's law

$$\mathbf{j} = \frac{1}{\mu_0} (\nabla \times \mathbf{B}) \quad (4.23)$$

in Faraday's equation

$$-\frac{\partial \mathbf{B}}{\partial t} = (\nabla \times \mathbf{E}) \quad (4.24)$$

we obtain a new expression for the induction equation:

$$\frac{\partial \mathbf{B}}{\partial t} = \nabla \times (\mathbf{v} \times \mathbf{B}) + \eta \Delta \mathbf{B} , \quad (4.25)$$

where $\eta = 1/\mu_0\sigma$ represents the magnetic diffusivity. It is related to the resistivity ϱ via $\varrho = \eta\mu_0$.

Recapitulating, the last sections, we obtain the following set of equations, we intend to solve. Terms added to the ideal MHD equations are colored red when stemming from the inclusion of an effective collision frequency and colored blue when origination from resistivity effects.

$$\frac{\partial \rho}{\partial t} + \nabla \cdot (\rho \mathbf{v}) = 0 \quad (\text{continuity eq.}) \quad (4.26)$$

$$\rho \left(\frac{\partial \mathbf{v}}{\partial t} + \mathbf{v} \cdot \nabla \mathbf{v} \right) = -\nabla p + \frac{1}{\mu_0} (\nabla \times \mathbf{B}) \times \mathbf{B} - \rho \nu \mathbf{v} \quad (\text{momentum eq.}) \quad (4.27)$$

$$\frac{\partial \mathbf{B}}{\partial t} = \nabla \times (\mathbf{v} \times \mathbf{B}) + \eta \Delta \mathbf{B} \quad (\text{induction eq.}) \quad (4.28)$$

$$\frac{\partial \epsilon}{\partial t} + \nabla \cdot (\epsilon \mathbf{v}) = -p \nabla \cdot \mathbf{v} + \frac{\nu}{2} (\rho \mathbf{v}^2 + \epsilon_n - \epsilon) . \quad (\text{energy eq.}) \quad (4.29)$$

It is noteworthy that our incorporation of resistivity or magnetic diffusivity adds another characteristic timescale to the system of equations under consideration. The diffusion time is given by

$$\tau_d = \frac{L^2}{\eta} . \quad (4.30)$$

For high diffusivity, this timescale can become smaller than other timescales that describe the system. This is particularly crucial for the calculation of the time step size for the numerical solution of the given set of equations (see chapter 5).

We note that the way we incorporate resistivity is not fully consistent with the implications by *Knight* [1973]. While we apply an isotropic and constant value for the resistivity, the resistance in *Knight* [1973] is only used for the parallel component of the currents. Moreover, it is related to the current density. We do not account for that. Yet we note, that we intend to investigate the fundamental principles of the interaction which justifies this idealized approach.

4.5 Alfvén Wave Reflection

It is accepted that multiple auroral footprints and repeated radio emission arcs manifest that Alfvén wave reflections play an important role in the Io-Jupiter interaction. Numerous publications concentrate on the reflection and transmission coefficients of the Alfvén waves at either the torus boundary or Jupiter's ionosphere (see section 2.6.1 and references therein). For Earth, also reflections at the auroral acceleration region have been studied [e.g. *Vogt and Haerendel*, 1998]. For Jupiter, *Su et al.* [2003]; *Chust et al.* [2005] and *Hess et al.* [2010] address this topic. In this section we moreover elucidate the change of sign behaviour of the Alfvénic perturbation during reflection at the different boundaries.

4.5.1 Reflections at Density Gradients

Generally, reflections occur due to variation of the wave phase speed, given by

$$V_{ph} = \frac{\omega}{k} = \pm V_A \quad (4.31)$$

for the Alfvén waves propagating parallel (+) and antiparallel (-) to the magnetic field, where k is the wave number. Figure 4.5.1 illustrates the reflection process in Io's rest frame, where the waves propagate along the Alfvén characteristics.

Following *Wright* [1987] and *Hess et al.* [2010] we will characterize the reflection process by the ratio of the wave length and the scale length of the plasma density gradient. For plasma scale lengths much smaller than a wave length

$$\frac{L}{\lambda} = \frac{\omega L}{V_A} \ll 1 , \quad (4.32)$$

the inhomogeneity can be described as a discontinuity. Under these circumstances, the reflection and transmission coefficients (C_R and C_T) for the amplitudes are given by

$$\text{transmitted:} \quad C_T = 2V_{A1}/(V_{A1} + V_{A2}) \quad (4.33)$$

$$\text{reflected:} \quad C_R = (V_{A1} - V_{A2})/(V_{A1} + V_{A2}) = 1 - C_T , \quad (4.34)$$

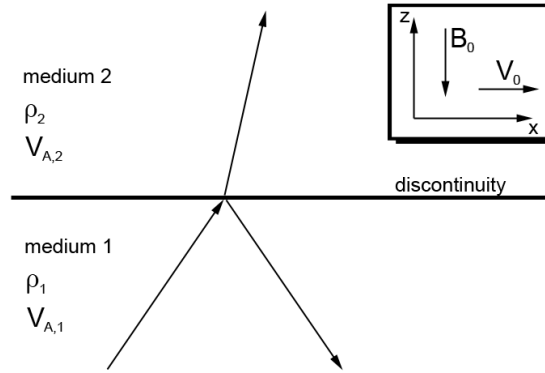


Figure 4.3: Schematic view of wave reflection at a discontinuity

with V_{A1} and V_{A2} defined as illustrated in Figure 4.5.1. Assuming a constant magnetic field across the discontinuity, the amplitudes depend only on the increase of the density:

$$\text{transmitted:} \quad C_T = 2\rho_2^{\frac{1}{2}} / (\rho_2^{\frac{1}{2}} + \rho_1^{\frac{1}{2}}) \quad (4.35)$$

$$\text{reflected:} \quad C_R = (\rho_2^{\frac{1}{2}} - \rho_1^{\frac{1}{2}}) / (\rho_2^{\frac{1}{2}} + \rho_1^{\frac{1}{2}}) . \quad (4.36)$$

While the long wavelengths close to Jupiter justify a thin layer approximation for the ionosphere, the inner Io plasma torus cannot be regarded in such manner, as the scaleheight of the density variation H_i is large compared to the wavelength. With the density model (5.9) which we will introduce in section 5.2.3, we can derive a scaleheight H_i of $\sim 1.1 R_J$ assuming a mean ion species with a mass of 22 amu and an average charge number of 1.3 [Kivelson *et al.*, 2004]. The typical wavelength is $\sim 0.2 R_J$ using $V_A = 200$ km/s and a typical period of 60 s which corresponds to the time the undisturbed plasma needs to convect past Io. Hence condition (4.32) is not fulfilled in the central torus.

A method commonly used in such cases is the WKB³ limit approach [e.g. Hess *et al.*, 2010]. Using 4.33 and $\Delta V_A = V_{A1} - V_{A2}$ we can derive with in the limit $V_{A2} \rightarrow V_{A1} = V_A$

$$C_{R,WKB} = \frac{2V_{A1}}{(V_{A1} + V_{A2})} - 1 \approx \frac{\Delta V_A}{2V_A} . \quad (4.37)$$

This expression written in differential nomenclature along the distance on the field line s gives

$$C_{R,WKB} = \frac{d \ln(V_A)}{2dx} dx . \quad (4.38)$$

In order to estimate the energy that is transmitted through a smooth Alfvén velocity gradient, we use the fact that the energy is proportional to the squared amplitude.

³The WKB approximation is a method for finding approximate solutions to linear partial differential equations with spatially varying coefficients.

As wave energy is not defined on scales smaller than a wavelength, we need to integrate over at least one wave cycle to compute the energy reflection coefficient:

$$C_{R,\lambda} = \left(\int_{-\frac{\lambda}{2}}^{\frac{\lambda}{2}} \frac{d \ln(V_A)}{2dx} dx \right)^2. \quad (4.39)$$

However, due to the plasma density depletion along the field line and hence the increase of V_A , the wavelength rapidly approaches the length scale.

Change of Sign during reflection

After we have discussed the amplitude of the reflection, we will now give a plausible explanation for the reversal of the sign of certain perturbations during reflection.

For the Alfvén wave, the correlation between magnetic field perturbation ($\delta\mathbf{B}$) and plasma velocity perturbation ($\delta\mathbf{V}$) is described in the polarization relation:

$$\frac{\delta\mathbf{B}}{B_0} = \pm \frac{\delta\mathbf{V}}{V_{A0}}, \quad (4.40)$$

for propagation parallel (+) and antiparallel (-) to the magnetic field. Thus, at Io, where $\mathbf{B}_0 \parallel -z$, the magnetic field and velocity perturbation are anti-correlated for waves traveling northward and correlated for waves traveling southward. When the incident wave meets an extremely dense boundary ($\rho_1 \ll \rho_2$), the velocity perturbation in the massive and thus immovable medium is negligible ($\delta V_2 = 0$). The velocity perturbation is thus reflected in the opposite sense, in analogy to the reflection from a "fixed end". Contrary, the magnetic field perturbation is reflected with conserved sign. This scenario occurs when Alfvén waves are reflected at the Jovian ionosphere. We note that in this case at locations the incident and the reflected wave intersect, the return wave weakens the residual velocity perturbation while it enforces the magnetic perturbation.

In the opposite case, when $\rho_1 \gg \rho_2$, the reflection conserves the sign of $\delta\mathbf{V}$ and thus this scenario corresponds to a "free end" reflection. Here, the magnetic field perturbation will reverse. We note that in this case at locations the incident and the reflected wave intersect, the return wave enforces the residual velocity perturbation while it weakens the magnetic perturbation. In any case, as the propagation direction reverses, one quantity, either $\delta\mathbf{B}$ or $\delta\mathbf{v}$, needs to be reverted upon reflection to fulfill the polarization relation (4.40).

4.5.2 Reflections at the Auroral Acceleration Region

Most concepts of the reflections at the AAR and the Ionosphere apply the so-called thin layer approximation, an analogy to the discontinuity approach we applied so far. Contrary to reflections that occur at density gradients, the phase velocity of the wave does not change due to resistivity. In fact, the reflection in this case depends on the contrast in conductivity. A detailed analysis for a so-called "lumped circuit model" was developed by *Vogt and Haerendel* [1998]. The authors expand a solution

by *Scholer* [1970] obtained for ionospheric reflections and apply it to a system of a combined system of AAR and ionosphere. They determine the reflection of the Electric field perturbation to be governed by

$$E_{\perp}^{+} = \frac{\Sigma_A - \Sigma_P(1 - \lambda_t^2 k_{\perp}^2)}{\Sigma_A + \Sigma_P(1 + \lambda_t^2 k_{\perp}^2)} E_{\perp}^{-}, \quad (4.41)$$

where Σ_A is the Alfvén conductance, Σ_P the Pedersen Conductance and k_{\perp} is the perpendicular wavelength. The superscripts denote the incident (+) and the reflected (-) wave perturbation. The parameter λ_t is defined by $\lambda_t = \sqrt{\Sigma_A/K}$, where K is the Knight-Parameter (4.16). *Vogt and Haerendel* [1998] conclude that for large perpendicular wavelengths, the ($1 \gg \lambda_t^2 k_{\perp}^2$) the AAR is transparent for the waves, whereas for small perpendicular wavelengths ($1 \ll \lambda_t^2 k_{\perp}^2$) the waves are predominantly reflected at the AAR. The authors note that in that case, the sign reversal is opposite, namely $C_{R,E}=1$ for the electric field perturbation and thus $C_{R,B}=-1$ for the magnetic field perturbation.

We note that the reflection coefficient depends on the perpendicular wavelength. In our model we are not able to generate the perturbation with the full spectrum in k_{perp} . We are for instance limited by the grid resolution. We do therefore not expect to obtain quantitatively realistic reflection coefficients. However, we can adjust the simulation parameters such that we obtain a reflection of the desired strength. As we intend to carry out fundamental studies this approach is sufficient for our aim.

A simple and more "hands-on" approach to Alfvén wave reflection was published by *Leneman* [2007]. The authors subsume laboratory experiments of Alfvén wave reflection. They find that the reflection coefficient at the boundary denoted by the index b is given by

$$C_{R,B} = \frac{B_R}{B_I} = \frac{\Sigma_b - \Sigma_A}{\Sigma_b + \Sigma_A} \quad (4.42)$$

For a good conductor, where $\Sigma_b \gg \Sigma_A$, they find that $C_{R,B}$ approaches 1, for a bad conductor or isolator ($\Sigma_b \ll \Sigma_A$), the experiments confirm that $C_{R,B}$ approaches -1.

Thus the magnetic field perturbation reverses sign upon reflection at the AAR, whereas the velocity (and electric field) perturbation is reflected in the unchanged sense.

In summary, we find multiple reflectors that are located in the travel path of the Iogenic Alfvén wave towards Jupiter's poles and the resulting MHD wave pattern composed of reflections of different order is particularly complicated. To make things even more complex, the sign of the single wave associated perturbations occasionally reverses upon reflection and thus the residual local perturbation often is a superposition of multiple interfering waves involving also the reflection history. Other phenomena related to the Io-Jupiter interaction like trans hemispheric electron beams are subject to the resulting distorted magnetic field. The subsequent section will deal with these beams.

4.6 Electron Beams

Trans-hemispheric electron beams generated in the acceleration region follow the magnetic field lines, penetrate the orbital plane and continue to the opposite hemi-

sphere, where they trigger secondary auroral emissions. We intend to follow the energetic particle beams along the magnetic field provided by our simulations. Although strictly speaking, the discussion of the beam generation mechanism is beyond the scope of this thesis, we still require at least a geometric concept of the intensity of beam generation we can derive from our simulated data. In a second step we will then map this intensity along the distorted magnetic field and obtain predicted local electron beam intensities. In order to find a good proxy parameter for the beam magnitude will briefly discuss the competing concepts and extract some constraints for our purpose.

While Alfvén waves transmit electric currents between Io and Jupiter with in general low energies per single particle, the aurora observations imply electrons accelerated to energies of 40-70 keV [Bonfond, 2010]. The superficial access to particle acceleration brought up in section 2.6.2 is the simple demand raised by maintenance of the electric currents. Outside the plasma torus the density of charge carriers decreases along the field line and also the cross section of the IFT becomes smaller. In order to conserve the current density, particles need to be accelerated. However, this picture does not provide any explanation for the mechanism that finally causes the acceleration. While radio observations yield results that favour cyclotron-maser instabilities as found in the earth's auroral emissions [Hess *et al.*, 2007], many other concepts like "double layers" or oblique kinetic Alfvén waves have been proposed mostly for the Earth's acceleration region. A list can be found in Table 1 in Borovsky [1993]. After all, most likely inertial effects in Alfvén wave propagation that trigger electric fields accelerate the electrons. For more perspicuity we consult some results obtained for the terrestrial aurora in the next paragraph.

Generally, upward accelerated electrons are associated with downward current regions in the aurora, albeit observations by Klumpar *et al.* [1988] and Carlson *et al.* [1998] for the Earth's aurora have shown that this attribution is not unambiguous [Mauk *et al.*, 2002]. Parallel electric fields related to the two branches of the current system are believed to accelerate the electrons in both directions. Phase space density (PSD) spectra of the observed particles provide hints of the acceleration mechanism. Electron beams generated by parallel electric fields show remnants of a coherent acceleration in the form of a peak in PSD for a certain energy (see Figure 2.11). Swift [2007] has demonstrated that field aligned electron acceleration by inertial Alfvén waves produces upward beams with a broad energy distribution without a PSD peak. In contrast to these strictly field-aligned acceleration mechanisms, a stochastic process (reminiscent of heating) can contribute significantly to the electron acceleration. For Jupiter this has been discussed by Frank and Paterson [2002a]. Williams *et al.* [1999] have shown that the PSD spectra of the beams observed by Galileo do not exhibit a significant peak but decrease monotonically with energy and follow a power law [Mauk *et al.*, 2001]. We thus tend to believe that the energetic equatorial electron beams are not strictly linked to one direction of the current system.

There are moreover attributes of the in-situ observational data at Io that favour this hypothesis. The Io-generated currents are generally directed upward (towards Io) on the Jupiter-facing side and downward (towards Jupiter) on the opposite side (see Figures 2.5 and 6.3). There is a current reversing layer between the two branches. It is located in the center of the geometrical wake downstream of Io and over the moon's disc, i.e. along the y -axis at $x \sim 0$ in Figure 4.4. In case of a

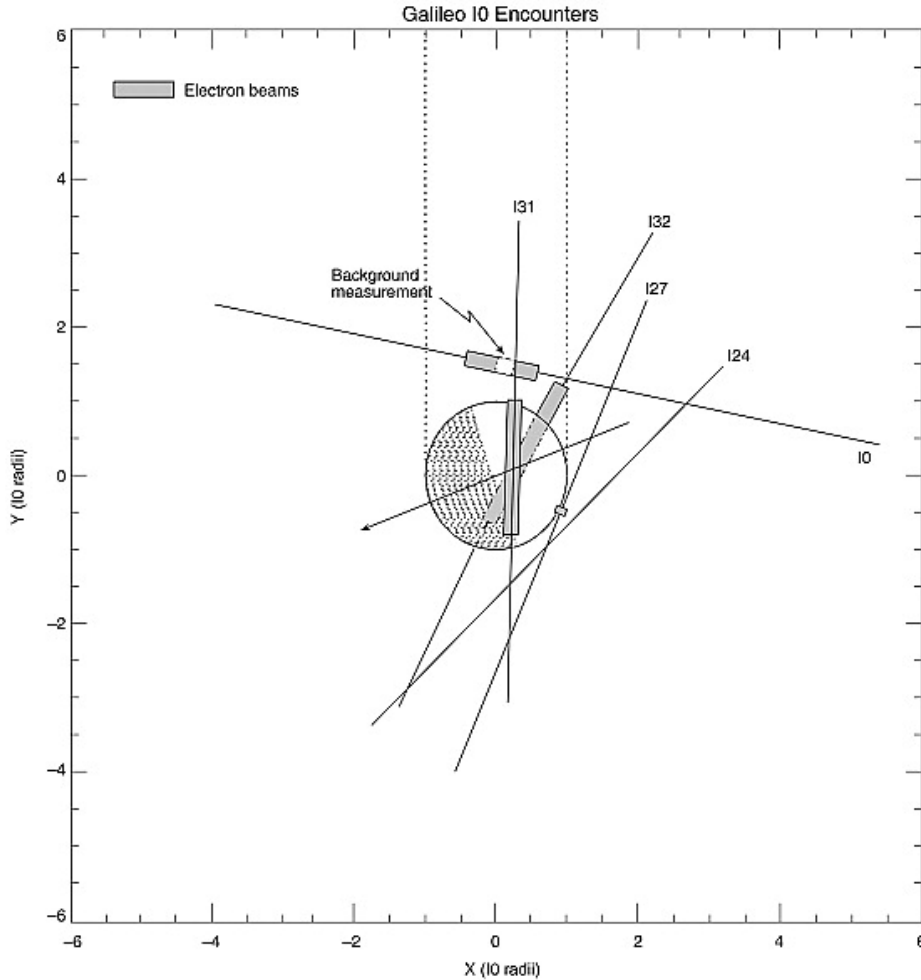


Figure 4.4: *Equatorial projection of Galileo flyby trajectories with field aligned energetic particle observations. Locations of detected beams are marked by rectangles along the trajectory [Williams and Thorne, 2003]. Note that other than in coordinate systems used so far, the y-direction is aligned with the corotational flow.*

distinct association of the beam with a predominant current direction towards or away from Jupiter, equatorial beams should be more likely to be detected on the anti-Jovian side. *Galileo* EPD observations are not consistent with this picture. For the *IO* flyby the radial profile of *Io*'s wake does not show any hint for an asymmetry between the Jovian and anti-Jovian part of the wake [Williams *et al.*, 1999]. Unfortunately the instrument performed a background scan just during the passage of the current reversing layer. In contrast, the *I31* trajectory is located almost entirely in the current reversing layer area of the *Io* current system and EPD data exhibits intense beams. Finally, *I32* does not feature a significant variation in the beam intensity as one would expect from the trajectory that covers the current reversing layer and the maximum downward current area. It is noteworthy that a strong filamentation of *Io*'s current system has been discussed [Chust *et al.*, 2005]. These highly structured currents would result in a more symmetric current-associated beam distribution over the poles. Still, the measured PSD spectra lack a peak representative for current system associated acceleration.

The criteria derived from *Galileo* EPD data favor an acceleration mechanism for the anti-planetward acceleration, which is reminiscent in its features of heating. The broad energy distribution as reported by *Williams and Thorne* [2003] is consistent with electron acceleration by inertial Alfvén waves [e.g *Swift*, 2007] and the upward acceleration mechanism appears to be distributed within both, the sub-Jovian and the anti-Jovian side of Io's Alfvén wings.

In our search for a suitable proxy parameter for the beam generation intensity, we find the Poynting flux density meets the geometrical implications elaborated in this section.

4.6.1 Poynting Flux as Surrogate for Electron Beam Intensity

Io's Alfvén wings communicate electromagnetic energy between Jupiter and Io. This energy balance is described by Poynting's theorem

$$\iint \mathbf{S} \, d\mathbf{A} = - \iiint \mathbf{j} \cdot \mathbf{E} \, dV \quad (4.43)$$

for an arbitrary Volume V with the surface normal $d\mathbf{A}$.

The Poynting flux density \mathbf{S} is given by

$$\mathbf{S} = \frac{1}{\mu_0} \mathbf{E} \times \mathbf{B} . \quad (4.44)$$

Using $\mathbf{E} + \mathbf{v} \times \mathbf{B} = 0$, we can write

$$\iint \mathbf{S} \, d\mathbf{A} = \iiint \mathbf{j} \cdot (\mathbf{v} \times \mathbf{B}) \, dV , \quad (4.45)$$

and finally

$$\iint \mathbf{S} \, d\mathbf{A} = \iiint -\mathbf{v} \cdot (\mathbf{j} \times \mathbf{B}) \, dV . \quad (4.46)$$

The energy needed for the electron acceleration is a fraction of the energy which is being communicated between Io and Jupiter. This energy becomes available by the work done by the $\mathbf{j} \times \mathbf{B}$ -force which slows down the corotating plasma in the Jovian ionosphere. Based on equation 4.46 we will use the Poynting flux density to calculate the energy flux communicated to the AAR.

Interestingly, the direction of the Poynting flux density depends on the rest frame under consideration. In the rotating system of Jupiter, we find $\mathbf{E} \cdot \mathbf{j} > 0$ in the Jovian ionosphere and $\mathbf{E} \cdot \mathbf{j} < 0$ at Io. This condition means that in this frame Jupiter represents a load whereas Io serves as a generator (see *Mauk et al.* [2002] for a detailed discussion). The Poynting flux density in the Alfvén wing is directed towards Jupiter. In Io's rest frame, this interrelation is reversed. Io represents the load ($\mathbf{E} \cdot \mathbf{j} > 0$) in this system and the Jovian ionosphere acts as the generator. The Poynting flux density is directed towards Io. For the physically reasonable

definition of the Poynting flux density it is also indispensable to account for the rest frame under consideration. While in the plasma rest frame \mathbf{S} is given by

$$\mathbf{S} = \frac{1}{\mu_0}(\mathbf{E} \times \mathbf{B}) = -\frac{1}{\mu_0}(\mathbf{v} \times \mathbf{B}) \times \mathbf{B}, \quad (4.47)$$

modified quantities have to be introduced in Io's rest frame which we apply in our simulations:

$$\mathbf{S}' = \frac{1}{\mu_0}(\mathbf{E}' \times \mathbf{B}') = -\frac{1}{\mu_0}(\mathbf{v}' \times \mathbf{B}') \times \mathbf{B}'. \quad (4.48)$$

While the magnetic field is identical in both frames ($\mathbf{B} = \mathbf{B}'$), the primed plasma bulk velocity is given by the expression

$$\mathbf{v}' = \mathbf{v} - \mathbf{v}_{0\perp} \quad (4.49)$$

The simplified geometry used for our simulations, where $\mathbf{v}_{0\perp} = \mathbf{v}_0$ then leads to

$$\mathbf{S} = -\frac{1}{\mu_0}((\mathbf{v} - \mathbf{v}_0) \times \mathbf{B}) \times \mathbf{B} \quad (4.50)$$

For an isolated view of the Io-Jupiter interaction with no other sources and sinks for energy than Io and the Jovian ionosphere, the energy $\Delta\varepsilon$ that is dissipated in a volume that contains the load is given by the Poynting flux through the surface \mathbf{A}_s perpendicular to the background magnetic field \mathbf{B}_0 between generator and load. For our simulation, where \mathbf{B}_0 is parallel to the z-axis, this is given by

$$\Delta\varepsilon = \iint \mathbf{S}'|_z d\mathbf{A}_s \quad (4.51)$$

where

$$\mathbf{S}'|_z = \frac{1}{\mu_0}(\mathbf{E}' \times \mathbf{B}')|_z = (\mathbf{v} - \mathbf{V}_0)_\perp|_z \frac{B^2}{\mu_0} \quad (4.52)$$

and $d\mathbf{A}_s \parallel \mathbf{B}_0$. Altogether, the Poynting flux describes the energy transport to the acceleration region and it matches the aforesaid morphological requirements derived from the EPD data. We therefore use the normalized Poynting flux density in the AAR as a proxy parameter for the intensity of generated energetic electron beam.

4.6.2 Equatorial Electron Beam Position

The Alfvén wave generated by Io follows the Alfvén characteristic towards Jupiter [Neubauer, 1980]. In Io's rest frame the propagation direction is tilted with respect to the background magnetic field by the Alfvén angle $\Theta_A = \arctan(M_A)$, with the Alfvénic Mach number M_A . The time required to reach the acceleration region in the northern (n) or southern (s) hemisphere is called one-way travel time $\tau_{n/s}$ (fig. 5.4). During this time the magnetic field line that carries the Alfvén wave is convected with the moving plasma. The longer the travel time, the further downstream it reaches the acceleration region. We call the three-dimensional region, where the particle acceleration takes place and which is fed by the Alfvén wave energy, the

volume of beam generation. Once a trans-hemispheric beam has formed in this volume, it follows the magnetic field line and passes the equatorial plane after the beam travel time t_b . Like the downstream shift of the beam generation volume, the downstream offset of the location where the beam penetrates the equatorial plane of Io grows due to field line convection with the combination of the one-way travel time and the beam travel time $\tau_{n/s} + t_b$.

Another element that has to be taken into account is the magnetic field direction. The locus of a field-aligned beam is given by the magnetic field topology it tends to follow. The magnetic field is perturbed and draped around Io due to the electromagnetic interaction. This draping is accompanied by a deceleration of the plasma. The convection time t_c , i.e. the time a plasma particle needs to cover the interaction distance of one Io diameter, becomes larger, the stronger the interaction. Thus the downstream offset is inversely proportional to the interaction strength. Accordingly, a simple relation for the downstream offset $\Delta x_{n/s}$ of electron beams from the north (n) and south (s) is

$$\Delta x_{n/s} = \int_0^{\tau_{n/s} + t_{b,n/s}} v_c dt \quad (4.53)$$

For the decelerated plasma at constant convection speed $v_c = 2R_{Io}/t_c$ this relation can be rewritten as a first order approximation as

$$\frac{\Delta x_{n/s}}{2R_{Io}} = \frac{\tau_{n/s} + t_{b,n/s}}{t_c} \quad (4.54)$$

The travel times $\tau_{n/s}$ are strongly coupled to Io's position in the torus which varies with system III longitude (cf. Figure 5.9). The convection time depends on the incoming plasma density. The denser the plasma, the stronger the interaction, i.e. the deceleration of the plasma and the longer the convection time. As the torus plasma density is a function of centrifugal latitude, the convection time is also coupled to Io's position in the torus, i.e. also to system III longitude. Hence, following equation 4.54, we expect the downstream offset of an electron beam at Io to vary with its orbital position. However, the local convection speed is not uniform but varies along a streamline in the vicinity of Io. Therefore it is necessary to model the plasma bulk velocity field and the magnetic field consistently to obtain reliable results. Furthermore the shape and morphology of the Io footprint in the Jovian aurora changes when Io moves within the torus [Bonfond *et al.*, 2008]. If the downward electron beams develop a complicated pattern it is likely that upward beams are also affected in this way. Jacobsen *et al.* [2007] have shown that nonlinear wave reflection processes significantly contribute to the variation of the footprint morphology. Therefore reflection processes at plasma density gradients have to be considered.

In order to take all the phenomena mentioned above into account, we apply a three-dimensional MHD model that calculates self-consistently the magnetic field and plasma velocity perturbations generated by the electromagnetic interaction of Io with the surrounding torus plasma. We allow for Alfvén wave reflections by incorporating equivalents of the different plasma regimes with individual densities.

We adjust the model parameters such that travel time constraints are met. How we build our model in detail is the subject of the next chapter.

Chapter 5

Numerical Implementation

5.1 The Solver: ZEUS-MP

The core of our numerical solver is based on ZEUS-MP, which is a massively parallel expansion of the non-commercial ZEUS code. Although based on former versions like ZEUS-2D and the three-dimensional ZEUS-3D, it differs significantly from the previous releases. This is not only due to the additional message passing implementation, but also owing to a new *Method of Characteristics* scheme coupled with a constrained transport algorithm. This routine is the main MHD algorithm inside the code and is called MOCCT. All versions of ZEUS are time dependent finite difference codes which solve, in the original version, the equations of ideal, non-resistive, non-relativistic magnetohydrodynamics. The number of operating dimensions varies with the version. While the numerical methods used in ZEUS-2D are thoroughly documented [Stone and Norman, 1992a; Stone et al., 1992; Stone and Norman, 1992b], ZEUS-3D is completely undocumented in peer-reviewed literature. The documentation for ZEUS-MP is sparse. Hayes et al. [2006] explain the rudimentary numerical scheme and message passing procedures. Nonetheless, open access to the source code makes it possible to adapt the original program to ones needs. Although this procedure is sometimes remarkably cumbersome, the benefits of convertibility of the program prevail.

During our research, we modified several routines of the code. Core routines like time step calculation and the grid generator were revised, extended and bugs were fixed. Moreover, we added new routines to the code demanded by the incorporation of resistivity. Due to scarceness of documentation, we will outline the modifications made in appendix 8.2, hopefully in favour of future users.

Finally our modified code solves equations (4.26) to (4.29). Resistivity and effective collision frequencies are domain based and thus features which can be activated either in the whole simulation volume or only in certain sub-domains. They can also be turned off entirely. We use different simulation setups optimized to address certain aspects of our studies balanced with the effective use of available computational resources. We introduce the different simulation configurations in the subsequent sections.

5.2 Simulation Geometry and Setups

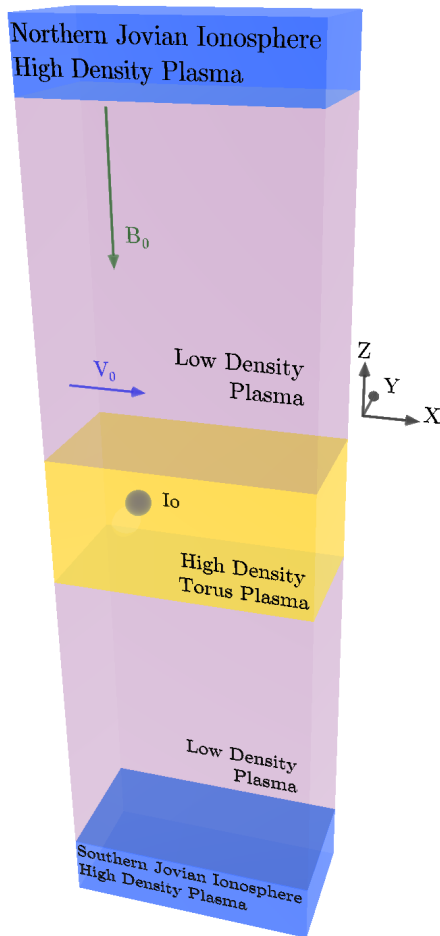


Figure 5.1: 3D sketch of the simulation box and the plasma regimes

We carry out all of our simulations in a rectangular box with a Cartesian staggered grid. The magnetic field direction in the initial state is directed anti-parallel to the z -direction and the field strength is homogeneous throughout the grid. The plasma is streaming along the x -axis and the velocity is isotropic in the initial state. The y -axis completes the right handed system. This setup represents the Io interaction for straight, rectified field lines where Jupiter's poles are located at the top and bottom of the simulation box. The satellite is placed in the origin of the coordinate system and we apply a field aligned plasma density profile in z -direction (an example is displayed in Figure 5.3). We use a dense plasma in the middle and at the top and bottom of our simulation box. These regimes represent the plasma torus and the northern and southern Jovian ionosphere respectively. There is no density variation in the x - and y -direction in the initial state. The plasma torus implementation is bordered by a dilute plasma representing the low density regime at high magnetic latitudes.

Io, serving as the obstacle, is implemented via the effective collision frequency ν (see section 4.1). This parameter is set in spherical volume representing Io and its atmosphere. It is zero in the rest of the simulation volume. We can modulate the nature of the interaction (i.e. weak or strong) by

adjusting ν or the density ρ of the incoming plasma (see section 4.4.1). The box dimensions and the exact characteristics of the density profile depend on the aim of the particular simulation carried out. We apply a basic setup to investigate the general topology of the reflection pattern and fundamental differences between weak and strong interaction. We introduce the features of this configuration in section 5.2.1.

The simulation of the energetic electron beams during the *Galileo* flybys demand a setup that is significantly more complicated, as it needs to quantitatively meet the initial conditions of the specific flyby. Unfortunately, numerical limitations and restrictions of model applicability complicate the formulation of the initial conditions in this case. We therefore dedicate section 5.2.2 to the treatment of this issue.

5.2.1 Basic Setup

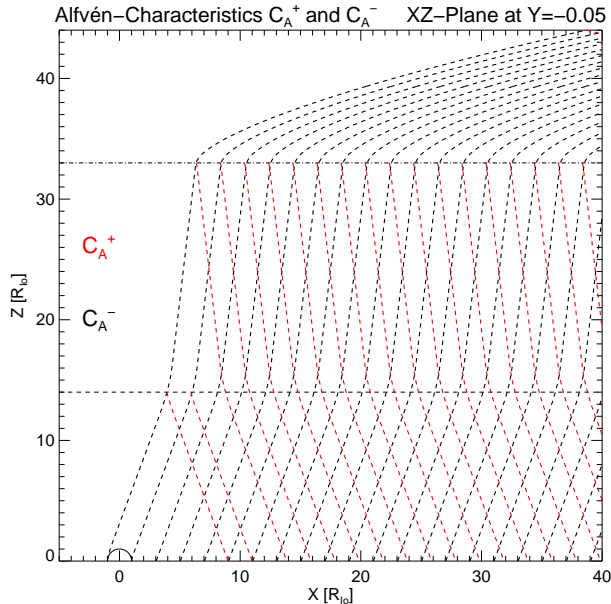


Figure 5.2: *Initial Alfvén characteristics of the undisturbed magnetoplasma in the northern hemisphere. Northward propagating waves follow C_A^- (in black), southward propagating waves follow C_A^+ (in red). Different plasma regimes separated by horizontal lines from top to bottom: Jovian ionosphere, depleted high latitude plasma, Io plasma torus*

We apply a basic setup for the investigation of the reflection geometry and the resulting MHD wave pattern morphology. As Io wobbles up and down in the plasma torus, the ambient plasma density varies notably. This modulates the strength of the interaction. As we mentioned in section 4.4.1, our model allows to modify the initial perturbation also via adjustment of the effective collision frequency ν . The benefit of tweaking ν while maintaining ρ is that the initial Alfvén characteristics remain the same for all simulation runs. All modifications of the original Alfvén characteristics are due to the interaction and depend on the perturbation amplitude. Thus, we apply the identical plasma density profile for all runs with a basic setup. It is characterized as follows:

We use constant density values for the torus, high latitude and ionospheric plasmas, each. The plasma density is ρ_0 inside our representation of the plasma torus and decreases to $\rho_0/10$ at the edge of the torus. The latter is the density value for the rare plasma outside the torus. We apply linear transitions between the plasma regimes. The density gradient spans $2 R_{Io}$. On the one hand this provides numerical stability due to limited steepness, on the other hand, the layer is thin enough to be regarded as a discontinuity. This allows a good determination of the point of reflection when following the wave paths. The Jovian ionosphere is represented by an increase in the plasma density up to $200 \rho_0$. The gradient extends over $12 R_{Io}$. The effect of this implementation is twofold. First, the wave is partly reflected while conserving the sign of the magnetic field perturbation (see section 4.5.1) as expected. Secondly, due to the large Alfvén angle (see Figure 5.2), we avoid that inevitable reflections from the simulation box boundaries reach the main area of interest between the torus and Jupiter’s ionosphere. This is important, as for the boundary conditions applied, the reflections from the grid edges have the opposite change of sign behavior and act like a negative plasma density gradient rather than a density increase as prevalent in the ionosphere. Figure 5.2 illustrates the initial undisturbed Alfvén characteristics of the simulation schemes. We would like to point out that no Alfvén wave reflection from the simulation box boundary can

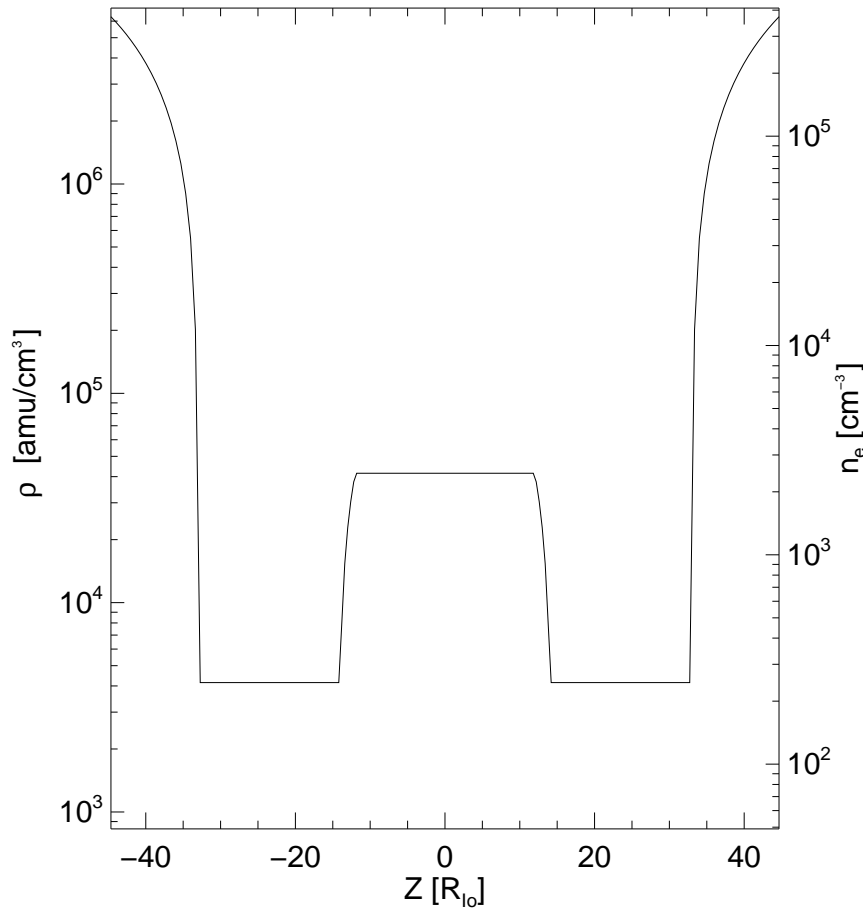


Figure 5.3: Plasma mass density and electron number density profile along z -axis as applied in basic setup simulations.

reach the inner simulation region between $\pm 33R_{Io}$.

Under aforementioned circumstances, the propagation angles are constant within the individual plasma regimes between density gradients in the initial state. Admittedly, this represents a simplification of the actual conditions. However, we have consciously chosen this setup for the benefit of easily identifying the single waves, different wave modes and reflections of higher orders.

Nonetheless, realistic reflection amplitudes as expected at smooth gradients are not incorporated in this setting. Although the wave amplitudes have certainly impact on the resulting MHD wave pattern when wave interference occurs, the location and path of the reflection is more in the focus of this work, rather than reflection intensity. In this regard, the basic setup is well suitable for the intended application.

5.2.2 Electron Beam Setup

One major objective in the investigation of equatorial electron beams in Io's wake is the analysis of the interdependence of the beam location on the interaction strength

changing with Io's position in the torus. As the beam follows the distorted magnetic field topology, we require a correct modeling of this distortion. Being a result of multiple superimposing and interfering Alfvén wave reflections a realistic field perturbation depends on a realistic formulation of the reflections. An authentic model would include both correctly, the locus of the reflection and the reflection amplitude.

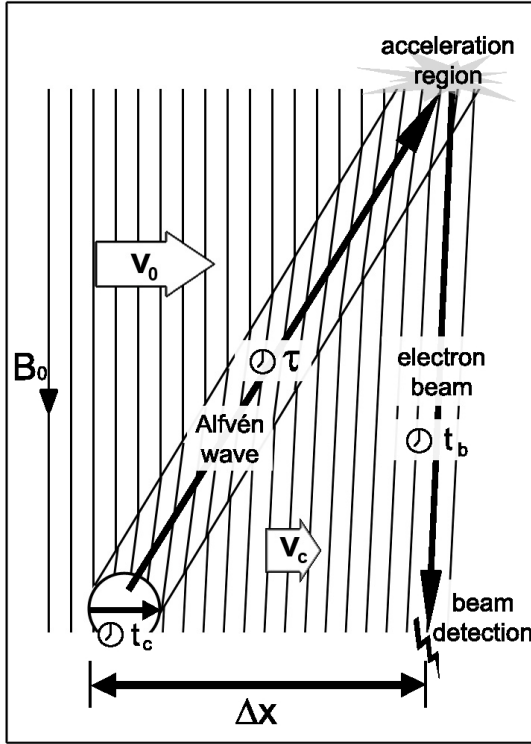


Figure 5.4: Sketch of the location of equatorial electron beams

For a genuine reflection amplitude a correct gradient in the Alfvén phase velocity profile along the field line is necessary as discussed in section 4.5. For the downstream location of equatorial beams, the Alfvénic travel time to the area of the beam generation and the convection speed of the plasma near and downstream of Io are additional crucial parameters. As illustrated in the Figure 5.4, the field line that carries the electron beam is convected past the obstacle for the Alfvénic travel time τ plus the beam travel time t_b . The greater the travel time, the larger thus is the displacement of the beam with respect to the initial Alfvén generator. For the observed electron energies (section 2.6.3) we can assume $t_b \ll \tau$ for the beam travel time and hence we neglect t_b in our considerations [Jacobsen et al., 2010]. The downstream offset of the beam Δx is given by the relation:

$$\Delta x = V_c \tau . \quad (5.1)$$

The convection speed V_c that we obtain from our simulations is controlled by the effective collision frequency and the incoming plasma density by the collision term in the momentum equation (4.17). The Alfvénic travel time to the acceleration can be calculated via integration of the Alfvén velocity profile along the field line

$$\tau_A = \int_0^{S_{AAR}} \frac{ds}{V_A(s)} , \quad (5.2)$$

where s is the distance along the field line and S_{AAR} is the field aligned distance to the acceleration region. Obviously, the Alfvén velocity profile is again needed for the determination of a crucial parameter in our simulation. As the local Alfvén speed is given by

$$V_A(s) = \frac{B(s)}{\sqrt{\mu_0 \rho(s)}} , \quad (5.3)$$

we need both, a model for the mass density $\rho(s)$ and a magnetic field model to

determine $\mathbf{B}(s)$. In the following sections we will introduce the models underlying the Alfvén velocity profiles used.

However, to fulfill the solenoidal constraint $\nabla \cdot \mathbf{B} = 0$ in the Cartesian simulation geometry applied in our model, we need to have a constant background magnetic field \mathbf{B}_0 . We intend to implement a Alfvén velocity profile $V'_A(s)$ in ZEUS which is as realistic as possible, ideally $V'_A(s) = V_A(s)$. Therefore, we introduce a forged density profile $\rho'(s)$ which fulfills:

$$V_A(s) = \frac{B(s)}{\sqrt{\mu_0 \rho(s)}} = \frac{B_0}{\sqrt{\mu_0 \rho'(s)}} = V'_A(s) \quad \text{or} \quad (5.4)$$

$$\rho'(s) = \frac{B_0^2}{\mu_0 V_A^2(s)}. \quad (5.5)$$

It is noteworthy, that this manipulation allows conservation of the most important parameters for our aim: the realistic Alfvén velocity profile and the accurate travel times.

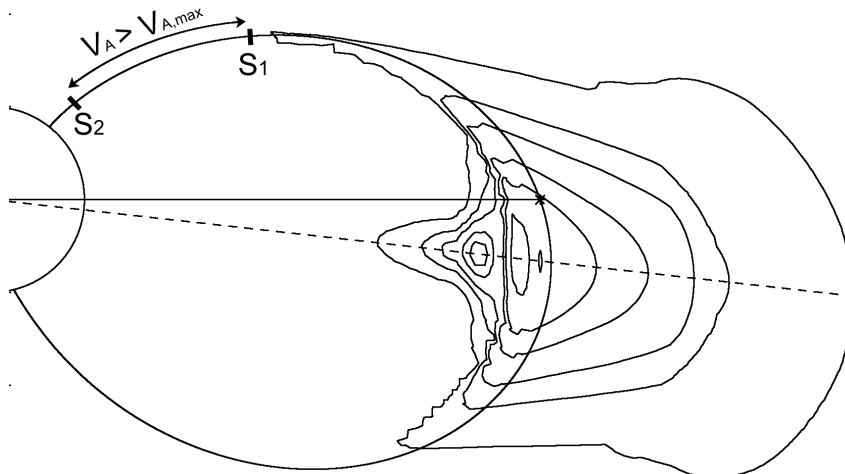


Figure 5.5: Sketch of travel time coordinates

Still, one model limitation has not been considered, yet. The genuine Alfvén velocity approaches the speed of light where the magnetic field strength rapidly increases, while the plasma becomes tenuous¹. In order to avoid relativistic effects and to stay within reasonable limits of simulation duration, we need to artificially keep the Alfvén speed below a threshold of $V_{A,\max} \geq V_A(s)$. For a constant magnetic field, this implies a minimum density $\rho_{\min} \leq \rho'(s)$. Thus we obtain an artificial Alfvén velocity profile $V'_A(s)$ where

$$V'_A = \begin{cases} V_A & \text{for } V_A < V_{A,\max} \\ V_{A,\max} & \text{for } V_A \geq V_{A,\max} \end{cases} \quad (5.6)$$

While apparently the Alfvén velocity profile $V'_A(s)$ becomes unrealistic in regions with relativistic V_A , we still can conserve the accuracy of the travel times by adjust-

¹Technically, without the Boris correction the equations even allow that the Alfvén speed exceeds the speed of light

ing the extent of the region where $V'_A(s) = V_{A,\max} \leq V_A(s)$:

$$\tau = \int_{s_1}^{s_2} \frac{ds}{V_A(s)} = \int_{s'_1}^{s'_2} \frac{ds}{V'_A(s)} = \tau' . \quad (5.7)$$

We denote by $s_1 = s'_1$ the point where $V_A(s)$ exceeds $V_{A,\max}$. Using $V'_A(s) = V_{A,\max} = \text{const}$ between s_1 and s'_2 , we can easily derive

$$s'_2 = \tau \cdot V_{A,\max} + s_1 . \quad (5.8)$$

Hereby we introduce primed coordinates which preserve the accurate travel time along the magnetic field direction and preserve the Alfvén velocity profile in the domain where $V_A \geq V_{A,\max}$. We therefore maintain the most important parameters for the aim of this study in a major part of the simulation volume, even though the model setup and geometry is idealized. In the following subsections we introduce the constituent models we use to derive the travel time preserving coordinates.

5.2.3 The Density Model

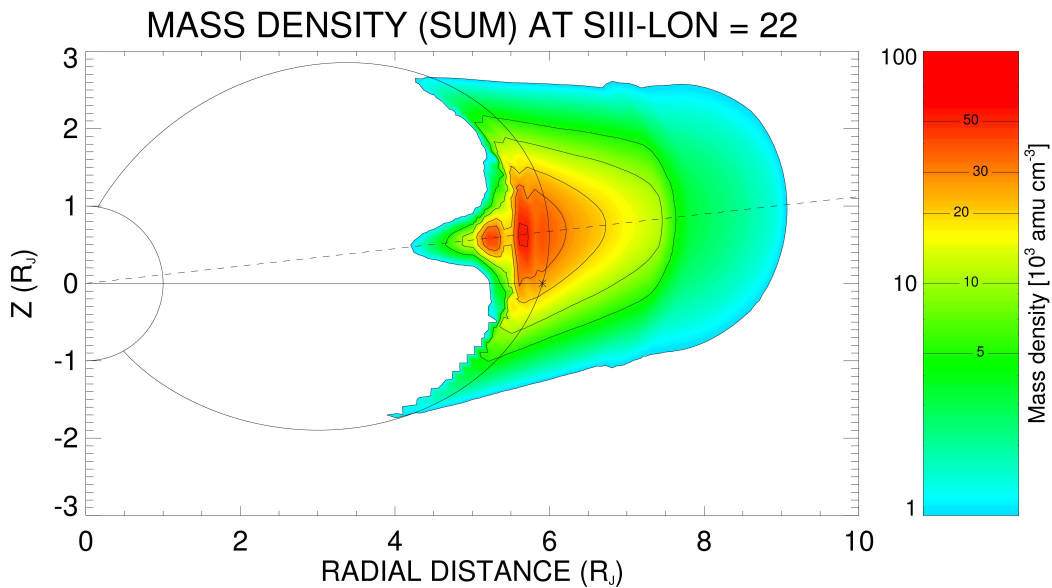


Figure 5.6: Mass density map at $\lambda_{III} = 22^\circ$ based on Bagenal [1994]. Io's position is marked with a star symbol. The dashed line represents the centrifugal equator.

On the basis of PLS and UVS measurements of the Voyager probes Bagenal and Sullivan [1981] developed an empirical plasma density model. The authors assume that the plasma diffuses along the field line under gravitational, centrifugal, pressure gradient and ambipolar electrostatic forces. This diffusive equilibrium model yields 2D density maps in a meridional plane for each major ion species and the electron density. However, there was an error by a factor of two in their calculations. Thus, an improved version of the model was published by Bagenal [1994], including additional plasma composition measurements. The author derives a scale

height approximation to the density distribution, given by

$$n_i(r, z) \approx n_0(r)e^{-z^2/H_i^2(r)} \quad , \text{ where} \quad (5.9)$$

$$(5.10)$$

$$H_i(r) = \sqrt{\frac{2k_B(T_{i\parallel}(r) + Z_i T_{e\parallel}(r))}{3M_i\Omega^2}} = 0.64\sqrt{\frac{T_i(r)(1 + Z_i C(r))}{A_i}} R_J . \quad (5.11)$$

Here Ω is the angular velocity of Jupiter, n_0 and $n_i(r, z)$ are the ion number densities at the centrifugal equator and at a height z above the centrifugal equator, respectively. Both number densities are defined on the same magnetic field line, that penetrates the centrifugal equatorial plane at distance r . T_i and T_e are the temperatures of ions and electrons and $C = T_e/T_i$. M_i is the effective ion mass, and Z_i and A_i represent the charge and mass number, respectively.

Based on the satellite observations the author infers radial profiles for electrons $n_{e,0}(r)$ and the most abundant ion species $n_{i,0}(r)$. Summation of the ion species yields the local mass density

$$\rho(r, z) = \sum_i n_i(r, z) A_i . \quad (5.12)$$

However, the density distribution along the field line in this model depends mainly on T_{\parallel} . Unfortunately, the ambient plasma has been shown to be thermally anisotropic. Due to the lack of observations of T_{\parallel} , the author assumes a ratio of $T_{\perp}/T_{\parallel} = 1/5$ and deduces T_{\parallel} from T_{\perp} measurements.

While *Bagenal* [1994] presents a showcase of the meridional plane for the equatorially symmetric case at $\lambda_{III} = 292^\circ$, where the magnetic and centrifugal equator coincide, we apply the model to the full circle in longitude as we need to consider longitudinal variations of $z(s)$ (the height above the centrifugal equator at a given distance s along the field line). An example for our calculation for $\lambda_{III} = 22^\circ$ is shown in Figure 5.6. It is noteworthy that *Bagenal* [1994] points out that extrapolation of the density distribution along the field to radial distances $< 5R_J$ might not yield reliable results and is highly sensitive to the magnetic field model used. Notwithstanding, in absence of other models in that range, we will use their model including extrapolation beyond $5R_J$. We shall see that most of the travel time is spent in the torus and outside $5R_J$. Thus the effect on the total travel time is small compared to other model uncertainties such as temporal and local time variability of the torus density (see section 2.4).

5.2.4 The Magnetic Field Model

The magnetic field model that underlies our simulations is the *VIP4* model published by *Connerney et al.* [1998]. As discussed before, the ambient magnetic field at Io's orbit is highly variable with System III longitude (see top panel in Figure 5.7). Variations in the local background magnetic field strength influence the Alfvén speed (2.3) and Alfvén Mach number (2.4) and hence need to be considered in the background parameters used in our model. As we are obliged to use a constant magnetic field value throughout our simulation box, we derive the local magnetic field strength at Io's position from the *VIP4* model and set this value as homogeneous background magnetic field in the initial and boundary conditions. Within

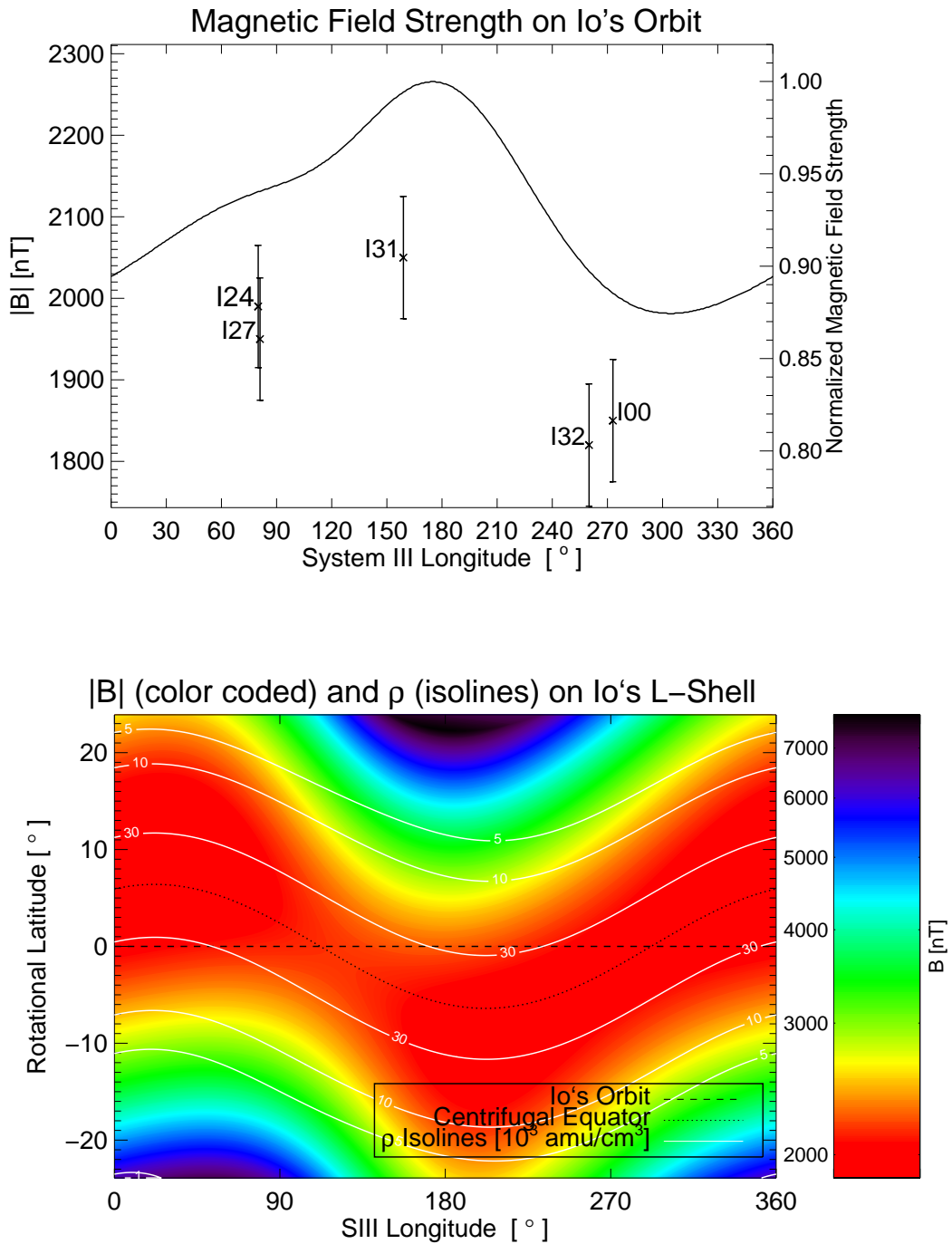


Figure 5.7: Top panel: VIP4 Magnetic field strength variations at Io's orbit (absolute and relative variation). Crosses represent values extracted from Galileo magnetometer data. Bottom panel: 2D magnetic field in color code on Io's L-shell. Over-plotted in white lines: Mass density isocontours in 10^3 amu/cm^3 . Dashed line: rotational equator/Io's orbit (see profile of top panel), dotted line: centrifugal equator (torus center).

the limits of our idealized model formulation we thus achieve a comparatively re-

alistic implementation of the initial perturbation in the generator region. However, *Galileo* observations during the Io flybys deviate considerably from the VIP4 model results (see crosses in top panel of fig. 5.7)². The magnetic field model seems to systematically overestimate the observations by roughly 10 percent. Using another magnetic field model does not improve this inconsistency. This is another hint that the magnetic field models are imperfect at least near Io and would most probably benefit substantially from including additional close range data e.g. provided by the *Galileo* and *Ulysses* missions. However, in absence of more accurate models, we stick to the VIP4 model. The color contours in the bottom panel of figure 5.7 illustrate the magnetic field on Io's L-shell. However, the term L-shell is a bit misleading, as Io's L-value varies on its orbit due to the dipole offset. Thus, precisely there is no 'single' L-shell and we might term it differently.

5.2.5 The Alfvén Velocity and Travel Times Model

We derive the Alfvén velocity profile along a magnetic field line by combining the magnetic field model and the density model. The result is illustrated in figure 5.8. The bottom panel clearly shows a variation of the local Alfvén speed on Io's orbit of more than 25 percent. Hence the Mach number of the incoming plasma is also subject to substantial variation. We display the calculated travel times for each hemisphere in figure 5.9. When Io is located most northern seen from the torus center at $\lambda_{III} \sim 202^\circ$, the northern travel time is minimal (~ 250 s), whereas the southern travel time peaks at ~ 700 s. The dotted line depicts the travel time needed outside a distance of $5 R_J$, i.e. the time the wave spends in the region where the density model we use is valid according to *Bagenal* [1994]. Beyond this point we tend to overestimate the travel time. However, the fraction of the latter, uncertain contribution of the total travel time is only minor and with other uncertainties of the density model in mind, such as temporal and local time variations, the effect is not substantially altering the gist of the interaction. In absence of other models valid for $R < 5 R_J$, we apply the model to the whole domain under consideration, nonetheless. It should be noted that our travel time calculations slightly differ from those published in *Bagenal* [1983]. The difference arises probably from the magnetic field model used. However, figure 5 in *Bagenal* [1983] which illustrates the magnetic field strength on Io's orbit differs substantially from our results shown in figure 5.7. For a simple tilted dipole model (tilt towards 202°), and following the dipole relation

$$|\mathbf{B}(r, \theta_M)| = \frac{\mu_0 M}{4\pi R^3} \sqrt{1 + 3 \sin^2 \theta_M} \quad (5.13)$$

the magnetic field strength should be maximum, where the magnetic latitude θ_M peaks at $\lambda_{III} = 22^\circ$ and 202° . The corresponding graphic 5 in *Bagenal* [1983] is in anti-phase with these expected results. We therefore recalculate the travel times using the VIP4 model. With the use of the relative angular velocity of Io, the travel time can be converted to the predicted lead angle (right axis in Figure 5.9).

Figure 5.10 shows a comparison for the northern hemisphere between the actual Alfvén velocity profile and our profile with forged density, that conserves the Alfvénic travel time labeled "ZEUS model" in the graphic. The top panel displays the travel

²As immediate vicinity of Io is strongly disturbed we do not use values at closest approach, but interpolate linearly the field between $\pm 5 R_{Io}$ to closest approach and estimate errors

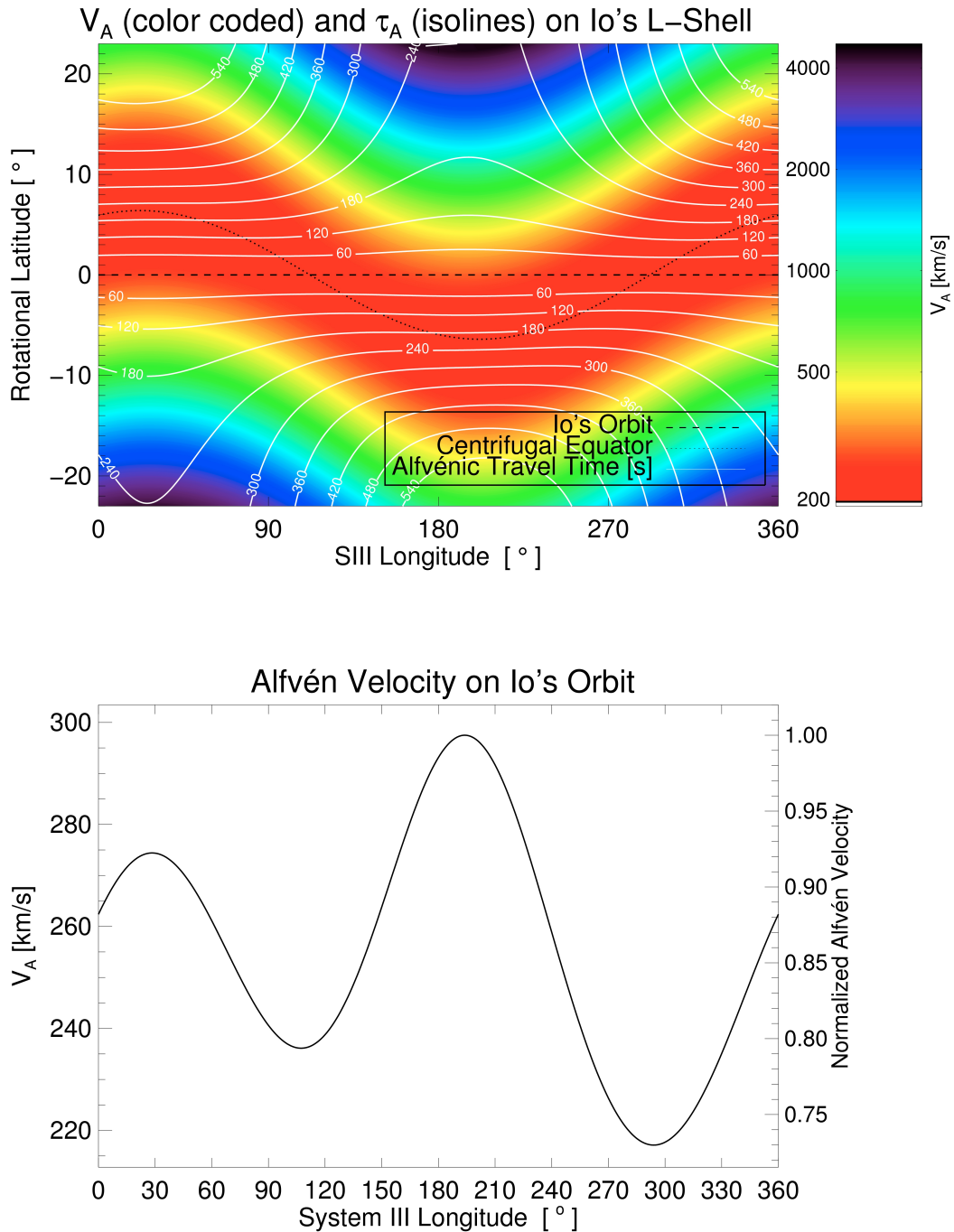


Figure 5.8: Properties on Io's magnetic shell inferred from combined VIP4 magnetic field model and Bagenal [1994] plasma density model. Top panel: Alfvén velocity (color code) and travel times (isocontours). Dashed line depicts Io's orbit and dotted line represents the centrifugal equator. Bottom: Alfvén velocity on Io's orbit in km/s and relative to maximum.

time against the distance along the field line. The middle panel displays the Alfvén velocity and the bottom panel shows a comparison of the density profiles. We note that over the major part of the travel time, the Alfvén velocities are identical for

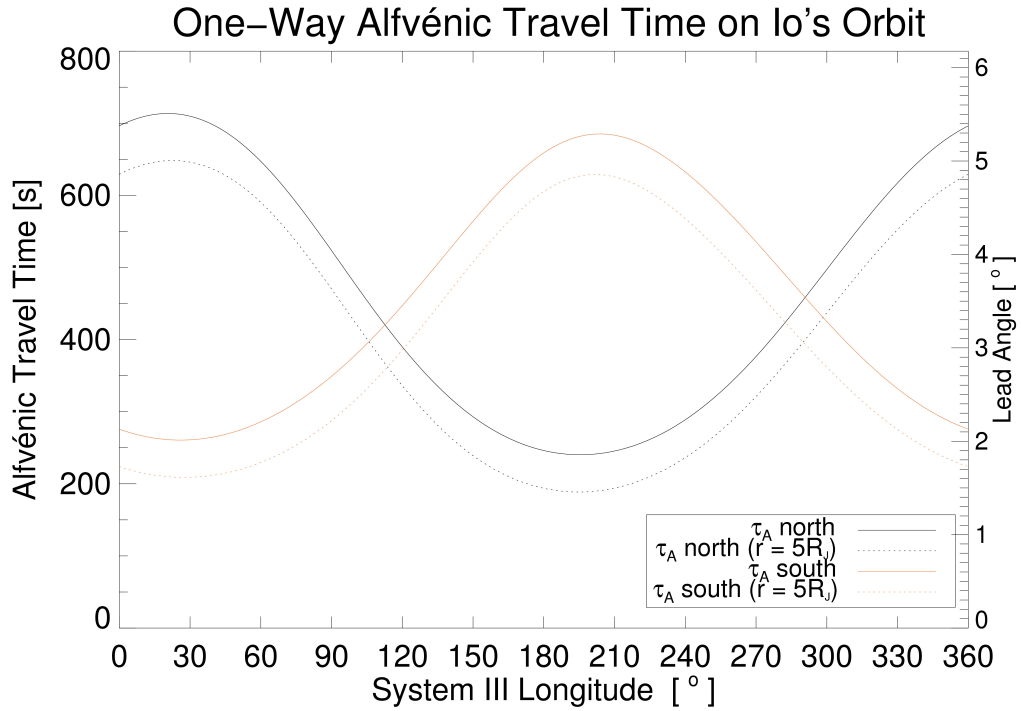


Figure 5.9: Travel times for a given longitude for northward and southward propagating Alfvén waves. Dotted lines display travel time spent outside $5R_J$.

both cases. In the top Panel the point is marked, where our profile and the genuine profile separate. It is located at $s=130 R_{Io}$ compared to a total extent of $170 R_{Io}$ of the northern hemisphere in our simulation setup. We note that also spatially, in the major part of the simulation box, the velocity profile we apply is identical to the original.

While we preserve the actual travel times to the reflection boundaries by using our model, we are less accurate in the reproduction of the downstream offset of the point of reflection. This is due to the use of a constant background plasma velocity in our model as opposed to the variation of the corotation velocity with the distance from the rotation axis. Along the field line the corotation velocity is given by

$$v_c(s) = \frac{2\pi r(s)}{T}. \quad (5.14)$$

Consequently the local propagation angle θ_A of the Alfvén wave along the field line is given by

$$\theta_A(s) = \arctan M_A(s) = \arctan \left(\frac{v_c(s)}{V_A(s)} \right). \quad (5.15)$$

In our implementation we apply $v_c(s) = V_0 = \text{const.}$ In the area we can calculate the error by examining the ratio

$$\frac{M_{A,\text{zeus}}(s)}{M_A(s)} = \frac{v_{c,0}}{V_{A,\text{zeus}}(s)} \frac{V_A(s)}{v_c(s)} \approx \frac{V_0}{v_c(s)} \quad (5.16)$$

Accordingly, we systematically overestimate the Alfvén Mach number in our simulation. The effect is displayed in Figure 5.11. The top panel shows the difference in

the Mach number between the original model (dash-dotted) and our model (solid). As the Mach number also determines the Alfvén angle, we can also compute the difference in this parameter. We show the discrepancy in the middle panel of Fig-

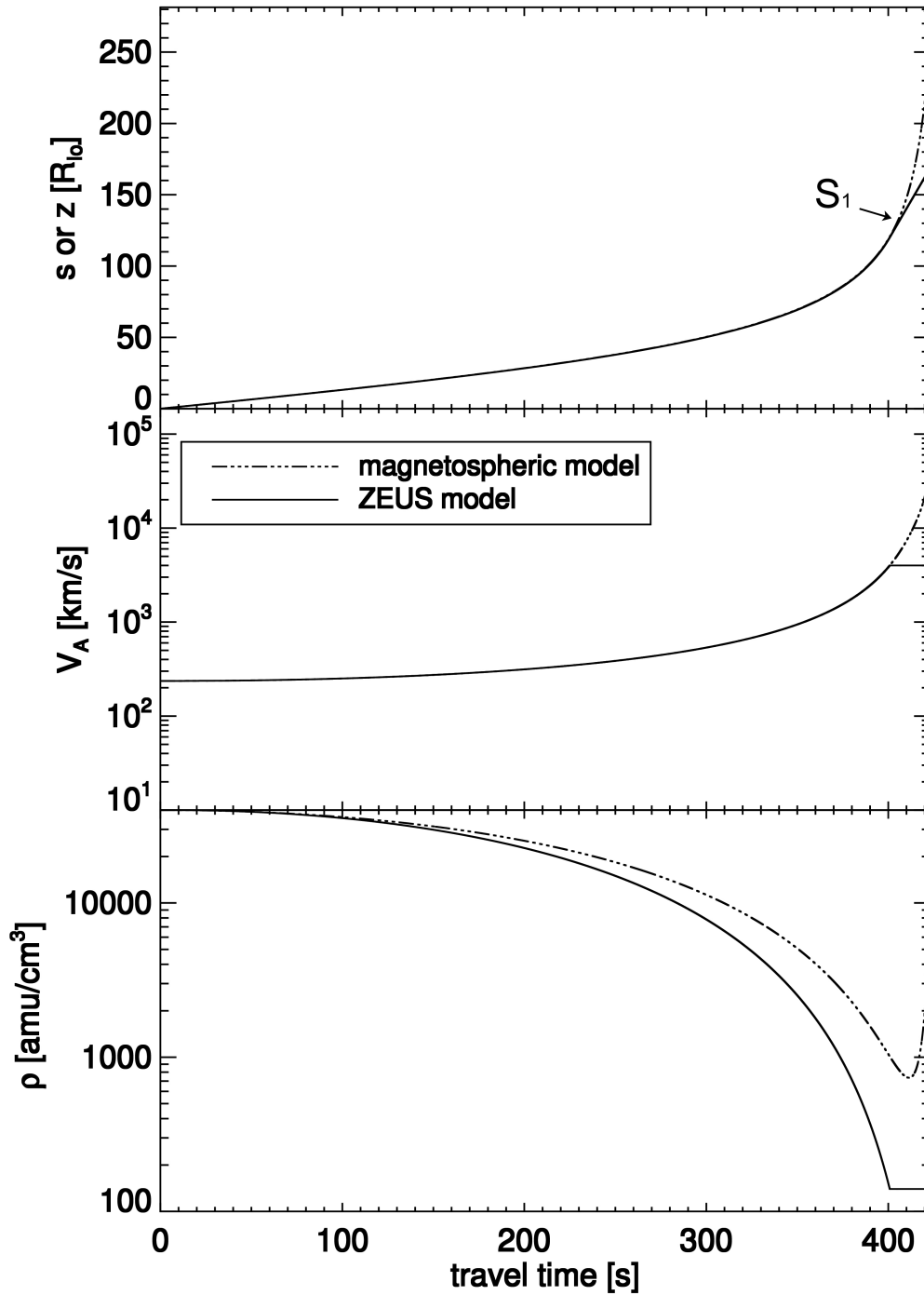


Figure 5.10: Comparison of the genuine (dash-dotted lines) and the forged Alfvén velocity profile (solid lines). Top panel: travel time against field-aligned distance. Middle panel: Alfvén velocity profile. Bottom panel: travel time against density.

ure 5.11. Superficially, the difference appears small. However, it takes effect during the whole travel time. We integrate the error along the propagation path and obtain the result illustrated in the bottom panel of Figure 5.11. We compare the difference and find, that we overestimate the lead angle by less than 0.5° . This value is small compared to uncertainties in the magnetic field model.

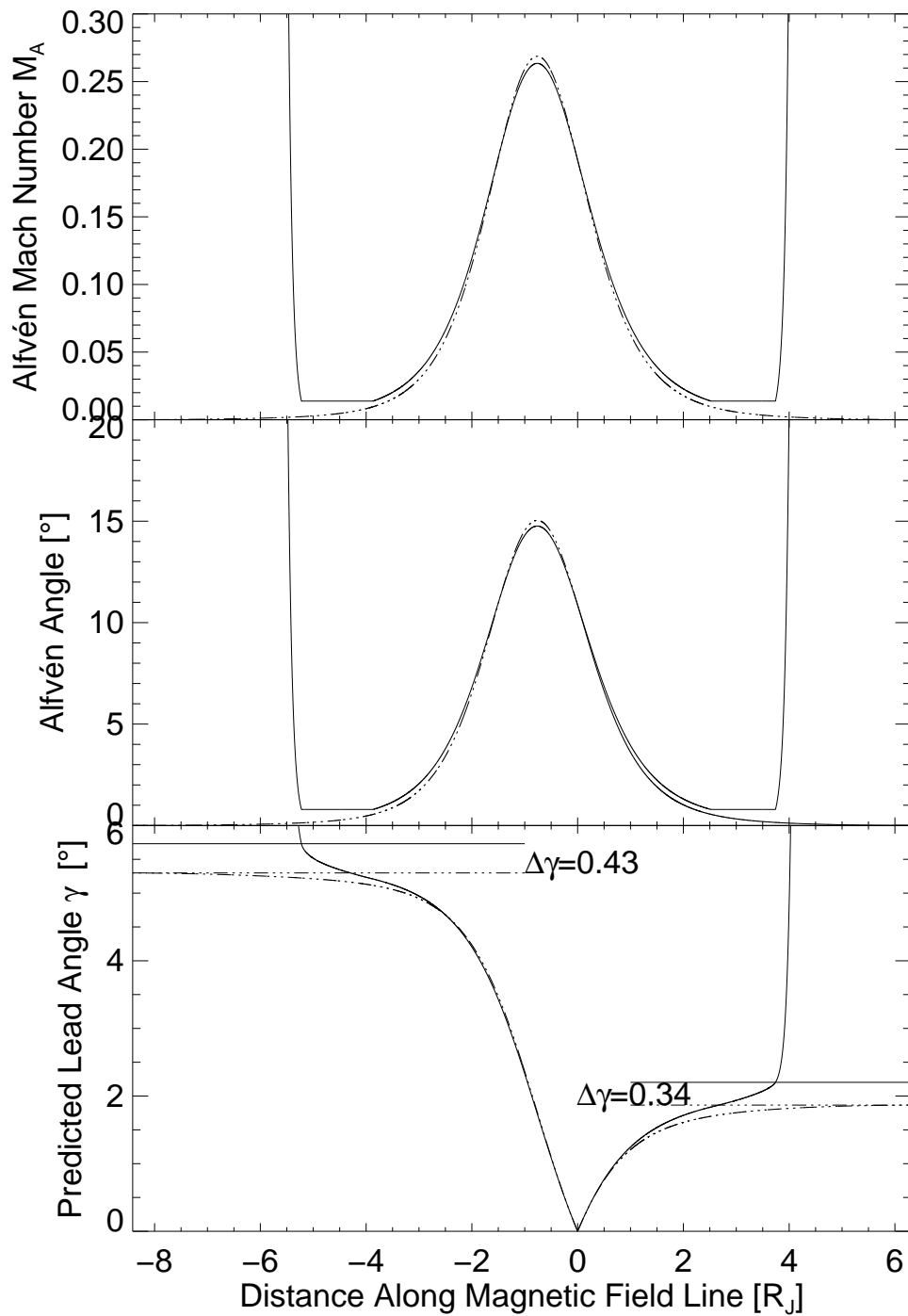


Figure 5.11: Comparison of Alfvén Mach number (top panel), Alfvén angle (middle panel) and lead angle (bottom panel) for the original (dash-dotted line) and our adapted Alfvén velocity profile (solid line) for $\lambda_{III} = 202^\circ$. Bottom panel labels indicate lead angle difference between the two profiles for the northern (right) and the southern (left) hemisphere

Part III

Results

Chapter 6

Io

6.1 Alfvén Wave Generation

In this section we present validation runs of our model. For this purpose we use a constant density value throughout the entire simulation box. From the beginning of the simulation, the effective collision frequency incorporated in (4.27) slows down the plasma in the sphere representing Io. The local perturbation in the velocity and magnetic field propagates along the primary Alfvén characteristics, i.e. along C_A^- for the northward traveling wave and along C_A^+ for the southward traveling wave. In order to facilitate comparison for different collision frequencies, the background parameters are identical for all simulation runs presented in this section. Thus the primary Alfvén characteristics that are indicative for the propagation direction of the waves are also identical. (Note that the complementary characteristic is not; see section 4.2). We scale the intensity of the plasma deceleration and hence the strength of the interaction by adjusting the effective collision frequency. In this paragraph we compare the basic differences between two generic simulation runs, one representing a weak and one representing a strong interaction scenario.

Figure 6.1 illustrates the velocity field near Io's equatorial plane at $z=-0.05 R_{Io}$. In the top panel which corresponds to the weak interaction scenario, the plasma in the central region where collisions occur is decelerated by $\sim 10\%$ of the background value V_0 . At the flanks where $|y| > 1 R_{Io}$ the plasma is accelerated but only slightly diverted around the obstacle. The bottom panel represents the strong interaction setup. The plasma is decelerated by $\sim 80\%$ of V_0 . In this case the plasma flow is strongly deflected at the flanks and very slow inside the collisional volume representing the satellite.

Figure 6.2 shows the magnetic field in the xz -plane plane at $y=-0.05 R_{Io}$. At some distance from the primary interaction region, the strength of the magnetic field is barely unchanged while the magnetic field is strongly draped around the obstacle. Inside the wing, the magnetic field direction approaches the direction of the Alfvén characteristics (dashed lines over-plotted in green). This agrees with the findings by *Neubauer* [1980]. In this region his analytical solution is valid for a homogeneous plasma density and pressure. According to this solution, two independent current

systems exist. One parallel to the primary Alfvén characteristic and one in the perpendicular plane. Both were extracted from our simulation data and are illustrated in figure 6.3. The weak interaction depicted in the top panel and the strong interaction in the bottom panel appear qualitatively similar. However it is notable, that the inner part of the Alfvén wing is almost free of currents for the strong interaction setup.

In figure 6.4 both basic plasma properties, the magnetic field and the bulk velocity, are combined. The major differences between the two cases studied here are most obvious in this plot. For a weak interaction, the direction of the magnetic field is barely changed and plasma velocity perturbations are small compared to the background value. This scenario is reminiscent of the pure Alfvén wing model presented by *Drell et al.* [1965]. The red wing is the signature of the slow mode wave, a slight modification of the Alfvén characteristics by the slow mode disturbance can be observed. The strong interaction setup in contrast exhibits substantial draping of the magnetic field lines. In fact they are almost aligned with the direction of the C_A^- -characteristic. Additionally, the plasma velocity field is strongly perturbed and substantially decelerated to almost halt inside the wing. Both attributes are indicative for the current loop model [*Goldreich and Lynden-Bell, 1969*]. The slow mode wave is not visible due to color-coding. The amplitude of the Alfvénic perturbation is much larger, so that the color-code chosen can not resolve the slow wing.

Thus, via the implementation of effective collisions, we have successfully modelled the two extreme scenarios that are being discussed for Io. Although it is simplified in the formulation of the wave generator region, we have demonstrated in this paragraph that our model reproduces a far field perturbation in agreement with theoretical expectations. We now use our numerical approach to study regions of the far field interaction, where the analytical solutions are no longer valid. Changes in the ambient medium along the travel path of the MHD waves and wave-wave interactions are unresolvable with present analytical approaches. With the numerical model at hand we can investigate Io's MHD wave field nonetheless.

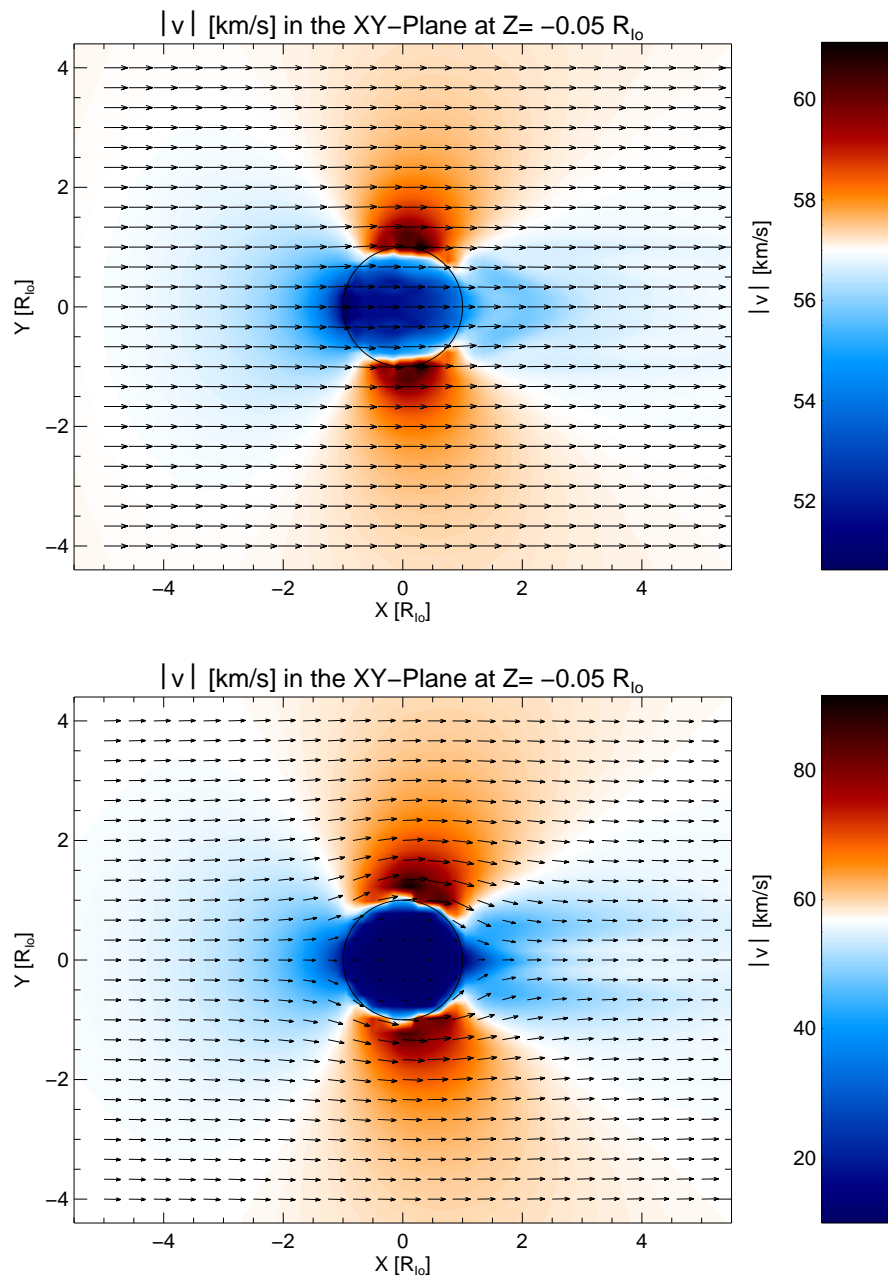


Figure 6.1: Total plasma bulk velocity in color-code. Arrows represent velocity components in the equatorial plane. Top panel: Weak interaction; Bottom panel: Strong interaction.

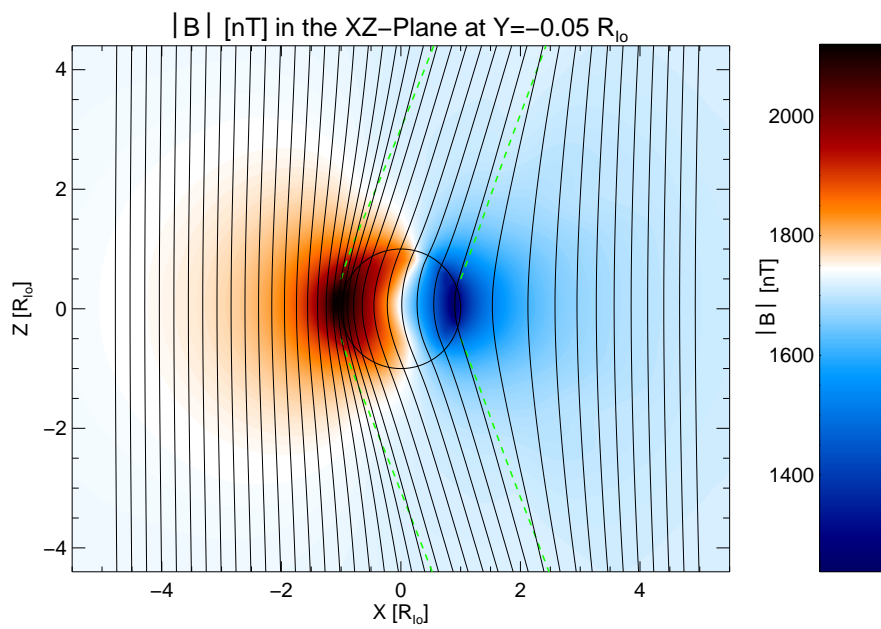


Figure 6.2: Magnetic field lines and absolute strength (color-coded) in the XZ-plane for a strong interaction. Dashed lines: Primary Alfvén characteristics.

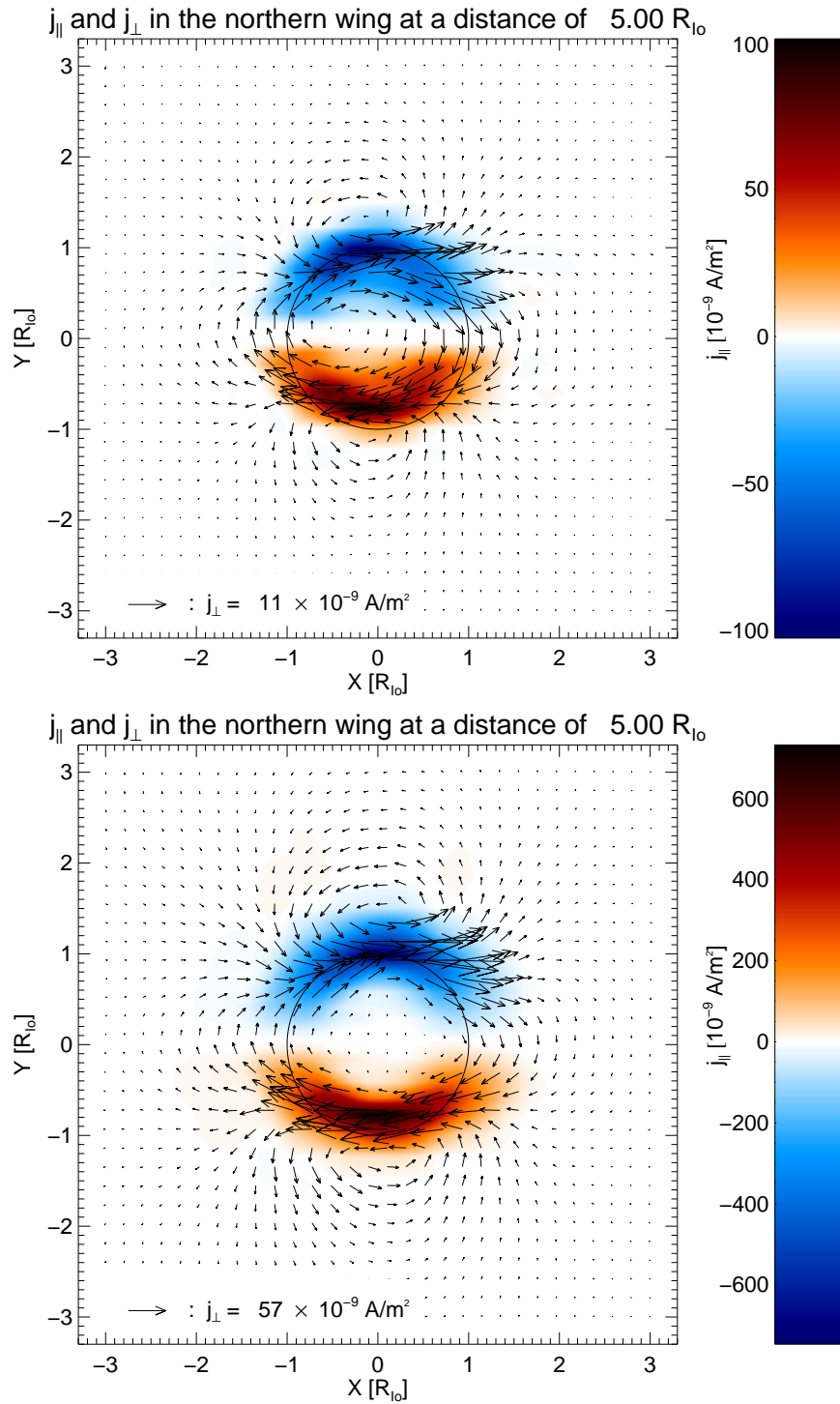


Figure 6.3: Current density parallel and perpendicular to the northern C_A^- -characteristic. 2D vector field (arrows) of j_{\perp} and amount of j_{\parallel} (color-coded). The cross section represents a plane perpendicular to C_A^- at a distance of $5 R_{Io}$ from the origin. The circle marks the projection of Io's disc along C_A^- .

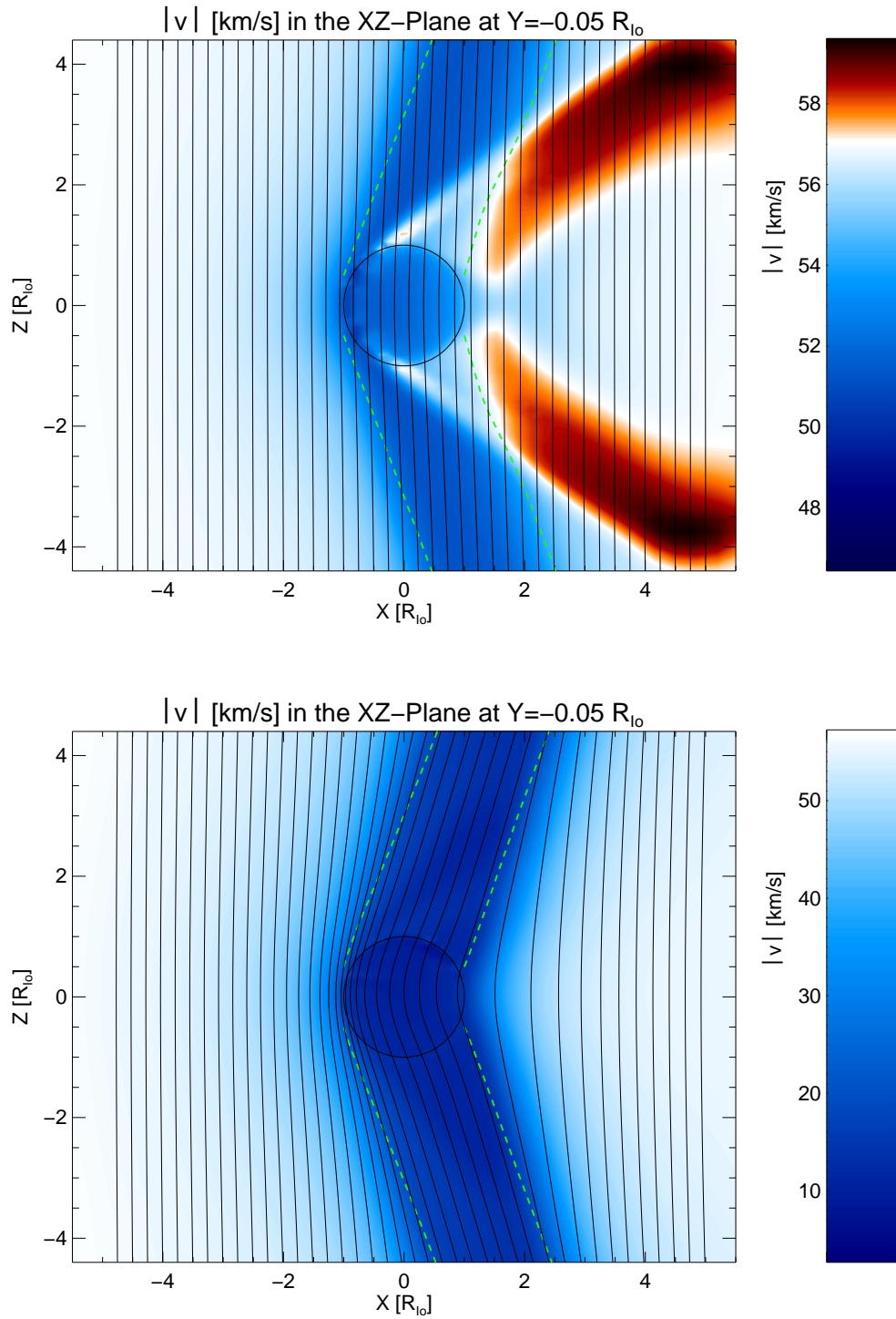


Figure 6.4: Plasma bulk velocity (color-coded) and magnetic field lines in a x - z -plane at $y = -0.05R_{I_o}$.

6.2 Alfvén Wave Reflection

For the simulations presented in this section, we use the basic setup described in section 5.2.1. The initial parameters were chosen as collected in table 2.1. We again compare two different scenarios. As in the previous section, one represents a weak, one a strong interaction. The effective collision frequencies and thus the initial perturbation were chosen as described in the previous section. At first glance, Figure 6.5 demonstrates how the variation of the interaction strength leads to fundamentally different wave fields. We now discuss the single scenarios and elaborate the differences.

The superficial appearance of the velocity field of the quasilinear interaction setup shown in color-code in the top panel of figure 6.5 exhibits rhombic features as expected for weak perturbation amplitudes (see figure 5.2). Additionally, the plot reveals the slow mode wave emerging from Io. The sign of the velocity perturbation associated with the Alfvén wave is conserved during reflection at a negative density gradient such as the first reflection at the torus boundary. Conversely, the sign reverses upon reflection at increases of the plasma density. Such positive gradients can be found e.g. at the representation of the Jovian ionosphere but also when the reflected wave from the ionosphere reenters the plasma torus. The sign reversal properties are opposite for the magnetic field perturbation. In summary, these observations are in accordance with theoretical expectations (section 4.5). As each partial reflection forks another branch of the Alfvén wave system, even for the quasilinear setup (weak interaction) multiple waves intersect and interfere. To guide the reader's eye, we follow the Alfvén characteristics connected to the source region and visualize them superimposed on the color contour plot. The line colors and arrows represent the propagation direction and the line style denotes the sign of the velocity perturbation with respect to the background bulk velocity. The line thickness expresses the intensity of the perturbation and thus decreases for each reflection process. For symmetry reason we only show one hemisphere. Hence, characteristics emerging from the bottom of the plot originate from the southern hemisphere. Lines for higher order reflections are omitted in favour of lucidity. However, the line style does not necessarily agree with the sign of the velocity perturbation derived from the color code, owing to wave interference, e.g. superposition of the slow mode wave. Due to multiple fork processes upon reflection, the pattern becomes more complicated further downstream of Io. Nonetheless, the direction of the Alfvén characteristics is almost translation invariant. Moreover, reflection at plasma regime boundaries occurs at an angle similar to the angle of the incident wave. Hence, the regular law of reflection is a good approximation for weak interactions.

The wave pattern in the plot illustrating the strong interaction simulation run is strikingly different. The gross morphology exhibits less detail than found in the weak interaction scenario. It features a large area of positive velocity perturbation (red color) that represents super-corotating plasma. The Alfvén characteristics are far from translation invariance. Locally a rhombic structure might be found, but this is not representative for the full reflection pattern. In summary both patterns have little in common. In fact, only the initial Alfvén wave launched from Io illustrated by the solid black line most left in the figure is almost identical.

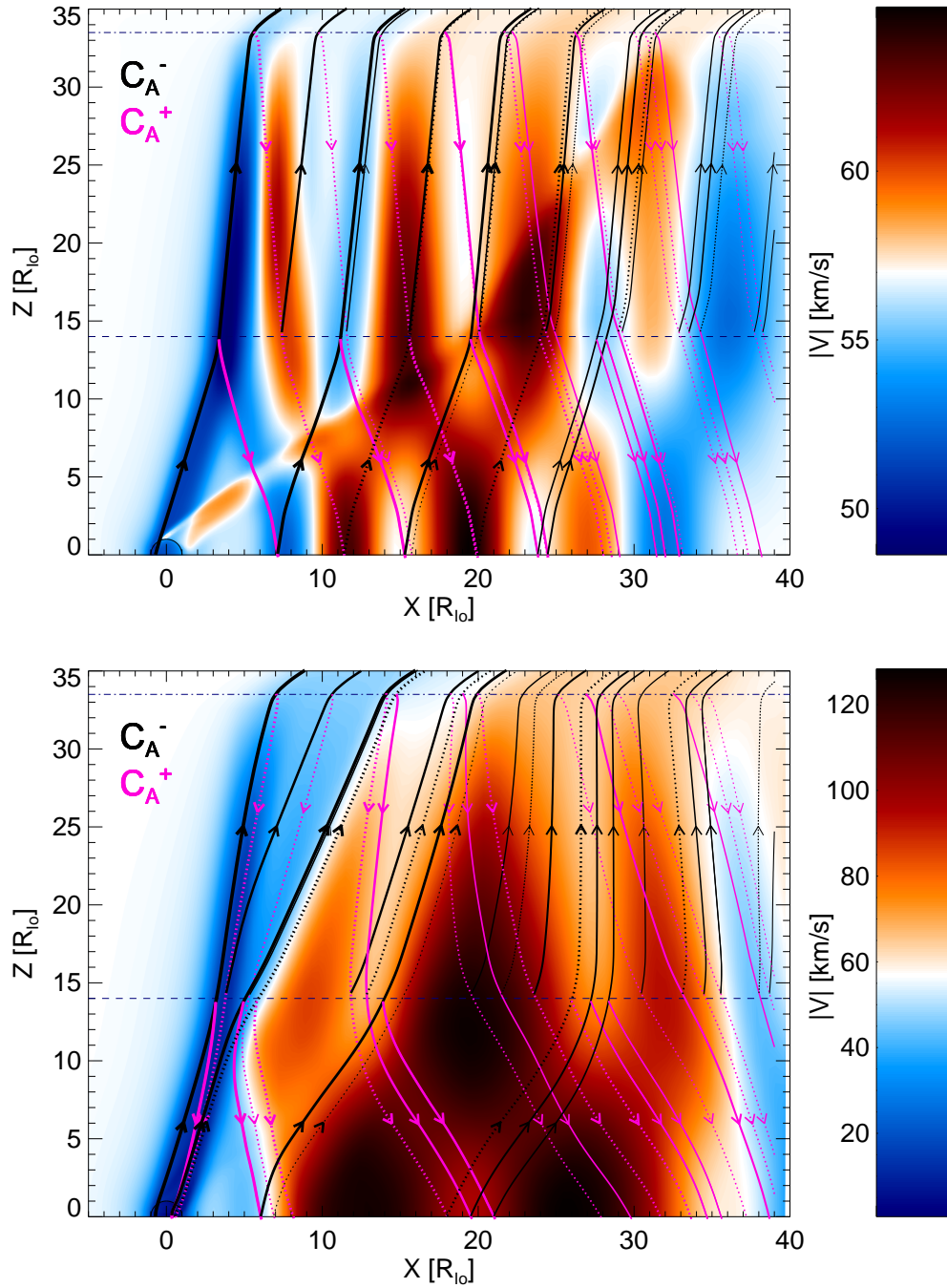


Figure 6.5: Plasma bulk velocity (in color-code) in the northern hemisphere in a xz -plane at $y=-0.05 R_{Io}$. Over-plotted: Alfvén characteristics: C_A^- in black and C_A^+ in magenta. Line styles of the Alfvén characteristics depict a change of sign of the perturbation. Solid lines represent a negative velocity perturbation, i.e. a deceleration with respect to the background value, dashed lines represent acceleration. Line thickness decreases with each reflection/transmission process in order to illustrate the decay in amplitude of the waves upon reflection. Top panel: weak interaction; Bottom panel: strong interaction. Note that line diminution is not to scale and that the local line style may not agree with sign of the velocity perturbation in color-code due to wave interference/superposition.

Remarkably, the first reflections of the initial Alfvén wave at the torus edge and the ionosphere are almost anti-parallel to the incident wave. At a second glance, this apparent puzzle can be assessed by the definition of the Alfvén characteristics (4.9). If $V_p \ll V_A$, which is representative for the initial Alfvén wave generated by strong interaction, the relative contribution of the plasma bulk velocity to the Alfvén characteristics is small. Recalling the almost perfect alignment of the magnetic field with the wing axis (see section 6.1) the expression

$$C_A^\pm = \mathbf{V}_p \pm \frac{\mathbf{B}}{(\mu_0 \rho)^{1/2}}$$

is hardly influenced by the plasma velocity term and the two characteristics are approximately anti-parallel. This is a fundamental difference between weak and strong interaction and not compatible with a regular law of reflection. However, downstream of Io there are areas where the angle of reflection is even larger than the incident angle. This occurs in regions, where $V_p > V_0$, i.e. where super-rotation takes place. Hence, in this case the regular law of reflection does not apply, either. Besides the bulk velocity term, the magnetic field direction also contributes to the characteristics. Due to sign reversal during reflection, there are significant lateral changes in the magnetic field direction (as opposed to the weak interaction, where the perturbation is generally small). A combination of all these effects lead to the Alfvén characteristics depicted in the bottom panel of Figure 6.5.

These cardinal differences between the two scenarios discussed here also outcrop in the cross sectional view of figure 6.5. The most prominent cross section was extracted at the top side of the Jovian ionosphere at $z=33 R_{JO}$ as it is believed to represent the Io footprint morphology. We will discuss this feature for the different runs in the upcoming section.

6.3 Footprint Morphology

The most striking features of the Io-Jupiter interaction are the auroral footprints in the Jovian ionosphere. Despite our model does not include micro-physical processes that cause e.g. the UV emission, we can follow the argumentation in section 4.6.1 and thus we can evaluate the footprint morphology via the Poynting flux density in Jupiter's auroral regions. Figure 6.6 illustrates the Poynting flux density for the two scenarios under discussion. Already at first glance, they look strikingly different. The top panel shows more discrete and clearly separated spots for weak interaction. Each of the spots marks a local maximum of the Poynting flux density which itself corresponds to a certain Alfvén wave or reflected Alfvén wave reaching the Ionosphere (compare to figure 6.5). Note that the majority of the spots exhibits negative Poynting flux, i.e. it is directed towards Io. This is consistent with our consideration in section 4.6.1. However, there are areas where, due to the local configuration of the signs of the velocity and magnetic field perturbation, the predominant direction is reversed. We would like to point out that their contribution to the total energy flux is small.

By contrast, the morphology of the footprint pattern associated with a strong interaction displays less distinct and more elongated features. The total flux is a hundred times larger than simulated for a weak interaction. The corresponding

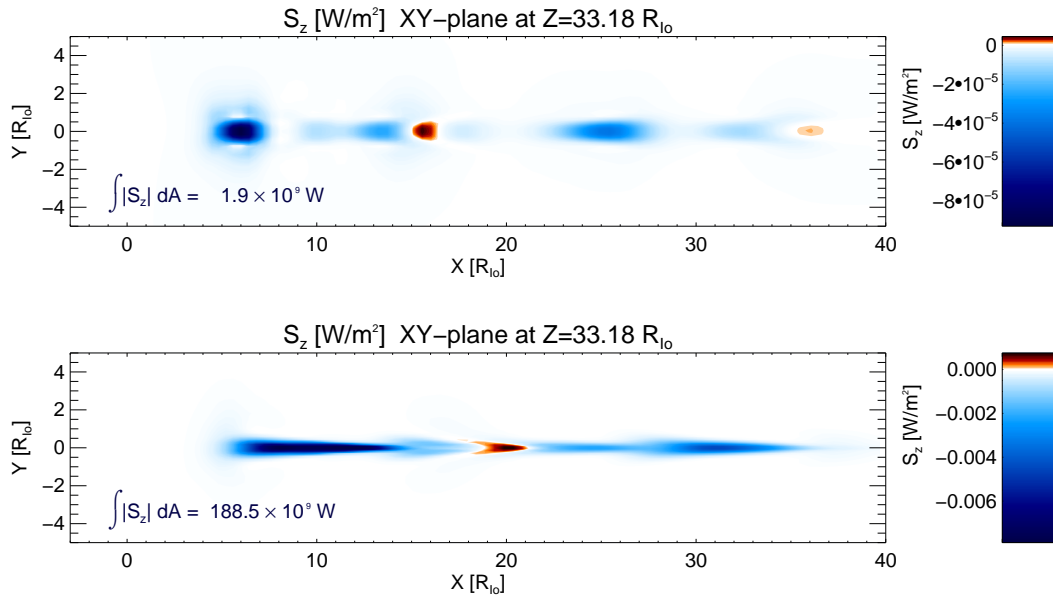


Figure 6.6: Poynting flux density in the northern Jovian ionosphere (x - y -plane at $z=33 R_{Io}$). Top panel: weak interaction; bottom panel: strong interaction.

wave field features can also be identified. The representation for e.g. the first long spot extending from $x=6 R_{Io}$ to $x=14 R_{Io}$ is the fan-shaped structure most upstream of the MHD wave pattern in Figure 6.5. It consists of higher order reflections that intersect and merge as opposed to the weak interaction data set, where they form separate spots. Thus, the diffuse appearance of the nonlinear wave pattern is reflected by the footprint morphology.

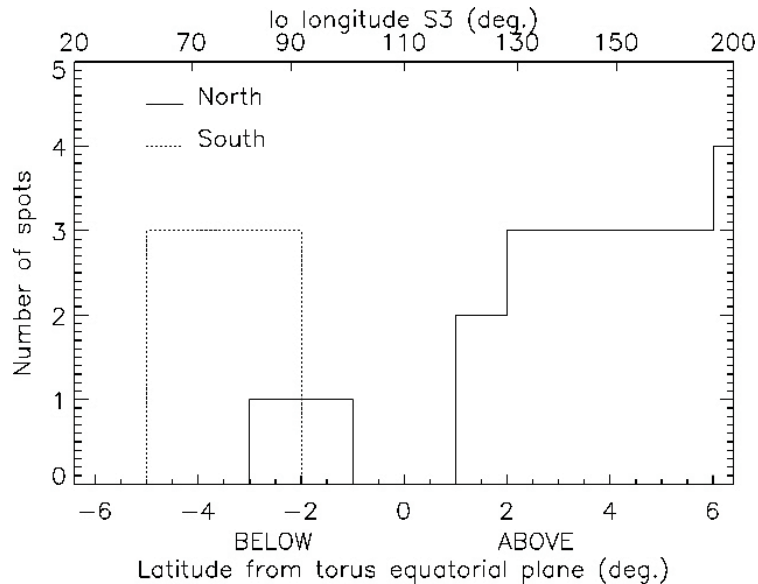


Figure 6.7: Number of multiples observed in the corotational wake of the MAW against centrifugal latitude for the northern and southern hemisphere [after Gérard et al., 2006].

If we recall the equivalence between strong interaction and Io residing in the torus center as well as weak interaction corresponding to Io located in the outer torus, we

find that our results agree with observational evidence by *Gérard et al.* [2006]. The authors notice that the number of distinct multiples trailing the main spot decreases when Io moves towards the inner torus. In fact they observe no multiples when Io is center-most in the plasma torus (see figure 2.14).

Based on our simulations we find two reasons for the footprint merging. First of course, the irregular reflections almost antiparallel to the incident wave lead to vanishing distance between the single spots for increasingly strong interaction. On the other hand, even an intermediate interaction strength leads to elongation of the cross section of the reflected Alfvén wing (see Figure 6.8a). In the northern Alfvén wing the C_A^+ -characteristic is modified compared to the background $C_{A,0}^+$ -characteristic outside the wing. The two differ mainly in the x-component as illustrated in figure 6.8. The consequence is an elongated reflected wing, that more easily merges with another (also elongated) structures (cf. 6.8c).

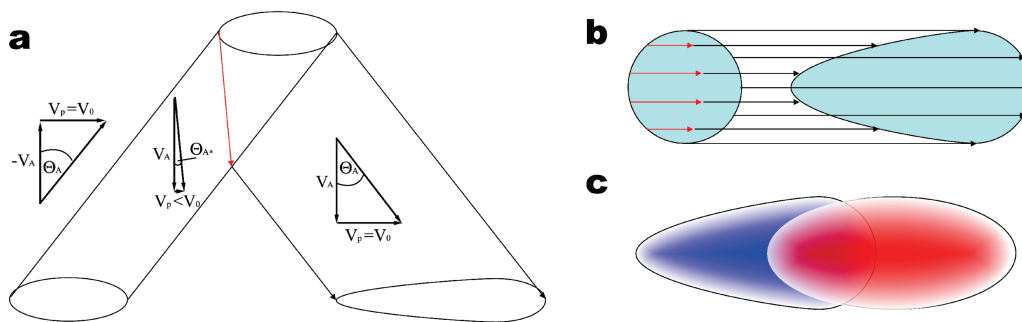


Figure 6.8: Schematic illustration of elongation of the Alfvén wing during reflection.

However, in the Jovian magnetosphere other than in our simulations presented in this section, the geometrical properties of the reflection change continuously as Io moves between the reflection boundaries of the torus edges. This effect is also partly responsible for changing inter-spot distances and eventually footprint merging. Nonetheless, this conception can not account for all phenomena observed (see section 2.7.2). Our simulation of irregular reflections due to a variation of interaction strength and the impact on the footprint morphology thus contributes to the understanding of footprint merging and the occurrence and temporary disappearance of multiple footprints.

Influence of the AAR

For the simulations shown in this section we implemented a resistive layer representing Jupiter's ionosphere. It is located at $\sim 3 R_{Io}$ equatorward of the ionospheric boundary (see e.g. Figure 6.11). The resistivity has been chosen to be sufficiently high to reflect almost the entire wave amplitude. This represents an extreme scenario, probably not occurring in the Jovian system. However, we intend to investigate the fundamental differences caused by the presence of a resistive layer. Thus it is helpful to isolate these effects. Therefore, we avoid ionospheric reflections by reflecting the whole wave amplitude at the AAR.

One of the major differences between Figures 6.9 and 6.5 is the absence of super-rotating plasma in and near the equatorial plane. In fact, for a strong interac-

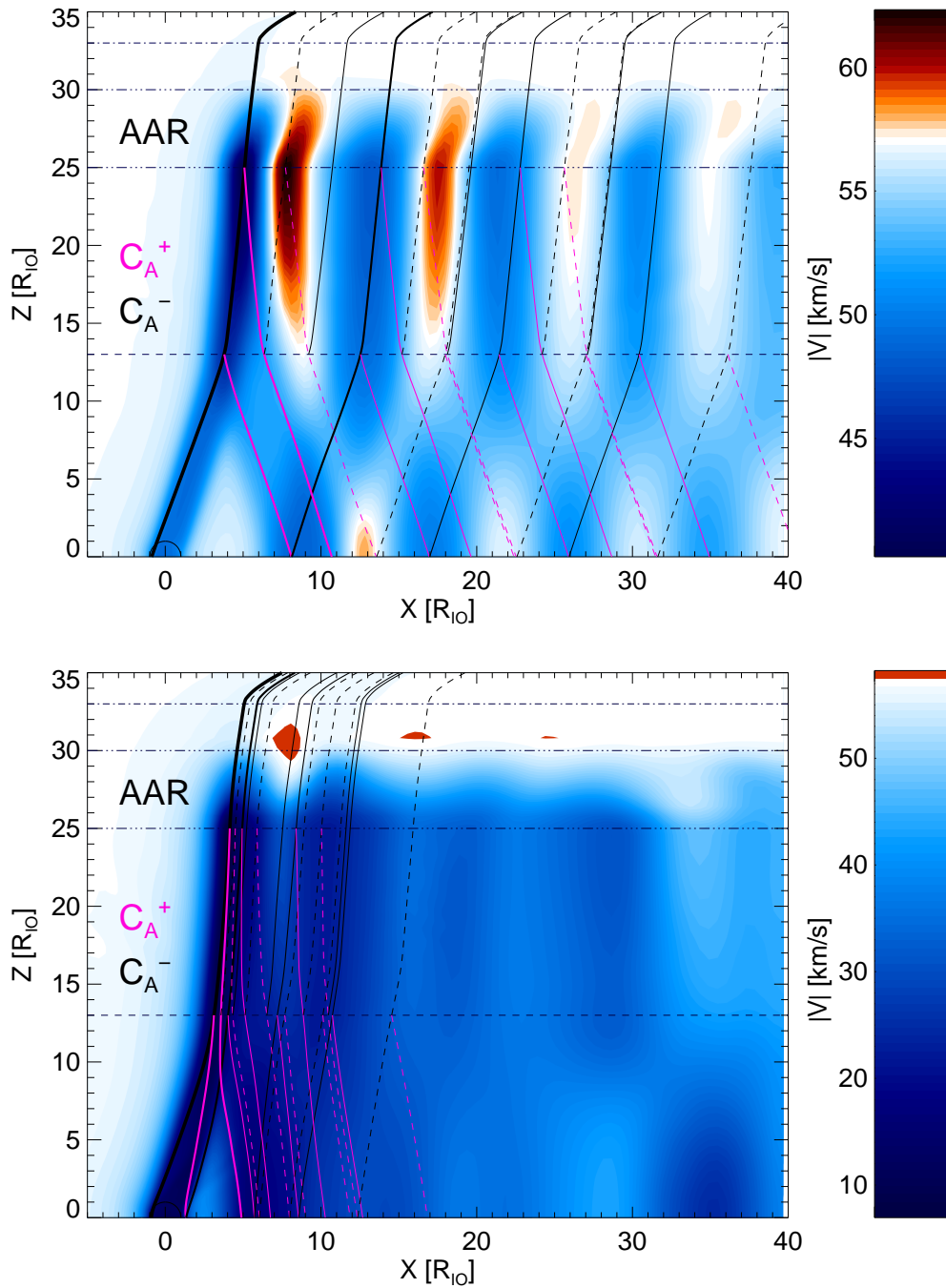


Figure 6.9: Plasma bulk velocity (color-coded) in the northern hemisphere in a xz -plane at $y = -0.05 R_{Io}$. Over-plotted: Alfvén characteristics : C_A^- in black and C_A^+ in magenta. The line style of the Alfvén characteristics depicts change of sign behaviour of the perturbation. Solid lines represent a negative velocity perturbation, i.e. a deceleration with respect to the background value, dashed lines represent acceleration. The line thickness decreases with each reflection/transmission process in order to illustrate the decay in amplitude of the waves upon reflection. Top panel: weak interaction; Bottom panel: strong interaction. Note that the line diminution is not to scale and that local line style may not agree with sign of the velocity perturbation in color-code due to wave interference/superposition.

tion (bottom panel) there is no significantly super-corotating plasma at all in the plane shown in Figure 6.9. The cause of this profound qualitative difference is the reverted change of sign behaviour of the AAR compared to the one of the ionosphere. The AAR enforces the velocity perturbation because the return wave has the same sign of the velocity perturbation as the incident one. A wave leaving the dense plasma torus is also reflected this way. Thus, these two boundaries do not revert the original negative velocity perturbation of the Alfvén wing during reflection. The only reflection boundary where the sense of δV is reverted is the positive density gradient a wave meets that has been reflected from the AAR and is encountering the plasma torus. In Figure 6.9 this is represented by change of line style from solid to dashed. However, this occurs for the first time after the wave has already undergone two reflection processes. Thus, the amplitude of this positive velocity perturbation with respect to the background bulk velocity is already diminished. The wave with reverted δV then is reflected from the Jovian ionosphere. During this reflection the sign is retained. In the area, where the two waves with positive δV (i.e. dashed line style) overlap, they constructively interfere. This is expressed by the red stripe in the top panel of Figure 6.9 between torus and AAR around $x=8 R_{Io}$.

Conversely, the magnetic field perturbation (not shown) of the wave reflected at the AAR weakens the one of the incident pulse, because the sign reverses during the reflection. Hence, the resulting magnetic field distortion δB is weaker than the one for ionospheric reflections.

The sign reversal properties give rise to other differences between simulations with and without AAR. The topology of the Alfvén characteristics over-plotted in Figure 6.9 is similar to the ones without AAR (Figure 6.5) for weak interaction (top panels), but notably different for strong interactions (bottom panels).

For the linear interaction scenario, the rhombic appearance of the Alfvén characteristics prevails when we replace the ionospheric reflector by an AAR. Nonetheless, this is mainly due to the small perturbation amplitude as both weak interaction runs do express only a small difference to the undisturbed Alfvén characteristics (cf. Figure 5.2). By contrast, the similarity between the two strong interaction runs with and without AAR is minor. While the ionospheric reflector bends the Alfvén characteristics in the downstream direction where we find super-corotating plasma (red areas in Figure 6.5), The Alfvén characteristics for AAR reflections are much steeper with respect to the undisturbed magnetic field direction. Hence, the downstream displacement per reflection is smaller. The same number of forked reflection characteristics is over-plotted in Figures 6.5 and 6.9, yet, it extends considerably less in the corotational direction for AAR reflections (Figure 6.9). The smaller Alfvén angle can be attributed to two effects. First, the destructive superposition of the magnetic field perturbation of incident and returning wave leads to a weakly disturbed magnetic field topology (compared to the one we obtain for ionospheric reflections). Secondly, the constructive interference for the velocity perturbation results in a small downstream plasma velocity component. If we recall the definition of the Alfvén characteristics (4.9) we thus obtain a large z-component resulting from the magnetic field direction and a small x-component due to small plasma velocities. This leads to steep Alfvén characteristics as illustrated in the bottom panel of Figure 6.9.

In order to deduce the probable footprint morphology from our simulation includ-

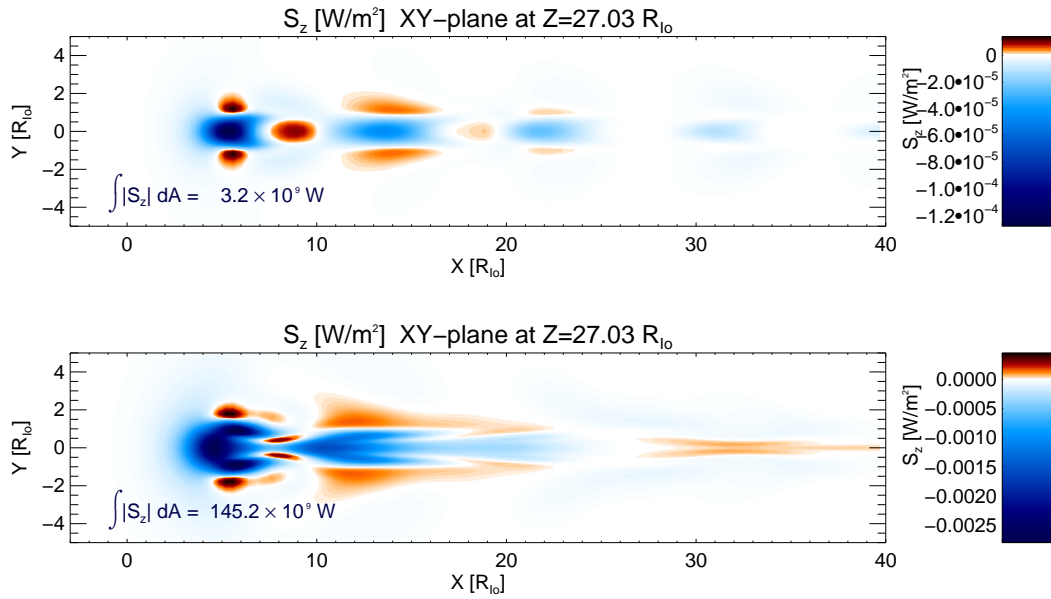


Figure 6.10: Poynting flux density in the northern AAR (x - y -plane at $z=27 R_{I_0}$). We interpret this morphology as analogous to the footprint morphology. Top panel: weak interaction; bottom panel: strong interaction.

ing the AAR, we need to make some additional assumptions. As we have implemented the AAR as a very effective reflector, almost no Poynting flux associated with the Alfvénic disturbance reaches the ionospheric boundary. Hence, the method we applied in section 6.3 is not suitable for runs including an AAR. In the AAR, electrons are believed to be accelerated in both directions, parallel and antiparallel to the magnetic field. Electrons that are precipitating into the ionosphere are believed to generate the auroral emissions. We make use of the confinement of these beams to the magnetic field direction. The idea is to calculate the Poynting flux density in the AAR and map it along the magnetic field to the ionosphere. As we have seen in Figure 6.9, almost the entire Alfvénic perturbation is reflected, so that the magnetic field between AAR and ionosphere is basically undisturbed. Thus, we can simply map the Poynting flux density we obtain in the AAR along the undisturbed magnetic field direction (z -direction). As this is a parallel mapping we can more easily interpret the Poynting flux density in the AAR to represent simultaneously the auroral footprint morphology. The result is shown in Figure 6.10. Despite major discrepancy between ionospheric and AAR wave reflection, the qualitative morphology is similar in Figures 6.6 and 6.10. While weak interaction results in a patchy topology and distinct features, the strong interaction produces a more continuous footprint. However, for the nonlinear interaction with AAR we obtain a structure that can be divided in a spot feature and a separated tail feature. Also, the extent in y -direction is bigger for the strong interaction scenario with AAR. Nonetheless the qualitative agreement between our simulations and the observations discussed in section 6.3 prevails and is mostly independent of the nature of the reflector and the associated sign reversal behaviour.

Notwithstanding, besides the qualitative consistency in the footprint morphology, the implementation of an AAR produces a wave pattern strikingly different from results with pure ionospheric reflections. We thus will revisit observational evidence and search for implications that favor one of the two competing concepts.

The first major difference is the presence of super-corotating plasma in Io's geometrical wake region. This has never been observed so far. However, only one flyby was geometrically suitable to address this question, namely the *Galileo* I31 flyby. It was the only pass that stayed in the wake over more than $15 R_{Io}$. The exact range of the in-wake trajectory is difficult to determine, as after closest approach, the spacecraft has a velocity component in z-direction. Thus it leaves magnetic shells containing the wake region earlier than inferred from the mere radial position (cf. Figure 4.4).

The observed plasma velocity data was published in *Frank and Paterson [2002a]*. There are no traces of super-corotating plasma. This fact rather favors AAR reflections.

Additionally, we notice in our simulations that incident and reflected waves interfere multiply in a very concentrated region downstream of Io. It has been discussed whether colliding Alfvén wave packages become filamented [e.g. *Seufert, 2008*]. There is also observational evidence for wave filamentation [*Chust et al., 2005*].

Both criteria seem to favour AAR reflections. However, the discussion presented here so far is too dichotomic. Our simulations represent two extreme opposing scenarios with exclusively ionospheric or AAR reflections. This might be to some extent misleading as none of the concepts can be found in a pure form in the Jovian system but rather an intermediate scheme. Nevertheless, we find that our main conclusions concerning the footprint morphology and spot number are independent of the nature of the reflector.

6.4 Equatorial Electron Beams

The aim of this section is to study the spatial distribution and locations of the anti-planetward electron beams near Io. Besides Io, there are other satellites, that interact similarly with a planetary magnetosphere, for example Europa, Ganymede, Callisto and Enceladus. The principle results of our work might be applicable to those satellites as well.

On the basis of the concept illustrated in figure 2.17, one would anticipate that the electron beam generated at some longitudinal distance downstream would not hit Io. Yet, the *Galileo* observations prove that energetic particles, most likely accelerated close to Jupiter, precipitate onto Io's poles. As we have learnt before, the magnetic field is increasingly aligned with the wing axis for a more intense interaction strength. In the extreme case of a saturated interaction that is reminiscent to the current loop model, a magnetic flux tube is rigidly connected to Io. Hence, in this case a trans-hemispheric beam generated in the IFT would certainly hit Io. However, this scenario is unlikely to hold for all positions of Io in the torus, as the interaction strength varies substantially. To find out whether the interaction is strong enough to cause sufficient field line bending so that a TEB can reach Io,

| Flyby | Date & Time | type | S_{III} lon [°] | centr. lat [°] | ΔB_x [nT] | ΔV [km/s] |
|-------|---------------------|---------------|----------------------|-------------------|----------------------|----------------------|
| I0 | 12/07/1995 17:45:46 | wake | 272.6 | 1.92 | 400 ¹ | 25 ² |
| I31 | 08/06/2001 04:59:20 | polar (north) | 159.4 | 4.87 | -550 ¹ | -45.4 ³ |
| I32 | 10/16/2001 01:23:21 | polar (south) | 260.2 | 3.19 | 850 ¹ | ∅ ⁴ |

Table 6.1: List of Galileo flyby parameters and observations.

we carry out simulations with our MHD model. We investigate the position of the electron beams for three different model setups. One is a basic setup as described in section 5.2.1 and two make use of our travel time model (section 5.2.2). In one of the latter cases we included a resistive layer representing the AAR.

For the first set of simulations (one for each flyby on which electron beams were detected) we apply an enhanced version of the basic setup. It is enhanced in the sense, that we adjust the simulation box dimensions such that the over-all Alfvén wave travel time matches the one we deduce from our travel time model. We moreover enlarge the extent of the torus plasma regime to account for estimates of the travel time to the locations of maximum reflection coefficients for typical wavelengths. Finally, we position Io in such way that our estimated northward and southward Alfvénic travel times are met. Although we enhanced the basic setup in terms of travel times, we still have constant densities within the different plasma regimes and linear density transitions between them. Thus we obtain a sharp reflection boundary. In summary this setup hence satisfies the travel time constraints, but does not quantitatively reproduce reflection coefficients. The results obtained with this simulation configuration are published in *Jacobsen et al.* [2010]. However, we will mostly concentrate on results obtained more recently with the two remainder simulation setups. For the sake of completeness we will sum up and compare the findings to the latest results in due course.

To further improve the model and as we have now the opportunity to use considerably larger computational resources, we developed a plasma density model, that, over most of the distance, conserves the field aligned Alfvén velocity profile derived from a combination of the VIP4 magnetic field model [*Connerney et al.*, 1998] and the plasma density model [*Bagenal*, 1994] (see section 5.2.5). We calculate a specific density profile along the magnetic field for the given System III longitude of each Galileo flyby which observed extended equatorial electron beams near Io. An example of such a density profile for the Galileo I31 flyby is depicted in Figure 6.11. We concentrate on Galileo flybys which reported electron beams over a longer period. This applies to the I0, I31 and I32 passes. We note that other orbits, namely I24 and I27 exhibit energetic beam features. However, as one can see in Figure 4.4, the beams on these upstream passes were spatially narrow compared to the ones observed on the downstream and polar flybys. We outline the orbital parameters of the passes considered in the present thesis in Table 6.1. Furthermore, Table 6.1 contains peak values of the magnetic field and plasma velocity perturbations near Io. We allow for these measurements by adjusting the effective collision frequency we apply for Io in such a manner that we approximately reproduce these peak values with our simulation.

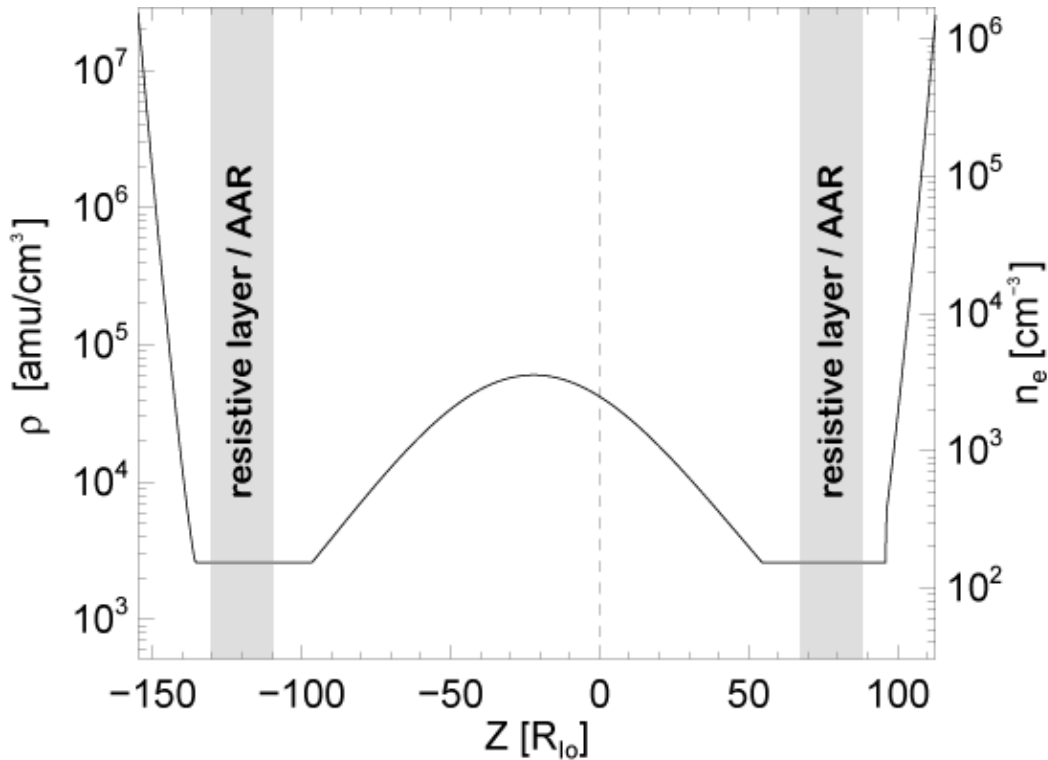


Figure 6.11: Plasma density profile along the magnetic field lines as applied in simulation runs for the Galileo I0 flyby. Dashed line marks Io's position.

Once we obtained the simulation results, we determine the location of equatorial beams with a two step method. As specified in section 4.6, the Poynting flux describes the energy transport to the AAR and it matches the morphological requirements derived from the Galileo EPD data. We therefore use the normalized Poynting flux density in the acceleration region as a proxy parameter for the intensity of generated beam. In the second step, we map this structure along the distorted magnetic field to the equatorial plane or, more precise, the plane of the flyby under consideration. We track the field lines using a fourth order Runge-Kutta algorithm in all three dimensions.

Morphology of Beam Generation and Main Spot

Figure 6.12 displays examples for the Poynting flux density (PFD) in the north for the I31 flyby scenario. While the top two panels correspond to the simulation including a resistive layer representing the AAR, the bottom two panels show the results from the same plane but from a simulation run without resistivity. As we consider the electron beams to be bi-directional the pattern displayed represent the initial morphology of the generated trans-hemispheric beam on the one hand, but also the morphology of the MAW and RAW spots that are caused by planetward ac-

¹Extracted from PDS MAG data sets

²Extracted from Frank and Paterson [2000]

³Extracted from Frank and Paterson [2002b]

⁴Not published to our knowledge

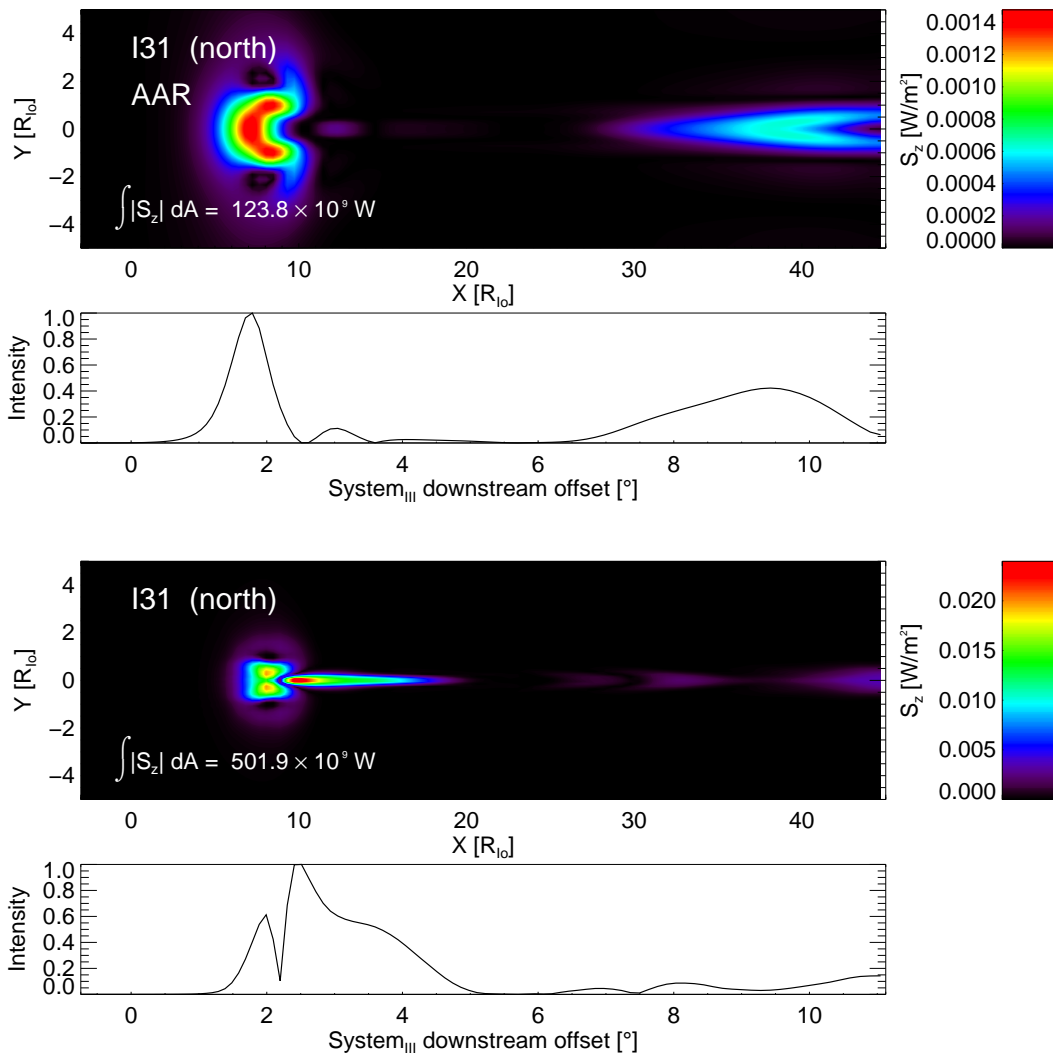


Figure 6.12: *First panel: Poynting flux density in the northern AAR for the I31 flyby setup. Second panel: Normalized intensity profile against angular downstream offset for $y=0$. Third and fourth panel: Same as first and second panel, respectively, but without reflections at a resistive layer*

celerated electrons on the other hand. The difference between the runs is profound. Due to magnetic diffusion, the morphology of the beam generation area is broader in the y -direction. Moreover, as diffusion also happens in the upstream direction, the lead angle of the beam onset in the corotational direction is smaller compared to the run without resistivity and the associated enhanced magnetic diffusion. These findings are similar to the ones we obtain in section 6.3. The integrated Poynting flux is much larger for the non-resistive simulation. This is mainly due to the substantial fraction of the wave that is already reflected within the AAR when it penetrates the layer we extract for the plot. We chose an extraction layer at a depth of $5 R_{I_o}$ in the AAR, i.e. where the wave has entered the resistive area by $5 R_{I_o}$. This depth is to some extent arbitrary but with our choice we try to balance two aspects of the AAR. On the one hand there are dissipative effects, as the wave amplitude decreases rapidly when the wave enters the resistive domain and the magnetic dif-

fusion broadens the wave structure. On the other hand we need to account for the fact that the beam is generated inside the AAR.

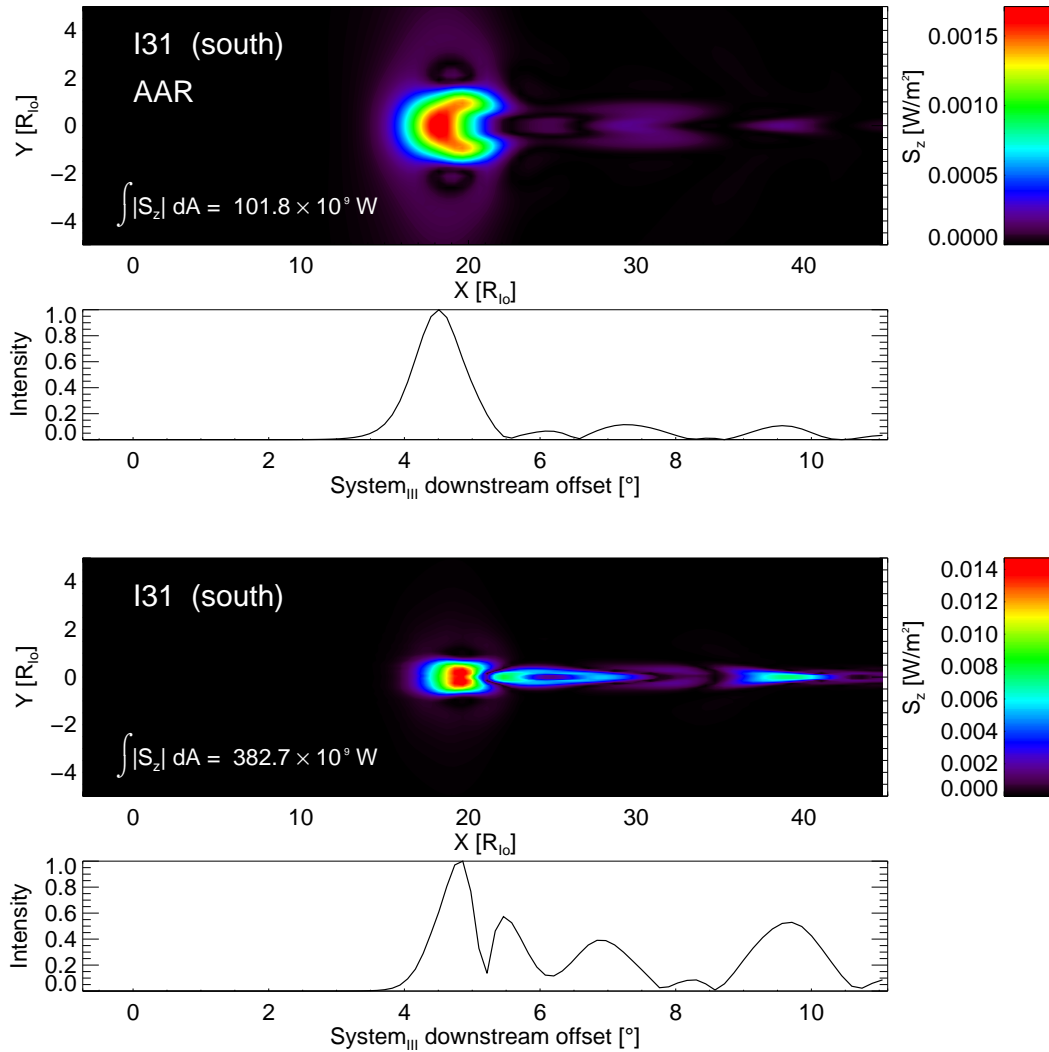


Figure 6.13: Same as Figure 6.12 but in the southern hemisphere.

Field Aligned Mapping Procedure

Figure 6.14 illustrates the field aligned mapping. The dark solid lines are magnetic field lines in the central the x-z-plane. The colored lines are specific field lines that correspond to the maximum (solid) and 50% intensity levels (dashed). Here green color denotes the beam from the northern to the southern hemisphere and red color represents a beam originating in the south. The corresponding plasma density profile is represented in Figure 6.11.

It is notable that these colored field lines possibly cross each other. This is no contradiction to the solenoidality of the magnetic field, but an effect of the visualization. As stated before we follow the beams in three dimensions. The plot only shows a projection of the beam to the pictured plane. Thus in three dimensions the magnetic

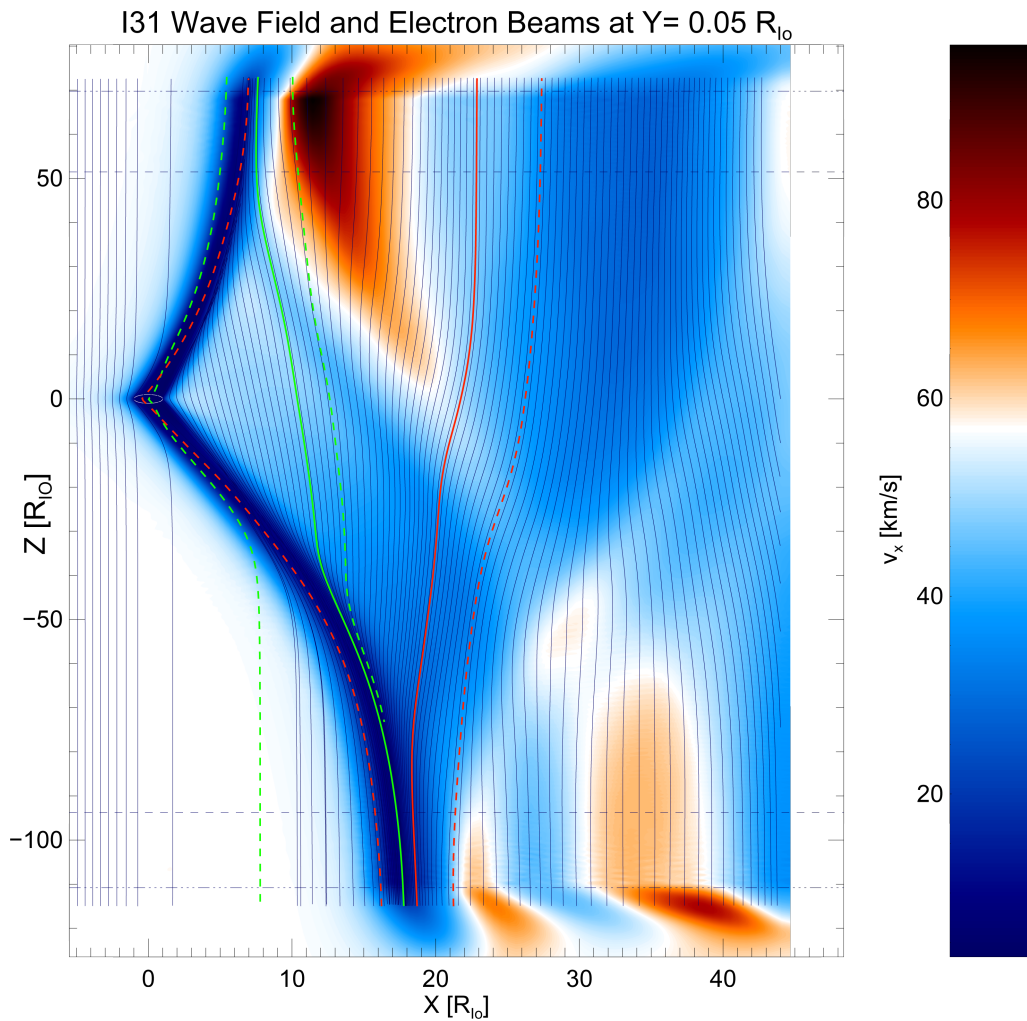


Figure 6.14: Orbit I31 simulation with resistive layer. Magnetic field lines (solid, black) and traced electron beams generated in the north (green) and in the south (red). Background: X component of the plasma velocity in color contours.

field lines do not cross. The apparent crossing in Figure 6.14 is merely a manifestation of the complexity of the magnetic field perturbation pattern we follow with the beams. For clarity of the figure we did not apply three dimensional integration but neglect the y-component for the background magnetic field lines (depicted by dark, thin solid lines). They are intended to guide the eye and to give an idea of the magnetic field perturbation in the downstream region and thus our aim was to avoid too complex structures that arise when showing the projection of 3D-integration.

Figure 6.14 also exhibits that we continue to follow the magnetic field lines after penetration of the equatorial plane to the conjugate hemisphere. We present the result of this trans-hemispheric mapping in section 6.5.

Again, a comparison of simulations with and without resistive layer again reveals differences. While Figure 6.14 displays no significant super-corotation near the equator, Figure 6.15 exhibits strongly super-corotating regions in Io's geometrical wake. Furthermore, the field line carrying the maximum beam intensity (solid red

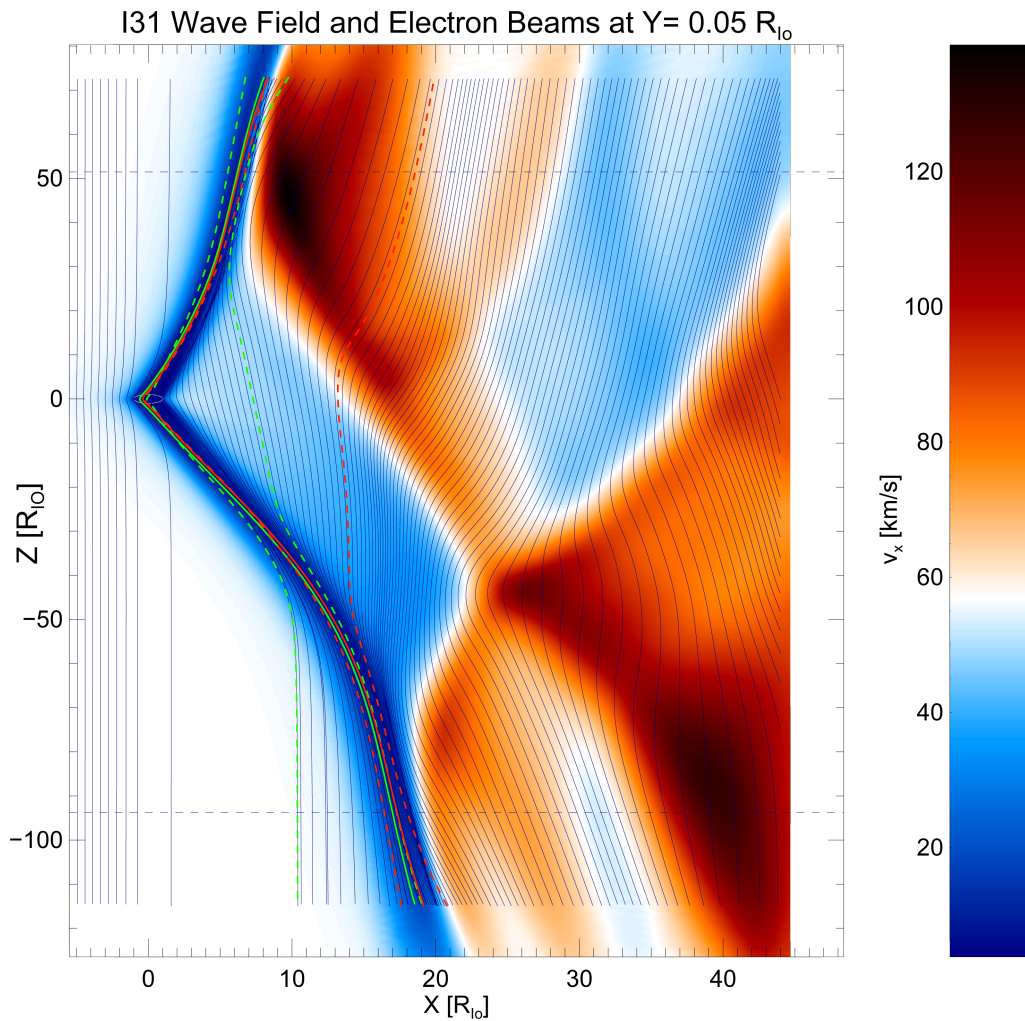


Figure 6.15: Same as Figure 6.14 but without resistive AAR.

and green lines in Figures 6.14 and 6.15) hit I_0 in the ionospheric reflection scenario and are located downstream when the resistive AAR reflects the Alfvén waves. However, the electron beam is in part in both cases connected to I_0 as indicated by the first 50% intensity line in the Figures 6.14 and 6.15.

The differences can be contributed to the change of sign behaviour of the magnetic field and plasma velocity perturbations upon reflection as discussed in section 6.2. The AAR reflector reverses the sign of the magnetic field perturbation of the incoming and the returning wave. Thus the resulting magnetic field distortion is small where both waves superimpose. The effect can be best observed if one compares the region super-corotating plasma in the northern hemisphere (red area near $10 < x < 20 R_{I_0}$). While the magnetic field represented by the dark, solid lines is strongly bent in the upstream direction for a ionospheric reflector setup (Figure 6.15), the field lines are approximately straight and aligned with the z -direction when pure AAR reflections take place (Figure 6.14). Hence in the latter case, electron beams generated at some distance downstream follow the weakly disturbed magnetic field and penetrate the equatorial plane with a larger offset in the coro-

tational direction if strong reflections at a resistive layer take place. Conversely, in the ionospheric reflection concept the beams pursue the draped magnetic field topology and more likely reach Io. We will now investigate the impact on the two-dimensional beam structure in the equatorial plane.

Equatorial Beam Intensity Pattern

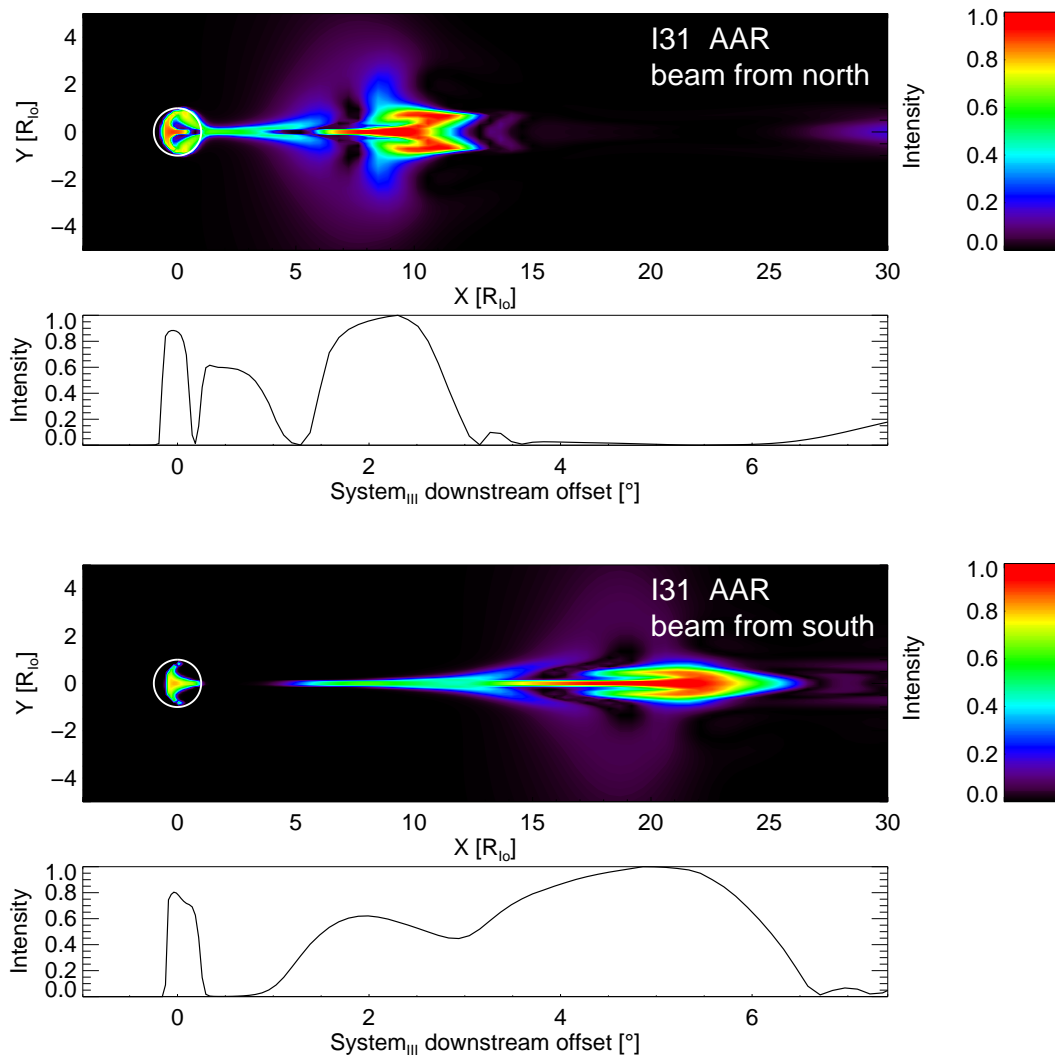


Figure 6.16: Equatorial beam intensities on Galileo I31 orbit. First panel: Color contours of two-dimensional intensity topology of the beam origination in the northern AAR. Second panel: Central intensity profile along x-axis of the northern beam. Third and Fourth panels: Same as First and second panels but for the beam originating in the southern hemisphere.

The beam intensity pattern we deduce for the equatorial plane for the I31 flyby is exposed in Figures 6.16 and 6.17. Figure 6.16 represents our simulation results including reflections at the AAR. We notice, that both beams (from the north and south) cover partly the disc of Io. Towards the wake of Io, the structure tapers and becomes narrow in the y-direction. For the beam from the south (panel three and four of Figure 6.16) there is a gap in the downstream direction before at some dis-

tance we observe beams again. We investigated, that this gap is not based on data that exhibits low beam intensity, but we find data voids in these regions which are interpreted as zero intensity. This is due to our field line tracking procedure. The lack of data occurs at locations, where no field line we track from the north or south penetrates the flyby plane. Thus we tend not to over-interpret the gap structure. This applies also for the v-shaped low intensity feature on Io's disc for the northern beam (first and second panel of (Figure 6.16). Farther downstream, we observe the main maximum in the beam intensity. Unlike the local maximum on Io's disc, the locations of the oppositely directed beams do not coincide. The main beam feature is located further downstream for the beam from the south. This can be contributed to the larger downstream offset of the southern beam generation region and the local distortion of the magnetic field mainly in the corotational direction (cf. Figure 6.14).

Comparison between the two setups with present (Figure 6.16) and absent (Figure 6.17) resistive layer once more displays considerable differences. The rough morphology for the simulations with reflections at the AAR is much broader than the ones we observe for sheer ionospheric reflections. This is most likely due to the magnetic diffusion of the wave structure in the AAR and thus a broadening of the effective beam generation region. Moreover, in the setup without resistivity, the downstream offset of the main maximum of the southern beam, although significantly elongated, is smaller compared to the one we obtain when the wave is reflected at the AAR. We attribute this discrepancy to the inverse change of sign behaviour upon reflection for the two simulation concepts. Nonetheless, both scenarios exhibit beam features (albeit with different extent and intensity) on Io's disc.

We will now in detail analyze how the simulated beam features close to Io compare to the *Galileo* in-situ data for the different flybys.

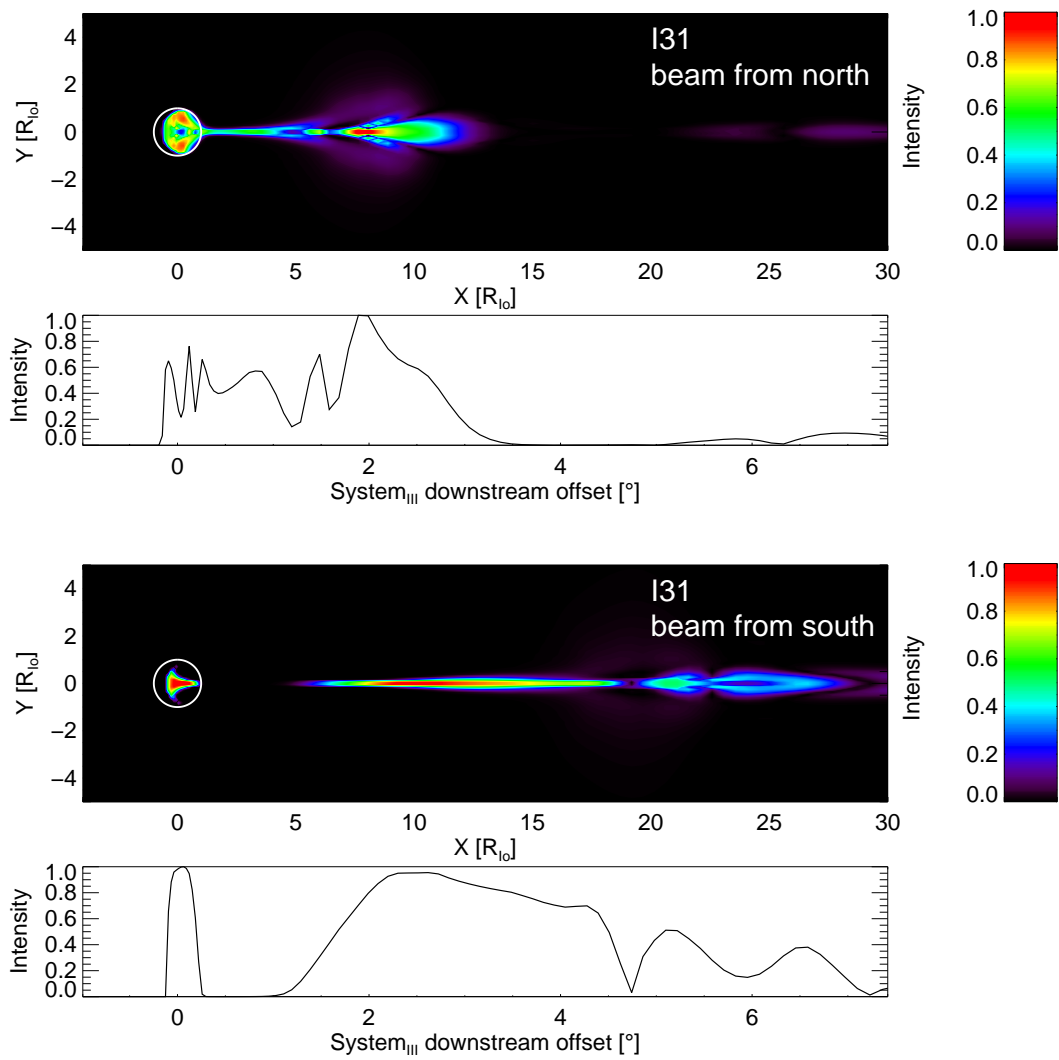


Figure 6.17: Equatorial beam intensities on Galileo I31 orbit. First panel: Color contours of two-dimensional intensity topology of the beam origination in the northern AAR. Second panel: Central intensity profile along x-axis of the northern beam. Third and Fourth panels: Same as First and second panels but for the beam originating in the southern hemisphere.

Comparison with In-Situ Data

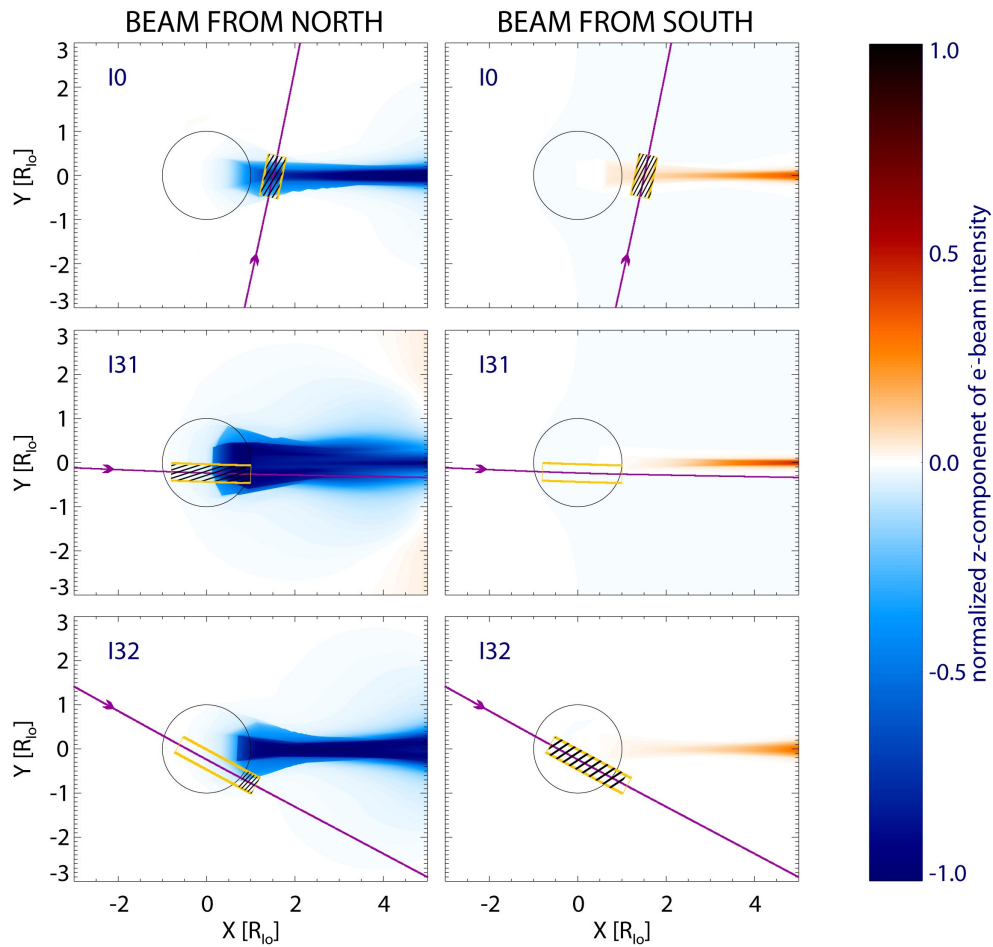


Figure 6.18: Equatorial electron beams for the Galileo I00, I31 and I32 flybys. Left column: Beams from the north; Right column: Beams from the south. Simulation results are coded in color contours. The sign of intensity represents beam direction. Negative values designate beams from the south. Spacecraft trajectories in magenta and yellow boxes represent locations of in-situ beam detection. Hatched parts of the boxes indicate detection of beams in the direction (from north or south) shown in the specific panel.

In the course of our studies, we started with a basic setup mainly characterized by constant plasma densities for the different plasma regimes and linear gradients in between. Based on the fact that the ratio of Alfvénic travel time and convection time has been identified as crucial parameter to characterize the interaction, we adjusted the extent of the simulation box as whole and the torus dimensions to meet travel time requirements. We applied this updated model also for the investigation of the electron beams that have been observed over Io's poles and in the close wake. The results have been published in *Jacobsen et al.* [2010]. We recapitulate the essential findings here to elaborate the improvements that arise from the model optimization.

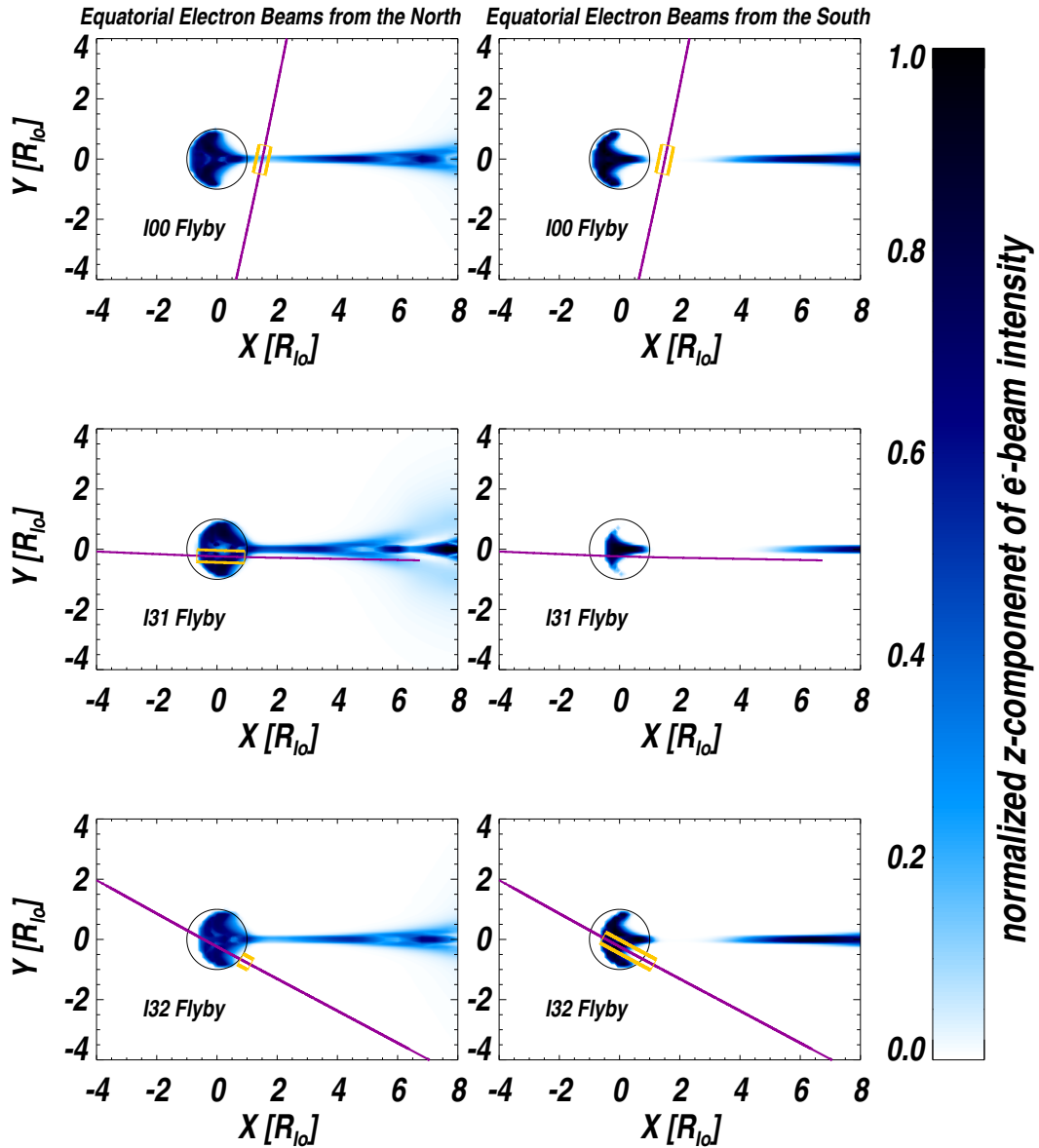


Figure 6.19: Equatorial electron beams for the Galileo I00, I31 and I32 flybys. Left column: Beams from the north; Right column: Beams from the south. Simulation results are coded in color contours. Spacecraft trajectories in magenta and yellow boxes represent locations of in-situ beam detection in the direction (from north or south) shown in the specific panel.

Figure 6.18 displays the Galileo probe trajectory for the different flybys with respect to Io. The yellow rectangles framing parts of the trajectory mark areas where

field aligned electron beams have been observed by the EPD detector based on the findings by *Williams and Thorne* [2003]. Additionally, we carefully inspected the EPD data ourselves and categorized the beams according to the beam direction. Thus we separate the results for southward (left column of Figure 6.18) and northward (right column of Figure 6.18) beams. The hatched parts of the yellow boxes indicate beam detection in the corresponding direction. We conclude in *Jacobsen et al.* [2010] that our numerical model successfully reproduces most features of the observations. The *I00* simulation reflects the small width of the beam structure in the radial direction (i.e. the y -direction in our model) compared to the wake extent. We moreover notice beams in both directions, albeit not with equal intensity, in accordance with the observational data. The *I31* flyby, being a norther polar flyby demonstrated almost entirely beams from the north, as beams from the opposite direction were shielded by Io. Our model provides also electron beams over the north polar regions, however, the beam onset is slightly shifted to the downstream hemisphere. Only the very end of the period in which beams were observed displays weak intensity from the south. Our results conform with this, although the northward beam on the right is extremely weak in the modeled data. The consistency between EPD observations and our model results is weaker for the south polar *I32* orbit. While we succeed in obtaining electron beams from the north closely behind Io in accordance with observations, we fail to have intense beam structures on the disc of Io. In fact the beam onset seems to be systematically displaced in the corotational direction. One may hypothesize that this might be due to temporal changes of the interaction parameters such as the incoming plasma density or enhanced volcanic activity on Io. Nonetheless we can not rule out that the idealizations in our model contribute to this discrepancy.

One of the main idealizations incorporated in the basic density profile design is the relatively sharpness of density gradients. Thus we obtain very localized reflections. By contrast, the genuine field aligned density profile of the torus plasma is smooth. Hence the Alfvén wave leaving the torus experiences gradual reflections on its propagation path. As the resulting perturbation field is likely dissimilar for gradual and sharp reflections, we can anticipate that the electron beams bound to the distorted magnetic field will follow different tracks and produce unequal equatorial beam morphologies.

To account for this shortcoming of the basic setup, we developed the travel time model described in section 5.2.5. We thus conserve the genuine Alfvén velocity profile over large parts of the simulation volume and are hence confident to obtain more realistic reflections at density gradients. The results we obtain with this set of simulations for the comparison with in-situ data are summarized in Figure 6.19. Over all we notice a good agreement with the observations. For the *I00* wake pass, the tapered width of the beam in the wake region is qualitatively reproduced, albeit the simulated structure is even more narrow than the observations for the beam from the north. The beam from the south we derive from our model data is not present where it has been observed. However, this is due to data gaps resulting from the field aligned structure tracking as argued before. It is most likely that the beam structure continues between $0 < x < 3R_{Io}$. The in-situ data for the *I31* flyby over Io's north pole conforms to our simulation results. Especially the beam onset is better resolved than for the model with a basic setup (cf. Figure 6.18). Beams from the south are present according to our simulations but shielded by Io. This was not the case when using the basic setup. A major improvement in fitting the

EPD data can be noted for the *I32* flyby. In contrast to results obtained with a basic model design, we notice an intense northward beam structure over the south polar region. However, we can not confirm beams from neither the north nor the south in the trajectory section where *Galileo* emerges from behind Io's disc.

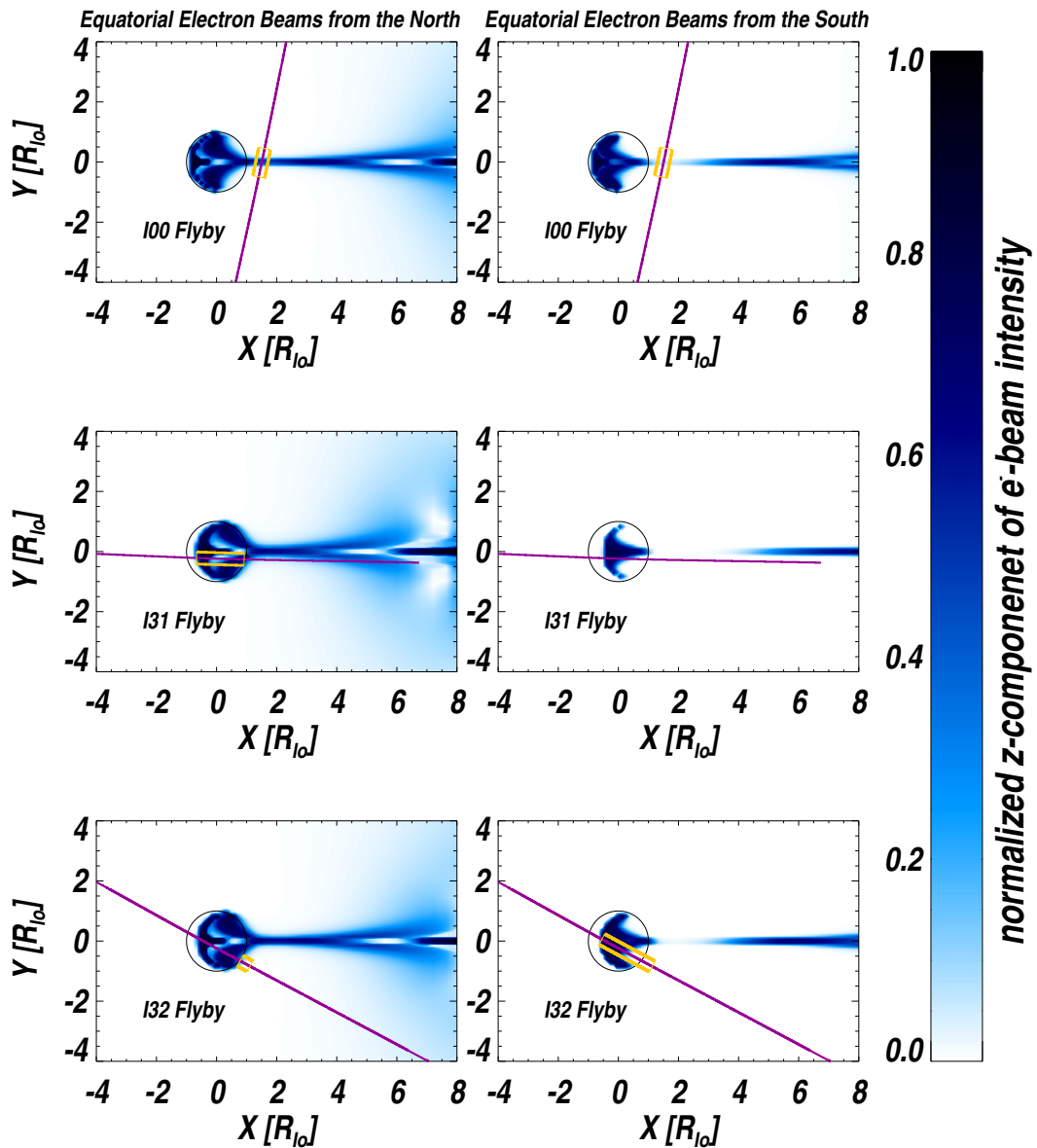


Figure 6.20: Same as Figure 6.19 but for a simulation concept with reflections at a resistive layer instead of ionospheric reflections.

As we have seen before, the replacement of ionospheric reflections by introduction of a resistive layer representing the AAR has significant impact on the downstream wave field. We thus carried out our numerical experiments with a configuration similar to the latter one, but with AAR reflections. We present the results in Figure 6.20. At first glance they are similar to the ones obtained with absent resistivity (Figure 6.19). Still some minor differences can be observed. First the beam structure in the wake is broader in the y -direction. This slightly favors the agreement between EPD data and simulation results for the *I00* wake pass. Moreover we notice a beam from the south in our model data where it has been measured in-situ. The larger extent in the radial y -direction we infer from our model makes us expect observable beam structures from the north in the wake region also for the *I31* orbit. This is however not supported by in-situ measurements. On the other hand the location southward beam onset is again well reproduced in our simulation. The same holds for the onset of the beam from the south measured on the *I32* pass displayed in the bottom right panel of Figure 6.20. Compared to the non-resistive setup, the agreement between model and *I32* flyby data is slightly improved for the beam originating in the northern hemisphere is better, as we notice a beam partly filling the yellow box.

Over all we can conclude that the qualitative structure of the simulated beams is in compliance with in-situ measurements. This holds generally for all simulation setups we apply, but the agreement is better for the model concept based on the travel time model with smooth density gradients. Although each model setup replicates certain features of the observations better than others, we commonly observe tapering of the beam structure in the wake. The agreement with the observed beam onset is better for the both smooth gradient simulations compared to the basic setup with slight advantages for the AAR reflection model. As all models use the same integrated travel times for each hemisphere, the robustness of certain features encourages us to conclude that the Alfvénic travel times are one of the main controlling factors for the electron beam morphology. On the other hand, the shape of the plasma density gradient used seems to have a larger impact on the electron beam locations than the nature of the reflector.

6.5 Trans Hemispheric Electron Beams

Observations of a leading spot feature by *Bonfond et al.* [2008] gave rise to hypothesis that the electron beams observed in the equatorial plane continue to the conjugate hemisphere and cause additional auroral spots. This is by now generally agreed on in the scientific community. On the basis of our simulation data we can extend the method we use to infer the beam morphology in the equatorial plane so that we are able to obtain the morphology of the trans hemispheric auroral spot feature. We display the results in Figures 6.21 and 6.22.

The main differences between simulations with (Figure 6.21) and without (Figure 6.22) resistive reflector have been pointed out before. The increased width of the beam features in y -direction that we observe for runs with AAR reflections also applies to the TEB spot we obtain. For a geometric configuration we have for the I31 scenario, i.e. Io is far north in the torus, we would expect the TEB spot to be preceding the main auroral spot in the south. A comparison with Figure 6.13 reveals that this is the case. The MAW maximum is located at 4.5° downstream of Io's magnetic longitude, whereas the southern TEB intensity has a first local maximum at 2.5° downstream offset. Hence it would be leading the MAW by approximately 2° . Traces of the beam are even noticeable at an angular downstream offset as small as 1° with respect to Io's longitude (see Figure 6.21). On the other hand, we suspect the northern TEB spot to be located tailward from the MAW. The simulations with AAR reflections yield a lead angle of 1.5° for the northern main spot (Figure 6.13). The maximum of the TEB structure is located at approximately 5° . Resulting in an approximate downstream distance of 3.5° .

Interestingly, the TEB onset in the upstream direction almost coincides with the main spot location. This indicates, that in our simulations some field lines are trapped inside the Alfvén wings. They are noticeable as the parts of the equatorial beam feature that is visible on Io's disc (cf. Figure 6.16 where the Alfvén wing starts and if we follow them to the poles, they coincide with the MAW feature marking the imprint of the Alfvén wing. This can be interpreted as hints that at least in part a rigid connection of magnetic field lines with Io indicative for the current loop model occurs. However, large parts of the beams are located at considerable distance from the Alfvén wings and consequently we would not attribute the whole nature of the interaction to a single concept.

Since recently systematical analysis of Jupiter UV auroral footprints and classification (MAW, RAW and TEB spots) by *Bonfond et al.* [2009] provides additional constraints for our simulated beams and thus will not be overlooked. The implications for our simulations arise from the observed distances between single spots and will be addressed in the following paragraph.

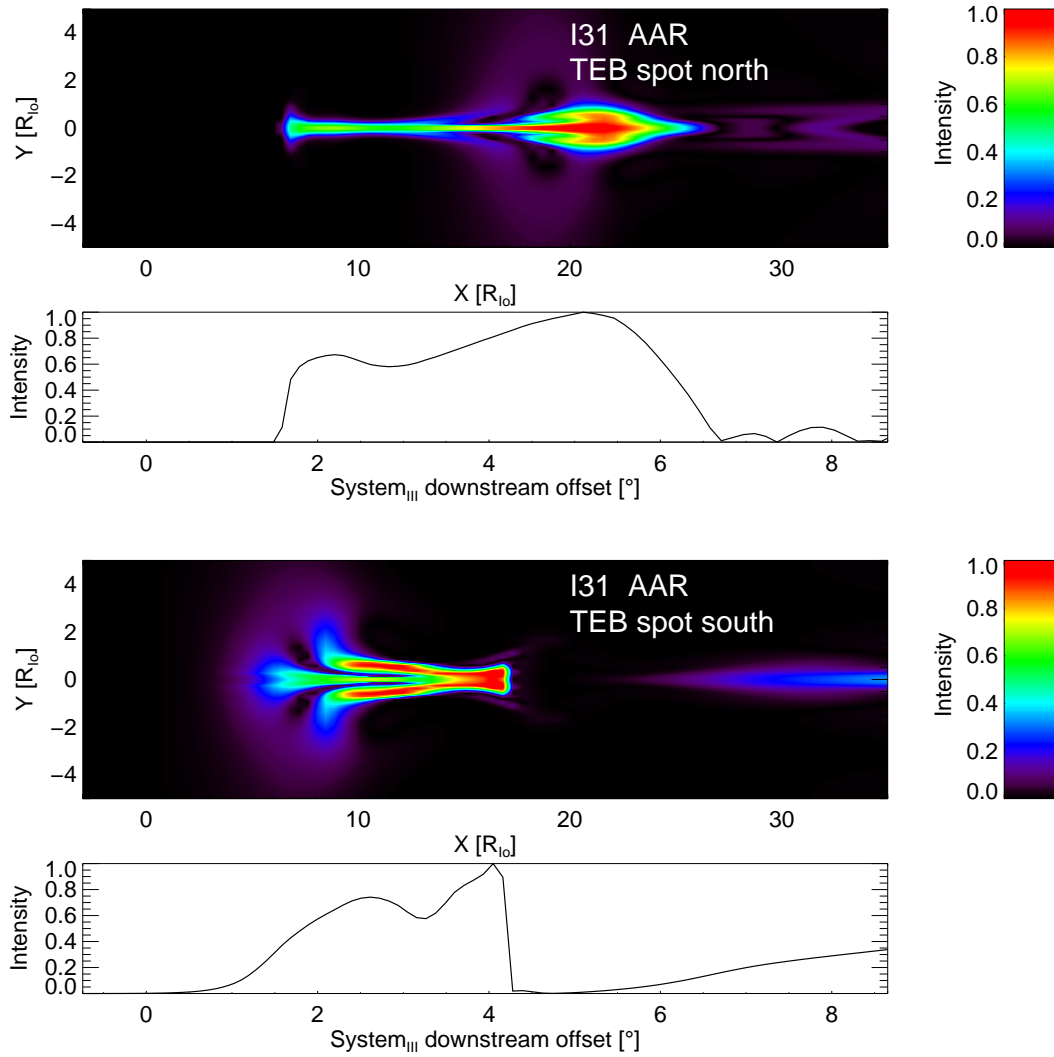


Figure 6.21: Intensity of the auroral feature caused by the trans-hemispheric electron beams for the Galileo I31 orbit. Data produced by simulations including a resistive AAR layer. First panel: Color contours of two-dimensional intensity topology of the TEB feature in the northern Jovian ionosphere. Second panel: Central intensity profile along x-axis of the northern TEB spot. Third and Fourth panels: Same as First and second panels but for the beam originating in the southern hemisphere.

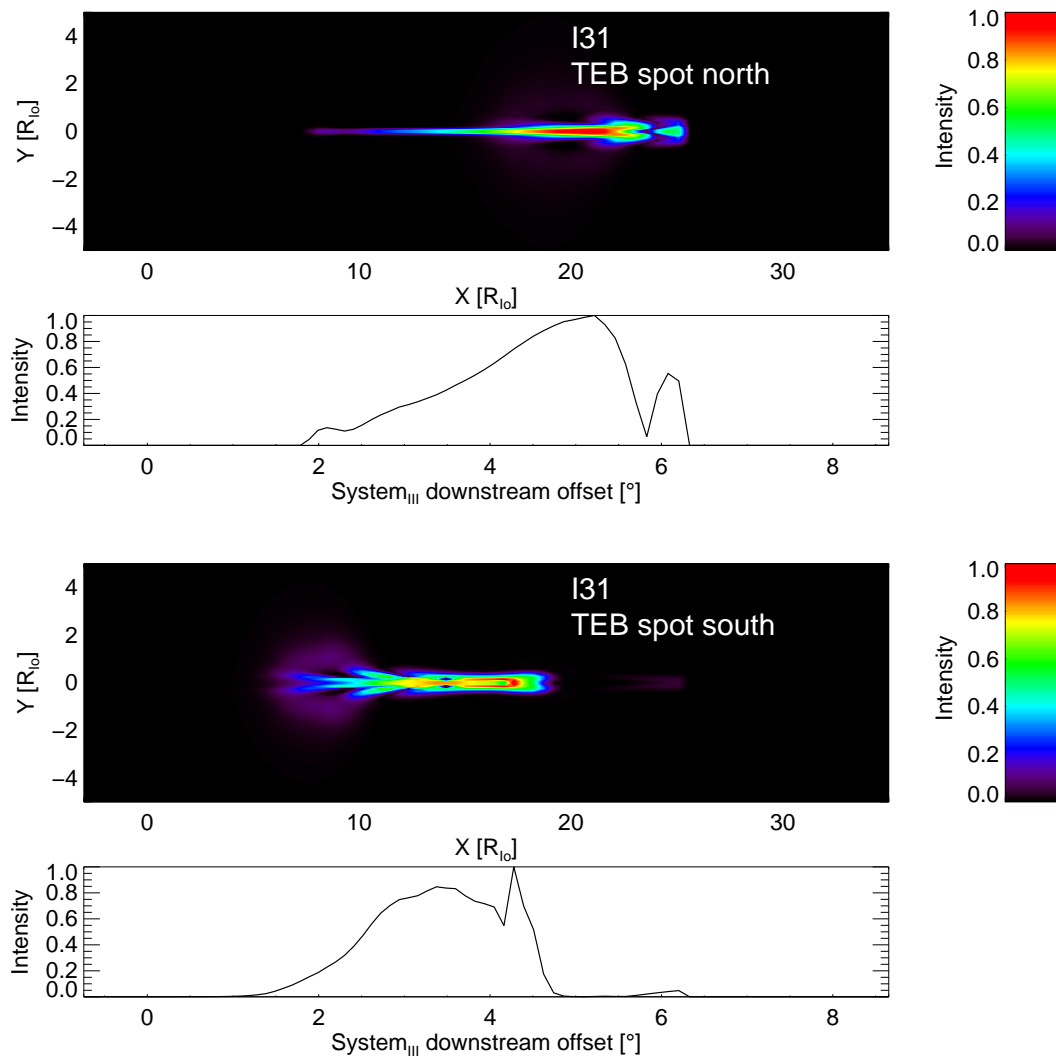


Figure 6.22: Same as Figure 6.21 but data produced by simulations without resistive AAR layer.

6.6 Inter-Spot Distances

6.6.1 Estimates Derived From the Travel Time Model

Before we present the results of our simulations concerning the inter-spot distances, we will try to obtain an estimated offsets for the RAW and TEB spots with respect to the MAW footprint from our travel time model. Other than lead angle predictions [e.g. *Bagenal, 1994*] this has not been done before. We will moreover validate our travel time model by comparison with observational data. Finally we will evaluate our simulation results in this context.

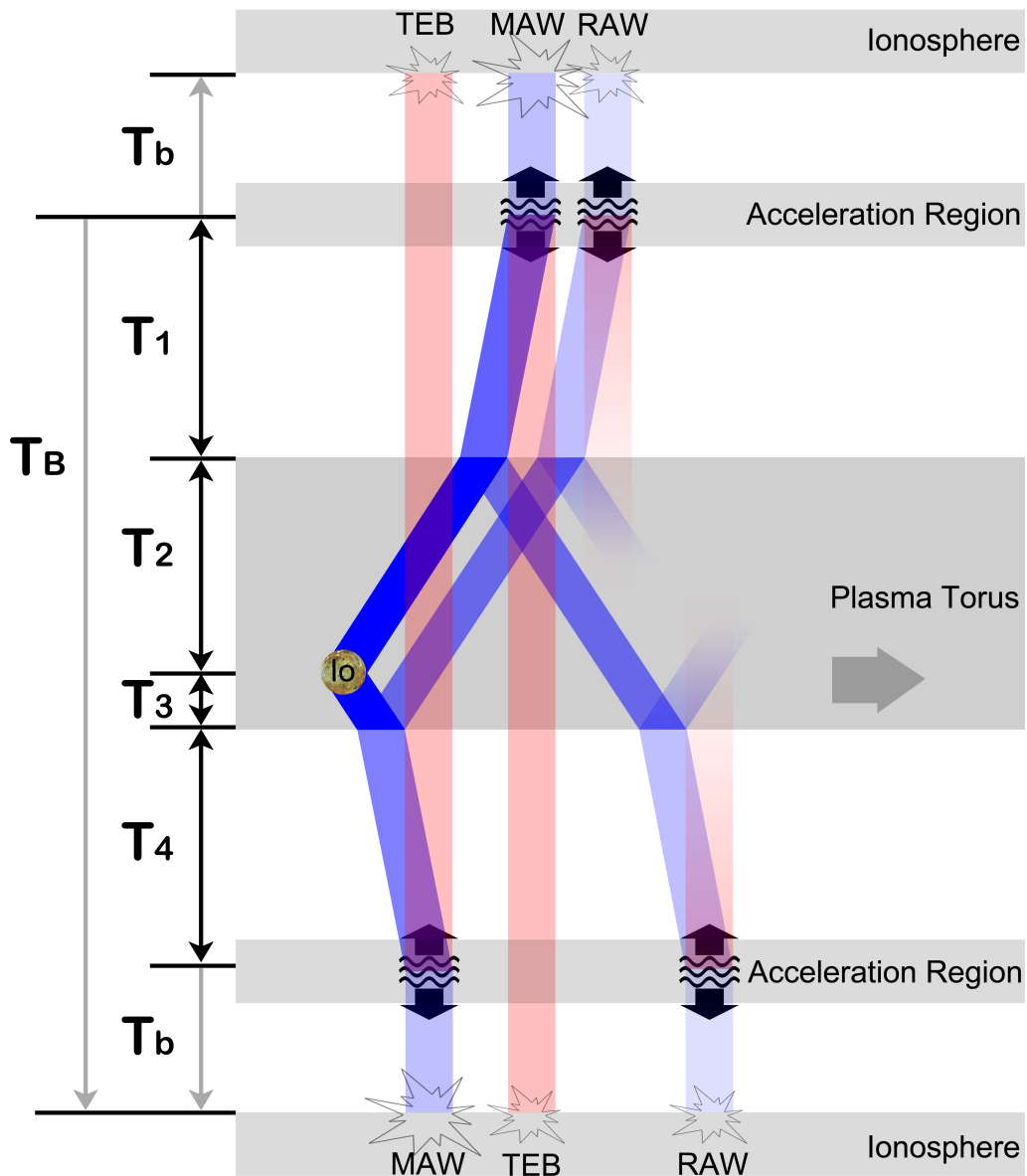


Figure 6.23: Schematic view of reflections and notation of different travel time constituents.

Figure 6.23 shows the different constituents of the over-all travel time between the northern and southern ionosphere. A wave generated at Io would use T_2 to reach the torus boundary and then T_1 to continue to the northern Jovian AAR. A south-

ward propagating wave would take T_3 and T_4 , respectively, to get to the southern AAR. We term the beam travel times t_b for planetward acceleration and T_B for the trans-hemispheric beam. Based on these constituents, we can derive integrated travel times for the waves that generate auroral footprints. The subscripts N, S denote the footprints in the north and south, respectively.

$$\begin{aligned}
\text{MAW footprints: } T_{MAW,N} &= T_2 + T_1 + T_b & (6.1) \\
& T_{MAW,S} &= T_3 + T_4 + T_b \\
\text{RAW footprints: } T_{RAW,N} &= T_3 + T_3 + T_2 + T_1 + T_b \\
& T_{RAW,S} &= T_2 + T_2 + T_3 + T_4 + T_b \\
\text{TEB footprints: } T_{TEB,N} &= T_3 + T_4 + T_B \\
& T_{TEB,S} &= T_2 + T_1 + T_B
\end{aligned}$$

As the beam travel times are small compared to the other travel times [Jacobsen *et al.*, 2010], we can easily neglect these. Thus we can determine the travel time differences:

$$\begin{aligned}
\text{MAW} \leftrightarrow \text{RAW: } \Delta T_{MR,N} &= 2T_3 & (6.2) \\
& \Delta T_{MR,S} &= 2T_2 \\
\text{MAW} \leftrightarrow \text{TEB: } \Delta T_{MT,N} &= (T_3 + T_4) - (T_2 + T_1) \\
& \Delta T_{MT,S} &= (T_2 + T_1) - (T_3 + T_4) \\
\text{TEB} \leftrightarrow \text{RAW: } \Delta T_{TR,N} &= T_3 + T_2 + T_1 - T_4 \\
& \Delta T_{TR,S} &= T_2 + T_3 + T_4 - T_1 .
\end{aligned}$$

We can further assume, that the travel time outside the torus is similar for both hemispheres ($T_1 \approx T_4$). Test with our density model have shown, that in our simulations the strongest reflections occur at the outermost part of the torus and thus the out-torus travel time is generally small compared to the in-torus travel time

$$\begin{aligned}
T_2 + T_1 &\approx T_2 & := T_N & (6.3) \\
T_3 + T_4 &\approx T_3 & := T_S
\end{aligned}$$

Thus we obtain only one travel time for each hemisphere: T_N for the north and T_S for the south.

It should be noted that we do not have a single and sharp reflection interface but a gradual reflection. Moreover the reflection coefficient depends on the perpendicular wavelength k_\perp and thus the location of the strongest reflection also is a function of k_\perp . Consequently, there is no unique torus reflection boundary as we presume in this idealized concept illustrated in Figure 6.23 and the assumption 6.3 might not be valid for all generated waves. However, the vast majority of models agrees that reflection occurs at large distances from Io. As we merely want to obtain a rough estimate of the travel time difference, we will use the approximation in Equation 6.3 and continue.

The travel time difference can now be expressed as:

$$\begin{aligned}
 \text{MAW} \leftrightarrow \text{RAW: } \Delta T_{MR,N} &= 2T_S & (6.4) \\
 &\Delta T_{MR,S} &= 2T_N \\
 \text{MAW} \leftrightarrow \text{TEB: } \Delta T_{MT,N} &= T_S - T_N \\
 &\Delta T_{MT,S} &= T_N - T_S \\
 \text{TEB} \leftrightarrow \text{RAW: } \Delta T_{TR,N} &= T_S + T_N \\
 &\Delta T_{TR,S} &= T_N + T_S
 \end{aligned}$$

Our combined plasma density and magnetic field model yields the northern and southern travel times (see Figure 5.9) and we can thus calculate the differences given in Equation 6.4. Since the magnetic field is rotating with Jupiter, the travel time difference is directly related to a difference in longitude. We obtain the latter by conversion:

$$\Delta\lambda_{III} = \Omega \cdot \Delta T \quad (6.5)$$

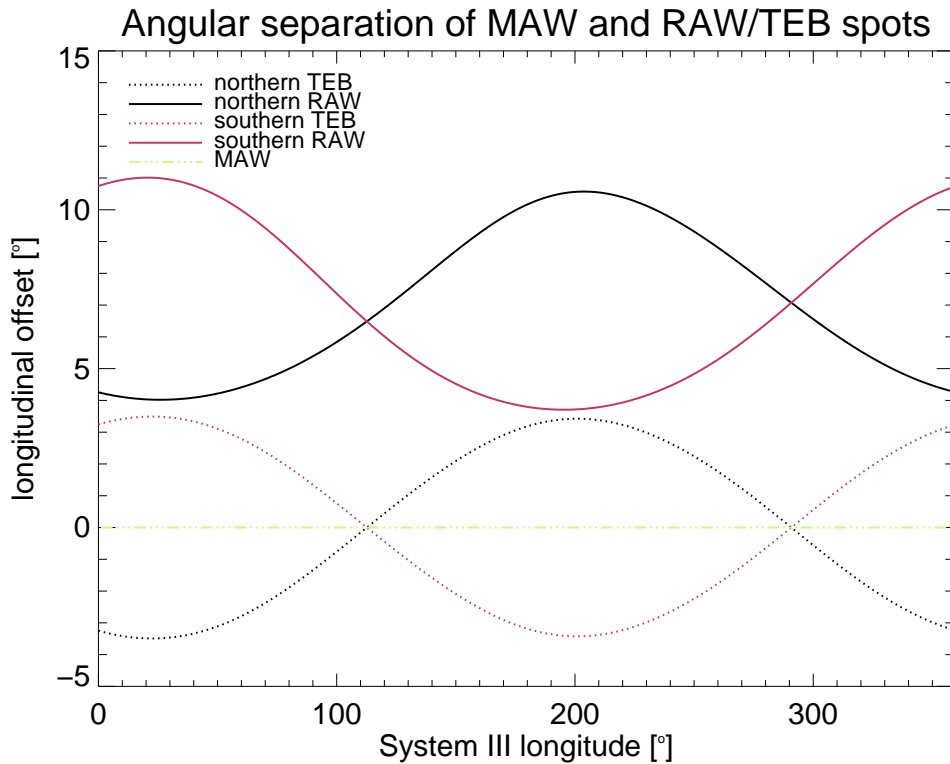


Figure 6.24: Estimated inter-spot angular separation between the MAW spot and the TEB and RAW spots for both hemispheres.

We notice that this assumption only holds for fully corotating plasma and thus a at most weakly disturbed plasma velocity field in the area downstream of the interaction and the main Alfvén wing. Moreover, in the method we apply, we implicitly map the TEB along undisturbed field lines (cf. Figure 6.23). Thus, this approach only provides good estimates for weak/linear interaction. On the other hand we

can make use of this limitation. If we compare the travel time model predictions and the observations we can estimate the importance of nonlinear effects. In a second step we can also test whether our MHD simulations including nonlinear processes provide better agreement with the observations than the linear travel time model.

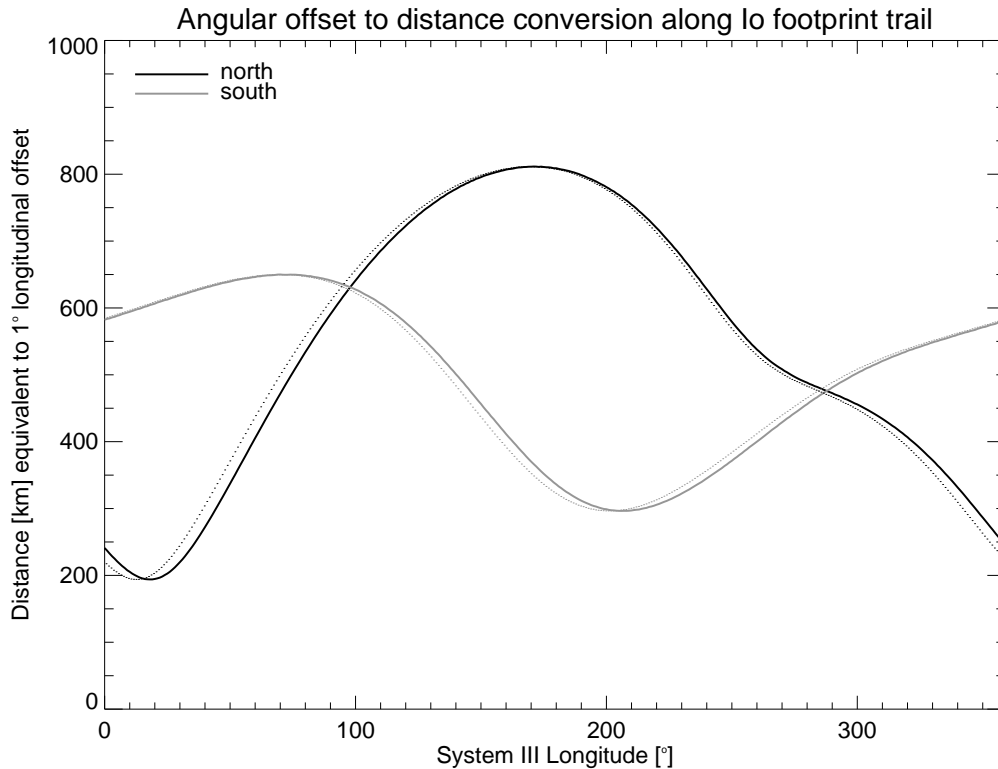


Figure 6.25: Conversion between angular separation and distance along the Io footprint track derived from the VIP4 magnetic field model. Dotted curves represent the conversion when taking into account the lead angle of the MAW with respect to Io's longitude.

6.6.2 Comparison with Observations

Figure 2.18 taken from *Bonfond et al.* [2009] shows the observations of the inter-spot distances in kilometers. To compare our estimates given in longitudinal offset we demand a conversion. As the VIP4 magnetic model yields also the latitudes of the footprint track¹ (cf. Figure 2.13), we can use spherical geometry and convert the System III offset to kilometers for a given longitude. The result is illustrated in Figure 6.25. Following the principle of obtaining an estimate for the inter-spot distances we do not take geometric flattening into account but approximate Jupiter by a perfect sphere. Also, the distances given in Figure 6.25 correspond to one degree along the circle of latitude calculated for Io's longitude not exactly along the footprint path. However, an inspection of Figure 2.13 reveals a small change in latitude for the typical longitudinal footprint separation of usually below 10° (Figure 6.24).

¹In fact the VIP4 model was optimized for the latitudinal footprint mapping [Connerney *et al.*, 1998].

Thus also the effect of the lead angle of the MAW spot with respect to Io's longitude is small for the conversion. This is represented by the dotted curves in Figure 2.13. With these tools at hand we can convert the angular offset derived from our travel time model to distances as used by *Bonfond et al.* [2009].

The result is shown in Figure 6.26. The star symbols mark locations of TEB footprint observations and the grey diamonds represent observed spots identified as RAW signatures. The solid line denotes our estimate for the TEB location, and the dotted line the one we infer for the RAW spot.

First of all, we note that due to the variation of the conversion factor along the Io footprint track (Figure 6.25) the sinusoidal character of the estimated angular separation (Figure 6.24) is not transferred to the prediction of the inter-spot distances in kilometers. This is a fundamental difference to indications by *Bonfond et al.* [2009] (cf. Figure 2.18). Our assessment of the TEB locations fits the observations well in both hemispheres and mostly within error margins of the observations. However, the agreement between predicted and observed RAW locations is much worse. In combination, these two points provide valuable information. We will extract it in the subsequent paragraphs.

Equations 6.4 indicate that the TEB offsets correspond either to the northern or southern Alfvénic travel times T_N and T_S . We recall that it is only valid for linear interaction. Due to the good reproduction of the observations, we might conclude that our travel time model is reasonable and that the magnetic field distortion is weak or almost symmetric for both hemispheres. If this was true and our model gives realistic travel times, we would also expect the RAW spot predictions to match the observations, as these are based on a linear combination of T_S and T_N (Equations 6.4). This is not the case. We hypothesize that this is due to nonlinear effects in the region downstream of the Alfvén wing. These have a greater impact on the RAW than on the TEB feature, as the integrated Alfvén wave travel path in this case is much longer than the one we anticipate for the TEB spot. Nonlinear processes decrease the inter-spot distances and eventually merge the different footprint to one (see sections 2.7.2 and 6.3). Hence, the dotted lines in Figure 6.26 constitute rather an upper limit for the RAW locations as they represent the ideal linear scenario of the interaction. Indeed, the vast majority of the observed locations are below the upper limit. We find runaway values (around $\lambda_{III}=130^\circ$ and $\lambda_{III}=240^\circ$) outside the margin given by our curve. However, these occur in a range of System III longitude, where other observations exist and the extreme values appear exceptional. This might be due to temporal torus density variations or these spots might be contributed to reflections of higher order.

We can further hypothesize that the discrepancy between the curve and the observations is modulated by Io's position in the torus as it is related to the importance of nonlinear effects. In the previous sections 6.2 and 6.3 we concluded that nonlinear effects are strongest when Io resides near the torus center and weakest when Io is located at the torus edge. Thus the disagreement in Figure 6.26 between our prediction curve and the RAW observations should be greatest near System III longitudes of $\lambda_{III}=112^\circ$ and $\lambda_{III}=292^\circ$. The consistency should be better near System III longitudes of $\lambda_{III}=22^\circ$ and $\lambda_{III}=202^\circ$. If we moreover take into account the length of the travel path through the disturbed medium, we can also differentiate between the latter two System III longitudes. We would expect the agreement to be best for $\lambda_{III}=202^\circ$ for the southern RAW spot and for $\lambda_{III}=22^\circ$ for the northern RAW spot.

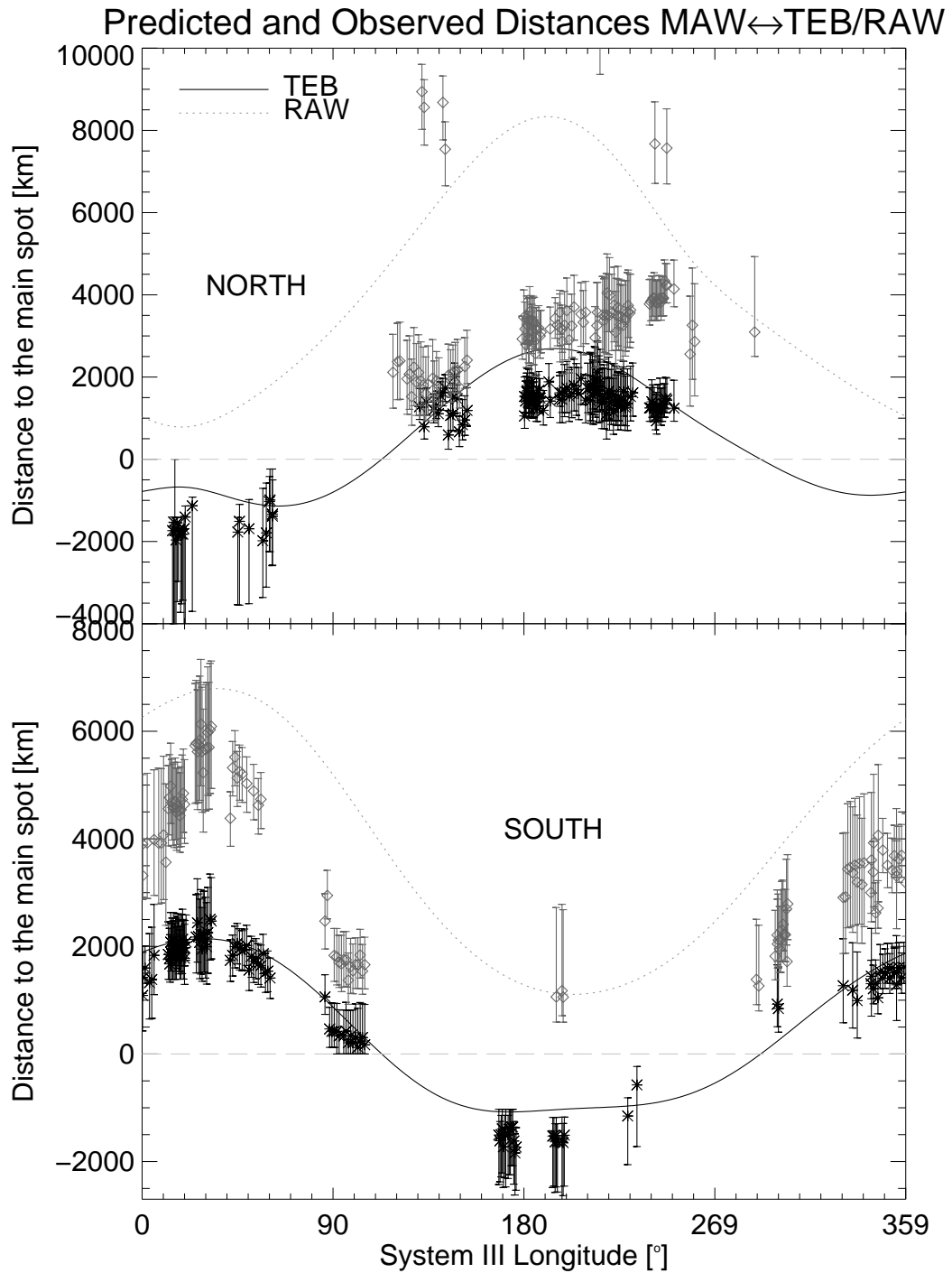


Figure 6.26: Same as Figure 2.18 but with over-plotted estimates for footprint separation derived from our travel time model. Solid line denoted estimated TEB offset and dotted line represents the predicted RAW dislocation.

However, the data density is too sparse to finally conclude whether this hypothesis holds and future observations should be examined concerning this matter.

6.6.3 Comparison with Simulation Results

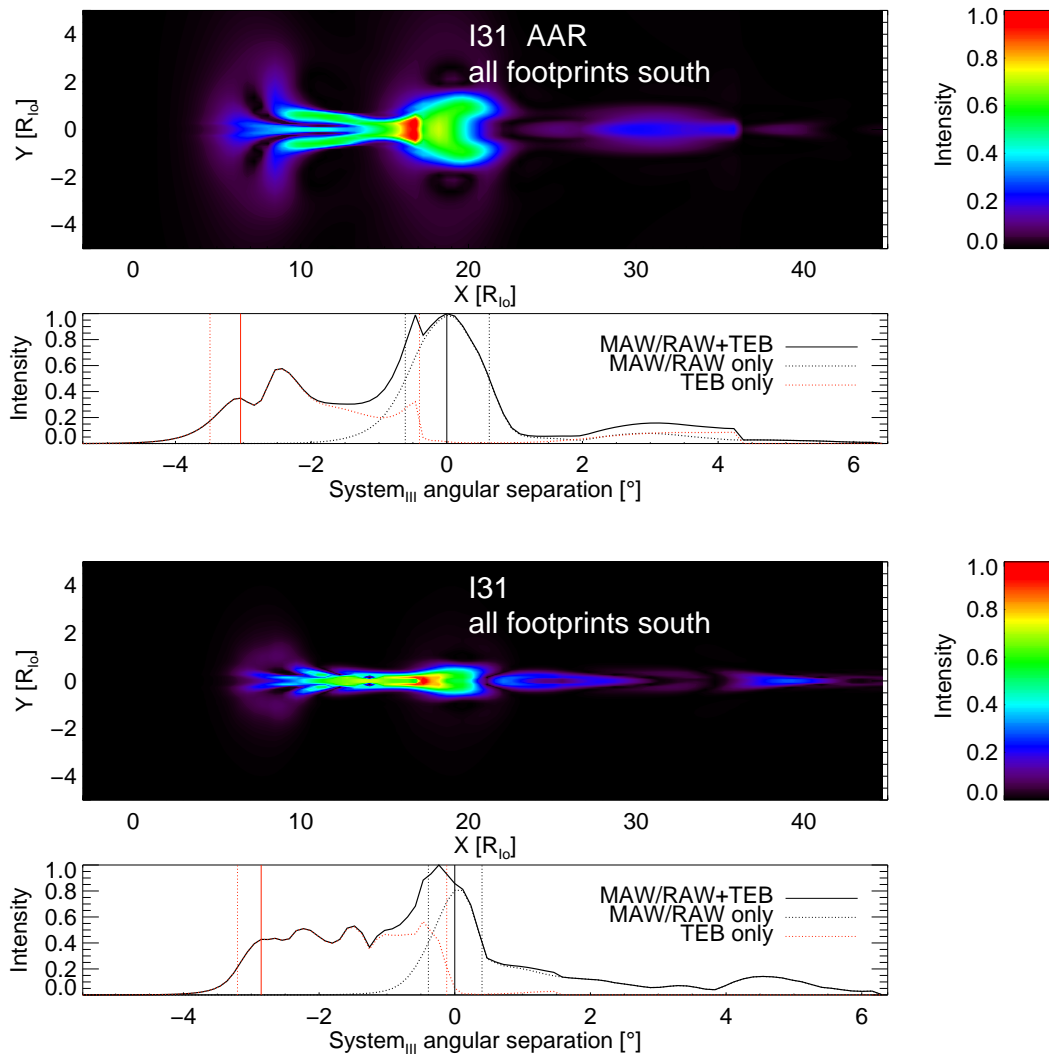


Figure 6.27: Estimated auroral emission for Galileo I31 flyby in the southern ionosphere. First panel: Color contours of the summation of Alfvén wing (MAW and RAW) and TEB footprint intensity. Second panel: Y-integrated profiles of emission intensities normalized to the maximum intensity of the summation of MAW/RAW and TEB emissions (solid line). Dotted curves represent isolated MAW/RAW intensity (black) and TEB intensity (red). Angular offset is calculated relative to MAW intensity maximum marked by vertical solid line. Dotted vertical lines represent 50% levels of the maximum MAW intensity. Third and fourth panel: Same as first and second panel but for the southern ionosphere.

Now we will relate our simulations results to the observations and the travel time model estimates. We obtain the TEB footprint morphology with the methods described in the previous section. However, we lack a concept for the relative intensity of the TEB morphology with respect to the Alfvén wing footprint intensity. In absence of models predicting the ratio of energy transferred to the AAR and the energy of the beam that finally reaches the conjugate ionosphere, we use a straight forward approach. We simply add the Poynting flux density of the Alfvén wings

and the one mapped of the mapped trans hemispheric beams. We are not intending to give a realistic footprint emission intensity profile with all details, but our aim is to identify local maxima and extract the angular offset with respect to the main maximum.

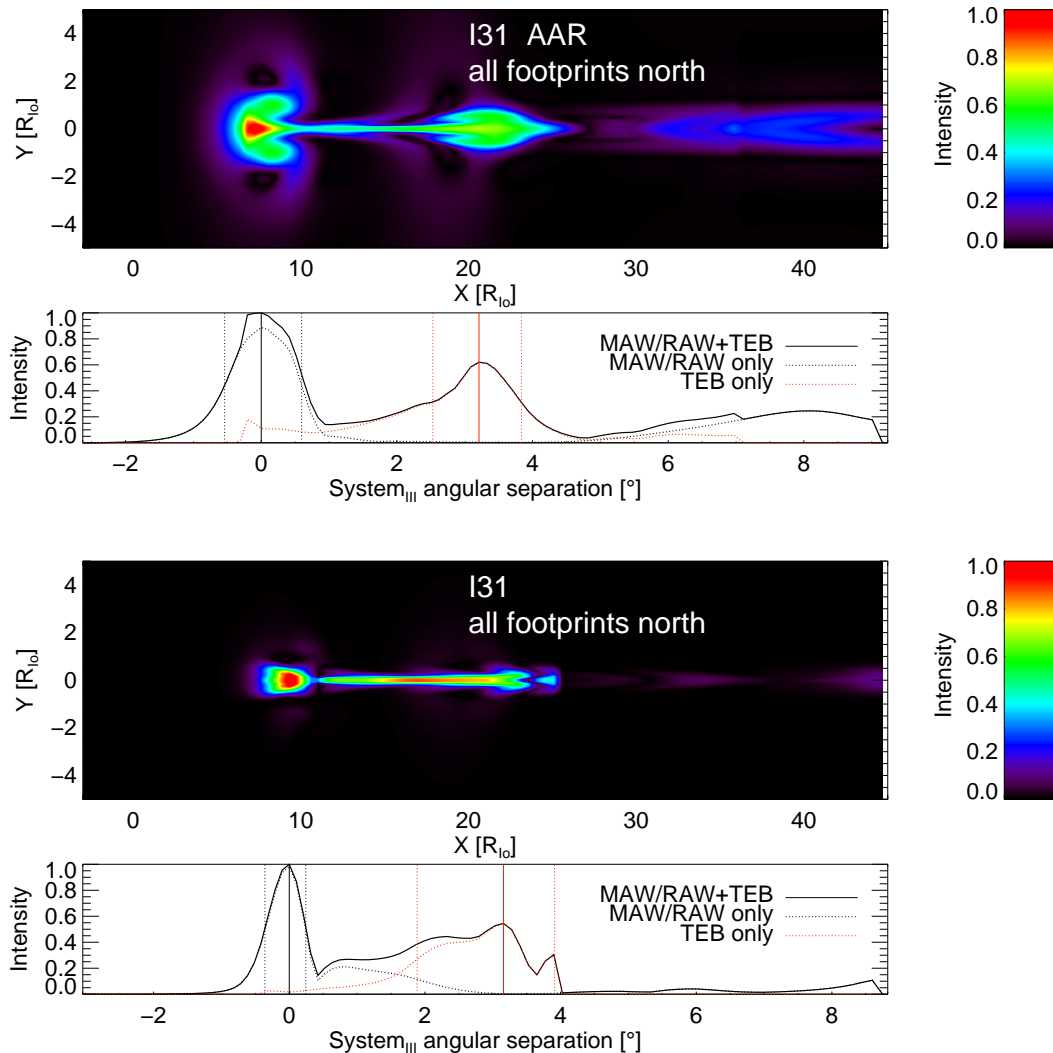


Figure 6.28: Same as Figure 6.27 but for the northern ionosphere.

In sections 6.3 and 6.5 we have seen that the footprint and beam generation morphology is also highly structured in the y -direction. We find different locations for local maxima depending on the y -coordinate we use for our profile along the x -direction. Thus there is not a unique downstream offset we can assign to a local maximum owing to the variation in the y -direction. In the genuine observational geometry, the y -direction corresponds to the latitudinal sense. Also for observations the identification of structures in the latitudinal direction is challenging. First, the bunching of magnetic field lines when approaching the polar regions maps the equatorial interaction region around Io of roughly $3 R_{Io}$ to an area with a width of only a few hundred kilometers in latitude. In this small domain, the resolution of lateral features is difficult. Secondly, the observation geometry is not normal to the ionospheric boundary. The values obtained are always line-of-sight

integrated. Although correction algorithms are applied to reconstruct the source of the emission, it is challenging to get information in the latitudinal direction.

We will thus integrate the Poynting flux density along the y -direction. This is a simple but reasonable approach to a line-of-sight integration and gives unambiguous values for the emission maxima locations. The result for the Galileo I31 flyby scenario is displayed in Figure 6.27 for the northern and southern hemisphere.

The second and fourth panel represent the angular offset we infer for the TEB and RAW features with respect to the MAW spot. The zero value is adjusted to match the location of maximum MAW intensity. We note, that this location does not necessarily coincide with the total intensity maximum due to TEB addition. As the contribution factors are only a rough estimate, we will use the pure MAW intensity to determine the zero offset value and the pure TEB profile to obtain the location of the beam maximum. However, the rating of the TEB maximum in our data is a difficult undertaking. We could either interpret the most upstream local maximum as leading spot or alternatively the total max of the TEB intensity represented by the dashed curve in panel two in Figure 6.27. The total max yields an upstream offset of -2.5° while the first local maximum suggests an angular separation of -3.2° . The situation is worse for the simulation setup including ionospheric reflections, as the local maxima are less pronounced and the intensity retains an almost constant level over a large distance (dashed red curve in panel four of Figure 6.27). Furthermore, as we do not know the quantitative criteria that were applied in the classification of the HST footprint observations, we can neither synchronize our method to it. Hence we will determine the total max of the TEB intensity and use 50% levels as errors.

The quantitative assessment of the RAW locations is likewise difficult. Thus we manually extract the RAW angular separation. Values are thus to be interpreted carefully.

In Figure 6.29 we display the angular separation of the TEB spot with respect to the MAW footprint. The solid lines represent the estimation derived from our travel time model, black and grey symbols correspond to data values by *Bonfond et al.* [2009] (see Figure 6.26) converted to angular offset. Colored symbols denote our simulation results for the different flybys with and without resistive layer reflections. We note that our travel time prognosis fits the observations particularly well, especially for the trailing spot. The agreement is slightly better for the southern TEB than for the northern beam spot. We observe a small systematic underestimation of the leading spot offset. Our simulation results compare likewise well to the predictions, mostly within the error margins, corresponding to the 50% intensity levels (cf. Figure 6.27). Consistency in Figure 6.29 between simulations with AAR reflections and those with ionospheric reflections seems to be slightly larger for the trailing spot. The leading spot offsets are larger for the simulation setup with a resistive layer (red x-symbols compared to diamond symbols). However, the number of simulations is small and within error margins there is no convincing discrepancy between ionospheric and AAR reflection runs for the TEB spot position. In summary owing to the good agreement, we assume that our travel time model yields good estimates for the northern and southern Alfvénic travel times T_N and T_S and thus the TEB offset. Furthermore, the simulations reproduce the observed offsets reasonably well. We observe no substantial differences caused by the nature of the reflector.

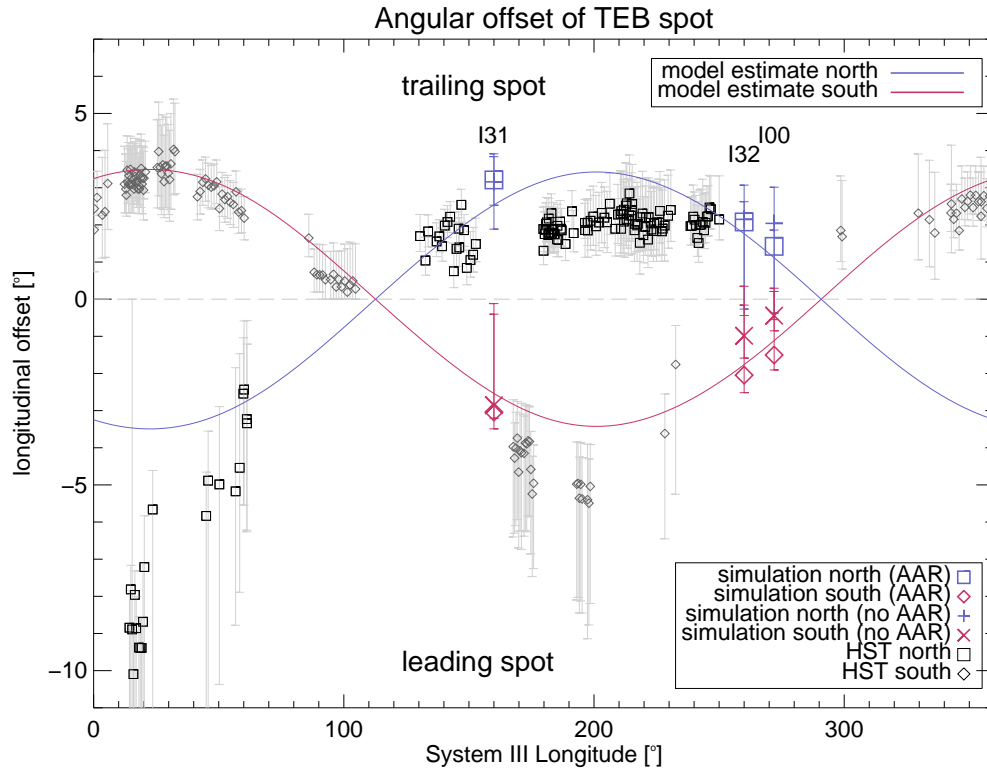


Figure 6.29: Angular separation of the TEB spot offset against system III longitude. We use blue color for the northern and red for the southern hemisphere. Solid lines represent the predictions derived from our travel time model. Black and grey symbols correspond to HST observations by Bonfond et al. [2009]. Colored symbols show our simulation results (see legend for details).

We present the angular separation of the RAW spot with respect to the MAW footprint in Figure 6.30. Lines and symbols correspond to the designation used in Figure 6.29. We note that the consistency between our RAW locations prediction based on travel time estimation is worse than for the TEB locations. This is to some extent expected as the solid curves represent the ideal linear reflection scenario and are thus to be interpreted as upper limits for the offset. In fact, the vast majority of the observed and also all simulated RAW footprint locations is below this upper limit. Concerning our simulation results we observe larger influence of the nature of the reflector (AAR or ionospheric reflections). For the southern RAW spot, the simulation runs without resistive layer reflections (red x-symbols) yield larger angular offsets. This can most likely be attributed to the concentration of reflections in the near downstream region for AAR reflections reported in section 6.3. However, this does not apply for the northern RAW spot location for the simulated flyby scenarios judging from the data points in Figure 6.30. Yet one has to keep in mind, that the identification of the RAW spots in our data is delicate. For instance in panel 4 of Figure 6.27 one might identify a structure at an offset beyond 8° as traces of another maximum which might correspond to the maximum around 8° in panel 2. In this case the discrepancy for the I31 runs would be smaller and the basic understanding of compressed morphology we infer for nonlinear AAR reflections in section 6.3 would also apply here. Hence, due to uncertainty of RAW spot identification

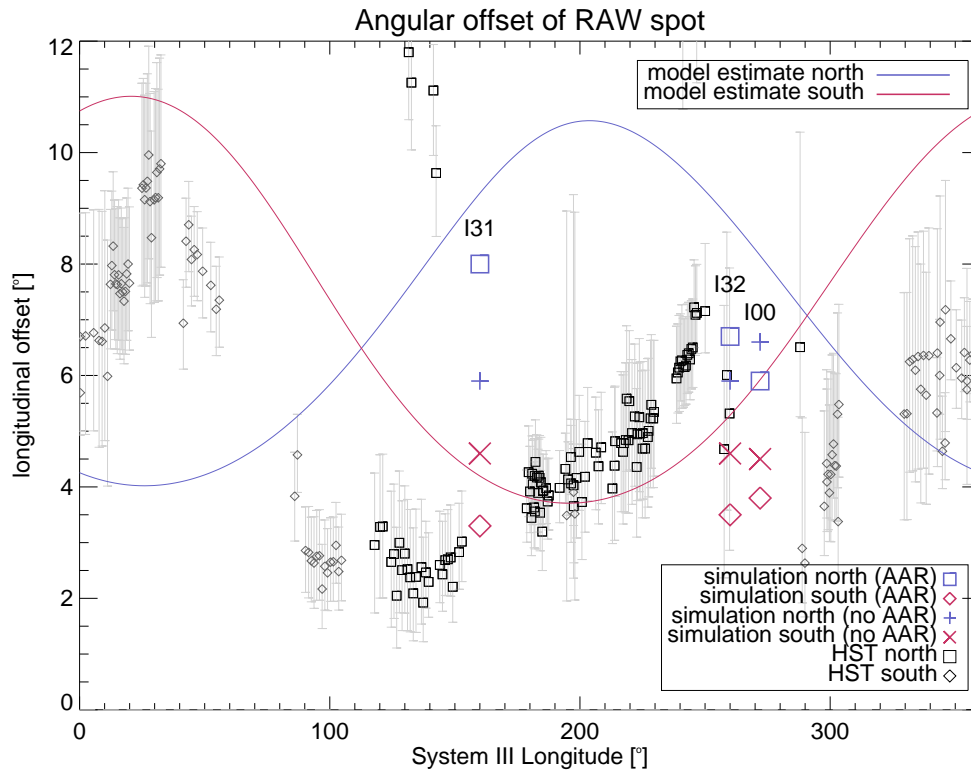


Figure 6.30: Same as Figure 6.29 but for RAW spot offsets.

we need to interpret our findings carefully. Yet, we note one important point. As we use the travel time model for the RAW offset estimates on the one hand and for the dimensioning of our simulation box on the other hand, we can identify nonlinear effects as cause for the lower deviation of RAW footprint locations with respect to the predictions.

Chapter 7

Enceladus

In this section we will discuss possible Alfvén wave reflections occurring at Enceladus. We will evaluate different direct and indirect indications of reflections in the observations and finally compare our simulation results to the measurements.

7.1 Hints for Alfvén Wave Reflections

There is evidence that Alfvén wave reflection occurs at Enceladus. Indirectly, the observation of electron beams [Pryor *et al.*, 2011], either in the form of precipitating electrons that cause auroral emission, or in the form of trans-hemispheric electron beams verifies the existence of an AAR. We have seen that reflections can occur at such a boundary.

However, there are direct observations that suggest the existence of Alfvén wave reflection at Enceladus. On the *Cassini E4* flyby, not only energetic electron beams were detected downstream of Enceladus [Pryor *et al.*, 2011], but also a positive B_x component of the magnetic field perturbation in the corotational wake [e.g. Jia *et al.*, 2010a]. The MAG data is shown in Figure 7.1.

The large scale structure can be divided into three major parts:

- *Region A*: A negative ΔB_x near closest approach and associated with the central region of the northern Alfvén wing.
- *Region B*: A positive ΔB_x located at $4 \lesssim x \lesssim 16R_E$ downstream and $5 \lesssim z \lesssim 28R_E$ north of Enceladus.
- *Region C*: A negative ΔB_x further downstream located at $16 \lesssim x \lesssim 30R_E$ downstream and $28 \lesssim z \lesssim 55R_E$ north of Enceladus.

We suggest that aforesaid distortion of the magnetic field in positive x -direction (*Region B*) represents the signature of a reflected Alfvén wave in the corotational wake of Enceladus. This structure has not been associated with Alfvén wave reflection before.

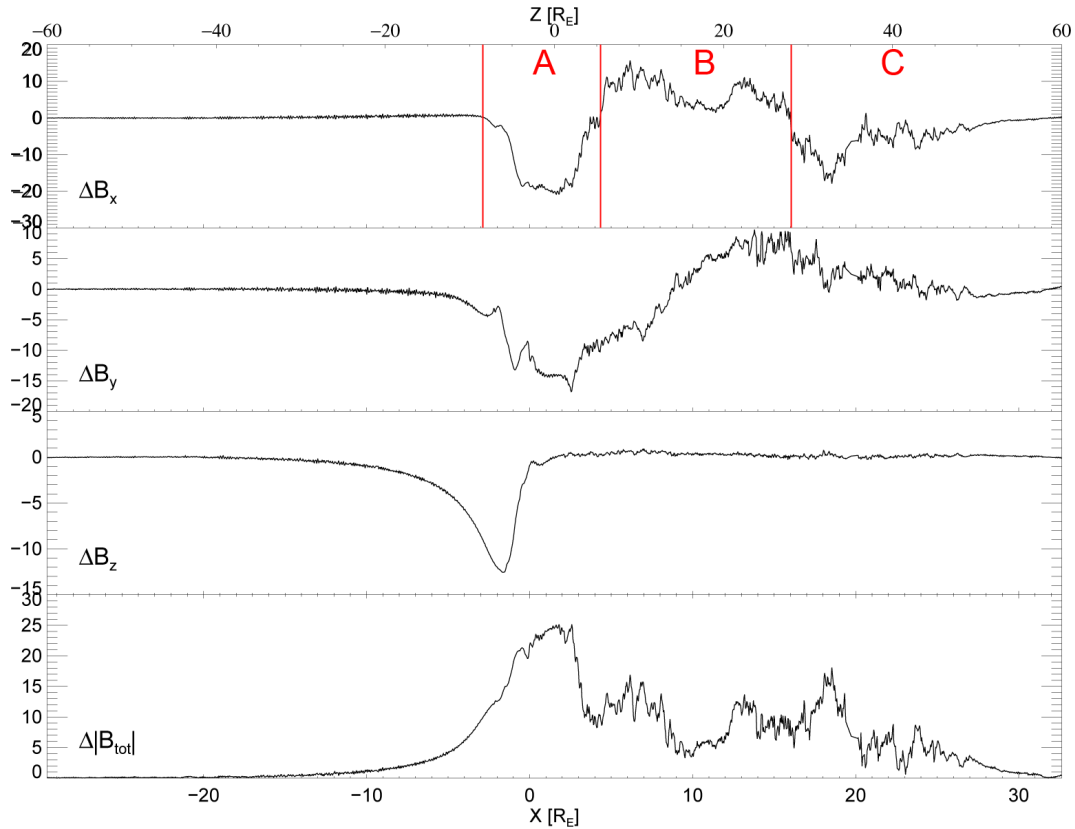


Figure 7.1: Detrended magnetic field data during *E4* flyby.

The *E4* trajectory was orientated basically in the north-south direction. It is displayed in Figure 7.2. For the central northern wing we in general expect a perturbation in the opposite sense (i.e. negative ΔB_x). However, a positive B_x perturbation can be found on the flanks of the wing. Yet, the structure is located at considerable distance downstream of Enceladus and thus we suggest that it represents the signature of a reflected Alfvén wave instead of being associated with the primary Alfvén wing. It is moreover too far north to be related to a direct interaction with the plume and the amplitude. We note that *Farrell et al.* [2010] propose a dust population extending up to 20 R_E north of Enceladus that they conclude to interact with the plasma in the form of deceleration. This would presumably cause also a negative B_x perturbation and thus we do not hold this effect responsible for the magnetic field distortion observed in Region B.

Based on our studies so far, we deduce that - if related to Alfvén wave reflection - the sign of the perturbation can be explained by two different reflection scenarios. On the one hand, it can be the signature of a reflected wave that reverted the magnetic field perturbation upon reflection from the north which is indicative of negative plasma density gradient or AAR reflections. On the other hand, the positive B_x perturbation can be caused by a reflected wave from the south with conserved sign of magnetic field, representative of ionospheric reflections.

Before we discuss the possible reflection at the different boundaries, we note that two other flybys (*E5* and *E6*) with almost identical trajectory (see Figure 7.2) did not exhibit a substantial B_x perturbation in the wake. A comparison of the data of

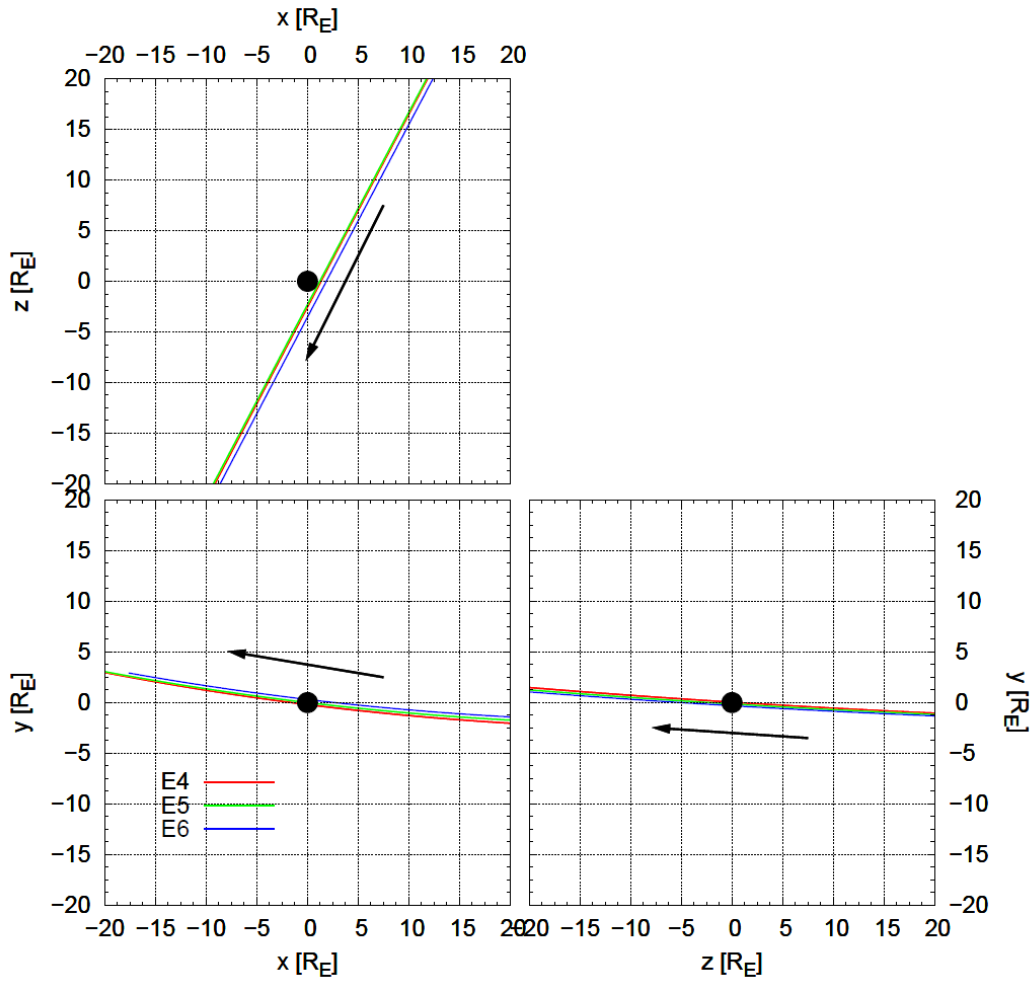


Figure 7.2: Projections of Cassini E4-E6 trajectories.

all three flybys with similar geometry is given in Figure 7.3. (It contains also the data of *E3*. We will not address this flyby.)

While the B_x component during *E5* flyby does not show any perturbation at some R_E downstream, the *E6* measurements demonstrate a low positive B_x perturbation. The maximum perturbation in the wing was ~ 28 nT for *E5* and ~ 19 nT for *E4* and *E6*. Superficially, this fact suggests that the interaction was stronger for the *E5* flyby, but the magnitude of ΔB_x has to be weighted with the squareroot of the ambient plasma density. The RPWS experiment measurements show that the upstream electron density was roughly a factor of two higher for *E5* compared to *E4* and *E6*. The values are taken from *Jia et al.* [2010b]. Table 7.2 is an excerpt from this paper. The comparison of the maximum magnetic field perturbations between *E5* and *E6* and the plasma density ratio yields

$$\frac{28nT}{19nT} = 1.47 \sim \sqrt{2} = \sqrt{\frac{n_e(E5)}{n_e(E6)}}. \quad (7.1)$$

We notice that the increased magnetic field perturbation can be roughly explained by the higher plasma density only and thus we do not need to assume stronger interaction for the *E5* flyby.

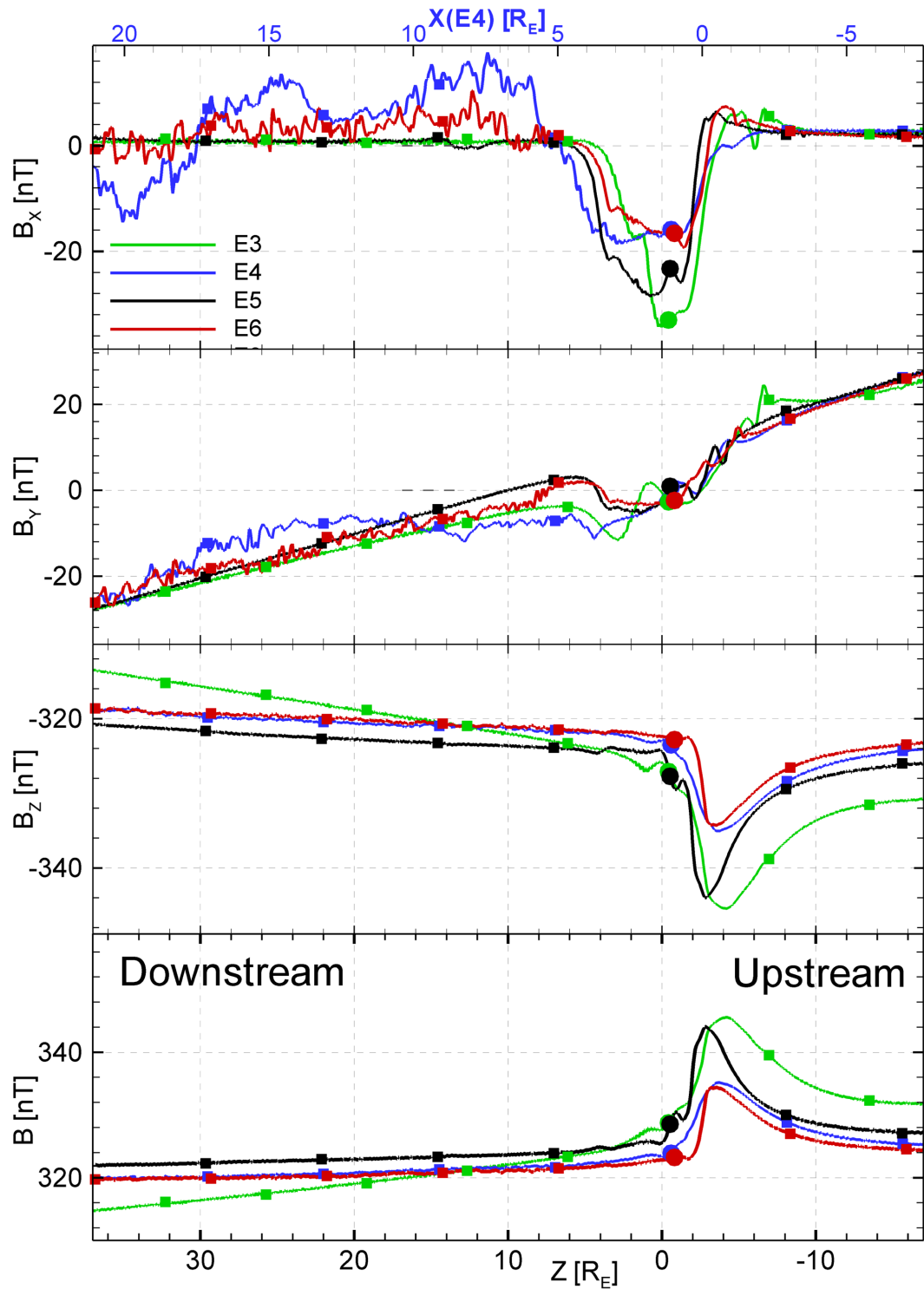


Figure 7.3: Comparison of magnetic field measurements of E3-E6 flybys [after Jia et al., 2010b].

Besides the measured electron density, the authors provide values used in their simulations that produced the best agreement with the *Cassini Magnetometer* (MAG) observations. While the plume production rate is similar for all flybys, the momentum-loading rate is much higher for E5. While the latter quantities are not directly

| Flyby | E4 | E5 | E6 |
|--|------------|------------|------------|
| Date | 08/11/2008 | 10/09/2008 | 10/31/2008 |
| Closest Approach [R_E] | 1.2 | 1.1 | 1.8 |
| Plume gas production rate [10^{28} s^{-1}] | 2.4 | 2.6 | 2.6 |
| Plume gas production rate [kg s^{-1}] | 680 | 740 | 740 |
| Momentum-loading rate [kg s^{-1}] | 0.8 | 1.3 | 0.9 |
| Upstream density [cm^{-3}] | 55 | 90 | 45 |

Table 7.1: Excerpt from Jia et al. [2010b]

| M_A | $E6$ $n_e=45 \text{ cm}^{-3}$ | $E4$ $n_e=55 \text{ cm}^{-3}$ | $E5$ $n_e=90 \text{ cm}^{-3}$ |
|-------------------------|----------------------------------|----------------------------------|----------------------------------|
| $V_0=26.4 \text{ km/s}$ | 0.104 | 0.115 | 0.147 |
| $V_0=16.7 \text{ km/s}$ | 0.066 | 0.073 | 0.093 |

proven by observations but deduced from numerical experiments, they need to be interpreted carefully. Nonetheless, we subsume that the upstream plasma density was larger for the *E5* flyby compared to *E4* and *E6*, while the interaction strength was similar or enhanced for *E5*. In the latter case, the absence of downstream magnetic field perturbations during *E5* could be attributed to a saturated interaction, eventually resulting in a current loop configuration. In this case the magnetic field is perfectly aligned with the Alfvén wing axis and the incident and reflected waves would be confined to the wing. For a background magnetic field aligned with the z -axis ($B_0 \parallel e_z$) we estimate whether the alignment by determining the Alfvén angle or the Alfvén Mach number by

$$\tan(\theta_A) = \frac{V_0}{V_A} = \frac{B_x}{B_z} = M_A. \quad (7.2)$$

We consider two concepts for V_0 : One represents full corotation leading to a relative velocity of $V_0=26.4 \text{ km/s}$, the other is based on Wilson et al. [2009], who report that the plasma at Enceladus' orbit is sub-corotating by 25%, which leads to a value of $V_0=16.7 \text{ km/s}$.

We notice that in the case of fully corotating plasma, the value of the observed maximum magnetic field perturbation for the *E5* flyby is considerably smaller than needed for saturation. For sub-corotating plasma the measured perturbation on the *E5* pass of $\sim 28 \text{ nT}$ is close to the saturation value of 30 nT . However, the values for *E4* and *E6* are likewise close to saturation. Thus we lack an explanation why in

| $\Delta B_{x,\text{max}}$ | $E6$ $n_e=45 \text{ cm}^{-3}$ | $E4$ $n_e=55 \text{ cm}^{-3}$ | $E5$ $n_e=90 \text{ cm}^{-3}$ |
|------------------------------------|----------------------------------|----------------------------------|----------------------------------|
| $V_0=26.4 \text{ km/s}$ | 34 nT | 37 nT | 48 nT |
| $V_0=16.7 \text{ km/s}$ | 21 nT | 24 nT | 30 nT |
| observed $\Delta B_{x,\text{max}}$ | $\sim 19 \text{ nT}$ | $\sim 19 \text{ nT}$ | $\sim 28 \text{ nT}$ |

one case we observe a configuration best explained by a current loop and in two comparable cases we observe detached reflections.

If the existence or non-existence of reflections in the wake can not be ascribed to the properties of the initial wave generator, it might be related to the attributes of the reflector. Hence, we now discuss the possible reflection boundaries in this regard.

The ionospheric boundary is not likely to exhibit considerable temporal changes that would affect the return wave amplitude in a way that the reflections are literally turned off. Although the sign of southern ionospheric reflections corresponds to the observed positive ΔB_x , we will thus rather inspect the two remainder reflection boundary types. The negative plasma density gradient along the propagation path of the Alfvén waves leads to partial reflections. Similar to the Io scenario, the density profile can be approximated by a scaleheight model [Persoon *et al.*, 2006]. The gradient then only depends on the scaleheight value, but not on the initial equatorial value. Thus if the scaleheight does not undergo major changes on the time scale of months, we would expect reflections to be comparably intense for all the three flybys under debate. Moreover, the Alfvén phase velocity gradient is smooth compared to the one assumed for the Io torus. Persoon *et al.* [2006] report a scaleheight of $\sim 0.5 R_S$ (cf. Figure 2 in Persoon *et al.* [2006]). We carried out numerical experiments with that value and did not observe notable reflections. We also used the lower value of 0.39 inferred from the error bar provided by the authors and obtain similarly weak (i.e. non-detectable) reflections. However, as described in section 5.2.5 we are only able to follow the genuine Alfvén velocity profile along the field line for plasma densities above a chosen threshold. Yet, the location where the threshold is reached is close to Saturn’s ionosphere. If reflections occur beyond this point, they are thus mistakable with reflections from the AAR, as these display the same change of sign behaviour. Unless the “torus” scaleheight near Enceladus is subject to major fluctuation on the time scale of months, we can conclude that reflections caused by a negative plasma density gradient do not likely contribute significantly to the magnetic field signature observed in Enceladus’ wake. The remainder reflector, the AAR, has been indirectly confirmed by observations energetic electron beams from the north during the *E4* flyby and moreover by northern auroral footprint observations [Pryor *et al.*, 2011]. Furthermore, the positive sign of the downstream magnetic field perturbation is consistent with reflections originating from the northern AAR. As the AAR represents a potential drop, that is proportional to the current density (see section 4.3) [Knight, 1973], we could anticipate, that the effectiveness of the AAR as a reflector is also related to the current density. In this sense it constitutes a variable reflection boundary depending on the incident current density topology and magnitude.

Regardless of the exact reason for a possible variability of the AAR as electron accelerator and wave reflector, this conception is consistent with the large number of non-detections of footprints and the observation of just a single TEB event. It could also account for the observed substantial differences in the magnetic field perturbation between almost identical flybys. We identify the AAR as the most probable transient reflector, as reflections due to plasma depletion along the wave propagation path are most likely weak and ionospheric reflection coefficients do presumably not display large variation on the timescale of months. However, the amount of data is sparse to finally conclude and we note that there might be other explanations for the positive B_x component. Nonetheless our aim is to investigate the role

| Flyby | E4 | E5 | E6 |
|--|------------|------------|------------|
| Date | 08/11/2008 | 10/09/2008 | 10/31/2008 |
| Closest Approach [R_E] | 1.2 | 1.1 | 1.8 |
| Plume gas production rate [10^{28} s^{-1}] | 2.4 | 2.6 | 2.6 |
| Plume gas production rate [kg s^{-1}] | 680 | 740 | 740 |
| Momentum-loading rate [kg s^{-1}] | 0.8 | 1.3 | 0.9 |
| Upstream density [cm^{-3}] | 55 | 90 | 45 |

Table 7.2: *Enceladus flyby parameters. Excerpt from Jia et al. [2010b]*

of Alfvén wave reflections in global M-I coupling and thus having weighted all the factors we will use a resistive layer as reflector in our numerical simulations. We will present the results in the following paragraphs.

7.2 Magnetic Field Data

For the simulations of the Enceladus interaction we use a homogeneous, constant background plasma density. We do this on the one hand because a density depletion along the magnetic field did not lead to significant reflections in test runs. On the other hand, a high plasma density decreases the computational resources needed. The value for the plasma density corresponds to an electron density of $n_e=55 \text{ cm}^{-3}$ in accordance to the *E4* RPWS measurements. We chose the box dimensions such that the one-way travel time of the Alfvén wave is 120 s which is the value we obtain using the density model by *Persoon et al. [2006]* with the lowest scaleheight within the given errors. The plume is located below $z=1 R_E$. It is represented by a 3 dimensional Gaussian peak in the effective collision frequency ν . It extends over $4 R_E$ in x- and y-direction, and $10 R_E$ in z-direction.

We note that a conversion of the trajectory data was necessary for the comparison between *Cassini* MAG observations and our modelled results. As the z-axis in the Enceladus interaction system (ENIS; the coordinate system in which the trajectory is provided) is aligned with Saturn’s rotational axis, it is not located in a fixed L-shell due to field line bending. By contrast, in our geometry with unbended magnetic field lines, the z-axis of our simulation is located on Enceladus’ L-Shell. In fact the y-coordinate is a measure for the L-Shell difference with respect to Enceladus orbit and the x-z plane at $y=0$ represents Enceladus’ L-shell. To remedy this discrepancy, we transform the ENIS trajectory coordinates to the corresponding values in our coordinate system. Therefore we calculate the L-shell for each point of the spacecraft trajectory in the ENIS system and find the corresponding y-value on our simulation grid. This method is necessary because we interpret the data at high z-values, where this effect is not negligible. The difference between the two trajectories is illustrated in the bottom panel of Figure 7.4. The solid line represents our correction, the dash-dotted line is the trajectory in ENIS. Figure 7.4 displays our simulation results. The top panel contains a comparison of the observed MAG B_x perturbation in black and our simulation data projected onto the spacecraft trajectory (red). Over all, we notice qualitative agreement in major aspects. Most importantly, our results display a positive ΔB_x in the wake (*Region B*), albeit it is located further

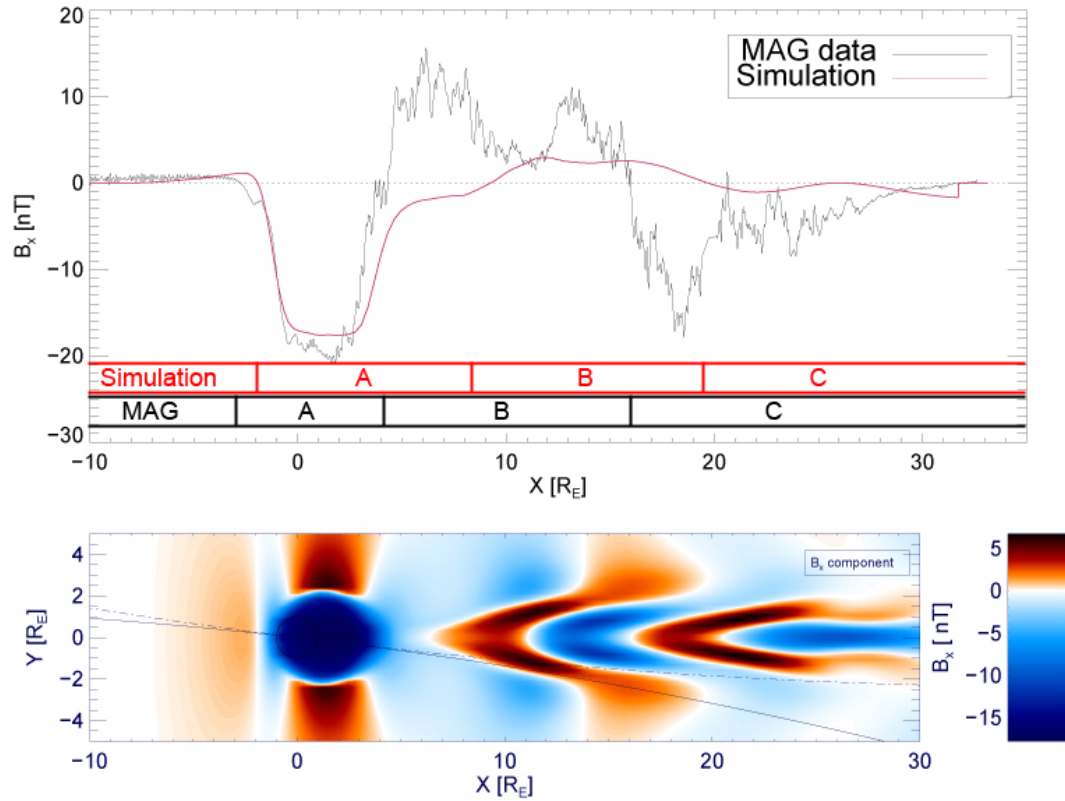


Figure 7.4: Top panel: Simulated (red) and observed (black) x -component of the magnetic field. (Region labels see text). Bottom panel: B_x component on the plane defined by spacecraft velocity vector and y -direction. Solid line: adapted trajectory; Dash-dotted line: ENIS trajectory.

downstream than in the magnetometer data and the perturbation is considerably weaker. Moreover, our results roughly match the MAG Alfvén wing signature (Region A) in both, amplitude and extent. We also find a weak equivalent to Region C in our data, although it does neither exactly match amplitude nor location. However, the intention is not the perfect numerical reproduction of the observations, but to obtain hints whether the magnetic signature observed on the *E4* flyby can be attributed to Alfvén wave reflections. The bottom panel of Figure 7.4 shows the B_x component in the plane defined by the y -direction and the spacecraft velocity vector. As the direction of the latter is not constant the plot represents a curved plane and it is obtained by combining y -profiles through our data volume at each trajectory point. This presentation illustrates how pensive the profile we display in the top panel is. The use of the original ENIS trajectory for instance would have yielded a considerably different profile. Also a variation of the plume dimensions in y -direction have certainly an impact on the measured B_x profile. Nonetheless, we note that based on our simulation a spacecraft moving predominantly in the corotational direction would measure a positive B_x perturbation in the wake.

7.3 Equatorial Electron Beams

A paper presently in press by *Pryor et al.* [2011] reports the detection of a highly energetic field aligned electron population during the *E4* flyby. We thus use our model to infer the location of a electron beam on the spacecraft trajectory. We use the simulation described above and apply the method we used for the determination of the equatorial electron beam morphology at Io. However, we do not track the magnetic field lines we use for the beam mapping to the equatorial plane, but to the plane defined by the y -direction and the spacecraft velocity vector as used in the bottom panel of Figure 7.4. By applying this method, we account for the high inclination of the spacecraft trajectory with respect to the equatorial plane. *Pryor et al.* [2011] detect the field aligned electrons at distances between $3.6 R_E$ and $23 R_E$ downstream of Enceladus. They report that the energy “flickers” between two levels of 1 eV and 1 keV. They observe the high energy electrons only at distances between $\sim 8 R_E$ and $\sim 16 R_E$.

We display our simulation result in Figure 7.5. We obtain an electron beam located in Enceladus’ corotational wake and detached from the satellite. This qualitatively agrees with *Pryor et al.* [2011]. Quantitatively, the beam extends from $\sim 5 R_E$ to $\sim 14 R_E$. Thus the total beam extent is too small in our numerical results. Nonetheless, the length corresponds to the extent of the observed high energy part of the beam. If we thus relate the positions of the high energy beam and our simulated beam morphology, the detected beam is displaced only $3 R_E$ downstream. However, we note that the spacecraft trajectory does not penetrate the beam area over the full length. We note that in this case the simulate beam is too far upstream, whereas the magnetic field signatures were located too far downstream. However, the set of initial parameters we need for our simulations is weakly determines. As we did not carry out extensive parameter studies, we, at this point, would like to stress, that we simulate a beam detached at some distance from Enceladus in accordance with the observations, which is a qualitative difference to the Io observations, so far.

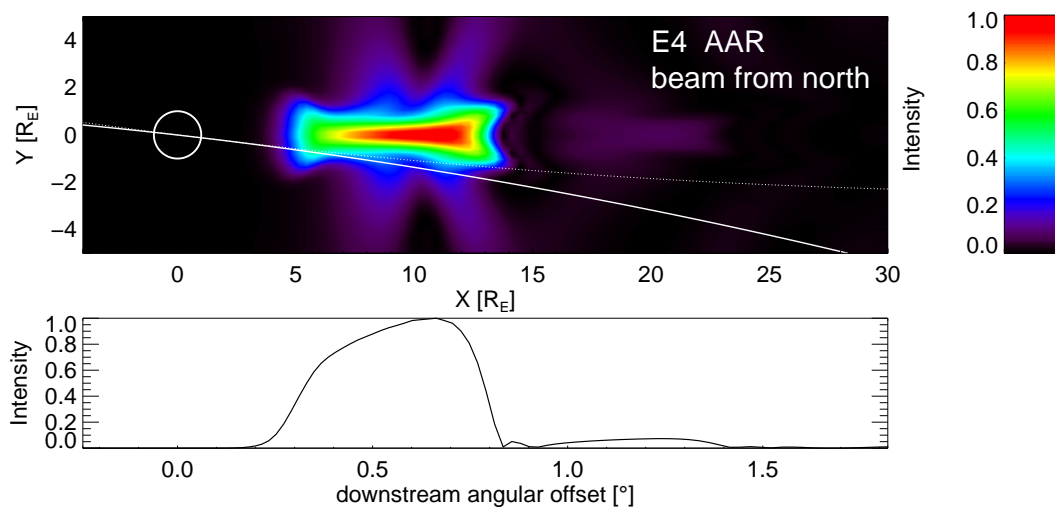


Figure 7.5: Beam intensity deduced from our simulation data for the *E4* flyby scenario. Solid line: Adapted Cassini trajectory. Dash-dotted line: Original ENIS trajectory

Chapter 8

Conclusions

In the thesis at hand we present results of our numerical MHD simulations of Io's interaction with the Jovian magnetospheric plasma. Our model is hitherto the only model that simulates self-consistently the magnetohydrodynamic wave field in three dimensions and for all plasma regimes located along the full length of a magnetic field line. This encloses the generator region and the torus plasma, the depleted plasma at high latitudes and the dense Jovian ionospheric plasma. Moreover, we incorporated a resistive layer in our simulation domain, that represents the auroral acceleration region.

In summary, the numerical model we developed in the course of our studies seems to be well suitable to investigate the electromagnetic interaction between a satellite and its parent planet. We applied the model to two scenarios so far and obtained results that were in qualitative agreement with the observations. The quantitative assessment of observational data is in most cases hampered by the idealizations implemented. However, these are necessary in order to simulate such a large domain with different plasma regimes with reasonable computational resources. Yet, despite the idealizations we seem to have conserved the basic features that control the interaction on large scales. We now recapitulate the quintessences of our findings.

We apply our model in a basic setup with constant plasma densities for the different plasma regime representations to investigate the influence of the different interaction parameters on the morphology of the footprint pattern. By varying the effective collision frequency only, we are able to isolate the influence of the interaction strength on the footprint pattern as opposed to a variation of the ambient plasma density which would also affect the Alfvén angle and thus the reflection geometry. Our results exhibit merging of multiples in the footprint trail with increasing interaction strength which eventually results in a single elongated spot. Thus, we qualitatively confirm observational findings by *Gérard et al.* [2006] who report the disappearance of multiple spots when Io is located centermost in the torus. Moreover, our analysis of the Alfvén characteristics exposes the breakdown of the regular law of reflection for strong, i.e. nonlinear interaction which ultimately causes the aforementioned footprint elongation and merging. A comparison of results obtained with ionospheric reflections and results with reflections occurring at a re-

sistive layer does not demonstrate significant implications on the general footprint pattern. Nonetheless, a detailed look at the reflection pattern displays notable differences. Both reflectors differ in terms of changing the orientation of the perturbation upon wave reflection. While reflections at the ionospheric boundary reverses the sign of the incoming velocity perturbation, it is conserved during reflection at a resistive layer such as our representation of an AAR. For ionospheric reflections, the sub-corotating plasma in the Alfvén wing is super-corotating in the reflected wing. Conversely, AAR reflections create a reflected wing with likewise sub-corotating plasma. Finally, this leads to a compression of the wave pattern in the downstream region for AAR reflections, and an expansion for ionospheric reflections. As the waves are thus densely packed when we apply a resistive reflector, we expect more wave-wave interactions because of multiply superimposing reflections. This might lead to Alfvén wave filamentation for which *Chust et al.* [2005] find observational evidence.

We moreover apply our numerical tool to the modeling of field-aligned energetic electron beams measured near Io by the *Galileo* spacecraft. We note that we do neither have a representation for the beam generation mechanism nor the electron propagation in our model. Instead we use the Poynting flux density transferred to the acceleration region as a measure for the intensity of the generated beam. In a subsequent step we map this beam generation morphology along the distorted magnetic field to the equatorial plane and thus deduce the topological properties of the equatorial electron beams. In early stages of our model we used again a basic setup with section-wise constant plasma densities and obtain good agreement with the observations. These results have been published in *Jacobsen et al.* [2010]. However, this setup is less accurate in reproducing the beam onset in the corotational direction. The implementation of a more realistic Alfvén velocity profile in large parts of our simulation box greatly improves the agreement with the observations. We successfully obtain electron beams over Io's poles and observe a beam taper in the wake. This is in accordance with the *Galileo* data. We note that the use of both reflector types investigated in this thesis leads to similar results concerning the equatorial beam topology.

We apply the method used to determine the location of equatorial beams also to infer the location of the TEB spot from our simulation data. We obtain qualitative agreement with HST observations of the beam spot separation with respect to the main Alfvén wing spot published in *Bonfond et al.* [2009]. Thus we confirm that the TEB spot is most likely the auroral imprint of the equatorial electron beams observed in-situ by *Galileo*. This can not be explained with beams that follow essentially undisturbed magnetic field lines, but requires a substantial field line draping around Io. The fact that some field lines tracked from the beam generation region are connected to Io suggests that in part the coupling between the satellite and Jupiter could resemble a current loop configuration. However, most of the field lines penetrate the equatorial plane downstream of Io. Hence they are detached and do not couple to Io.

Independent of our MHD simulations, we present a model for the Alfvénic wave travel times. We use this model to derive travel time differences for the waves that generate the different auroral spots. We then convert these travel time differences to angular separation and thus obtain estimates for the offset of the TEB and RAW footprints with respect to the MAW spot. These need to be interpreted as

upper boundaries for the footprint separation as they are based on the assumption of regular wave reflections associated with linear interaction. We compare this prediction to the observations by *Bonfond et al.* [2009] and obtain a good correlation for the TEB spots in both hemispheres. The value of the observed RAW offsets is systematically smaller than our upper boundary. We attribute this fact to the large influence of nonlinear effects on the reflection geometry which we observed in our fundamental numerical studies. The TEB location, however, is apparently less affected by these effects and thus conforms with our linear estimates. Although the separation of the TEB spot is still influenced by model uncertainties, this value is the most promising to remotely detect long-term changes in the plasma torus content, as observed between the *Voyager* and the *Galileo* encounters.

Besides the estimates, we also relate our simulation results to the set of footprint observations and note qualitative agreement. When compared to our prediction, we observe likewise a systematically smaller RAW footprint offset in our simulation than expected from the linear estimate. As we use boundary conditions, that contain the same travel times which represent the basis for the linear estimates, we can contribute this effect to nonlinear reflection properties. The TEB positions obtained with our model agree with the prediction to a larger extent. However, the unambiguous identification of the single spots in our data is in some cases difficult and thus the results have to be interpreted carefully. Nonetheless, they exhibit the same tendency as the observations.

In the last part of this work, we applied our model to a different scenario. We investigated the possibility of Alfvén wave reflections occurring at Enceladus. Magnetic field measurements of the Alfvén wing by *Dougherty et al.* [2006] and the detection of an auroral spot on Saturn [*Pryor et al.*, 2011] suggest that the interaction is similar to Io's interrelation with Saturn. On the *Cassini E4* flyby a unique magnetic field signature was observed. We interpret this perturbation that occurred alongside with an energetic electron beam detection as possible signature of a reflected Alfvén wave - a feature not yet observed in-situ at Io. We use our numerical model to support our hypothesis and find a good agreement between the simulated magnetic field data and the observations. Moreover, we determine the electron beam location and compare it to the observations. The location basically conforms with the area where the highest energies of the field aligned electrons have been observed.

After all, it remains a puzzle, why the magnetic signature coincident with an electron beam has been observed on only one of three almost identical flybys. However, some parameters crucial for the modeling of the Enceladus interaction are weakly determined or are known to undergo considerable changes such as the plume activity and position as well as the ambient plasma density. This substantially modifies the interaction. We argue that apart from the variability of the Alfvén wave generator, the reflector properties could have changed between the flybys. The latter is most likely for an AAR reflector as the field-aligned potential drop is related to the local current density. We anticipate that the reflection coefficient is likewise correlated with the current density. Thus the acceleration and reflection properties of an AAR might exhibit considerable variability depending on the Alfvén wave current amplitude and topology. This would be in accordance with 282 non detections of the Enceladus footprint, as opposed to 3 detections. Moreover this could be one explanation for the single occurrence of the characteristic magnetic field signature

simultaneously observed with an energetic electron beam. However, this hypothesis needs to be further investigated. In this regard, a fruitful improvement to the present model would be the incorporation of a resistivity that is related to the local current density.

In summary, our model yields appreciably good results concerning the Io interaction. Especially the location of electron beams and the qualitative footprint morphology agree well with the observations. Moreover, our model seems versatile enough to be applied to other interaction systems without major changes.

Part IV

Apendix

8.1 Coordinate Systems Jupiter

8.1.1 System III

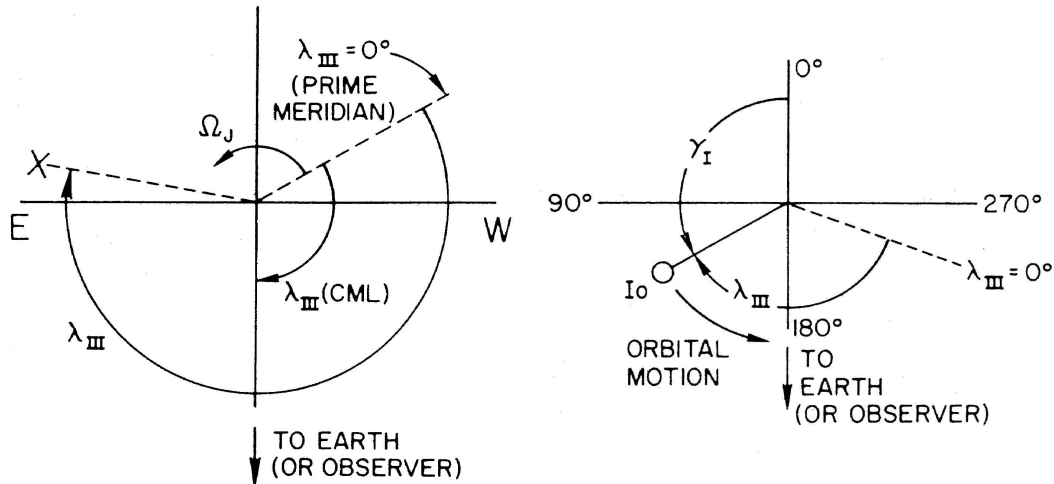


Figure 8.1: Illustration of the "System III" longitudinal reference system. A) Longitude is measured clockwise from prime meridian. Sub-earth longitude is called Central Meridian Longitude (CML). Jupiter rotates counter-clockwise with Ω_J . B) Io's phase angle γ_I is measured counter-clockwise from anti-CML meridian

Since Jupiter rotates differentially and does not possess a visible solid surface, it is difficult to find a clear convention for the zero meridian. While System I and System II were geared to certain unique cloud features and were valid for different ranges in latitude, System III was determined by the rotation rate derived from radio burst periodicity. The zero meridian was proclaimed the CML on January the 1st in 1957. Due to an error in the rotation period calculation, the original System III(1957) had a slip of $3^\circ/\text{a}$. This was corrected by a newer definition System III(1965). This has to be kept in mind when interpreting old data sets.

8.1.2 Latitudinal Reference Systems

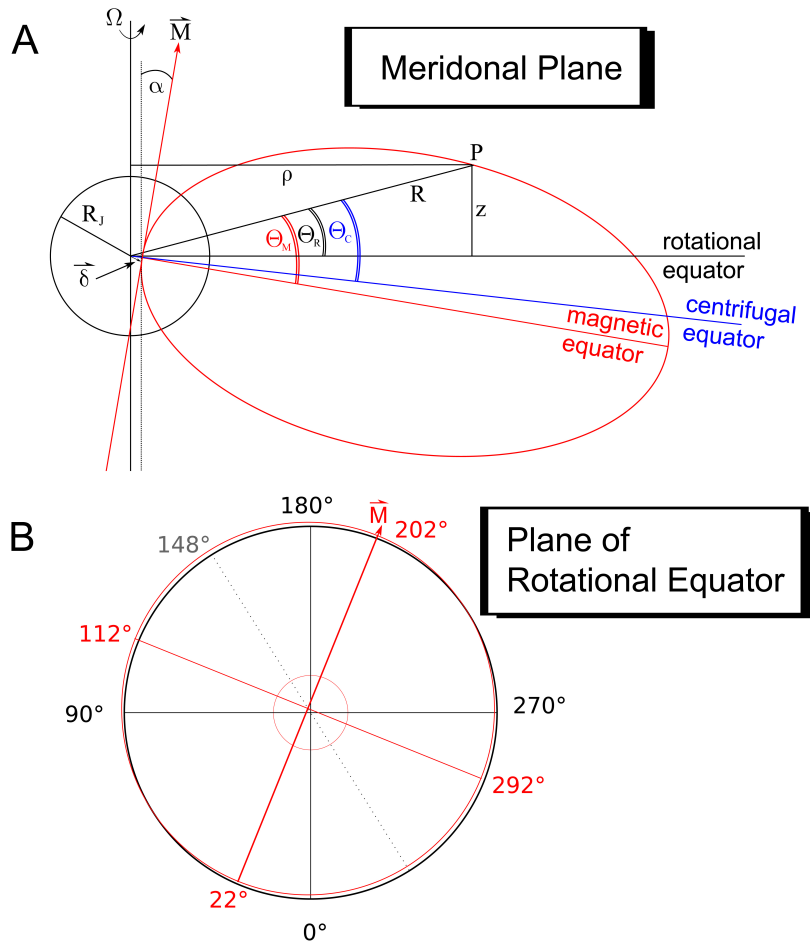


Figure 8.2: **A:** Side view of magnetic field topology (field line not to scale). Dipole offset by $0.131 R_J$: δ , magnetic dipole moment: \vec{M} , tilt of magnetic dipole moment: $\alpha=9.6^\circ$. Cylindrical coordinates of point P : distance from rotational axis: ρ , height above equator: z and System III longitude: λ_{III} . Angles: magnetic latitude: Θ_M , centrifugal latitude: Θ_C , rotational latitude: Θ_R . **B:** Top view with dipole offset towards $\lambda_{III} = 148^\circ$ and projected magnetic moment \vec{M} (after Bagenal [1983])

8.2 Code Modifications

Although highly time-consuming, especially due to the fact that ZEUS-MP is virtually undocumented, the bug fixes and code modifications are of little direct scientific use. Nonetheless, reproducibility of our results demands that we outline the code changes. Moreover and hopefully, future researchers will benefit from our experiences and apply their changes to the code more time efficiently. However, we will not provide a detailed citation of code lines, but simply mention where modifications were applied. Further details can be found in the comment lines we added to the ZEUS routines where they were changed.

Grid Generator

We modified the grid generator routine `ggen.F`. During initialization of the grid domains for the single cores index boundaries were overstepped. This bug was fixed.

Collisions

The implementation of collisions involved alteration of the routine `forces.F`. We included additional collision terms for all three components of the computed velocity to account for the modifications in the equation of motion. The additional term in the energy equation 4.29 was incorporated in the routine `pdv.F`. We appended a scalar field for the effective collision frequency to the `field` module in `mod_files.F`. We appended memory allocation for the field in `alloc_arrays.F`. The field is initialized in the central user problem routine.

Resistivity

We added a routine `resist.F`. It is called by routine `ct.F`, which was also changed. Due to operator splitting the calculation of the electromagnetic field (EMF) including resistivity effects needs to be calculated in several steps.

1. The 'usual' EMF is determined, then the magnetic field values are updated.
2. EMF resulting from resistivity is calculated and magnetic field values are updated again.

While the first part of the procedure is contained in the original `ct.F`, the second part was appended. Note: It is crucial to update the magnetic field values before carrying out step two as it needs the refreshed magnetic field.

Validation

A test scenario for the resistive term in the induction equation was developed. The initial state is a Gaussian two dimensional peak in the B_z -component in the x and

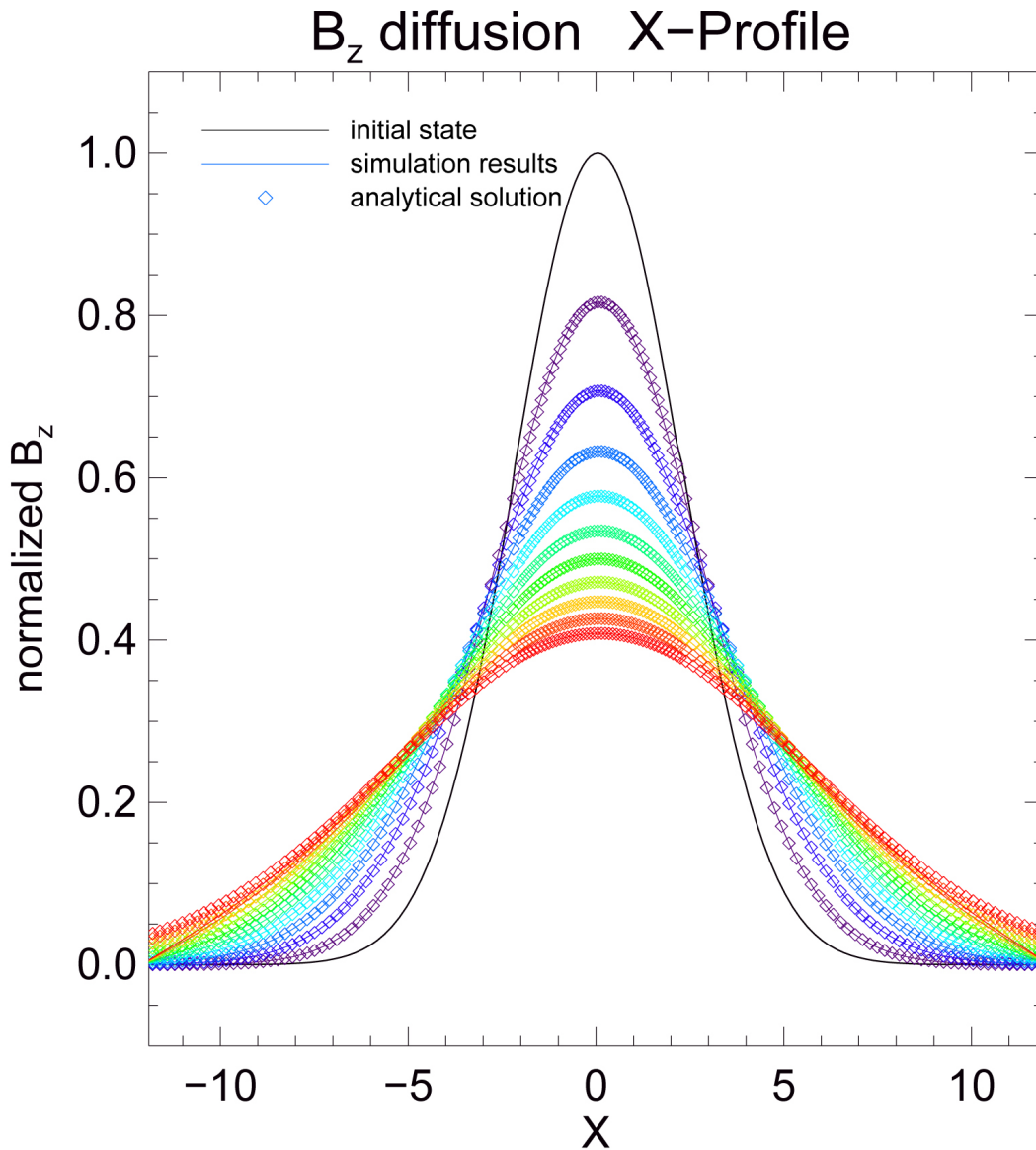


Figure 8.3: Test of resistivity term in the induction equation. Colors indicate temporal evolution. Black solid line shows the initial state, Lines signify the simulation result, diamond symbols represent the analytical solution. Red color indicates late times.

y direction. It is invariant along z . Plasma movement was prohibited to separate pure magnetic diffusion from plasma diffusion. The analytic solution is the easily obtained:

$$B_z(x, t) = \sqrt{\frac{t_0}{t}} \exp\left(-\frac{x^2}{4\eta t}\right) \quad (8.1)$$

Figure 8.3 displays a comparison of simulation results (diamond symbols) with the analytical solution (lines) for different timesteps. The solutions are identical within numerical errors at early times. At late times, the boundary conditions chosen prohibit magnetic diffusion out of the box. Thus the magnetic level near the boundaries in our simulation is higher than expected from the analytical approach. In the production runs, the diffusion coefficient is much smaller and box dimen-

sions larger, so that the effect is minor.

8.2.1 Time Step Size

The implementation of resistivity required modification of routines for the determination of the time step size `nudt.F` and `newdt.F`. As the diffusion time across the length Δx_i

$$\tau_d = \frac{(\Delta x_i)^2}{\eta} \quad (8.2)$$

can become smaller, than e.g. the characteristic time for e.g. the Alfvén wave given by

$$\tau_A = \frac{\Delta x_i}{V_A} \quad (8.3)$$

we needed to implement another time criterion to find the correct minimal characteristic time, which is then used to determine the numerical time step size.

Bibliography

- Bagenal, F.**, Alfvén wave propagation in the Io plasma torus, *Journal of Geophysical Research*, 88, 3013–3025, 1983.
- Bagenal, F.**, Empirical model of the Io plasma torus: Voyager measurements, *Journal of Geophysical Research*, 99, 11043–11062, 1994.
- Bagenal, F. and J. D. Sullivan**, Direct plasma measurements in the Io torus and inner magnetosphere of Jupiter, *Journal of Geophysical Research*, 86, 8447–8466, 1981.
- Baumjohann, W. and R. A. Treumann**, *Basic space plasma physics*, 1996.
- Bigg, E. K.**, Influence of the Satellite Io on Jupiter's Decametric Emission, *Nature*, 203, 1008–1010, 1964.
- Bonfond, B.**, The 3-D extent of the Io UV footprint on Jupiter, *Journal of Geophysical Research (Space Physics)*, 115, (A14), A09217, 2010.
- Bonfond, B., D. Grodent, J. Gérard, A. Radioti, J. Saur and S. Jacobsen**, UV Io footprint leading spot: A key feature for understanding the UV Io footprint multiplicity?, *Geophysical Research Letters*, 35, L05107, 2008.
- Bonfond, B., D. Grodent, J. Gérard, A. Radioti, V. Dols, P. A. Delamere and J. T. Clarke**, The Io UV footprint: Location, inter-spot distances and tail vertical extent, *Journal of Geophysical Research (Space Physics)*, 114, (A13), A07224, 2009.
- Borovsky, J. E.**, Auroral arc thicknesses as predicted by various theories, *Journal of Geophysical Research*, 98, 6101–6138, 1993.
- Bridge, H. S., J. W. Belcher, A. J. Lazarus, J. D. Sullivan, F. Bagenal, J. R. L. McNutt, K. W. Ogilvie, J. D. Scudder, E. D. Sittler and V. M. Vasyliunas**, Plasma observations near Jupiter - Initial results from Voyager 2, *Science*, 206, 972–976, 1979.
- Broadfoot, A. L., M. J. Belton, P. Z. Takacs, B. R. Sandel, D. E. Shemansky, J. B. Holberg, J. M. Ajello, H. W. Moos, S. K. Atreya, T. M. Donahue, J. L. Bertaux, J. E. Blamont, D. F. Strobel, J. C. McConnell, R. Goody, A. Dalgarno and M. B. McElroy**, Extreme ultraviolet observations from Voyager 1 encounter with Jupiter, *Science*, 204, 979–982, 1979.
- Brown, R. A. and J. F. H. Chaffee**, High-Resolution Spectra of Sodium Emission from IO, *The Astrophysical Journal*, 187, L125+, 1974.

- Burke, B. F. and K. L. Franklin**, Observations of a Variable Radio Source Associated with the Planet Jupiter, *Journal of Geophysical Research*, 60, 213–217, 1955.
- Burton, M. E., M. K. Dougherty and C. T. Russell**, Model of Saturn's internal planetary magnetic field based on Cassini observations, *Planetary and Space Science*, 57, 1706–1713, 2009.
- Carlson, C. W., J. P. McFadden, R. E. Ergun, M. Temerin, W. Peria, F. S. Mozer, D. M. Klumpar, E. G. Shelley, W. K. Peterson, E. Moebius, R. Elphic, R. Strangeway, C. Cattell and R. Pfaff**, FAST observations in the downward auroral current region: Energetic upgoing electron beams, parallel potential drops, and ion heating, *Geophysical Research Letters*, 25, 2017–2020, 1998.
- Chust, T., A. Roux, W. S. Kurth, D. A. Gurnett, M. G. Kivelson and K. K. Khurana**, Are Io's Alfvén wings filamented? Galileo observations, *Planetary and Space Science*, 53, 395–412, 2005.
- Clarke, J. T., G. E. Ballester, J. Trauger, R. Evans, J. E. P. Connerney, K. Stapelfeldt, D. Crisp, P. D. Feldman, C. J. Burrows, S. Casertano, I. J. S. Gallagher, R. E. Griffiths, J. J. Hester, J. G. Hoessel, J. A. Holtzman, J. E. Krist, V. Meadows, J. R. Mould, P. A. Scowen, A. M. Watson and J. A. Westphal**, Far-Ultraviolet Imaging of Jupiter's Aurora and the Io "Footprint", *Science*, 274, 404–409, 1996.
- Clarke, J. T., L. B. Jaffel and J. Gérard**, Hubble Space Telescope imaging of Jupiter's UV aurora during the Galileo orbiter mission, *Journal of Geophysical Research*, 103, 20217–20236, 1998.
- Clarke, J. T., J. Ajello, G. Ballester, L. Ben Jaffel, J. Connerney, J. Gérard, G. R. Gladstone, D. Grodent, W. Pryor, J. Trauger and J. H. Waite**, Ultraviolet emissions from the magnetic footprints of Io, Ganymede and Europa on Jupiter, *Nature*, 415, 997–1000, 2002.
- Combi, M. R., K. Kabin, T. I. Gombosi, D. L. DeZeeuw and K. G. Powell**, Io's plasma environment during the Galileo flyby: Global three-dimensional MHD modeling with adaptive mesh refinement, *Journal of Geophysical Research*, 103, 9071–9082, 1998.
- Connerney, J. E. P. and T. Satoh**, The H_3^+ ion: a remote diagnostic of the jovian magnetosphere, in *Astronomy, physics and chemistry of H_3^+* , vol. 358 of *Royal Society of London Philosophical Transactions Series A*, 2471 ff., 2000.
- Connerney, J. E. P., M. H. Acuna and N. F. Ness**, Voyager 1 assessment of Jupiter's planetary magnetic field, *Journal of Geophysical Research*, 87, 3623–3627, 1982.
- Connerney, J. E. P., R. Baron, T. Satoh and T. Owen**, Images of Excited H_3^+ at the Foot of the Io Flux Tube in Jupiter's Atmosphere, *Science*, 262, 1035–1038, 1993.
- Connerney, J. E. P., M. H. Acuña, N. F. Ness and T. Satoh**, New models of Jupiter's magnetic field constrained by the Io flux tube footprint, *Journal of Geophysical Research*, 103, 11929–11940, 1998.
- Crary, F. J. and F. Bagenal**, Coupling the plasma interaction at Io to Jupiter, *Geophysical Research Letters*, 24, 2135–2138, 1997.

- Deift, P. A. and C. K. Goertz**, The propagation of Alfvén waves along Io's flux tube, *Planetary and Space Science*, 21, 1417–1429, 1973.
- Delamere, P. A., F. Bagenal, R. Ergun and Y. Su**, Momentum transfer between the Io plasma wake and Jupiter's ionosphere, *Journal of Geophysical Research (Space Physics)*, 108, 1241, 2003.
- Dols, V.**, The interaction of Io and the jovian magnetic field: Io's Alfvén wings and particle acceleration, Master's thesis, University of Alaska Fairbanks, 2001.
- Dols, V., J. C. Gérard, J. T. Clarke, J. Gustin and D. Grodent**, Diagnostics of the Jovian Aurora Deduced from Ultraviolet Spectroscopy: Model and HST/GHRS Observations, *Icarus*, 147, 251–266, 2000.
- Dols, V., P. A. Delamere and F. Bagenal**, A multispecies chemistry model of Io's local interaction with the Plasma Torus, *Journal of Geophysical Research (Space Physics)*, 113, (A12), A09208, 2008.
- Dougherty, M. K., K. K. Khurana, F. M. Neubauer, C. T. Russell, J. Saur, J. S. Leisner and M. E. Burton**, Identification of a Dynamic Atmosphere at Enceladus with the Cassini Magnetometer, *Science*, 311, 1406–1409, 2006.
- Drell, S. D., H. M. Foley and M. A. Ruderman**, Drag and Propulsion of Large Satellites in the Ionosphere: An Alfvén Propulsion Engine in Space, *Journal of Geophysical Research*, 70, 3131–3145, 1965.
- Farrell, W. M., W. S. Kurth, R. L. Tokar, J. Wahlund, D. A. Gurnett, Z. Wang, R. J. MacDowall, M. W. Morooka, R. E. Johnson and J. H. Waite**, Modification of the plasma in the near-vicinity of Enceladus by the enveloping dust, *Geophysical Research Letters*, 37, L20202, 2010.
- Frank, L. A. and W. R. Paterson**, Intense electron beams observed at Io with the Galileo spacecraft, *Journal of Geophysical Research*, 104, 28657–28670, 1999.
- Frank, L. A. and W. R. Paterson**, Return to Io by the Galileo spacecraft: Plasma observations, *Journal of Geophysical Research*, 105, 25363–25378, 2000.
- Frank, L. A. and W. R. Paterson**, Galileo observations of electron beams and thermal ions in Jupiter's magnetosphere and their relationship to the auroras, *Journal of Geophysical Research (Space Physics)*, 107, 1478, 2002a.
- Frank, L. A. and W. R. Paterson**, Plasmas observed with the Galileo spacecraft during its flyby over Io's northern polar region, *Journal of Geophysical Research (Space Physics)*, 107, 1220, 2002b.
- Frank, L. A. and W. R. Paterson**, Plasmas observed near local noon in Jupiter's magnetosphere with the Galileo spacecraft, *Journal of Geophysical Research (Space Physics)*, 109, (A18), A11217, 2004.
- Geissler, P. E. and D. B. Goldstein**, *Plumes and their deposits*, 163 ff., Springer Praxis Books / Geophysical Sciences, 2007.
- Gérard, J., J. Gustin, D. Grodent, P. Delamere and J. T. Clarke**, Excitation of the FUV Io tail on Jupiter: Characterization of the electron precipitation, *Journal of Geophysical Research (Space Physics)*, 107, 1394, 2002.

- Gérard, J., A. Saglam, D. Grodent and J. T. Clarke**, Morphology of the ultraviolet Io footprint emission and its control by Io's location, *Journal of Geophysical Research (Space Physics)*, 111, (A10), A04202, 2006.
- Goertz, C. K.**, Io's interaction with the plasma torus, *Journal of Geophysical Research*, 85, 2949–2956, 1980.
- Goertz, C. K. and P. A. Deift**, Io's interaction with the magnetosphere, *Planetary and Space Science*, 21, 1399–1415, 1973.
- Goldreich, P. and D. Lynden-Bell**, Io, a jovian unipolar inductor, *The Astrophysical Journal*, 156, 59–78, 1969.
- Grodent, D., B. Bonfond, J. Gérard, A. Radioti, J. Gustin, J. T. Clarke, J. Nichols and J. E. P. Connerney**, Auroral evidence of a localized magnetic anomaly in Jupiter's northern hemisphere, *Journal of Geophysical Research (Space Physics)*, 113, (A12), A09201, 2008.
- Gurnett, D. A., A. Lecacheux, W. S. Kurth, A. M. Persoon, J. B. Groene, L. Lamy, P. Zarka and J. F. Carbary**, Discovery of a north-south asymmetry in Saturn's radio rotation period, *Geophysical Research Letters*, 36, L16102, 2009.
- Haff, P. K., G. L. Siscoe and A. Eviatar**, Ring and plasma - The enigmas of Enceladus, *Icarus*, 56, 426–438, 1983.
- Hayes, J. C., M. L. Norman, R. A. Fiedler, J. O. Bordner, P. S. Li, S. E. Clark, A. ud-Doula and M. Mac Low**, Simulating Radiating and Magnetized Flows in Multiple Dimensions with ZEUS-MP, *The Astrophysical Journals*, 165, 188–228, 2006.
- Hess, S., F. Mottez and P. Zarka**, Jovian S burst generation by Alfvén waves, *Journal of Geophysical Research (Space Physics)*, 112, (A11), A11212, 2007.
- Hess, S. L. G., P. Delamere, V. Dols, B. Bonfond and D. Swift**, Power transmission and particle acceleration along the Io flux tube, *Journal of Geophysical Research (Space Physics)*, 115, A06205, 2010.
- Hill, T. W. and D. H. Pontius**, Plasma injection near Io, *Journal of Geophysical Research*, 103, 19879–19886, 1998.
- Hill, T. W. and V. M. Vasylūnas**, Jovian auroral signature of Io's corotational wake, *Journal of Geophysical Research (Space Physics)*, 107, 1464, 2002.
- Hoang, S., N. Meyer-Vernet, M. Moncuquet, A. Lecacheux and B. M. Pedersen**, Electron density and temperature in the Io plasma torus from Ulysses thermal noise measurements, *Planetary and Space Science*, 41, 1011–1020, 1993.
- Jacobsen, S.**, Die nichtlineare Wechselwirkung von Ios Alfvénflügeln mit dem Plasmatorus und der Jupitermagnetosphäre, Master's thesis, University of Cologne, 2006.
- Jacobsen, S., F. M. Neubauer, J. Saur and N. Schilling**, Io's nonlinear MHD-wave field in the heterogeneous Jovian magnetosphere, *Geophysical Research Letters*, 34, L10202, 2007.

- Jacobsen, S., J. Saur, F. M. Neubauer, B. Bonfond, J. Gérard and D. Grodent**, Location and spatial shape of electron beams in Io's wake, *Journal of Geophysical Research (Space Physics)*, 115, (A14), A04205, 2010.
- Jia, Y., C. T. Russell, K. K. Khurana, J. S. Leisner, Y. J. Ma and M. K. Dougherty**, Time-varying magnetospheric environment near Enceladus as seen by the Cassini magnetometer, *Geophysical Research Letters*, 37, L09203, 2010a.
- Jia, Y., C. T. Russell, K. K. Khurana, Y. J. Ma, W. Kurth and T. I. Gombosi**, Interaction of Saturn's magnetosphere and its moons: 3. Time variation of the Enceladus plume, *Journal of Geophysical Research (Space Physics)*, 115, A12243, 2010b.
- Jia, Y., C. T. Russell, K. K. Khurana, Y. J. Ma, D. Najib and T. I. Gombosi**, Interaction of Saturn's magnetosphere and its moons: 2. Shape of the Enceladus plume, *Journal of Geophysical Research (Space Physics)*, 115, (A14), A04215, 2010c.
- Jia, Y., C. T. Russell, K. K. Khurana, G. Toth, J. S. Leisner and T. I. Gombosi**, Interaction of Saturn's magnetosphere and its moons: 1. Interaction between corotating plasma and standard obstacles, *Journal of Geophysical Research (Space Physics)*, 115, (A14), A04214, 2010d.
- Jones, S. T. and Y. Su**, Role of dispersive Alfvén waves in generating parallel electric fields along the Io-Jupiter fluxtube, *Journal of Geophysical Research (Space Physics)*, 113, (A12), A12205, 2008.
- Khurana, K. K.**, Euler potential models of Jupiter's magnetospheric field, *Journal of Geophysical Research*, 102, 11295–11306, 1997.
- Khurana, K. K., M. G. Kivelson, V. M. Vasyliunas, N. Krupp, J. Woch, A. Lagg, B. H. Mauk and W. S. Kurth**, *The configuration of Jupiter's magnetosphere*, 593–616, 2004.
- Khurana, K. K., C. T. Russell and M. K. Dougherty**, Magnetic portraits of Tethys and Rhea, *Icarus*, 193, 465–474, 2008.
- Kivelson, M. G., F. Bagenal, W. S. Kurth, F. M. Neubauer, C. Paranicas and J. Saur**, *Magnetospheric interactions with satellites*, 513–536, 2004.
- Kliore, A. J., G. Fjeldbo, B. L. Seidel, D. N. Sweetnam, T. T. Sesplaukis, P. M. Woiceshyn and S. I. Rasool**, The atmosphere of Io from Pioneer 10 radio occultation measurements, *Icarus*, 24, 407–410, 1975.
- Klumpar, D. M.**, *Near equatorial signatures of dynamic auroral processes*, 265–276, 1990.
- Klumpar, D. M., J. M. Quinn and E. G. Shelley**, Counter-streaming electrons at the geomagnetic equator near 9 earth radii, *Geophysical Research Letters*, 15, 1295–1298, 1988.
- Knight, S.**, Parallel electric fields, *Planetary and Space Science*, 21, 741–750, 1973.
- Kopp, A.**, Modifications of the electrodynamic interaction between Jupiter and Io due to mass loading effects, *Journal of Geophysical Research*, 101, 24943–24954, 1996.

- Kriegel, H., S. Simon, J. Müller, U. Motschmann, J. Saur, K. Glassmeier and M. K. Dougherty**, The plasma interaction of Enceladus: 3D hybrid simulations and comparison with Cassini MAG data, *Planetary and Space Science*, 57, 2113–2122, 2009.
- Kupo, I., Y. Mekler and A. Eviatar**, Detection of ionized sulfur in the Jovian magnetosphere, *The Astrophysical Journal*, 205, L51–L53, 1976.
- Lellouch, E., M. A. McGrath and K. L. Jessup**, *Io's atmosphere*, 231 ff., Springer Praxis Books / Geophysical Sciences, 2007.
- Leneman, D.**, Reflection of Alfvén waves from boundaries with different conductivities, *Physics of Plasmas*, 14, (12), 122109, 2007.
- Linker, J. A., M. G. Kivelson and R. J. Walker**, An MHD simulation of plasma flow past Io - Alfvén and slow mode perturbations, *Geophysical Research Letters*, 15, 1311–1314, 1988.
- Linker, J. A., M. G. Kivelson and R. J. Walker**, The effect of mass loading on the temperature of a flowing plasma, *Geophysical Research Letters*, 16, 763–766, 1989.
- Linker, J. A., M. G. Kivelson and R. J. Walker**, A three-dimensional MHD simulation of plasma flow past Io, *Journal of Geophysical Research*, 96, 21037–21053, 1991.
- Louarn, P.**, Acceleration in magnetospheres, in *Solar Variability: From Core to Outer Frontiers*, edited by A. Wilson, vol. 506 of *ESA Special Publication*, 233–243, 2002.
- Lyons, L. R.**, Generation of large-scale regions of auroral currents, electric potentials, and precipitation by the divergence of the convection electric field, *Journal of Geophysical Research*, 85, 17–24, 1980.
- Lysak, R. L. and Y. Song**, A three-dimensional model of the propagation of Alfvén waves through the auroral ionosphere: first results, *Advances in Space Research*, 28, (5), 813–822, 2001.
- Marklund, G. T., N. Ivchenko, T. Karlsson, A. Fazakerley, M. Dunlop, P. Lindqvist, S. Buchert, C. Owen, M. Taylor, A. Vaivalds, P. Carter, M. André and A. Balogh**, Temporal evolution of the electric field accelerating electrons away from the auroral ionosphere, *Nature*, 414, 724–727, 2001.
- Mauk, B. H. and J. Saur**, Equatorial electron beams and auroral structuring at Jupiter, *Journal of Geophysical Research (Space Physics)*, 112, (A11), A10221, 2007.
- Mauk, B. H., D. J. Williams and A. Eviatar**, Understanding Io's space environment interaction: Recent energetic electron measurements from Galileo, *Journal of Geophysical Research*, 106, 26195–26208, 2001.
- Mauk, B. H., B. J. Anderson and R. M. Thorne**, *Magnetosphere-Ionosphere Coupling at Earth, Jupiter, and Beyond*, 97 ff., 2002.
- McGrath, M. A., E. Lellouch, D. F. Strobel, P. D. Feldman and R. E. Johnson**, *Satellite atmospheres*, 457–483, 2004.

- Mitchell, D. G., W. S. Kurth, G. B. Hospodarsky, N. Krupp, J. Saur, B. H. Mauk, J. F. Carbary, S. M. Krimigis, M. K. Dougherty and D. C. Hamilton**, Ion conics and electron beams associated with auroral processes on Saturn, *Journal of Geophysical Research (Space Physics)*, 114, (A13), A02212, 2009.
- Moncuquet, M., F. Bagenal and N. Meyer-Vernet**, Latitudinal structure of outer Io plasma torus, *Journal of Geophysical Research (Space Physics)*, 107, 1260, 2002.
- Morabito, L. A., S. P. Synnott, P. N. Kupferman and S. A. Collins**, Discovery of currently active extraterrestrial volcanism, *Science*, 204, 972, 1979.
- Neubauer, F. M.**, Nonlinear standing Alfvén wave current system at Io - Theory, *Journal of Geophysical Research*, 85, 1171–1178, 1980.
- Neubauer, F. M.**, The sub-Alfvénic interaction of the Galilean satellites with the Jovian magnetosphere, *Journal of Geophysical Research*, 103, 19843–19866, 1998.
- Peale, S. J., P. Cassen and R. T. Reynolds**, Melting of Io by tidal dissipation, *Science*, 203, 892–894, 1979.
- Pearl, J., R. Hanel, V. Kunde, W. Maguire, K. Fox, S. Gupta, C. Ponnampereuma and F. Raulin**, Identification of gaseous SO₂ and new upper limits for other gases on Io, *Nature*, 280, 755–758, 1979.
- Persoon, A. M., D. A. Gurnett, W. S. Kurth and J. B. Groene**, A simple scale height model of the electron density in Saturn's plasma disk, *Geophysical Research Letters*, 33, L18106, 2006.
- Piddington, J. H. and J. F. Drake**, Electrodynamical Effects of Jupiter's Satellite Io, *Nature*, 217, 935–937, 1968.
- Pilipenko, V., E. Fedorov, M. J. Engebretson and K. Yumoto**, Energy budget of Alfvén wave interactions with the auroral acceleration region, *Journal of Geophysical Research (Space Physics)*, 109, (A18), A10204, 2004.
- Porco, C. C., P. Helfenstein, P. C. Thomas, A. P. Ingersoll, J. Wisdom, R. West, G. Neukum, T. Denk, R. Wagner, T. Roatsch, S. Kieffer, E. Turtle, A. McEwen, T. V. Johnson, J. Rathbun, J. Veverka, D. Wilson, J. Perry, J. Spitale, A. Brahic, J. A. Burns, A. D. Del Genio, L. Dones, C. D. Murray and S. Squyres**, Cassini Observes the Active South Pole of Enceladus, *Science*, 311, 1393–1401, 2006.
- Prangé, R., D. Rego, D. Southwood, P. Zarka, S. Miller and W. Ip**, Rapid energy dissipation and variability of the Io-Jupiter electrodynamic circuit, *Nature*, 380, 460, 1996.
- Pryor, W. R., A. M. Rymer, D. G. Mitchell, T. W. Hill, D. T. Young, J. Saur, G. H. Jones, S. Jacobsen, S. W. H. Cowley, B. H. Mauk, A. J. Coates, J. Gustin, D. Grodent, J.-C. Gérard, L. Lamy, J. D. Nichols, S. M. Krimigis, L. W. Esposito, M. K. Dougherty, A. J. Jouchoux, A. I. F. Stewart, W. E. McClintock, G. M. Holsclaw, J. M. Ajello, J. E. Colwell, A. R. Hendrix, F. J. Crary, J. T. Clarke and X. Zhou**, The auroral footprint of Enceladus on Saturn, *Nature*, in press, 2011.
- Ray, L. C., Y. Su, R. E. Ergun, P. A. Delamere and F. Bagenal**, Current-voltage relation of a centrifugally confined plasma, *Journal of Geophysical Research (Space Physics)*, 114, (A13), A04214, 2009.

- Roth, L., J. Saur, K. D. Retherford, D. F. Strobel and J. R. Spencer**, Simulation of Io's Auroral Emission: Constraints on the Atmosphere in Eclipse, *Icarus*, submitted, 2011.
- Saur, J. and D. F. Strobel**, Atmospheres and Plasma Interactions at Saturn's Largest Inner Icy Satellites, *The Astrophysical Journal Letters*, 620, L115–L118, 2005.
- Saur, J., F. M. Neubauer, D. F. Strobel and M. E. Summers**, Three-dimensional plasma simulation of Io's interaction with the Io plasma torus: Asymmetric plasma flow, *Journal of Geophysical Research*, 104, 25105–25126, 1999.
- Saur, J., F. M. Neubauer, D. F. Strobel and M. E. Summers**, Interpretation of Galileo's Io plasma and field observations: I0, I24, and I27 flybys and close polar passes, *Journal of Geophysical Research (Space Physics)*, 107, 1422, 2002.
- Saur, J., F. M. Neubauer, J. E. P. Connerney, P. Zarka and M. G. Kivelson**, Plasma interaction of Io with its plasma torus, 537–560, 2004.
- Saur, J., B. H. Mauk, D. G. Mitchell, N. Krupp, K. K. Khurana, S. Livi, S. M. Krimigis, P. T. Newell, D. J. Williams, P. C. Brandt, A. Lagg, E. Roussos and M. K. Dougherty**, Anti-planetward auroral electron beams at Saturn, *Nature*, 439, 699–702, 2006.
- Saur, J., F. M. Neubauer and N. Schilling**, Hemisphere coupling in Enceladus' asymmetric plasma interaction, *Journal of Geophysical Research (Space Physics)*, 112, (A11), A11209, 2007.
- Saur, J., N. Schilling, F. M. Neubauer, D. F. Strobel, S. Simon, M. K. Dougherty, C. T. Russell and R. T. Pappalardo**, Evidence for temporal variability of Enceladus' gas jets: Modeling of Cassini observations, *Geophysical Research Letters*, 35, L20105, 2008.
- Schenk, P.**, *Atlas of the Galilean Satellites*, Cambridge University Press, 2010.
- Scholer, M.**, On the motion of artificial ion clouds in the magnetosphere, *Planetary and Space Science*, 18, 977–1004, 1970.
- Seufert, M.**, Dynamische Wechselwirkung von Alfvénwellenpaketen, Master's thesis, University of Cologne, 2008.
- Seufert, M., J. Saur and F. M. Neubauer**, Multi-frequency Electromagnetic Sounding of the Galilean Moons, *Icarus*, in press, 2011.
- Shain, C. A.**, Location on Jupiter of a Source of Radio Noise, *Nature*, 176, 836–837, 1955.
- Shkolnik, E., G. A. H. Walker and D. A. Bohlender**, Evidence for Planet-induced Chromospheric Activity on HD 179949, *The Astrophysical Journal*, 597, 1092–1096, 2003.
- Shkolnik, E., G. A. H. Walker, D. A. Bohlender, P. Gu and M. Kürster**, Hot Jupiters and Hot Spots: The Short- and Long-Term Chromospheric Activity on Stars with Giant Planets, *The Astrophysical Journal*, 622, 1075–1090, 2005.

- Simon, S., J. Saur, F. M. Neubauer, U. Motschmann and M. K. Dougherty**, Plasma wake of Tethys: Hybrid simulations versus Cassini MAG data, *Geophysical Research Letters*, 36, L04108, 2009.
- Simon, S., J. Saur, H. Kriegel, F. M. Neubauer, U. Motschmann and M. K. Dougherty**, Influence of negatively charged plume grains and hemisphere coupling currents on the structure of Enceladus' Alfvén wings: Analytical modeling of Cassini magnetometer observations, *Journal of Geophysical Research (Space Physics)*, in press, 2011.
- Smith, R. A. and C. K. Goertz**, On the modulation of the Jovian decametric radiation by Io. I - Acceleration of charged particles, *Journal of Geophysical Research*, 83, 2617–2627, 1978.
- Smith, B. A., E. M. Shoemaker, S. W. Kieffer and I. A. F. Cook**, The role of SO₂ in volcanism on Io, *Nature*, 280, 738–743, 1979a.
- Smith, B. A., L. A. Soderblom, T. V. Johnson, A. P. Ingersoll, S. A. Collins, E. M. Shoemaker, G. E. Hunt, H. Masursky, M. H. Carr, M. E. Davies, A. F. Cook, J. M. Boyce, T. Owen, G. E. Danielson, C. Sagan, R. F. Beebe, J. Veverka, J. F. McCauley, R. G. Strom, D. Morrison, G. A. Briggs and V. E. Suomi**, The Jupiter system through the eyes of Voyager 1, *Science*, 204, 951–957, 1979b.
- Smyth, W. H., C. Peterson and M. L. Marconi**, A Consistent Understanding of the Ribbon Structure for the Io Plasma Torus at the Voyager 1, 1991 Ground-Based, and Galileo J0 Epochs, *Journal of Geophysical Research (Space Physics)*, in press, 2011.
- Southwood, D. J. and M. W. Dunlop**, Mass pickup in sub-Alfvénic plasma flow - A case study for Io, *Planetary and Space Science*, 32, 1079–1086, 1984.
- Spahn, F., J. Schmidt, N. Albers, M. Hörning, M. Makuch, M. Seiß, S. Kempf, R. Srama, V. Dikarev, S. Helfert, G. Moragas-Klostermeyer, A. V. Krivov, M. Sremčević, A. J. Tuzzolino, T. Economou and E. Grün**, Cassini Dust Measurements at Enceladus and Implications for the Origin of the E Ring, *Science*, 311, 1416–1418, 2006.
- Spencer, J. R., J. C. Pearl, M. Segura, F. M. Flasar, A. Mamoutkine, P. Romani, B. J. Buratti, A. R. Hendrix, L. J. Spilker and R. M. C. Lopes**, Cassini Encounters Enceladus: Background and the Discovery of a South Polar Hot Spot, *Science*, 311, 1401–1405, 2006.
- Spencer, J. R., S. A. Stern, A. F. Cheng, H. A. Weaver, D. C. Reuter, K. Retherford, A. Lunsford, J. M. Moore, O. Abramov, R. M. C. Lopes, J. E. Perry, L. Kamp, M. Showalter, K. L. Jessup, F. Marchis, P. M. Schenk and C. Dumas**, Io Volcanism Seen by New Horizons: A Major Eruption of the Tvashtar Volcano, *Science*, 318, 240–, 2007.
- Squyres, S. W., R. T. Reynolds and P. M. Cassen**, The evolution of Enceladus, *Icarus*, 53, 319–331, 1983.
- Steffl, A. J., P. A. Delamere and F. Bagenal**, Cassini UVIS observations of the Io plasma torus. III. Observations of temporal and azimuthal variability, *Icarus*, 180, 124–140, 2006.

- Stone, J. M. and M. L. Norman**, ZEUS-2D: A radiation magnetohydrodynamics code for astrophysical flows in two space dimensions. I - The hydrodynamic algorithms and tests., *The Astrophysical Journals*, 80, 753–790, 1992a.
- Stone, J. M. and M. L. Norman**, ZEUS-2D: A Radiation Magnetohydrodynamics Code for Astrophysical Flows in Two Space Dimensions. II. The Magnetohydrodynamic Algorithms and Tests, *The Astrophysical Journals*, 80, 791–818, 1992b.
- Stone, J. M., D. Mihalas and M. L. Norman**, ZEUS-2D: A radiation magnetohydrodynamics code for astrophysical flows in two space dimensions. III - The radiation hydrodynamic algorithms and tests, *The Astrophysical Journals*, 80, 819–845, 1992.
- Su, Y., R. E. Ergun, F. Bagenal and P. A. Delamere**, Io-related Jovian auroral arcs: Modeling parallel electric fields, *Journal of Geophysical Research (Space Physics)*, 108, 1094, 2003.
- Su, Y., S. T. Jones, R. E. Ergun, F. Bagenal, S. E. Parker, P. A. Delamere and R. L. Lysak**, Io-Jupiter interaction: Alfvén wave propagation and ionospheric Alfvén resonator, *Journal of Geophysical Research (Space Physics)*, 111, (A10), A06211, 2006.
- Swift, D. W.**, Simulation of auroral electron acceleration by inertial Alfvén waves, *Journal of Geophysical Research (Space Physics)*, 112, (A11), A12207, 2007.
- Thomas, N.**, The variability of the Io plasma torus, *Journal of Geophysical Research*, 98, L18737, 1993.
- Thomas, N., F. Bagenal, T. W. Hill and J. K. Wilson**, *The Io neutral clouds and plasma torus*, 561–591, 2004.
- Tokar, R. L., R. E. Johnson, T. W. Hill, D. H. Pontius, W. S. Kurth, F. J. Crary, D. T. Young, M. F. Thomsen, D. B. Reisenfeld, A. J. Coates, G. R. Lewis, E. C. Sittler and D. A. Gurnett**, The Interaction of the Atmosphere of Enceladus with Saturn’s Plasma, *Science*, 311, 1409–1412, 2006.
- Tomás, A. T., J. Woch, N. Krupp, A. Lagg, K. Glassmeier and W. S. Kurth**, Energetic electrons in the inner part of the Jovian magnetosphere and their relation to auroral emissions, *Journal of Geophysical Research (Space Physics)*, 109, (A18), A06203, 2004.
- Vasyliūnas, V. M.**, Electric field and plasma flow: What drives what?, *Geophysical Research Letters*, 28, 2177–2180, 2001.
- Vasyliūnas, V. M.**, Relation between magnetic fields and electric currents in plasmas, *Annales Geophysicae*, 23, 2589–2597, 2005.
- Vogt, J. and G. Haerendel**, Reflection and transmission of Alfvén waves at the auroral acceleration region, *Geophysical Research Letters*, 25, 277–280, 1998.
- Waite, J. H., M. R. Combi, W. Ip, T. E. Cravens, R. L. McNutt, W. Kasprzak, R. Yelle, J. Luhmann, H. Niemann, D. Gell, B. Magee, G. Fletcher, J. Lunine and W. Tseng**, Cassini Ion and Neutral Mass Spectrometer: Enceladus Plume Composition and Structure, *Science*, 311, 1419–1422, 2006.

- Warwick, J. W. and G. A. Dulk**, Faraday Rotation on Decametric Radio Emissions from Jupiter, *Science*, 145, (3630), 380–383, 1964.
- Williams, D. A. and R. R. Howell**, *Active volcanism: Effusive eruptions*, 133 ff., Springer Praxis Books / Geophysical Sciences, 2007.
- Williams, D. J. and R. M. Thorne**, Energetic particles over Io's polar caps, *Journal of Geophysical Research (Space Physics)*, 108, 1397, 2003.
- Williams, D. J., B. H. Mauk, R. E. McEntire, E. C. Roelof, T. P. Armstrong, B. Wilken, J. G. Roederer, S. M. Krimigis, T. A. Fritz and L. J. Lanzerotti**, Electron Beams and Ion Composition Measured at Io and in Its Torus, *Science*, 274, 401–403, 1996.
- Williams, D. J., R. M. Thorne and B. Mauk**, Energetic electron beams and trapped electrons at Io, *Journal of Geophysical Research*, 104, 14739–14754, 1999.
- Wilson, R. J., R. L. Tokar and M. G. Henderson**, Thermal ion flow in Saturn's inner magnetosphere measured by the Cassini plasma spectrometer: A signature of the Enceladus torus?, *Geophysical Research Letters*, 36, L23104, 2009.
- Wolf-Gladrow, D. A., F. M. Neubauer and M. Lussem**, Io's interaction with the plasma torus - A self-consistent model, *Journal of Geophysical Research*, 92, 9949–9961, 1987.
- Wright, A. N.**, The interaction of Io's Alfvén waves with the Jovian magnetosphere, *Journal of Geophysical Research*, 92, 9963–9970, 1987.
- Wright, A. N. and S. J. Schwartz**, The transmission of Alfvén waves through the Io plasma torus, *Journal of Geophysical Research*, 94, 3749–3754, 1989.
- Zarka, P.**, Auroral radio emissions at the outer planets: Observations and theories, *Journal of Geophysical Research*, 103, 20159–20194, 1998.
- Zhang, J., D. B. Goldstein, P. L. Varghese, N. E. Gimelshein, S. F. Gimelshein and D. A. Levin**, Simulation of gas dynamics and radiation in volcanic plumes on Io, *Icarus*, 163, 182–197, 2003.
- Zhang, J., D. B. Goldstein, P. L. Varghese, L. Trafton, C. Moore and K. Miki**, Numerical modeling of ionian volcanic plumes with entrained particulates, *Icarus*, 172, 479–502, 2004.

Danksagung

Zuallererst möchte ich mich bei Prof. Dr. Joachim Saur, dem Betreuer meiner Arbeit bedanken. Er war eine große Unterstützung, hat mich stets motiviert und hat durch seine Fähigkeit auch komplizierte plasmaphysikalische Zusammenhänge anschaulich zu erklären sehr zum Gelingen dieser Arbeit beigetragen. Ich hatte immer das Gefühl, dass er großes Vertrauen in meine Forschung hat. Er hat es andererseits aber auch verstanden bei allem Optimismus meinen kritischen Blick für die Ergebnisse zu schärfen.

Herrn Prof. Dr. Fritz Neubauer möchte ich für die Übernahme des Koreferats danken. Er hat gewissermassen die Basis für diese Dissertation geliefert. Zum einen fachlich durch seine eigenen Arbeiten auf diesem Gebiet, zum anderen hat er mich motiviert, die Io-Jupiter Wechselwirkung zum Gegenstand meiner Diplomarbeit zu machen, auf welcher die vorliegende Arbeit aufbaut. Besonders habe ich aber bei verschiedensten Fragestellungen von seinem großen Erfahrungsschatz und Wissen profitiert.

Alexandre (Lex) Wennmacher gebührt mein Dank für die Weitergabe seines profunden Computerwissens. Im Rahmen meiner Tätigkeit in der Systemgruppe habe ich dadurch sehr viel lernen können.

Ein besonderes Dankeschön geht auch an die Korrekturleser dieser Arbeit Emmanuel Chané, Mario Seufert und Lorenz Roth, sowie Sven Simon für fachlichen Rat und Diskussionen über die Cassini MAG Beobachtungen.

Über die Jahre gesehen habe ich mit vielen Kollegen das Büro geteilt. Hervorheben möchte ich Emmanuel Chané, Olga Alexandrova, Nico Schilling und Heiko Backes. Danke für den Spaß bei der Arbeit. Besonders Emmanuel Chané, der mit mir in der Endphase das Büro teilen musste danke ich darüberhinaus für sein offenes Ohr, Rat, Motivation und kritische Fragen.

Meinen Mitstreitern im Studium Markus (Mabo) Fels, Olaf Koch, Jörn Löhken, Tom Andert und dem längsten Studiengefährten Lars Nieradzick danke ich für die super Zeit. Ohne Euch weiß ich nicht, ob ich durchgehalten hätte.

Allen Kollegen vom Institut für Geophysik danke ich für das außerordentlich gute Arbeitsklima aber auch für off-topic Mensa Gespräche, gemeinsame Fußballspiele, Grillabende und Skiurlaube. Es war eine tolle Zeit für mich am IGM in Köln, die ich nie vergessen werde.

Ganz besonders möchte ich mich auch bei meinen Eltern bedanken, denn ich habe ihnen viel Geduld abverlangt. Nichtsdestotrotz haben sie immer an mich geglaubt und mich nach Kräften finanziell und moralisch unterstützt.

Besonderer Dank gebührt meiner Freundin Daniela, die mir stets zur Seite stand. Sie musste vor allem in der heißen Phase viel ertragen und hat mir heldenhaft den Rücken frei gehalten. Danke dafür!

Lebenslauf



Sven Jacobsen

Luxemburger Str. 83

50674 Köln

geb. am 25.06.1976 in Hamm (Westf.)

Staatsangehörigkeit: Deutsch

Schulausbildung

1982 – 1986

Mariengrundschule Büderich, Werl

1986 – 1995

Ursulinengymnasium, Werl, Abschluss: Abitur

Hochschulstudium

10/1996 – 05/2007

Universität zu Köln

Studium der Geophysik

Abschluss: Diplom Geophysiker

seit 07/2007

Universität zu Köln

Promotionsstudium Geophysik

Berufliche Tätigkeiten

07/1999 – 05/2007

Studentische Hilfskraft am

Institut für Geophysik der Universität zu Köln

seit 07/2007

Wissenschaftlicher Mitarbeiter am

Institut für Geophysik der Universität zu Köln